# Heat Transfer and Flow Measurements in an Atmospheric Lean Pre-Mixed Combustor

BY: DAVID GOMEZ RAMIREZ

Dissertation submitted to the faculty of the
Virginia Polytechnic Institute and State University
in partial fulfillment of the requirements for the degree of

Doctor of Philosophy
in
Mechanical Engineering

**Committee Members**
Srinath V. Ekkad, Chair
Brian Y. Lattimer
Kevin T. Lowe
Wing F. Ng
Danesh K. Tafti

6/3/2016
Blacksburg, Virginia

Keywords: Heat transfer, gas turbine combustor, infrared thermography, particle image velocimetry.

# ABSTRACT

Heat Transfer and Flow Measurements in an Atmospheric Lean Pre-Mixed Combustor
(June 2016)

David Gomez Ramirez

Chair of Advisory Committee: Srinath V. Ekkad

Energy conservation, efficiency, and environmental responsibility are priorities for modern energy technologies. The ever increasing demands for lower pollutants and higher performance have driven the development of low-emission gas turbine engines, operating at lean equivalence ratios and at increasingly higher turbine inlet temperatures. This has placed new constraints on gas turbine combustor design, particularly in regards to the cooling technologies available for the combustor liner walls. To optimize combustor thermal management, and in turn optimize overall engine performance, detailed measurements of the flame side heat transfer are required. However, given the challenging environment at which gas turbine combustors operate, there are currently only limited studies that quantify flame side combustor heat transfer; in particular at reacting conditions.

The objective of the present work was to develop methodologies to measure heat transfer within a reacting gas turbine combustor. To accomplish this, an optically accessible research combustor system was designed and constructed at Virginia Tech, capable of operating at 650 K inlet temperature, maximum air mass flow rates of 1.3 kg/s, and flame temperatures over 1800 K. Flow and heat transfer measurements at non-reacting and reacting conditions were carried out for Reynolds numbers (Re) with respect to the combustor diameter ranging from $\sim 11\,500$ to $\sim 140\,000$ (depending on the condition). Particle Image Velocimetry (PIV) was used to measure the non-reacting flow field within the burner, leading to the identification of coherent structures in the flow that accounted for over 30% of the flow fluctuation kinetic energy along the swirling jet shear layers. The capability of infrared (IR) thermography to image surface temperatures through a fused silica (quartz) glass was demonstrated at non-reacting conditions. IR thermography was then used to measure the non-reacting steady state heat transfer along the combustor liner. A peak in heat transfer was identified at $\sim 1$ nozzle diameter downstream of the combustor dome plate. The peak Nusselt number along the liner was over 18 times higher than

that predicted from fully developed turbulent pipe flow correlations, which have traditionally been used to estimate flame side combustor heat transfer.

For the reacting measurements, a novel time-dependent heat transfer methodology was developed that allowed for the investigation of transient heat loads, including those occurring during engine ignition and shutdown. The methodology was validated at non-reacting conditions, by comparing results from an experiment with changing flow temperature, to the results obtained at steady state. The difference between the time-dependent and the steady state measurements were between 3% and 17.3% for different mass flow conditions. The time-dependent methodology was applied to reacting conditions for combustor Reynolds numbers of $\sim 12\,000$ and $\sim 24\,000$. At an equivalence ratio of $\sim 0.5$ and a combustor Reynolds number of $\sim 12\,000$, the peak heat load location in reaction was shifted downstream by 0.2 nozzle diameters compared to the non-reacting cases. At higher equivalence ratios, and more visibly at a Reynolds number of $\sim 24\,000$, the heat transfer distribution along the combustor liner exhibited two peaks, upstream and downstream of the impingement location ($X/D_N = 0.8 - 1.0$ and $X/D_N \approx 2.5$). Reacting PIV was performed at $\mathrm{Re} = 12\,000$ showing the presence of a strong corner recirculation, which could potentially convect reactants upstream of the impingement point, leading to the double peak structure observed.

The methodologies developed have provided insight into heat transfer within gas turbine combustors. The methods can be used to explore additional conditions and expand the dataset beyond what is presented, to fully characterize reacting combustor heat transfer.

# GENERAL ABSTRACT

Heat Transfer and Flow Measurements in an Atmospheric Lean Pre-Mixed Combustor
(June 2016)

David Gomez Ramirez

Chair of Advisory Committee: Srinath V. Ekkad

Energy conservation, efficiency, and environmental responsibility are priorities for modern energy technologies. The ever increasing demands for lower pollutants and higher performance have driven the development of low-emission gas turbine engines, operating at lean equivalence ratios and at increasingly higher turbine inlet temperatures. This has placed new constraints on gas turbine combustor design, particularly in regards to the cooling technologies available for the combustor liner walls. To optimize combustor thermal management, and in turn optimize overall engine performance, detailed measurements of the flame side heat transfer are required. However, given the challenging environment at which gas turbine combustors operate, there are currently only limited studies that quantify flame side combustor heat transfer; in particular at reacting conditions.

The objective of the present work was to develop methodologies to measure heat transfer within a reacting gas turbine burner. To accomplish this, an optically accessible research combustor system was designed and constructed at Virginia Tech. In addition to the heat transfer methods developed, flow measurements were performed using Particle Image Velocimetry (PIV), a well stablished technique, to complement the heat transfer data. The heat transfer measurement techniques relied on infrared (IR) emission from the hot burner walls.

First, initial heat transfer and flow studies on a non-reacting annular combustor model are presented. These measurements used traditional experimental methods and served as a starting point for the development of the methods at reacting conditions. The main considerations for the design of the reacting combustor system are then presented. Non-reacting data was taken on the designed test section, to better understand the flow and heat transfer without the added complications introduced by a flame. After characterizing the behavior at non-reacting conditions, the measurements were extended to reacting cases.

A novel methodology based on the IR emission from the hot liner walls was developed to characterize the burner heat loads. The method is non-intrusive (does not rely on sensors attached to the wall), time-accurate (can capture the time evolution of the heat loads, at shutdown or ignition for instance), and can resolve the spatial distribution of the heat transfer.

The methodologies developed have provided insight into heat transfer within gas turbine combustors. The methods can be used to explore additional conditions and expand the dataset beyond what is presented, to fully characterize reacting combustor heat transfer.

A mis padres, hermanos, abuelos y tios. Gracias por darme la fuerza para seguir adelante.

# ACKNOWLEDGEMENTS

I am incredibly grateful to have had the opportunity to study a Doctorate degree in Mechanical Engineering at Virginia Tech. I did not reach this point on my own, and I owe the successful completion of this degree to the many fantastic people who have helped me along the way.

I would like to first thank my advisor, Professor Srinath V. Ekkad, for believing in me and supporting me at all times. When he gave me the task of building a research combustor, I did not quite grasp what it entailed or whether I had the skills necessary (in retrospect, I certainly did not). Dr. Ekkad however, never doubted me and was always encouraging. Thank you Dr. Ekkad for your mentorship, and for giving me the amazing opportunity of pushing forward your vision on combustor heat transfer. I would like to also thank the members of my advisory committee, Dr. Lattimer, Dr. Lowe, Dr. Tafti and Dr. Ng for their guiding comments. At the times when I approached you for insight, you always kindly agreed to guide me.

This work would not have been possible without the support of the project sponsors: DOE-NETL University Turbine Systems Research (UTSR) program and Solar Turbines Incorporated. In particular, I would like to thank Robin Ames from NETL for his help and support over the years. Thanks to Dr. Hee-Koo Moon, Dr. Yong Kim, and Dr. Ram Srinivasan from Solar Turbines Incorporated for bringing industry's perspective into the project with their technical insights and for supporting the development of the research combustor (including the industrial hardware they donated for testing).

Thanks to the amazing Mechanical Engineering staff. In particular, I want to thank Diana Israel for always receiving me at her office with a smile, ready to help me with the procurement of all the equipment we purchased for this project. Thank you Diana.

Thank you to my labmates and friends (for the most part one and the same). Thanks to those who are still here: Jaideep, Sridharan, Prashant, Sandeep and Ranjana, Siddhartha, Andrew, John, Chu, Suhyeon, Javier, Andrea, Elisa, Marian, Bharath, Samruddhi, Shubham, Suhyeon, and Prethive; to those who have long left Blacksburg: Deepu, Sakshi, Shreyas, Barboza, Tyagi, Hardik, Ryan, Ravi, Vivek, Sukhi, Allan, Sean, Kevin, Bahare, Cissi; and to those friends from before my time in Blacksburg that continued to stay in touch: Alejandro, Esau, Jose Eduardo, Salvador, Hector, Karla, Bishoi, Ishara, Enrique, Ladislav. Thank you for

dragging me out of the lab to relax from time to time, for spending time with me, and helping me overcome the challenges I faced. In particular I would like to acknowledge Sandeep Kedukodi and Siddhartha Gadiraju who collaborated with me in this project. Siddhartha Gadiraju helped me while building the facility and taking experiments, this work would not have been possible without his help.

I want to thank as well the people who first encouraged me to pursue graduate school and who helped me when I first came to the United States, Gloria Faus Landeros, Barbara Maggi, Diane Robinson, Dr. James M. Russell, and Dr. John McNabb. Your teachings continue to guide me to this day.

Finally I would like to thank my amazing family, thank you for helping me become who I am, instilling in me my work ethic, and supporting me every step of the way.

# TABLE OF CONTENTS

# LIST OF FIGURES

# LIST OF TABLES

# PREFACE

The work in this dissertation is organized as follows and is based on manuscripts that have been prepared, submitted, or accepted for publication. The first chapter is an introduction to the topic of gas turbine combustor heat transfer and flow; its importance and the current state of affairs. The second chapter delves into initial low temperature, non-reacting measurements performed in a two-times scaled up annular combustor model. These measurements were a continuation of past studies performed by previous researchers in the group and provided a baseline of the measurements and capabilities available at low temperatures and at non-reacting conditions. Two heat transfer techniques are presented in Chapter 2: IR thermography using wall heaters at steady state, and liquid crystal thermography to capture the transient temperature change on a surface. Ideas from the techniques applied for the annular combustor were later used to develop the methodologies presented in chapters 4 and 5 for the optical combustor measurements. Chapter 2 was based on work presented at the AIAA Propulsion and Energy 2014 Forum and Turbo Expo 2015. Chapter 3 introduces the facility that was designed and built to simulate realistic combustor operation. The facility includes an industrial fuel nozzle, kindly donated by Solar Turbines Incorporated (the SoLoNOx nozzle), capable of operation at reacting conditions. Chapter 3 was based on work submitted to Turbo Expo 2016. Chapter 4 includes a comprehensive set of measurements for the isothermal (non-reacting/low pressure) heat transfer and flow field within the optical combustor developed. These measurements were key to understand combustor heat transfer without the additional complications introduced by sharp property gradients as occur during combustion. Reacting measurements are presented in chapter 5 including heat load and flow characterizations, and compared against the isothermal steady state measurements presented in chapter 4. Due to time constraints, Chapter 5 includes only limited data. Analysis and development of methodologies was favored over acquiring a large dataset. The experimental techniques developed can be later used to further characterize the reacting combustor at different conditions. The research work presented in Chapters 4 and 5 is either being prepared for submission or is currently under review in several journals. Finally, chapter 6 summarizes the contributions of this work and proposes future avenues of research. Given the at times conflicting nomenclature, a nomenclature was included per chapter.

# CHAPTER 1.

# INTRODUCTION

For a simple ideal Brayton cycle, operating with an ideal gas with no composition change and constant properties, the efficiency ($\eta$) of the cycle increases with increasing pressure ratio ($r$) across the compressor of the gas turbine engine. The specific work output ($W$) from the machine is in turn dependent on both the pressure ratio and the temperature obtained at the exit of the combustor ($T_3$). The expressions for efficiency and specific work output for the idealized cycle are given by Equations 1 and 2 [1].

$$\eta = 1 - \left(\frac{1}{r}\right)^{\frac{(\gamma-1)}{\gamma}} \tag{1}$$

$$\frac{W}{c_p T_1} = t\left(1 - \frac{1}{r^{(\gamma-1)/\gamma}}\right) - \left(r^{\frac{(\gamma-1)}{\gamma}} - 1\right) \tag{2}$$

Where $t = T_3/T_1$, $T_1$ is the compressor inlet temperature (ambient in general), and $\gamma$ and $c_p$ are respectively the ratio of specific heats and the specific heat at constant pressure for the working fluid. From the isentropic p-T relation, the pressure ratio can be expressed in terms of the turbine inlet ($T_3$) and outlet temperatures ($T_4$) as $r^{(\gamma-1)/\gamma} = T_3/T_4$. Therefore, achieving higher compression ratios (higher efficiencies) is limited by the maximum allowable temperature for the materials used in the turbine, leading to a wealth of research on improving the high temperature capacity of the turbine components [2]. The optimum specific work output is realized when $r^{(\gamma-1)/\gamma} = \sqrt{t}$. This again requiring higher turbine inlet temperatures at high efficiencies to achieve optimum specific work output (and reduce the size of the plant). In general, the overall behavior of ideal cycles is also valid when accounting for component losses in actual gas turbine engines [1]. The use of air bleeds from the compressor to cool down the hot gas path components reduce the mass flow that goes through the complete set of turbine stages, hence reducing the work output and efficiency.

Achieving the highest efficiencies and work outputs therefore impacts combustor design conditions. The higher compression ratio increases the temperature of the combustor inlet air, reducing its cooling potential. Since combustor components are not subject to centrifugal or large aerodynamic loadings (as is the case for the turbine and compressor rotating parts), their durability is primarily determined by thermal stresses and the reduced strength of the materials at higher temperatures. In view of the limited cooling potential of the inlet air, and the importance of the thermal stresses, thermal management of the combustor becomes a critical aspect to improve its durability.

Combustor durability targets for land based gas turbines are of the order of 30 000 hours [3]. Extensive use of novel materials and thermal barrier coatings extend the life of the burner walls and fuel nozzle [3,4,5,6]. Liner failures as reported in the open literature are shown in the work of Bradshaw et al. [7], Kim et al [8], and Price [3].

Tinga and coauthors [9] have recently analyzed the durability of a combustor liner based on the results from a computational model. The authors highlighted the limited amount of experimental data on flame side heat transfer for different burner configurations. In fact, validation of their numerical method was not possible given the lack of experimental data, and the authors were constrained to validate their method only qualitatively (based on the location and propagation of cracks in field engines). Reduced material strength at high temperatures, maximum thermal stresses at the location of maximum temperature gradients, and corrosion are the main conditions that drive combustor durability [8,9,10]. Per the discussion in [9], creep and low cycle fatigue (LCF, during startup and shutdown) are the main failure mechanisms for combustor liners. Creep consists of the cumulative permanent deformation materials develop while in stress (below the yield point) at high temperatures for extended periods of time. Creep can lead to interference problems between pieces as these deform beyond acceptable tolerance limits. In the turbine for instance, creep deformation leads to blade stretching which in extreme cases can interfere with the turbine shroud [10]. To capture the transient operation of the engine (relevant for LCF and total creep accumulation), a set of quasi-steady state simulations were performed by Tinga and coworkers [9] at representative operating points. The numerical results were interpolated to estimate the loads at other conditions. The authors showed that during fast transients, the stress characteristics can change drastically (going from compressive to tensile stress in some regions) and the entire flight history was required to assess the life of the liner.

There is however, in addition to improving durability, the conflicting requirement of reducing the formation of pollutants throughout the combustion process. Two types of pollutants are of concern: Nitric Oxides ($NO_x$), and unburned hydrocarbons (UHCs, including carbon monoxide – CO). $NO_x$ is primarily produced at higher flame temperatures by the oxidation of atmospheric nitrogen. Three reaction mechanisms lead to the formation of $NO_x$, including the thermal (Zeldovich) mechanism, the prompt mechanism, and via the formation of nitrous oxide at lower temperatures [11]. CO and UHCs on the contrary, result from incomplete combustion in the burner due to insufficient residence times or low temperatures. The optimum combustion temperature to minimize both $NO_x$ and CO emissions lies between $\sim 1700$ K and 1900 K according to results by Lefebvre and Ballal [12].

Modern gas turbine engines curtail $NO_x$ emissions by operating at lean equivalence ratios, hence reducing the flame temperature and the $NO_x$ production. To maintain high turbine inlet temperatures, introduction of coolant to the hot gas path via dilution holes or film cooling on the liner is limited. It is important to note that even when flame temperatures are reduced to $\sim$1700 K, this temperature is still well beyond the allowable temperature of common nickel super alloys ($\sim$ 1100 K [12, 13]) used to fabricate the walls of gas turbine burners. Reducing film cooling and dilution has the benefit of minimizing the formation of CO and UHCs near the burner walls, as introducing coolant into the combustion zone quenches intermediate reaction products and prevents complete combustion. However, film cooling has traditionally been an important technology to manage the convective heat load from the flame to the combustor liner. For this reason, reducing emissions also increases the thermal design challenge faced by the gas turbine combustor community.

Optimized cooling on the combustor liner has the benefit of improving burner durability, increase efficiency (by allowing a larger amount of air to go through the main gas path), and improve emissions. However, optimization of cooling on the liner is impossible without an accurate and thorough understanding of the flame side heat transfer, which to this date has not been characterized. This is the objective of the present research work; to improve our understanding of combustor thermal loadings and aid the design of next-generation gas turbine combustor systems.

## 1.1 COMBUSTOR DESIGN

The combustor is the component of the gas turbine where the fuel energy is introduced into the flow. A diagram of the main components of the gas turbine, including the combustion chamber at the outlet of the compressor is shown in Figure 1.

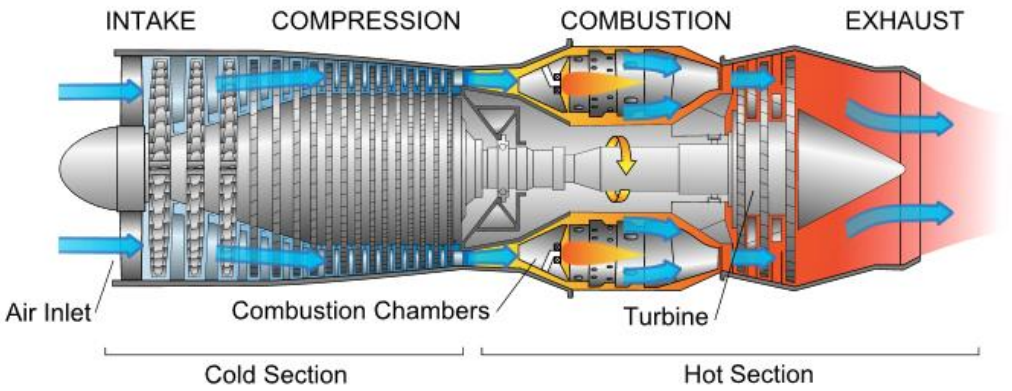


**Figure 1.** Diagram of a gas turbine engine showing the compressor, combustor, and turbine. Diagram by Jeff Dahl [14].

The most comprehensive accounts of combustor design practices are given by the work of Lefebvre and Ballal [12], and Mellor [13]. The authors detailed in their work every aspect of gas turbine combustion systems: from aerodynamics, to heat transfer and emissions. A conventional combustor design is shown in Figure 2 with labels indicating the components typical of earlier combustor systems [12, 13, 15]. These combustor designs consisted of a high pressure casing containing the flame tube or liner where combustion took place. The flame tube had holes strategically placed in the primary zone to foment flow recirculation and flame stability (primary holes). Openings to the end of the burner diluted the combustion gases and adjusted the temperature profile of the flow entering the turbine. Film cooling was critical in these burners to prevent failure of the flame tube (with emissions not being a primary concern in the design). The diffuser at the inlet of the combustor reduced the inlet velocity to the burner, leading to a lower pressure drop (to improve overall performance). The snout separated the compressor exit air into the primary gas path and secondary air path for the cooling and diffusion openings around the liner. Swirler fuel nozzles, mounted on the dome of the combustor, were used to generate a flow field ideal for flame stabilization in a short distance. Diffusion flames

were preferred over premixed ones, to further guarantee flame stability. The photograph shown in Figure 2 corresponds to a sectioned combustor from the Rolls-Royce Nene turbojet engine (1940s), which followed these earlier combustor design practices.

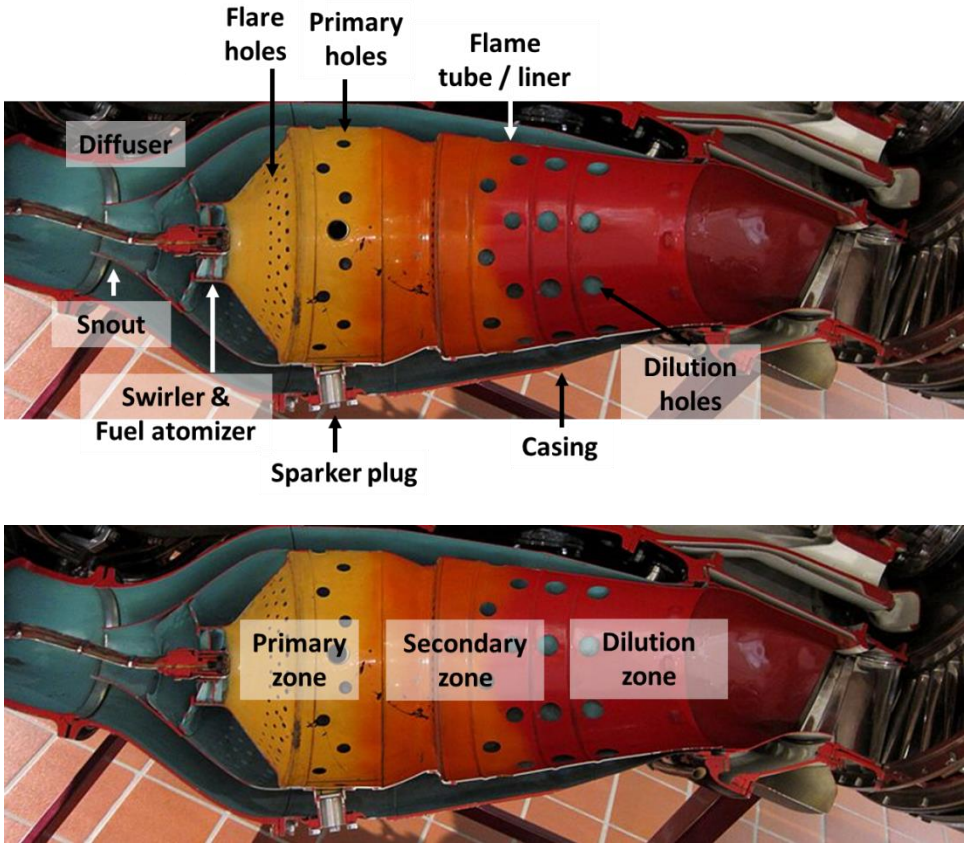


**Figure 2.** Sectioned Rolls-Royce Nene Turbojet combustor. Photograph by Oliver Cleynen [15].

The combustor is typically divided into three zones including the primary and secondary combustion zones, and the dilution zone. The primary zone is where the fuel is introduced, mixed with air, and ignited. This zone is where the flame is stabilized and where most of the fuel combustion takes place. The secondary zone introduces additional air and increases the residence time of the exhaust gases to achieve higher combustion efficiency (minimize UHCs). This was particularly important in early combustors operating with diffusion flames. As briefly described earlier, the final region is the dilution zone, where air is mixed with the exhaust gases to tailor the pattern factor (temperature profile) of the gas exiting the combustor. Downstream of the dilution zone (or in some cases as part of it), a transition piece is mounted to connect the combustor to the turbine section of the engine.

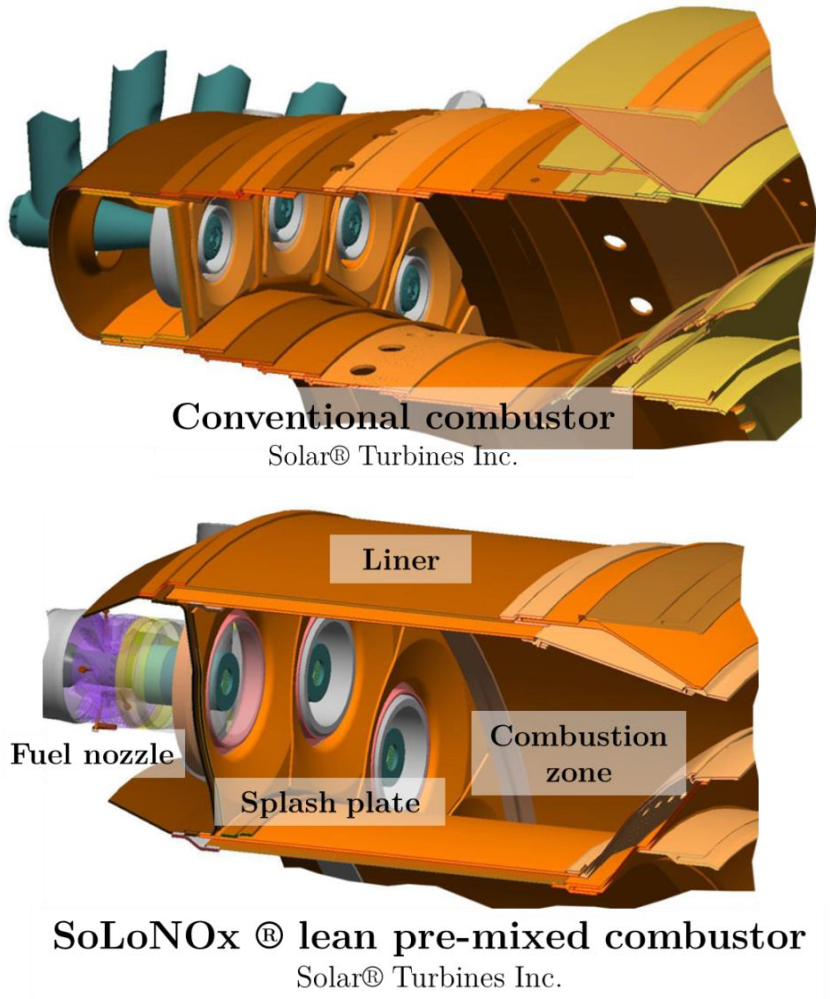


**Figure 3.** Comparison between a conventional and a modern SoLoNOx ® lean pre-mixed combustor design from Solar Turbines Incorporated. Permission requested, adapted from [16].

Modern combustors have introduced two main changes to traditional burners, 1) the use of fuel pre-mixing nozzles, and 2) the reduction of film cooling and dilution/mixing holes along the burner. A comparison between a conventional and a modern combustor design from Solar Turbines Incorporated, featuring their SoLoNOx® fuel nozzle is shown in Figure 3. The main driver for these innovations has been the stringent requirements on $NO_x$ emissions. The Environmental Protection Agency (EPA) in the United States limits $NO_x$ emissions of new stationary gas turbines firing natural gas to 15 ppm at 15% $O_2$ for installations over 250 MW [17], making pollution management a top priority in combustor design (similar requirements are in place for smaller engines). The $SoLoNO_X$ combustor features no film cooling along the liner.

Near the dome plate, the expended cooling air used on the backside of the dome splash plates (heat shields) exits along the flame tube. Only to the end of the combustion chamber, at the connection with the transition piece, film cooling and dilution holes are present. This contrasts with the conventional burner, which relied on film cooling and included mixing holes midway along the combustor.

A diagram showing the distribution of the compressor outlet air into the combustion systems for conventional and modern Solar Turbines Incorporated burners is shown in Figure 4. Due to the use of lean equivalence ratios and fuel-air pre-mixing, modern lean-premixed nozzles require higher air flow through the main gas path compared to conventional burners. In order to achieve the same turbine inlet temperatures, coolant air flow is reduced, again highlighting the crucial need for improved thermal management in modern combustors.

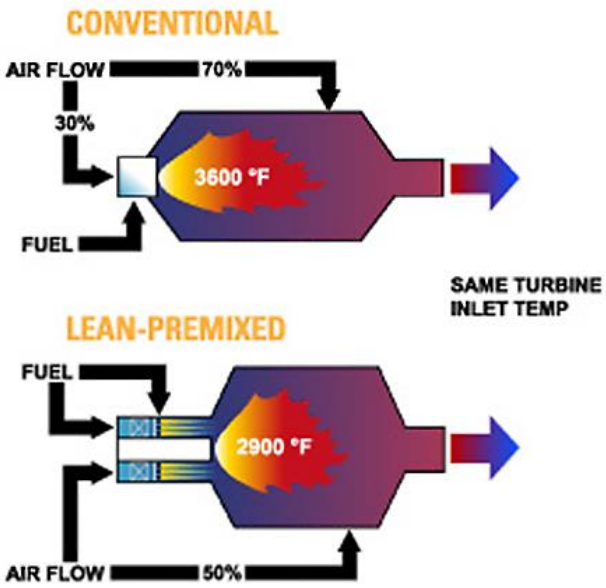


**Figure 4.** Air distribution in a conventional and a low emission combustor. Permission requested, taken from [18].

## 1.2 INTRODUCTION TO COMBUSTOR FLOW FIELD

Gas turbine combustors use swirl fuel nozzles to introduce swirl (tangential velocity component) into the flow before it enters into the combustion chamber. The swirling jet exiting the fuel nozzle generates flow features within the combustor primary zone that are essential for flame stability. The steady state flow [19] typically observed within a swirl stabilized gas turbine

combustor is shown in Figure 5. The salient features of the flow are the location of the shear layers and recirculation zones. The central recirculation zone (CRZ) brings hot combustion products back to the pre-mixed swirling jet exiting the nozzle, igniting the fresh mixture. The inner shear layer formed between the swirling jet exiting the fuel nozzle and the CRZ is where important coherent flow structures are observed that enhance the mixing between the fresh mixture and the recirculated gases. Understanding of the inner shear layer dynamics is hence important for flame location and stability, as well as mixing within the burner.

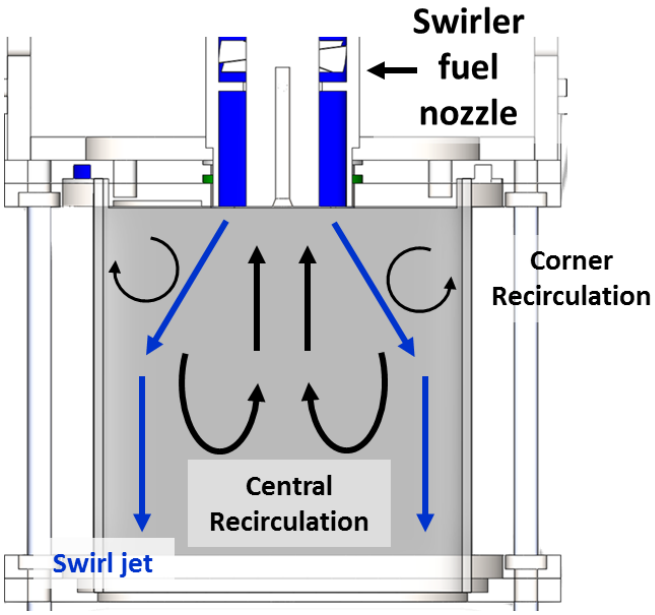


**Figure 5.** Schematic of the typical air flow distribution within a gas turbine combustor.

The CRZ allows for high intensity flames with high combustion efficiencies without the need of a blunt body for flame stabilization. No longer having to cool a blunt body, swirl fuel nozzles simplify cooling requirements while maintaining flame stability, short combustor length, and high combustion efficiency [13].

Swirling flows within combustors have been extensively studied for the past 50 years; with current work focusing primarily on understanding the vortex breakdown (VB) leading to the central recirculation and unsteady phenomena that affect combustor operation. Comprehensive reviews on combustion in swirling flows were first written in the 1970s and early 80s by Lilley [20], Beér and Chigier [21], Syred and Beér [22], and Gupta et al. [23]. The vast contributions of

the research community led to the current understanding and characterization of the central recirculation zone (CRZ), formed as the swirling jet exiting the fuel nozzle expands into the combustion chamber, recovering axial pressure, and eventually triggering the breakdown of the vortex and subsequent backflow [19]. This can be briefly demonstrated by applying the radial momentum balance equation within a simplified can combustor of radius $R$ ($r = 0$ at the burner axis) with quasi-cylindrical flow (streamlines aligned axially). The radial equilibrium equation for such conditions, at steady state and with laminar flow, is given by Equation 3 [24, 25].

$$\frac{\partial P}{\partial r} = \frac{\rho w^2}{r} \tag{3}$$

Integrating from the axis of the combustor to the liner wall ($r = 0 \rightarrow r = R$), and differentiating with respect to the axial coordinate ($x$) yields Equation 4 [24].

$$\frac{\partial P}{\partial x}_{r=0} = \frac{\partial P}{\partial x}_{r=R} - \frac{\partial}{\partial x}\int_0^R \frac{\rho w^2}{r} dr \tag{4}$$

Per the discussion by Sloan and coworkers [24], as the flow expands from the nozzle exit diameter (throat) to the combustor primary zone, the tangential component of the velocity ($w$) decreases due to conservation of angular momentum. This leads to a decrease in the integral term along $x$, i.e. $\frac{\partial}{\partial x}\int_0^R \frac{\rho w^2}{r} dr < 0$ (further enhanced by viscous effects). This in turn causes a strong positive pressure gradient along the axis of the combustor for sufficiently large inlet tangential velocities, eventually overcoming the axial momentum, and triggering a recirculation at the centerline of the burner. The mechanisms leading to vortex breakdown are known to be primarily inertia dominated, with viscous forces having only a minor role [24].

Recent work on combustor flow field has focused on the unsteady behavior and instabilities that emerge in combustor flows as detailed by the work of Lieuwen [26], Lucca-Negro and O'Doherty [27], Syred [28], and Huang and Yang. [19]. Different types of VB, as well as periodic oscillations in the flow such as the Precessing Vortex Core (PVC) and the presence of axial-radial vortices, have been identified [28,29,30]. The PVC and axial-radial eddy shedding are detailed in the work by Syred et al. [22,28].

The size and characteristics of the CRZ and PVC are heavily dependent on the flow properties and velocity profiles at the exit of the nozzle [24,31,32]. Hallet and Toews [33] succinctly demonstrated experimentally and theoretically the impact the inlet velocity radial profiles have on the onset of flow reversal. Larger recirculation zones have been observed when using a central hub or a diverging fuel nozzle [20]. Seminal flow visualizations by Faler and Leibovich [30] described the dependence of the vortex breakdown phenomena on Reynolds numbers up to 10 000 with respect to the nozzle diameter. At their highest tested Reynolds numbers only two breakdown modes, axisymmetric and spiral, were identified. As the Reynolds number was increased, their observations indicated an upstream shift of the recirculation bubble location. In addition to the Reynolds number, the swirl number ($S$) is another important parameter often used to characterize rotating flows within burners. The swirl number is defined according to Equation 5, as the ratio of the axial flux of tangential momentum ($G_\phi$) to the axial flux of axial momentum ($G_X$) over the combustor diameter ($R$).

$$S = \frac{G_\phi}{R\, G_X} \tag{5}$$

The swirl number is often used during design to ensure vortex breakdown. Syred [28] reported that the central recirculation zone is only formed for swirl numbers beyond a threshold value of 0.6-0.7. The swirl number impacts the geometry of the recirculation zone, with increasing swirl numbers leading to a longer recirculation and an upstream shift of the recirculation bubble [24]. The swirl number moreover defines the proportion of recirculated mass flow, important for flame stability.

Recent studies in combustor flows include the work of Terhaar and coauthor [34], who have used axial injection to modify the flow profile entering a model combustor and study its effects on the formation and characteristics of the vortex breakdown. The authors identified a conical type of VB that was triggered at high axial flow injection rates. Carmack et al. [35] have studied radial and axial swirl nozzles used in industrial engines to show the differences in the recirculation bubble and flow characteristics. Strakey and Yip [36] performed isothermal flow field measurements using a representative slot swirler yielding a swirl number of 1.17 and a peak swirl angle of 51°. The authors compared instantaneous flow realizations and the corresponding

time-average at non-reacting conditions showing elements of the PVC. Strakey and Yip commented on the unsteadiness and turbulence in the flow, but did not focus on its quantification [36]. These results served as a benchmark for the isothermal flow measurements presented in Chapter 4.

Ji and Gore [37] studied the time averaged and instantaneous turbulence and vorticity for an unconfined swirl stabilized flame using a nozzle with a swirl number of 2.4. Their results had limited extent and covered only a portion of the flow field, but provided tremendous insight into the importance of the instantaneous flow and the changes occurring between isothermal and reacting flows. Their main observations were that the mean and instantaneous velocities increased in reaction (leading to larger turbulent kinetic energy), and that the eddy length scales became smaller in reaction leading to a more uniform velocity field.

Reynolds-Averaged Navier Stokes (RANS) calculations are routinely used in industry to simulate the flow within combustors. Strakey and Yip [36] have shown however that unsteady RANS models underpredicted the isothermal flow fluctuations. Modeling efforts by Grinstein [38] have focused on predicting swirling flows of practical importance, for which the author stressed that it is critical to rely on accurate velocity radial profiles at the exit of the nozzle. In view of these requirements for the proper modeling of realistic swirling flows within gas turbine combustors, there is still a need to obtain flow and turbulence data for industrial injectors.

## 1.3 INTRODUCTION TO COMBUSTOR HEAT TRANSFER

The first attempts to semi-empirically characterize the heat transfer along the combustor liner walls were carried out by Lefebvre and coworkers [12,39]. The radiative component of the thermal load is relatively well understood, based on the work by Viskanta [40,41] and Lefebvre [42]. For internal convection, Lefebvre and Ballal [12] pointed out that the ”uncertainties regarding the airflow pattern, the state of the boundary layer development, and the effective gas temperature make the choice of a realistic model almost arbitrary”. The authors estimated the convective heat transfer according to early correlations for fully developed turbulent pipe flow, arguing that a similar formulation should apply within combustors when no film cooling is used. Lefebvre and Ballal [12] suggested Equation 6 to estimate the convective heat fluxes within combustors, highlighting the challenge of selecting appropriate reference mass flows, velocities and temperatures for the calculation.

$$Q_C'' = 0.02\ \mathrm{Re}_{C,\infty}{}^{0.8}\ \frac{k_\infty}{D_C}\ (T_\infty - T_W) \tag{6}$$

The authors further proposed a reduction of the 0.02 coefficient to 0.017 in the primary zone to account for reduced near wall gas temperatures. An example of their early analysis procedure can be found in [39], where they estimated the primary zone mass flow to be equal to 26% of the inlet mass flow to the burner. This was calculated from the estimated recirculated flow and the flow going through the swirl nozzle, respectively 16% and 10% of the combustor inlet flow. Knowledge of the flow distribution was hence critical for their analysis, information which may not be readily available without experimental and simulation work.

Lefebvre and Herbert [39] validated their final energy balance results (accounting for internal and external liner convection and radiation) against experimental engine wall temperatures in the primary zone with good agreement for different operating conditions. There is however in their work no discussion of peak heat loads or the distribution of the temperature field as data and experimental methods at the time were limited. Nevertheless, these calculations can be helpful in the early design phases of a gas turbine burner system, and were in fact used while designing the research combustor presented in this work.

Lefebvre's equation for convective heat transfer (Eq. 6) is approximately equal to evaluating the Dittus-Boelter heat transfer correlation, given by Equation 7, with $\mathrm{Pr} \approx 0.706$ (air). The gas properties for the Dittus-Boelter equation are typically evaluated at the local film temperature and the exponent $n_T$ is equal to 0.4 for $T_W > T_\infty$ and 0.3 for $T_W < T_\infty$.

$$\mathrm{Nu}_{Dittus-Boelter} = 0.023\mathrm{Re}_{C,f}^{0.8}\mathrm{Pr}_f^{n_T} \tag{7}$$

The Dittus-Boelter equation is accurate within $10\,000 < Re < 120\,000$, applicable only for wall to gas temperature differences of no more than 56 K, and cannot properly account for the temperature dependence of the gas properties [43, 44].

Since the time of the work by Lefebvre, there have been significant improvements to turbulent flow heat transfer correlations [45-48] and a more comprehensive understanding of the flow within combustors [19, 21, 26, 28], as discussed in the previous subsection. Work on heat

transfer enhancement in swirling flows and sudden flow expansions has also provided insight that can be applied to understanding convective loads within modern gas turbine burners. Dellenback et al. [49] for instance, worked on the experimental characterization of the heat transfer downstream of a sudden pipe expansion with swirling flow. While their swirl generator was not representative of combustor fuel injectors, it provided important details on the effects of swirl and Reynolds number ($Re_C < 51\,000$). The authors showed that increasing the swirl number resulted in larger heat transfer to the wall, and that the location of peak heat transfer consistently occurred upstream of the location of flow reattachment. Similar heat transfer investigations on turbulent decaying swirl flow have also been conducted without the sudden expansion to study the effects of swirl number and type of swirl generator [50]. Work on heat transfer in an abrupt expansion without swirling flow, such as that conducted by Baughn et al. [51], is also partly relevant to combustor flows as it exhibits a flow reattachment and subsequent formation of a corner recirculation region.

While combustor cooling technologies have been studied extensively in the open literature [12, 52, 53], combustor heat loads have not been fully characterized. Combustor convective heat transfer has been studied by Ekkad and coworkers for both can [35,54, 55] and annular [56, 57] combustor geometries, using approximated swirlers representative of industrial fuel nozzles. The work of these authors included isothermal (non-reacting) convective heat transfer measurements supplemented by numerical simulations and flow characterization using particle image velocimetry (PIV). The work by Patil et al. [56] reported Nusselt numbers several times higher than those obtained from the Dittus-Boelter equation, suggesting that the correlation underestimates the convective heat loads within burners. Recent work by Andreini et al [58] and Lorenzo [59] have also experimentally and computationally studied the isothermal convective heat transfer and flow within combustors using a three swirl nozzle combustor model. Their results include the effects of neighboring nozzles and of the cooling film at the start of the liner. Detailed PIV by the authors provided insight into the interaction between nozzles and the relationship between flow and convective heat transfer.

While most of the investigations to date have focused on the liner wall heat transfer, the dome of the combustor, where the fuel nozzles are installed, is also subjected to large thermal heat loads. These heat loads are primarily due to radiation from the flame. Typical dome designs include heat shields or splash plates that are installed over the dome wall as shown in Figure 6.

This double wall design allows for impingement cooling on the backside of the heat shield via hole arrays on the combustor dome. Several patents have been assigned to this effect [60, 61, 62]. All these inventions use different features on the backside of the heat shield or innovative arrangements of the impingement holes to maximize heat transfer while minimizing thermal stresses (due to temperature non-uniformities). Riahi and Borns [63] for instance, analyzed the effects of adding U-shaped ribs at the outer diameter of a circular heat shield to improve heat transfer and stress distribution (later patented [61]). After impinging on the backside of the splash plate, the spent coolant air exits into the primary zone of the combustor along the liner walls. This exiting flow not only provides film cooling close to the dome plate, but also modifies the convective heat transfer characteristics along the liner. The typical combustor dome arrangement shown in Figure 6 highlights the impinging coolant on the heat shield backside and the spent coolant flow along the liner.

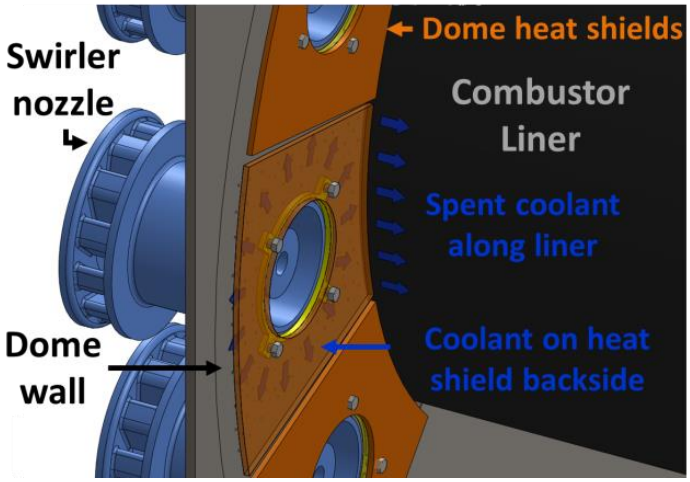


**Figure 6.** Sector model of a typical low emission annular combustor heat shield arrangement and coolant flows along the liner

Impingement heat shield cooling was briefly studied in the present work as well, using a transient methodology based on thermochromic liquid crystals (TLCs). Concepts from the transient TLC measurement were later used for the development of techniques for the reacting combustor. Impingement cooling fundamentals have been extensively studied in the past for single hole and multi hole arrangements with crossflow (see for instance [64-67]). Additionally, the effects of different features on the target surface have been investigated, including dimpled surfaces [68, 69], ribs [70, 71], grooves ([72]), fins ([73]), and others. There is a limited number

of application based studies relevant to combustor cooling. Spring et al. [74] studied a liner heat shield impingement cooling arrangement of 45 holes at jet Reynolds numbers of up to 34000 (based on hole diameter). The authors reported that standard correlations over predicted the overall heat transfer coefficients (HTCs) by 25%. Riahi and Borns [63] performed computational calculations to evaluate an innovative heat shield design with u-shaped ribs at the rim. They found that the ribs increased the impingement heat transfer coefficients and reduced the thermal stresses on the shield. Computational studies on a combustor heat shield with pedestal have also been performed by Luff and McGuirk [75]. The authors developed a conjugate heat transfer model to capture the solid-fluid interactions between the impingement jets and pedestals.

The effect that the outflow from the heat shield cooling has on the liner convective heat transfer has been recently studied by Andreini et al. [58]. They used a three swirler combustor model, with the swirlers arranged linearly to simulate an annular burner. No wall curvature effects were replicated by the model, which can be significant as shown by Patil et al. [56] and Gomez-Ramirez et al. [57]. Andreini and coworkers [58] modeled the outflow from the heat shield with a slot on the dome wall. The authors found that the slot coolant (with flows up to 3% of the main swirler flow) pushed the peak heat transfer downstream. The authors also performed Particle Image Velocimetry (PIV) in their test section to better relate the heat transfer to the flow field within their combustor model.

Current combustor designs rely on correlations and semi-empirical models, supplemented with extensive numerical and experimental work, to determine the most appropriate cooling scheme for the combustor walls [12, 76, 77, 78]. To accurately determine the thermal stresses to which the combustor liner is subjected, and to make a more efficient use of the available cooling air in modern low emission combustors, it is crucial to determine the convective component of the thermal load on the liner wall. However, estimating the convective heat load on the liner wall is not trivial, given the swirl dominated flow in the primary zone of gas turbine combustors.

## 1.4 MEASUREMENTS OF HEAT LOADS IN REACTION

In industry, combustor heat transfer is evaluated using numerical models [9, 77-79] with supporting experimental temperature measurements on the liner walls for validation. Liner wall temperatures of industrial combustors are determined using thermal paints and embedded thermocouples in dedicated combustor test rigs [76, 77]. Thermal paints provide a semi-

quantitative estimate of the combustor wall temperature distributions, while thermocouples yield a more accurate but spatially limited view of the temperature field. The placement of the thermocouples is hence often guided by the thermal paint results. Thermal paints however do not capture transient temperature fields, for instance during ignition or shut down, which may present the highest thermal stresses on the liner walls and impact burner durability. Measurements of heat fluxes along the liner walls in a reacting gas turbine combustor, to the knowledge of the author, are virtually non-existent in the open literature. There are however other communities that have performed heat flux measurements in reacting environments which provide insight into the important mechanisms and available tools.

An emerging technology with tremendous potential to characterize flame side heat transfer is thermographic phosphors (TPs) [80-84] (the present work uses IR thermography), which has been successfully used to study afterburners, internal combustion engines, and fire applications as summarized in the review by Aldén and coworkers [80]. A limitation of TPs is the temperature range over which reliable signals can be acquired. There are however TPs such as YAG:Dy that can measure over the temperature range of interest for gas turbines. Other limitations of TPs is their commercial availability, the preparation required (binder for the surface), and the need for an excitation source (usually an Nd:YAG laser).

Measurements of heat fluxes within internal combustion engines have been accomplished in the past using probes or gauges [85-87]. These types of sensors are often intrusive to the measured environment and have limited spatial resolution, but can provide excellent temporal histories of the measured variable. Furthermore, heat flux sensors have often limited operating temperatures, which can at most reach 1000°C and often require cooling [88].

Within the fire community, heat flux measurements from fires have relied on calorimeters and Schmidt-Boelter [89] heat flux sensors. A combination of two sensors can be used to determine the convective and radiative components in a fire environment using different methods, including using a cooled and uncooled sensor [88], using two thermopiles with different surface emissivities so as to differentiate the amount of radiation absorbed [90], and using heat flux sensors with and without windows that allow the transmission of radiation but limit convective heat transfer [91]. The spatial limitation of sensors has recently been addressed by the work of Rippe and Lattimer [92], who used infrared (IR) thermography to measure the total heat flux from a fire, including the radiative and convective components, to a target plate

under different configurations. Their calculation however relied on heat transfer correlations for the flame and back side convective heat transfer, which limits the applicability of the measurements to configurations where convective heat transfer does not adhere to standard geometries. Another notable exception to the use of heat flux sensors is the recent work by Hindasageri et al. [102] who used an infrared (IR) camera to monitor the temperature of a quartz plate and obtained the total heat flux for impinging flames with circular and rectangular fuel nozzles.

Flame impingement has also been studied in the open literature given its wide range of applications, and is analogous to the processes that occur within gas turbines burners. A comprehensive literature review on flame impingement was written by Baukal and Gebhart [93-95] where the authors summarized the experimental work performed prior to 1996. The authors reiterated the general lack of understanding and the importance of the relative contributions of radiative and convective heat transfer in flame impingement, as also pointed out by an earlier review done by Viskanta [96]. Baukal and Gebhart then proceeded to perform experiments to quantify the contributions due to non-luminous radiation and thermochemical heat release by using coatings to modify the target surface properties [97]. The authors found that radiative heat transfer accounted for 9.8% of the total heat flux delivered by flame impingement to a blackened surface with $\epsilon = 0.95$. A recent review by Chander and Ray [98] focused on the work performed between 1996 and 2005. The heat flux contribution of radiation to the surroundings of a combustion system depends heavily on the type of radiation being emitted by the flame. Luminous radiation due to soot particles in the flow leads to a significant heat flux that must be accounted for in the design of burners and combustors [12, 99]. On the other hand, non-luminous radiation from the flame due primarily to the emission bands of $H_2O$ and $CO_2$ yields only small contributions to the total heat transfer in flame impingement [100]. For this reason, most studies to date have neglected the effect due to radiation. However, studies by Keramida et al. [101] have demonstrated that ignoring non-luminous radiation may lead to a significant underestimate of wall heat loads. Keramida et al. [101] studied computationally the radiative heat transfer within a natural gas furnace. The authors compared experimental temperature measurements against computations with and without radiation modeling. The computations that incorporated radiation had a better agreement with the experimental data. The authors moreover showed that

including radiation in the model led to a four times increase in the percent of heat to the furnace wall.

## 1.5 PROJECT OBJECTIVES

In view of the importance of flame side heat transfer for the optimization of gas turbine combustor thermal management, and the lack of experimental data available, the objective of this research work was to develop methodologies and apply these to characterize heat transfer in a reacting combustor model. To better understand the heat transfer characteristics, a secondary objective was to measure the flow field within the research burner. One key element of the research work was to use actual combustor hardware, to create as realistic a model as possible. The research work hence focused on the aerodynamics and heat transfer of the low-emission SoLoNOx® fuel nozzle from Solar Turbines® Inc.

The project involved four main stages (corresponding to different chapters in this dissertation): 1) initial measurements on a simplified annular combustor rig, 2) development of a reaction capable combustor facility, 3) characterization of the research combustor at non-reacting (isothermal) conditions, and 4) development of heat transfer and flow measurements in reaction. Stage 1 complemented previous work in the research group [35, 54-56] and established a baseline of the current available methods to characterize heat transfer. Stage 2 involved the design of air and fuel systems; specification, selection, and procurement of equipment (valves, flowmeters, instrumentation, acquisition and control hardware, inline heater); and design, manufacturing, and assembly of a flexible research combustor housing the SoLoNOx nozzle. Stage 3 served to test the methodologies which were later implemented in stage 4. During stage 4, given time constraints, only limited data was taken, as detailed analysis was favored over the extent of the dataset. However, the ideas and methods developed can be applied to carry out further experiments and study reacting heat transfer and flow at a broader range of conditions than is presented in this dissertation.

## 1.6 NOMENCLATURE

| | |
|---|---|
| $c_p$ | Specific heat capacity at constant pressure [J $kg^{-1}$ $K^{-1}$] |
| CRZ | Central recirculation zone |

| | |
|---|---|
| $D_C$ | Combustor diameter [m] |
| $G_X$ | Axial flux of axial momentum [N] |
| $G_\phi$ | Axial flux of tangential momentum [N] |
| k | Thermal conductivity of the material [W $m^{-1}$ $K^{-1}$] |
| Nu | Nusselt number |
| $P$ | Pressure [Pa] |
| $Q''$ | Heat Flux [W $m^{-2}$] |
| $Q$ | Heat rate [W], flow rate [kg $s^{-1}$] |
| $r$ | Compression ratio ($P_2/P_1$) [dimensionless], radial distance [m] |
| $R$ | Combustor radius [m] |
| Re | Reynolds Number |
| $t$ | Temperature ratio ($T_3/T_1$) [dimensionless] |
| $T$ | Temperature [K] |
| VB | Vortex breakdown |
| $W$ | Specific work output [J $kg^{-1}$] |
| $x$ | Axial direction (along the combustor axis) |
| w | Tangential velocity [m $s^{-1}$] |
| $\rho$ | Density of the working fluid [kg $m^{-3}$] |
| $\eta$ | Thermal efficiency (net work output by heat input) |
| $\gamma$ | Ratio of specific heats |

**Subscript**

| | |
|---|---|
| 1 | Inlet to the gas turbine. |
| 2 | Outlet of the compressor (inlet of the combustor) |
| 3 | Outlet of the combustor (inlet of the turbine) |
| 4 | Gas turbine exhaust (outlet of the turbine) |
| C | Related to the combustor diameter |
| f | Related to the film temperature |
| $W$ | Related to the liner wall or surface |
| ∞ | Related to the working fluid temperature |

# CHAPTER 2.

# NON-REACTING, LOW TEMPERATURE MEASUREMENTS FOR THE ANNULAR COMBUSTOR MODEL

The studies presented in this chapter complement previous work by Patil et al. [54,56] and Carmack et al.[35], by providing flow and heat transfer measurements for an annular combustor model equipped with radial swirlers (based on [57, 103]). The ideas developed while performing these experiments were the basis for the measurements used in the reacting combustor. Three experiments were carried out: 1) Liner convective heat transfer calculations, 2) Particle image velocimetry for the annular combustor, 3) Dome heat shield backside cooling heat transfer and its effects on the liner convective heat transfer. The experimental test sections are first presented, followed by the methodologies and results obtained.

Most of the data in this chapter were taken in a representative two times scaled-up combustor model capable of operating at ambient pressures and temperatures, with provisions to install heaters along the walls for heat transfer measurements. The flow field induced by the radial swirlers (swirl number of 0.8 at the swirler outlet) inside the primary zone of the model annular combustor was characterized using two dimensional Particle Image Velocimetry (2D PIV). Measurements were taken at a Re number of $\sim 70000$ (based on the combustor total hydraulic diameter, this definition differed from that used in Chapters 4 and 5) to study the recirculation zone and the formation of the vortex in the swirling flow. Measurements of the vortex were also acquired for several Re numbers ranging between $\sim$ 30000 and $\sim 150000$ to study the vortex behavior at higher combustor inlet velocities.

Infrared (IR) thermography was used to measure the steady state convective heat transfer coefficients along the liner walls for three Re numbers including $\sim 70000$, $\sim 125000$, and $\sim 165000$. Heat transfer augmentation with respect to the Dittus-Boelter correlation for internal turbulent flow was calculated in order to study the enhancement due to the swirling flow.

A representative heat shield was also installed on the dome plate of the combustor model to reproduce industrial combustor arrangements and study the effects of the outflow from the combustor heat shield on the liner heat transfer. The heat shield back-side heat transfer was also characterized using a separate test section.

## 2.1 EXPERIMENTAL TEST SECTIONS USED

The main setup used for this study models the liner walls of one quarter of an annular combustor, scaled up by a factor of two to reduce the airflow required for similarity. A schematic of the setup is shown in Figure 7, further details are also available in Patil et al. [56]. As seen in the figure, the model is fitted with three radial swirlers. PIV and heat transfer measurements were taken relative to the middle swirler, which better reproduces engine flow conditions since it is not bounded by adjacent walls. Figure 7 also depicts the position of the windows used for the PIV and thermal IR acquisitions. For the heat transfer measurements, thin heaters were attached to the concave and convex wall (not shown in the diagram). The inner and outer radii of the annular section are 43.4 and 78.5 cm respectively, corresponding to a combustor hydraulic diameter ($D_H$ or $D$) of 70.2 cm.

The combustor model was connected to a wind tunnel equipped with a Cincinnati Fan SQAF-180 blower operated with a 15 HP AC electric motor. Immediately after the blower, intake air diffused into a settling chamber, after which the flow went through a flow straightener, a converging nozzle, and a second settling chamber with the same annular shape as the combustor model. The resulting flow was uniform at the intake of the test swirlers.

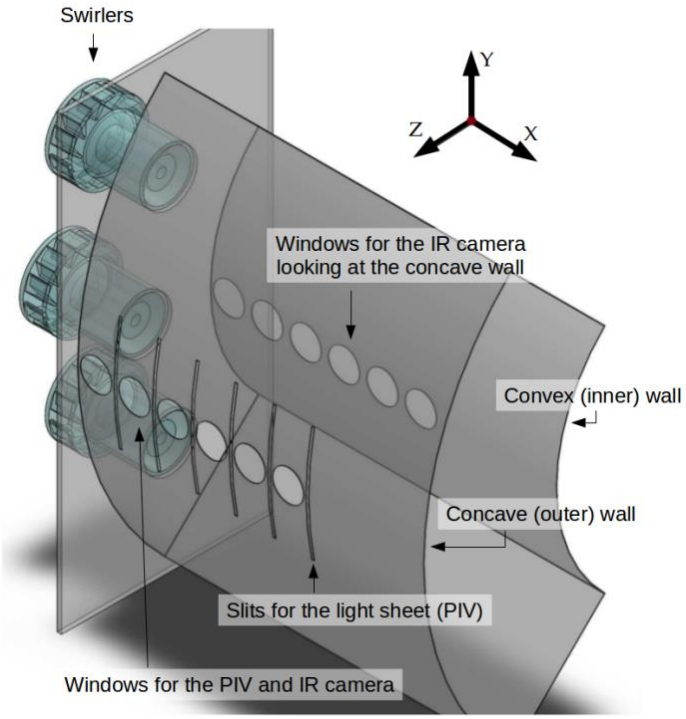


**Figure 7.** One quarter model of an annular combustor with radial swirlers. From [103], reprinted by permission of the American Institute of Aeronautics and Astronautics, Inc.

### 2.1.1 Annular combustor model with heat shields installed on the dome plate

To characterize the effect of the outflow from the heat shield on the liner heat transfer, experiments were performed in the same two times scaled up annular combustor model as shown in Figure 8. The difference in this setup compared to that shown in Figure 7 were the added heat shields and the impingement hole array on the dome.

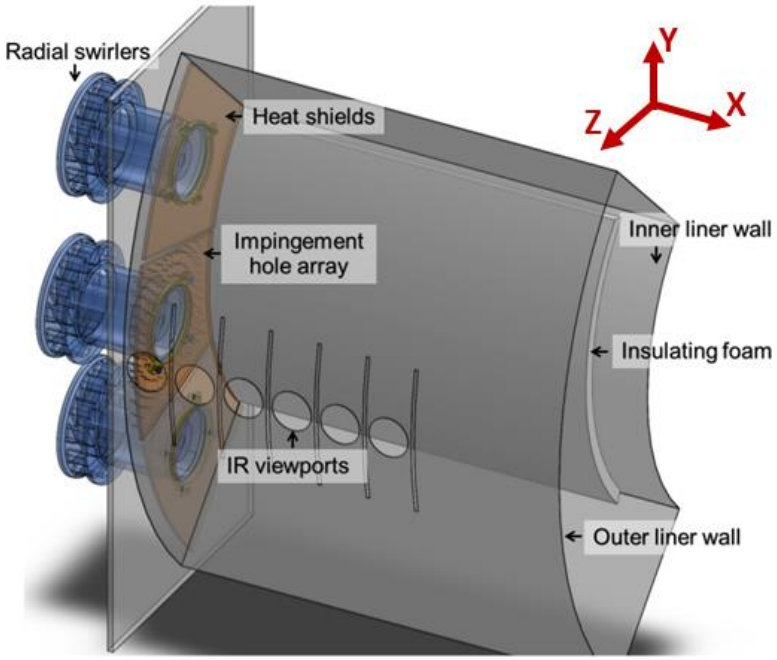


**Figure 8.** Experimental setup for the liner heat transfer measurements in the presence of secondary flows from the heat shield cooling. IR viewports also present on the opposite (inner) wall. From [57].

The impingement array and heat shield design, shown in Figure 9, were partially based on designs by Solar Turbines, Inc. (see for instance [60]). A total of 160 impingement holes were drilled around the middle swirler, with hole sizes of $D_1 = 1.524$ mm and $D_2 = 3.048$ mm. The ratio of the swirler outlet area to the total area of the impingement holes was 10.33. The model heat shields were 6.35 mm thick and were placed 6.35 mm (H) away from the dome wall; hence $X/D = 0$ in the results corresponds to 12.7 mm away from the dome wall (see Figure 10). The gap between the end of the shield and the liner wall was approximately 6.35mm as indicated in Figure 9.

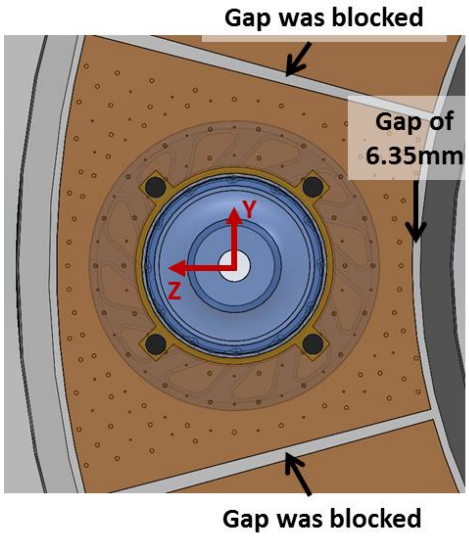


**Figure 9.** Detail of heat shield and impingement hole array (heat shield is transparent to display the impingement holes on the dome wall). From [57].

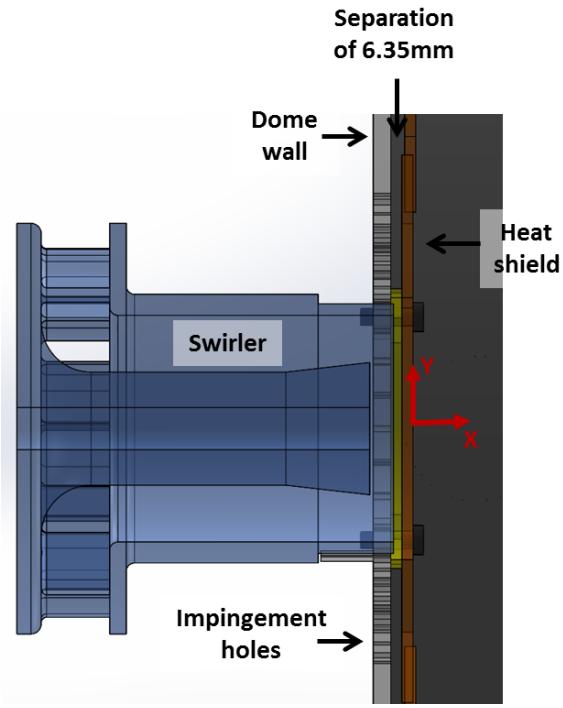


**Figure 10**. Cross-sectional view of the annular combustor model. The coordinate system for the data analysis is also shown. From [57].

Reynolds numbers of approximately 50000, 90000, and 130000 were tested based on the hydraulic diameter of the combustor annulus and the mean flow velocity upstream of the swirl nozzles as measured by a pitot probe (traversing the pitot yielded constant velocities upstream).

The static pressure drop across the combustor model was 317.6Pa, 1047.4Pa, and 1814.6Pa respectively for increasing Reynolds numbers ($\Delta P/P_2 = 0.3\%, 1\%, 1.8\%$).

### 2.1.2 Heat Shield Impingement Cooling Experimental Setup

The impingement hole arrangement used was an approximation of an array provided by Solar Turbines, Inc. and is shown in Figure 11. The hole array features 103 holes of 0.762 mm diameter arranged circumferentially around the swirl fuel nozzle. The distance between the outlet of the impingement hole and the target heat shield surface (H) was 4.166 hole diameters.

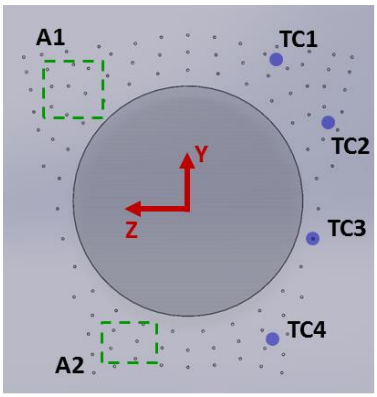


**Figure 11.** Impingement hole array for heat transfer measurements on the backside of the heat shield. Locations where the plenum temperature was measured are shown as TC1-TC4. The areas over which averaging was done to compare with correlations are shown as A1 and A2.

The experimental setup constructed is shown in Figure 12. The orifice plate and heat shield models were constructed using plexiglass ($k = 0.19$ Wm-1K-1 and $\alpha = 1.11046 \times 10^{-7}$ ms$^{-2}$) minimizing any conduction errors and providing optical access. The airflow was quantified and controlled upstream of the mesh heater using an orifice meter, yielding mass flow accuracies of 3%. A 0.7m long cylindrical settling tube with a 0.2m diameter was placed downstream of the mesh heater and served as a mixing plenum for the heated airflow. Approximately 0.3 m upstream of the hole plate, a honeycomb was used to straighten the flow. The setup was arranged vertically because the buoyancy of the heated gases led to significant stratification while testing horizontally.

Fine wire (0.076 mm wire diameter) T-Type thermocouples (TCs) were used for all temperature measurements, with an accuracy of $\pm 0.5$K per the manufacturer specifications. The temperature at four different locations approximately 1.3cm upstream of the hole plate for two

experimental runs are shown in Figure 13. The locations where the plenum temperatures were sampled are indicated in Figure 11. The mean temperature measured was used for the analysis, the difference between the calculated mean and the measurements for a given run were on average ~ 0.3K.

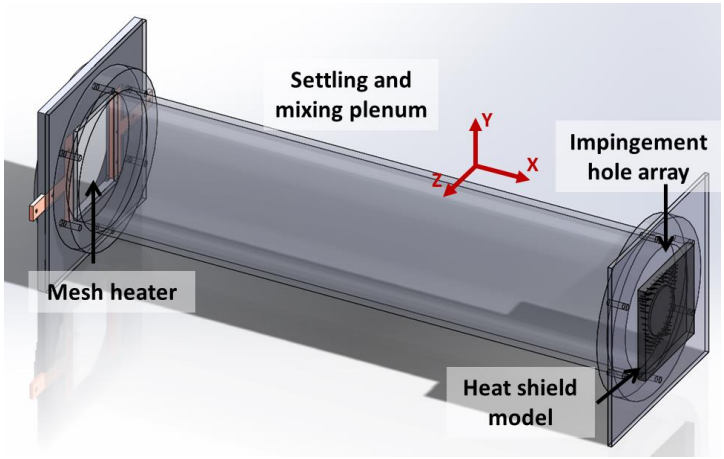


**Figure 12**. Experimental setup to measure impingement convective heat transfer on the backside of the heat shield. From [57].

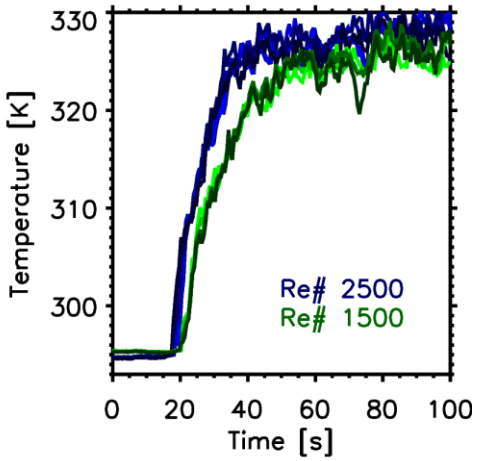


**Figure 13.** Plenum temperature for two different runs at the four different locations identified in Figure 11 (TC1-TC4).

## 2.2 METHODOLOGIES FLOW AND HEAT TRANSFER

### 2.2.1 Particle Image Velocimetry (PIV)

A Dantec Dynamics 200 mJ Nano-L dual laser system with a Flowsense EO 4M camera was used to acquire the PIV data. The system includes two Nd:YAG lasers with emission

wavelengths at 1064 and 532 nm. 50 image pairs were taken for each PIV run, and a minimum of two runs were taken per plane to ensure repeatability. The data presented combines at least two runs to reduce the random errors in the mean velocity profiles (a total of 100 images).

2D PIV data were collected along the length of the combustor, parallel to the liner walls (XY), to study the recirculation zone (RZ) and the formation of axial eddies. The XY axial plane at the centerline of the swirler is shown in Figure 14. Axial plane measurements were taken up to $X/D_H \approx 0.85$.

To study the formation and development of the vortex introduced by the radial swirlers, 2D PIV measurements were also done at planes perpendicular to the liner walls, also shown in Figure 14. The $X/D_H$ locations for the YZ cross-section planes are $X/D_H$ =0.14, 0.28, 0.43, 0.57, 0.72, and 0.86. The cross-sectional and axial planes depicted in Figure 14 are representative of the position and size of the actual measuring planes.

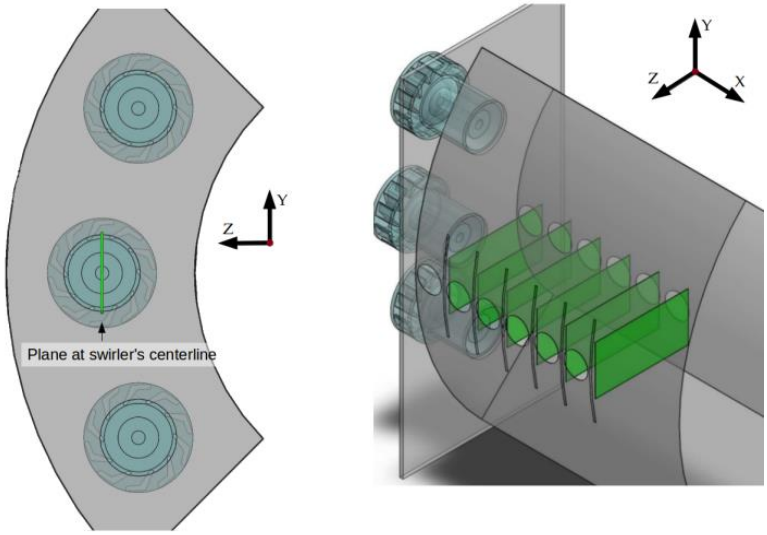


**Figure 14.** Location of the axial (left) and cross-section planes (right) for the 2D PIV measurements. From [103], reprinted by permission of the American Institute of Aeronautics and Astronautics, Inc.

The data acquisition methodology started first by calibrating and aligning the PIV system. The wind-tunnel was then set to the test Reynolds number. The airstream was seeded at the intake of the blower with a Rosco aerosol generator (model 1700). The seed particles consisted of glycol droplets with a diameter ranging from 0.25 to 60 μm and a specific gravity with respect to water of 1.12. Once the seeded flow reached the combustor model, the PIV acquisition

was started. The time between laser pulses was varied between 25 and 300 μs, depending on the measured mean flow velocity and the estimated velocity component perpendicular to the measuring plane. To determine the appropriate time between pulses, an initial measurement was done to estimate the flow velocity. Based on the maximum measured velocity and the desired spatial resolution, the final time between pulses was calculated. Care was taken to choose a delay between pulses that minimized the particles exiting the light-sheet due to the out of plane component of the velocity.

The data was analyzed using Dantec Dynamics' DynamicStudio v3.2 software package. The Flowsense camera provides 2048 × 2048 pixel (4 Megapixels) images with 4096 intensity levels per pixel. The image pairs were preprocessed with a threshold filter to eliminate any pixels with intensities within the background noise, minimizing spurious velocity correlations. After the threshold filter, the mean image was calculated (from the 50 image-pairs of the run) and subtracted from each individual image-pair. This eliminated any illuminated background in the image-pairs (particularly important close to the liner walls) and increased the contrast of the illuminated particles for more accurate correlations. The final image pairs were analyzed using an adaptive correlation procedure with a final interrogation area of 32 × 32 pixels and an initial interrogation area of 64 × 64 pixels. Neighborhood validation (3 × 3 median validation) was used to reduce the number of unphysical vectors for each correlation result. No window filters were implemented, and for this reason no overlapping of the interrogation areas was necessary.

From each PIV acquisition, vorticity ($|\Omega|$) and turbulent kinetic energy (TKE) were derived and averaged together. Eq. 8 corresponds to the formulation for the vorticity.

$$|\Omega| = \left|\boldsymbol{\nabla} \times \mathbf{V_{xy}}\right| = \frac{\partial \mathrm{V_y}}{\partial \mathrm{x}} - \frac{\partial \mathrm{V_x}}{\partial \mathrm{y}}, \tag{8}$$

where $\boldsymbol{\nabla}$ is the del operator and $\mathbf{V_{xy}}$ is the velocity vector in the measured plane with $\mathrm{V_x}$ and $\mathrm{V_y}$ components. The definition for TKE is given by Eq. (9).

$$\mathrm{TKE} = \frac{1}{2}\overline{(\mathrm{V_x}')^2} + \frac{1}{2}\overline{(\mathrm{V_y}')^2}, \tag{9}$$

where the over-bar indicates mean and the apostrophe refers to the unsteady component.

Maximum uncertainties in the time-averaged velocity field measured were 14.4% and 19.8% for the axial and cross-section planes respectively. A large portion of this uncertainty in the mean flow field is the result of the inherent variability in the vortex dominated flow. The actual experimental and data processing uncertainty was of 12%.

### 2.2.2 Steady state heat transfer using IR thermography

This measurement was slightly different between the initial investigation of heat transfer along the liner walls without any heat shield provisions as reported in [103] and the measurement including the heat shields [57]. The methodology and calculations were however the same for both.

To measure the steady state heat transfer coefficient, a thin heater was placed along a liner wall and the temperature was imaged using either a FLIR SC325 or FLIR SC640 IR camera through viewports on the opposite wall. The heater provides a constant heat rate determined from the relationship $P = V^2/R$ where P is the power consumed by the heater (equal to the heat rate provided at the liner wall $Q_w$), V is the voltage applied to the heater and R is the electrical resistance of the heater. A portion of the heat rate is lost by conduction to the liner wall, to minimize this loss an insulating layer was placed between the heater and the metallic liner wall. The conduction loss ($Q_{loss}$), emissivity of the heater, transmissivity of the IR window, and overall reflected temperature were characterized prior to the measurement. For the first experiments, with no heat shield, the heater was set to a heat flux between 1900 and 3300 W $m^{-2}$ depending on the test Reynolds number, resulting in wall temperatures of $\sim 323$ K. The second set of experiments, once the heat shield was included, were performed at $\sim 343$ K to reduce the uncertainty in the results.

A thin (<100$\mu$m) polyurethane plastic film was used as windows for the IR viewports. Both the emissivity of the heater surface and the transmissivity of the window changed depending primarily on the wall temperature. Although the calibration was performed at several temperatures, to minimize errors, the surface temperature during the experiment was maintained close to a calibration temperature for all the runs. The estimated uncertainty in the wall temperature associated with the calibration was $< 0.4$ K. The plastic film slightly distorts the IR image, hence a correction was implemented. The correction involved taking IR images of a constant temperature target with and without the plastic film. The images were adjusted to match

the correct temperature reading. Additionally, the calibration of the IR camera was performed before each measurement, including the determination of the emissivity, surface reflected temperature, and transmissivity of the plastic film.

The wall temperature ($T_w$) acquisitions were taken once the system reached steady state, after at least 60 minutes. Once steady state was reached, the wall temperatures showed random oscillations of ±0.2 K. A T-type TC was used to monitor the air temperature inside the combustor model ($T_\infty$). The heat transfer coefficient was calculated from Eq. 10, where A corresponds to the area of the surface heater.

$$h = \frac{Q_w - Q_{loss}}{A(T_w - T_\infty)} \tag{10}$$

The corresponding Nusselt (Nu) number was defined in terms of the hydraulic diameter of the entire annular combustor model ($D = 0.7m$) as given by Eq. 11.

$$Nu = \frac{hD}{k_{air}} \tag{11}$$

where $k_{air}$ is the thermal conductivity of the air at the operating temperature ($k_{air\,@\,21°C} = 0.0258$ $Wm^{-1}K^{-1}$). To obtain the heat transfer enhancement induced by the swirling flow, Nu was normalized by the Dittus-Boelter correlation for internal turbulent flow (Eq. 12), since modifications of it are generally used to estimate convective heat transfer within combustors [12].

$$Nu_0 = 0.0235 Re_A{}^{0.8} Pr^{0.4} \tag{12}$$

Where the Reynolds number for these measurements was defined according to Eq. 13, based on the hydraulic diameter (D) of the entire annular combustor (0.7 m), the velocity upstream of the dome plate (U), and the properties of dry air at the combustor model inlet temperature.

$$Re_A = \frac{UD}{\upsilon} \tag{13}$$

The addition of the heat shield modified slightly the internal geometry of the combustor model. In particular, the expansion of the swirling jets exiting the nozzle is delayed by the thickness of the shield and its support structure. Since the objective was to study solely the effect of the coolant outflow and not of the delayed expansion, two experiments were conducted once the heat shields were installed: with and without coolant outflow. For the baseline cases with no outflow from the backside of the heat shield, instead of blocking the impingement holes, the outflow was redirected away from the liner to the top and bottom walls of the combustor model. This was done to maintain approximately the same pressure drop characteristics and overall mass flowing through the swirlers at a given combustor Reynolds number.

Heat losses were characterized by supplying power to the heater at different levels and measuring the average heater temperature with no flow imposed (wind tunnel turned off). Since there is negligible convection and radiation losses, the observed mean temperature was due to the balance between the heat flux supplied and the losses due to conduction (radiation losses would also be accounted for by this analysis). The results obtained for the outer and inner walls relate the average heater temperature to the equivalent heat loss at the particular temperature. Heat transfer measurements were taken through the first 4 windows made on the liner walls, extending from $\mathrm{X/D} = 0$ to $\sim 0.6$.

### 2.2.3 Transient heat transfer using thermochromic liquid crystals

Measuring heat transfer using TLCs is a well established technique [104, 105]. TLCs are used to record the response of the surface temperature to a sudden change in the gas temperature. This transient response is then numerically modeled to obtain the heat transfer to the surface. For the present experiment, a 0.3 mm thick thermochromic vinyl sheet was procured from LCR Hallcrest coated with a 5 K wide TLC band (308 K - 313 K). The sheet was attached to the target plate (12.7mm thick) with the coating facing the impinging flow. The experiment consisted of setting the appropriate mass flow rate, followed by introducing a sudden temperature jump in the airflow via a mesh heater while recording the color change of the target surface. A CMOS video recorder was used at 30 frames per second with an image resolution of $720 \times 480$ pixels. The frames were transformed from the Red-Green-Blue (RGB) to the Hue-Saturation-Value (HSV) color model. The hue in the HSV model is defined from 0° to 360° and monotonically increases with temperature for TLCs. During each experiment, the TLCs were calibrated using a T-type

TC. The curve describing the equivalence between hue and surface temperature ($T_{sfc}$) is shown in Figure 15, along with a 5$^{th}$ order polynomial fit (Eq. 14).

$$T_{sfc}(t) = 2.603 \times 10^{-10}\mathrm{Hue}(t)^5 - 1.665 \times 10^{-7}\mathrm{Hue}(t)^4 + 4.067 \times 10^{-5}\mathrm{Hue}(t)^3 - 4.450 \times 10^{-3}\mathrm{Hue}(t)^2 + 0.2188\,\mathrm{Hue}(t) + 304.37 \quad (14)$$

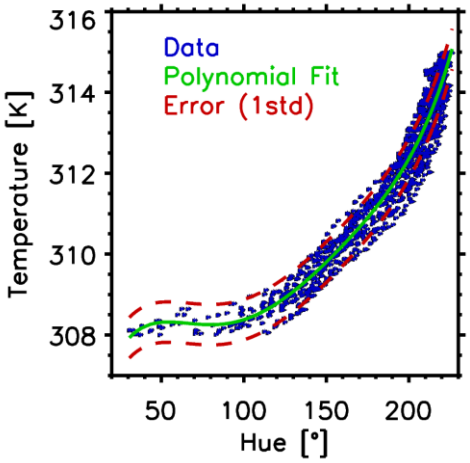


**Figure 15.** TLC calibration curve (308 K- 313K band). Spread in the data corresponds to different calibration runs.

The data for the calibration corresponds to different calibration runs which accounted for slightly different illuminations, and the hysteresis of the TLC band (calibration while going from low to high temperatures and vice-versa). The one standard deviation error in the polynomial fit is $\sim$ 0.5 K at all hues. The same TC was used for all the calibration tests, hence the difference in calibration is not due to TC biases (although it is related to the precision error in the TC). The total uncertainty in the calibration was estimated at 1.11 K, accounting for two standard deviations in the polynomial fit, and an independent thermocouple error of 0.5 K.

The target plate was approximated as a 1D semi-infinite solid. The analytical 1D semi-infinite solution for a step change in the convective boundary condition at time $t = 0$ is given by Eq. 15.

$$\frac{T_{sfc}(t) - T_i}{T_\infty(t) - T_i} = \Psi(t) = 1 - \exp\left(\frac{h^2 \alpha_{sfc} t}{{k_{sfc}}^2}\right) erfc\left(\frac{h\sqrt{\alpha_{sfc} t}}{k_{sfc}}\right) \quad (15)$$

To account for the varying mainstream gas temperature ($T_g$), Duhamel's integral method [106] was implemented as given by Eq. 16, with the step response function equal to $\Psi(t)$ and $F_k = T_\infty(t_0 + k\Delta t) - T_\infty(t_0 + (k-1)\Delta t)$, where k is a time step index. Note that $\Psi(t) = 0$ for $t < 0$.

$$T_{sfc}(t - t_0) - T_i = (T_\infty(t_0) - T_i)\Psi(t - t_0) + \sum_{k=1}^{n} F_k \left(\Psi(t - t_0 - k\Delta t)\right) \qquad (16)$$

The time ($t_{ref}$) taken for each pixel in the video recording to reach a given reference hue (equivalent to a reference temperature $T_{ref}$ per Eq. 14) was extracted. The mathematical model given by Eq. 16 was then evaluated for different heat transfer coefficients (h) until $T_{sfc}(t_{ref}) = T_{ref}$ within a tolerance of $\pm 0.01$ K. The advantage of using a broadband liquid crystal was that it provided a wider view of the surface temperature response and allowed for the selection of different reference temperatures. The results presented correspond to the average obtained from five reference temperatures including 309.2, 309.8, 310.4, 311.2, and 312 K (encompassing the entire band). The 1D semi-infinite assumption was maintained by keeping the video recordings shorter than 100 seconds ($Fo \approx 0.07$). The semi-infinite assumption is taken to be valid for $Fo < 0.1$ [107].

### 2.2.4 Numerical simulation for the heat shield backside cooling heat transfer

To further support the experimental studies, computational work was performed by Deepu Dilip [57]. This portion of his work is included in this dissertation because the discussion of the experiments partially relied on these numerical results. Figure 16 shows the generated mesh for the domain, including a close up view of the mesh over the target plate (a 4 million elements mesh is shown for clarity). The computational domain reproduced only one half of the geometry owing to its symmetry. Moreover, given the limited available computational resources, the heat shield (target surface) was further reduced in size compared to the experimental geometry. Only a part of the settling tube was modeled, with the inlet to the domain placed at approximately one-third of the diameter of the plenum tube. The target surface on the heat shield was modeled as a wall, with a constant heat flux of 12 000 $Wm^{-2}$. Heat transfer coefficients were calculated from the target surface temperature and the plenum bulk flow temperature (300 K). The pressure outlet condition in Figure 6 extends approximately 3 times the radius of the settling tube from the top edge of the target plate. No-slip wall boundary conditions were applied to all the faces of the

target plate, the sides of the settling tube and the walls of the impingement holes. Since the configuration consisted of the holes embedded as an array within a plate, no slip walls were provided at the surfaces where the inlet and outlet to the holes lie. Constant static pressures of 1484.6 Pa and 3326.6 Pa were supplied as inlet boundary conditions, corresponding to impingement hole Reynolds numbers of $\sim 1500$ and $\sim 2500$ respectively. A turbulence intensity of 0.5% was provided at the inlet and the length scale used was the diameter of the hole. A separate investigation found that the results were insensitive to different turbulence intensity and length scales at the inlet boundary.

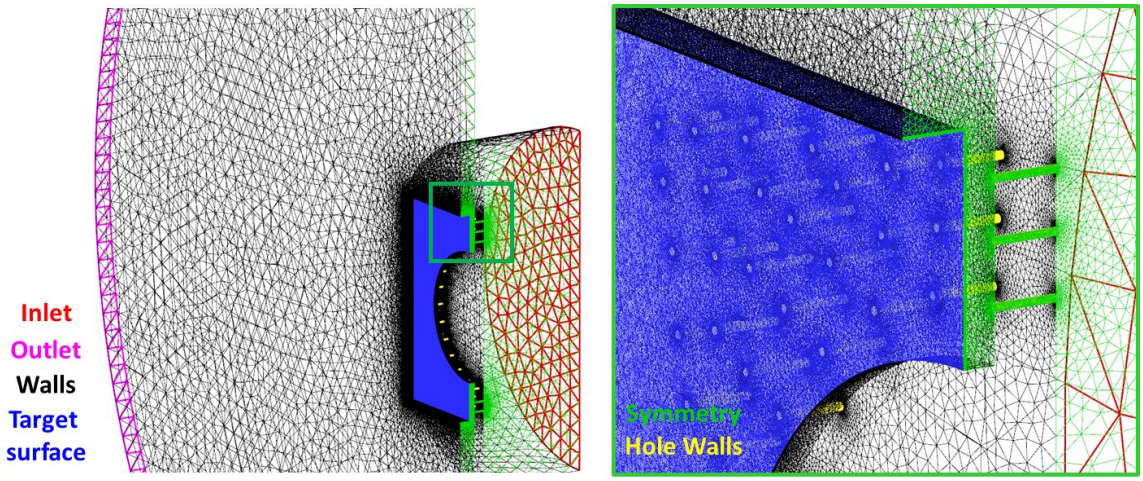


**Figure 16**. Computational domain and meshing strategy.

Among the different RANS models, the v2-f and the SST k-ω models have yielded the most accurate predictions in jet impingement studies [66, 108, 109]. The k-ω SST model was chosen for this work due to its relatively smaller computational cost in comparison to the v2-f model [110]. A grid per each Reynolds number case was generated to satisfy the wall $Y^+ \sim 1$ requirement of the k-ω SST model for each of the two Reynolds numbers simulated. The computational mesh was generated using ANSYS Mesh®. The inflation layers kept the maximum wall $Y^+$ for the first cell smaller than 1.5 in the entire surface of the target plate. Moreover, a reasonably good grid resolution in the other two coordinate directions was obtained in this region by maintaining the aspect ratios of the cells at $\sim 25$. The computational grid consisted of approximately 8 million elements and 26 million elements respectively for the two hole Reynolds numbers. A fine grid resolution in the other two coordinate directions was

maintained in the region near the target face, to retain the quality of the mesh and improve convergence.

Steady state simulations were performed in ANSYS® Fluent® 14.5. The SIMPLE algorithm was used for pressure velocity coupling and the equation for momentum, energy, and turbulent variables were solved to second order accuracy. Air as an incompressible ideal gas was modeled in order to account for any density variation due to temperature changes. The calculations were stopped when the residuals dropped by five orders of magnitude for the energy equation, three orders of magnitude for all other conservation equations, and when the wall temperature on the target plate reached a steady value.

The Grid Convergence Index (GCI) was also calculated by Deepu Dilip. Based on the average heat transfer coefficient on the target plate for three different meshes, the GCI for the fine grid was 0.47%. However, the uncertainty in the average value of the heat transfer coefficient gives no information regarding the local variation of discretization error, particularly in the vicinity of the impingement location where higher uncertainties are expected. Local GCI were also analyzed and were found to be $< 15\%$.

## 2.3 RESULTS OF ANNULAR COMBUSTOR STUDIES

### 2.3.1 Flow Field

PIV measurements of the first radial cross-section were taken at different Reynolds numbers to verify that the flow characteristics were constant independent of Reynolds number, as reported by Patil et al. [54,56]. The ZY cross-sections at $X/D_H = 0.14$ and $0.28$ are shown in Figure 17 for $Re = 70000$. The swirler location is indicated by the white outline of the swirler outlet in the figures. A strong counter-clockwise rotating vortex was observed, slightly offset vertically from the center of the swirler and with tangential velocities up to 7.1 times the combustor inlet velocity.

From the PIV measurements, the radial and tangential components of the velocity were derived. The radial and tangential velocities were determined with respect to the center of the swirler exit. The results of the circumferentially averaged velocity components for different Reynolds numbers at $X/D_H = 0.14$ are shown in Figure 18, where $r_s$ indicates the radial distance from the swirler center in the measurement plane. The profiles were approximately constant

independent of Reynolds number. The tangential velocity was always positive, indicative of the strong vortex at this $X/D_H$ location. The extent of the vortex can be deduced from the position of the peak tangential velocity, which was observed at $r_s/D_H = 0.1$. Further corroboration of this was that the flow converged towards the swirler center for $r_s/D_H < 0.07$ (negative radial velocities), consistent with a strong recirculation zone. The vortex was expanding from $r_s > 0.07$ with a peak normalized radial velocity at $r_s/D_H \approx 0.15$ of 2.5 ($V_r/V_\infty$). The normalized radial velocity away from the swirler center appeared to be larger for lower Reynolds numbers (normalized TKE also hints to follow this pattern close to the walls). The difference between cases was however within the errors of the PIV measurement, and therefore additional measurements would be needed to verify this observed trend. Normalized TKE and vorticity also remained relatively constant independent of Re (not shown).

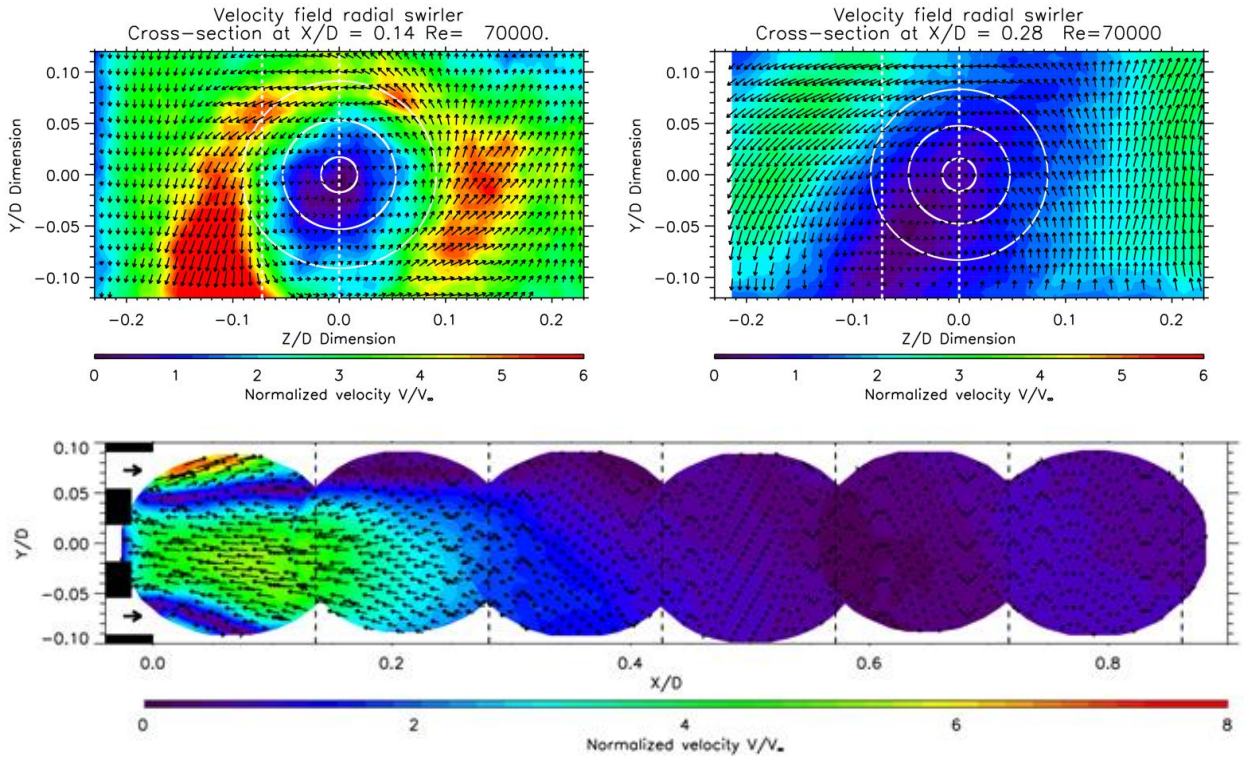


**Figure 17.** Velocity field of the first (left) and second (right) YZ cross-sections, showing the formation and development of the counter-clockwise rotating vortex. From [103], reprinted by permission of the American Institute of Aeronautics and Astronautics, Inc.

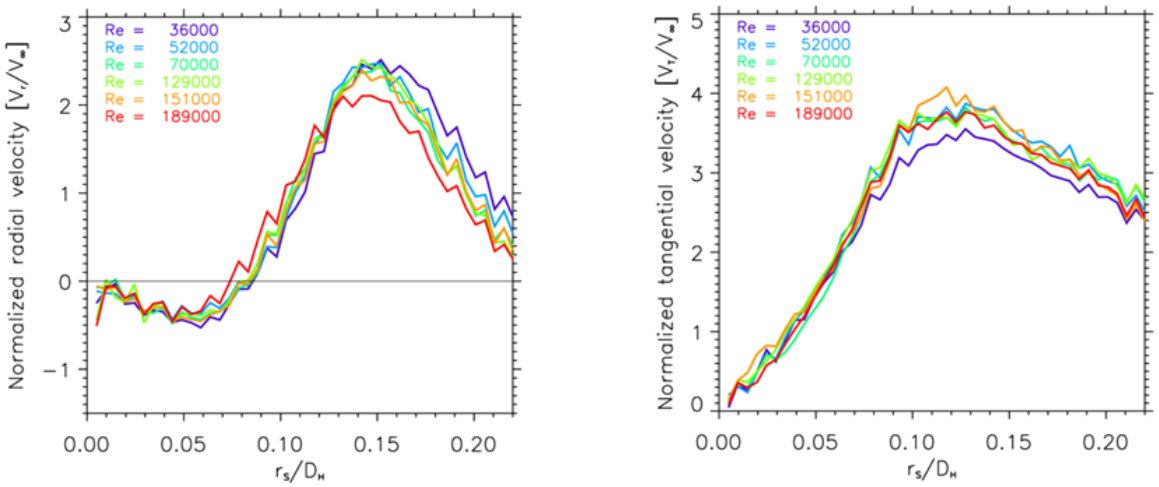


**Figure 18.** Circumferentially averaged radial (left) and tangential velocities (right) with respect to the swirler center. Cross-section taken at $X/D_H = 0.136$. From [103], reprinted by permission of the American Institute of Aeronautics and Astronautics, Inc.

Since the flow features were independent of Reynolds number, the remainder of the measurements were done only for $\mathrm{Re} = 70\,000$. It is important to highlight however that the flow was approximately incompressible for all the Re numbers studied, and that the flow features may change as compressible effects become significant.

Measurements observed a strong recirculation zone immediately at the outlet of the swirler, consistent with the expected results for swirl numbers greater than 0.6-0.714. The RZ is not symmetric with respect to the $\mathrm{Y/D_H} = 0$ line, expanding faster for $\mathrm{Y/D_H} < 0$. Close to the swirler outlet, the experiments showed that the recirculation zone extended from $\mathrm{Y/D_H} = -0.06$ to 0.04; a total extent of $\sim 0.1\mathrm{D_H}$.

The vertical extent of the RZ increased in the $\mathrm{Y/D_H}$ direction as the swirl induced vortex expanded into the primary zone of the combustor. The RZ zone in the experiment was noticeably weakened by $\mathrm{X/D_H} = 0.28$, indicating a decay of the vortex as it interacted with the liner walls. The vortex decay was also corroborated by the second YZ cross-section at $\mathrm{X/D_H} = 0.28$ shown in Figure 17 (right), and by the lower circumferentially averaged vorticity and TKE shown in Figure 19 (bottom).

The result from the first YZ cross-section (Figure 17) was in agreement with the features observed for the flow-field along the combustor, with the central location of the vortex shifted by about 0.02D in the negative $\mathrm{Y/D_H}$ direction and with a matching RZ extent.

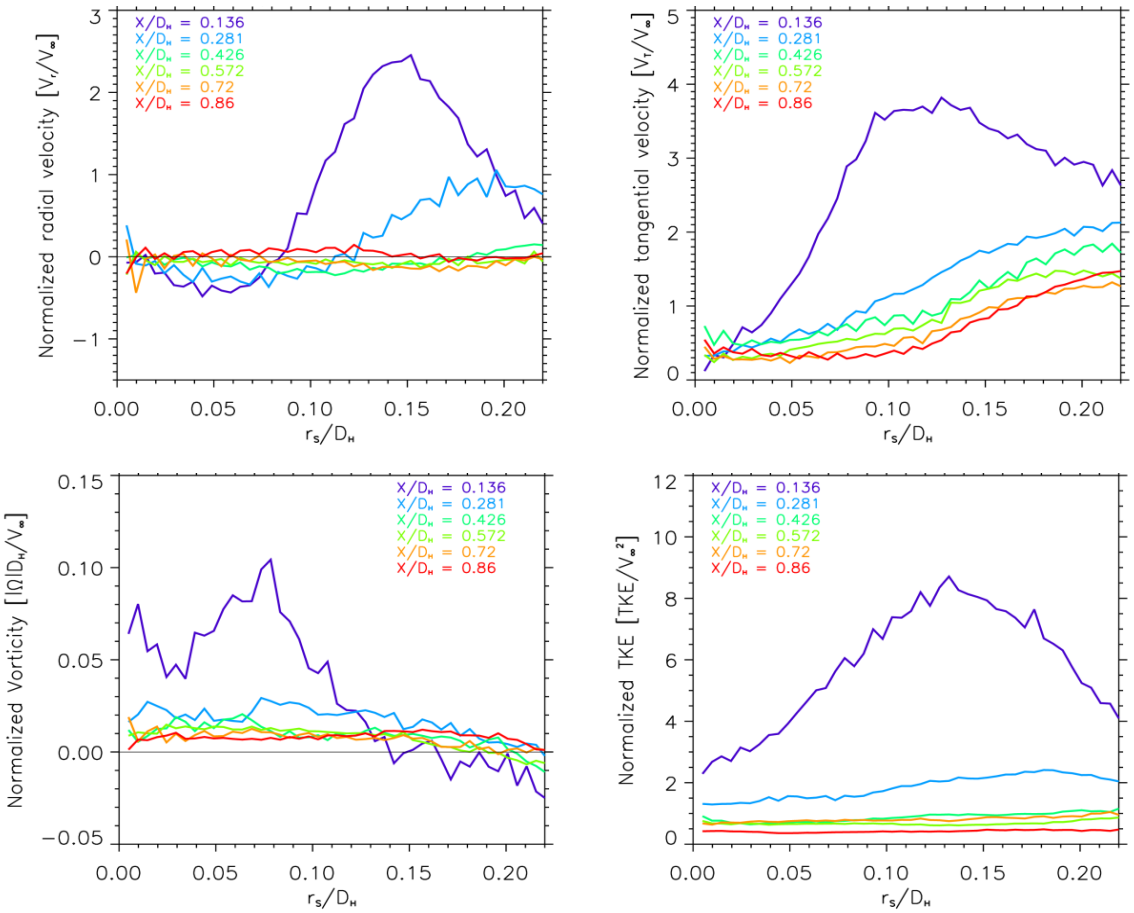


**Figure 19.** Circumferentially averaged quantities for Re = 70000 at different axial locations. Top left: Radial velocities. Top right: Tangential velocities. Bottom left: Vorticity. Bottom right: Turbulent kinetic energy. From [103], reprinted by permission of the American Institute of Aeronautics and Astronautics, Inc.

The circumferentially averaged tangential and radial velocities for the YZ cross-sections along the length of the combustor are shown in Figure 19. By $X/D_H = 0.28$ the flow had expanded completely into the combustor. The strength of the tangential velocities had also decayed significantly and shifted closer to the edge of the vortex. Past $X/D_H = 0.28$, positive tangential velocities were maintained, and a relatively constant value of $V_T/V_\infty \approx 1.5$ was observed close to the liner walls.

### 2.3.2 Liner Convective Heat Transfer without heat shield effects

The resulting Nusselt number distributions for Re = 70 000 are shown in Figure 20 for the concave and convex liner walls. The distributions were similar for Re ~ 130000 and~ 170000,

except that the Nusselt number had higher magnitudes. The independence of the distribution of Nusselt numbers with Reynolds number is consistent with the corresponding independence of the normalized flow field with Reynolds number. The magnitude of Nu however was expected to increase because the magnitude of the mixing within the flow field also increased.

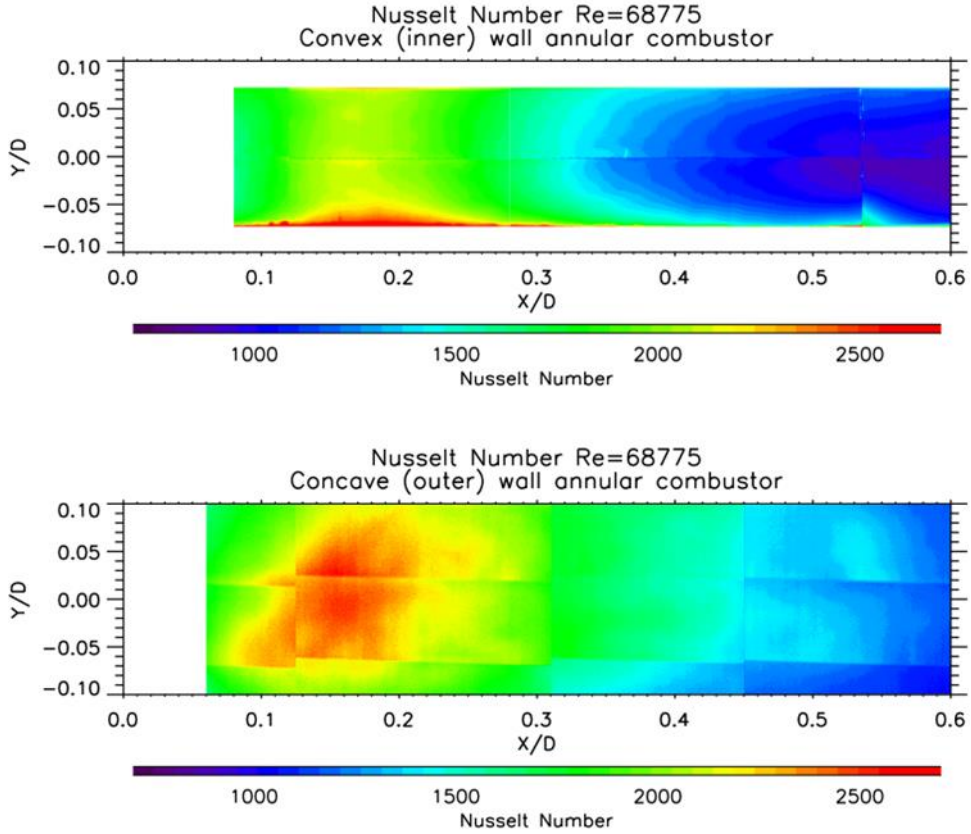


**Figure 20.** Heat transfer distribution along the liner walls. Top: Convex (inner) liner wall. Bottom: Concave (outer) liner wall. From [103], reprinted by permission of the American Institute of Aeronautics and Astronautics, Inc.

The $Y/D_H$ averages of the normalized Nusselt number distributions for the three Reynolds numbers tested and the numerical results are shown in Figure 21. The numerical calculations [111] again provided a qualitative comparison with the heat transfer results, reproducing approximately the location of the peak heat transfer. The magnitude of the heat transfer enhancement predicted by the numerical calculation is however much larger than the measured augmentation values. The trend of decreasing augmentation with Reynolds number was also reproduced by the CFD [111]. As the swirl-induced vortex decayed along the length of the combustor, the augmentation in heat transfer also decreased.

A decrease in augmentation with Reynolds number implies that at higher Re numbers, the increase in heat transfer due to the swirling flow is smaller compared to the expected increase in turbulent mixing intrinsic to the flow at these Re numbers. This decrease in augmentation may also be related to the suggested decrease in normalized radial velocities close to the liner walls with increasing Re numbers as seen in Figure 18.

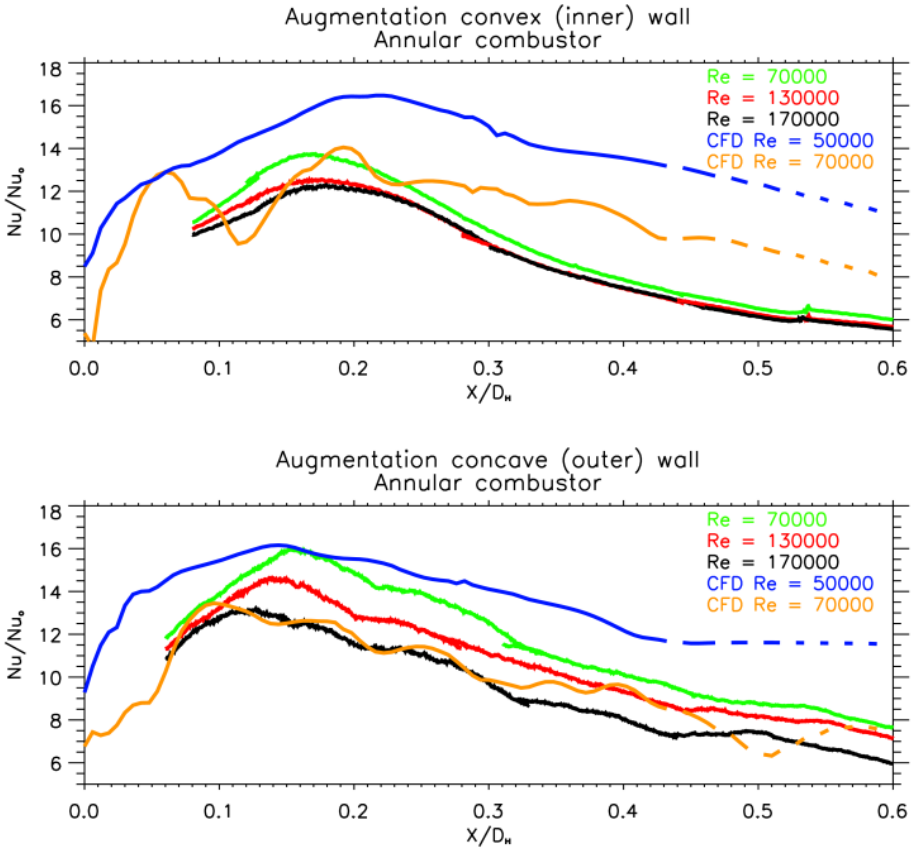


**Figure 21. $Y/D_H$** average heat transfer enhancement at different Re for the CFD [111] and experiment. Top: Convex (inner) wall. Bottom: Concave (outer) wall. From [103], reprinted by permission of the American Institute of Aeronautics and Astronautics, Inc.

For both walls, the peak heat transfer (without normalization) increased approximately linearly with Reynolds number, although additional data is required to better assess the relationship (Dittus-Boelter predicts Nusselt number to be proportional to $Re^{0.8}$). The location of the peak heat transfer at the convex (inner) wall moves farther from the swirler outlet as the Reynolds number increases. The behavior is opposite for the concave wall with the position of the peak heat transfer moving closer to the combustor inlet with increasing Reynolds number. These trends can be explained by looking at the velocity field for the $X/D_H = 0.14$ and 0.28

cross-sections (Figure 17), showing that the vortex shifts towards the outer wall ($Z/D_H = -0.2$). This induces a higher turbulent kinetic energy close to the concave (outer) wall, and hence higher heat transfer. The skewedness of the vortex at the outlet of the swirler seems to increase at higher Reynolds numbers, as suggested by the opposite direction of the shift in the location of maximum heat transfer enhancement for the liner walls.

### 2.3.3 Dome heat shield back-side cooling heat transfer

The normalized Nusselt number results from the experiment and computations for the heat shield cooling heat transfer are shown in Figure 22 for hole Reynolds numbers of $\sim 1500$ and $\sim 2500$. Spring et al. [74] used the impingement heat transfer correlation for an array of round nozzles from Martin [112], shown in Eq. 17, to compare their results against design calculations. This correlation accounts for the effects of crossflow and jet interference [66] and was also used as the reference $Nu_0$ for the impingement results shown in Figure 22.

$$Nu_{ref} = \frac{h_{ref} D_h}{k_{air}} = Pr^{0.42} \sqrt{f} \frac{1 - 2.2\sqrt{f}}{1 + 0.2(H/D_h - 6)\sqrt{f}} Re_j{}^{2/3} \tag{17}$$

The correlation is valid for $2000 < Re < 100\,000$, $H/D_h < 0.6/\sqrt{f}$, and $0.004 < f < 0.04$. The relative hole area f is the ratio of the impingement hole cross-sectional area to the target surface area covered by a single jet (given by a square of side L).

$$f = \frac{\pi D_h{}^2}{4L^2} \tag{18}$$

The target surface area per jet was calculated from the total area of the shield model (7938 $mm^2$) divided by the total number of impingement holes ($f = 0.0059$).

The CFD reproduced the overall pattern and magnitudes observed in the experiment. Figure 23 shows semi-quantitatively the relative heat transfer at the impingement point (indicated by the index *i*) between different jets. Both experiment and CFD predicted lower heat transfer rates for the inner circle of jets. The highest heat transfer rates in the experiment were observed between the inner and outer jet circles for the top and bottom of the array, which was

also approximately observed in the CFD. The jets located farthest away from the nozzle (at the corners of the impingement array) were in general lower in the experiment, which was not properly captured by the simulation.

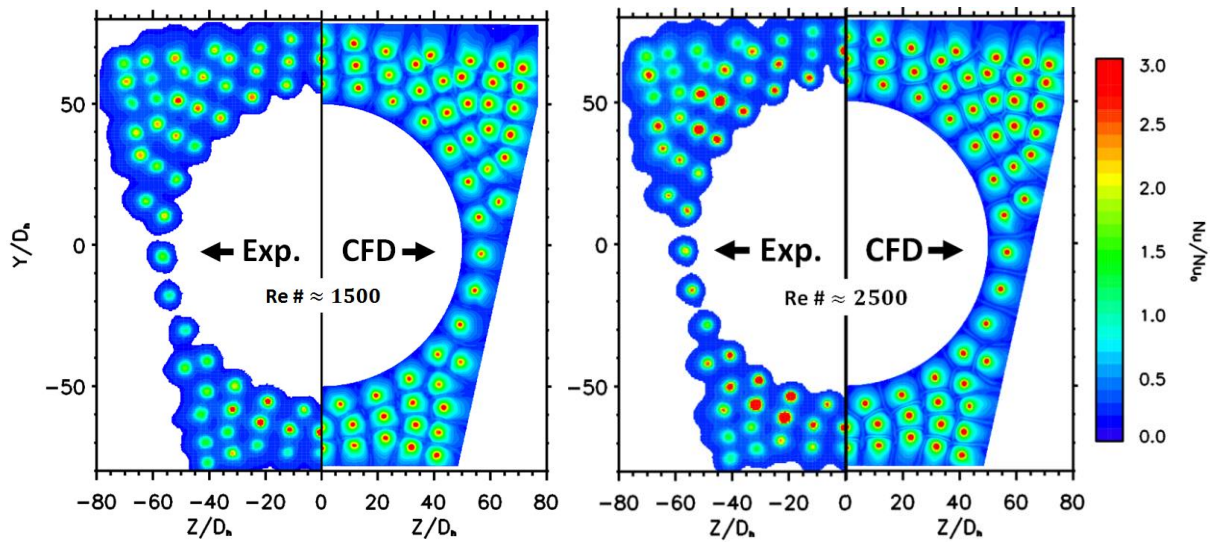


**Figure 22.** Normalized Nusselt number distributions for the heat shield backside.

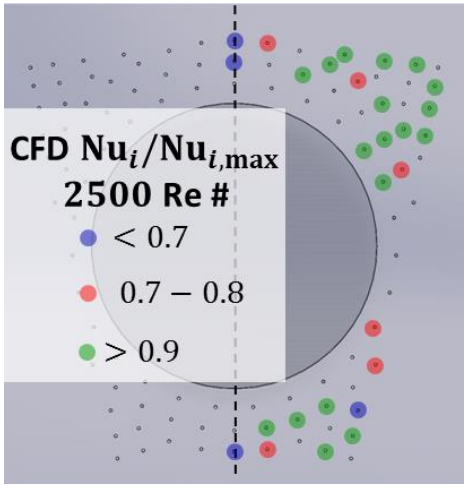


**Figure 23.** Qualitative diagram for the impingement point relative magnitude with respect to the maximum impingement point heat transfer observed for the simulation at Re = 2500

Two crossflow phenomena were at play in the tested impingement array, effects due to the radial pressure gradient generated as the spent flow exited the backside of the shield (impacting the inner jets), and jet distortion due to the crossflow occurring at larger radii. The back-pressure effects were also observed by the semi-enclosed jet impingement experiments

conducted by Obot and Trabold [113]. The authors observed that jets close to the bounding wall (in a maximum crossflow condition) displayed lower heat transfer coefficients than the jets located close to the outlet of the test section for a jet Reynolds number of 11 000. The computations predicted this phenomena qualitatively well. Per the numerical calculations for the 2500 Reynolds number case, the jets for $R/D_N < 60$ (innermost jet circle) had a mean pressure differential (inlet to outlet) of $1037.1$ Pa compared to the jets located at $70 < R/D_N < 80$ with 1051.7 Pa, further supporting the inner jets experiencing a larger backpressure. Crossflow effects on downstream jets have been well documented to degrade overall heat transfer by thickening the boundary layers at the target wall [66] as shown in the work by Kercher and Tabakoff [114].

The results from the correlation, experimental measurements, and computational results are compared in Table 1. The averages over the entire heat shield for the data available are shown as $\overline{\mathrm{Nu}}_{EXP}$ and $\overline{\mathrm{Nu}}_{\mathrm{CFD}}$. The computations overpredicted the mean Nusselt numbers obtained in the experiment by 44% and 28% for the 1500 and 2500 Reynolds number cases respectively. These results are consistent with the comments by Zuckerman and Lior [66] who stated that k-$\omega$ models overpredict heat transfer by at least 10-30%. For the 1500 Reynolds number case, the flow is in a transitional turbulent regime and hence it was expected that the experimental data would yield lower heat transfer than both the simulations and correlations (which apply to fully turbulent flows). The correlation result for the two turbulent Reynolds numbers (2500 and 4000) were 72% and 57% larger than the overall heat shield Nusselt number. The averaging however is significantly sensitive to the area considered, and this is an important aspect to consider while estimating practical heat transfer rates from correlations. Averaging over the entire shield incorporates areas under different crossflow and jet interaction conditions, as well as areas with reduced flow away from any impingement holes. Averages over smaller areas surrounded by jets (A1 and A2 as shown in Figure 11) yielded mean Nusselt numbers closer to the correlation, with a maximum overprediction of 18% and 22% for $\mathrm{Re} = 2500$ and $\mathrm{Re} = 4000$. Consistent discrepancies were observed by Spring et al. [74], where the authors found that the Martin [112] correlation overpredicted their liner heat shield Nusselt numbers by $\sim 25\%$. In the present study, the correlation was also evaluated at Reynolds numbers that are close to its applicability limit ($\mathrm{Re} = 2000$). Martin [112] in fact introduced a correction for low Reynolds numbers that may be insufficient.

**Table 1.** Comparison between averaged Nusselt numbers for correlations, CFD and experiments

| Re # | $\mathrm{Nu}_{\mathrm{ref}}$ | $\overline{\mathrm{Nu}}_{EXP}$ | $\overline{\mathrm{Nu}}_{EXP}$ A1 | $\overline{\mathrm{Nu}}_{EXP}$ A2 | $\overline{\mathrm{Nu}}_{\mathrm{CFD}}$ | $\overline{\mathrm{Nu}}_{\mathrm{CFD}}$ A1 | $\overline{\mathrm{Nu}}_{\mathrm{CFD}}$ A2 |
|---|---|---|---|---|---|---|---|
| 1500 | 7.4 | 3.8 | 5.2 | 4.5 | 5.5 | 6.7 | 6.3 |
| 2500 | 10.5 | 6.1 | 8.9 | 10.5 | 7.8 | 9.7 | 9.2 |
| 4000 | 14.3 | 9.1 | 11.7 | 12.5 | NA | NA | NA |

#### 2.3.3.1 Experimental uncertainty for the TLC measurements

Yan and Owen [107] analytically derived the relative error in the heat transfer coefficient from idealized TLC experiments. Based on the authors' formulations for a perfect step in the convective boundary condition for a semi-infinite plate (which neglected errors in the time synchronization and material properties), the minimum amplification of the errors occurs when $h\sqrt{t\alpha_{sfc}}/k_{sfc} \approx 0.82$, which corresponds to a $\psi_{opt} = 0.52$. These analytical errors were also inversely proportional to $T_\infty - T_i$. For the presented experimental results, the TLC band was selected to maintain most of the target surface normalized temperatures ($\psi$) between 0.4 and 0.6, while keeping the gas temperature at the maximum allowed by the mesh heater in the setup ($\sim$ 325 K). At the impingement location, because of the high heat transfer rates, $\psi$ was in general >0.6, leading to the highest errors in this area.

The errors considered in the uncertainty analysis included adding a random variation of $\pm$0.5K to the plenum temperature, a constant bias of $\pm$0.5K to the plenum temperature, a bias in the hue-temperature calibration of $\pm$1.11K, changes to the material properties ($\alpha$) of $\pm$10%, and synchronization errors of 0.3 seconds. These perturbations were individually applied to the data and the results were recalculated to obtain the error introduced. These errors were added in quadrature (assumed independent of each other) to yield the total uncertainty. The averaged error contributions from each source are shown in Table 2, with a total uncertainty of 10%. As an alternative to the perturbation results shown in Table 2, an empirical estimate of the uncertainty can also be obtained from the standard deviation of the five reference temperatures analyzed, which was on average 7.4% for the entire target plate. Near the impingement location, the high heat transfer rates minimized the difference between the gas and the surface temperatures, yielding larger uncertainties. The total uncertainty at the impingement location was on average 34%.

The total uncertainty in the impingement hole Reynolds numbers ($Re_j$) throughout a run was $\pm 13\%$, accounting for variations in the dynamic viscosity of the air as the gas temperature was increased, mass flow errors, and tolerances in the hole diameter of $\pm 10\%$.

**Table 2.** Uncertainty estimate for the heat transfer measurements on the backside of the heat shield

| Uncertainty source | HTC Error |
|---|---|
| $T_\infty$ bias $\pm 0.5$ K | 2.7% |
| $T_\infty$ random $\pm 0.5$ K | 0.3% |
| TLC calibration bias $\pm 1.11$ K | 9.1% |
| Thermal properties $\pm 10\%$ | 2.9% |
| Synchronization ($\pm 0.3$ sec.) | 1.5% |
| Total Uncertainty | 10% |

### 2.3.4. Effect of Dome Cooling Outflow on Liner Heat Transfer

The normalized Nusselt numbers measured along the liner walls with and without the spent air from the heat shield cooling are shown in Figure 24 and Figure 25 for the outer (concave) and inner (convex) liner walls respectively. The X and Y dimensions were normalized to the hydraulic diameter of the entire annulus ($D = 0.7$m). $X/D = 0$ corresponded to the top surface of the heat shield (see Figure 10). In terms of swirler diameters ($D_s$) the measurements included $Y/D_s = \pm 0.32$ and extended up to $X/D_s = 3$. The $Y/D$ averages for the normalized Nusselt numbers along the combustor are shown in Figure 26.

The flow field within gas turbine combustors has been extensively studied [20]. The rotating flow exiting the swirler fuel nozzle outlet expands into the combustion chamber and impinges on the liner wall creating a local convective heat transfer maximum. Between the point of impingement and the dome wall, a corner recirculation vortex is formed. This corner recirculation is associated with a local minima in heat transfer along the liner as observed in the presented results. In the absence of outflow from the backside of the heat shield, the location of the local convective heat transfer minima remains constant at $X/D < 0.015$ for the inner liner and $X/D \approx 0.035$ for the outer one. When the spent air from the heat shield exited along the liner, the local minima was pushed downstream by $0.05 - 0.07D$. This behaviour was expected since the outflow generates a crossflow along the liner that shifts the impingement location and the corner recirculation vortex. In the absence of outflow, the impingement location remained

relatively constant at $X/D \approx 0.18$ and $X/D \approx 0.28$ for the convex and concave walls respectively. When outflow was present, the impingement location was shifted downstream by $0.03 - 0.07D$.

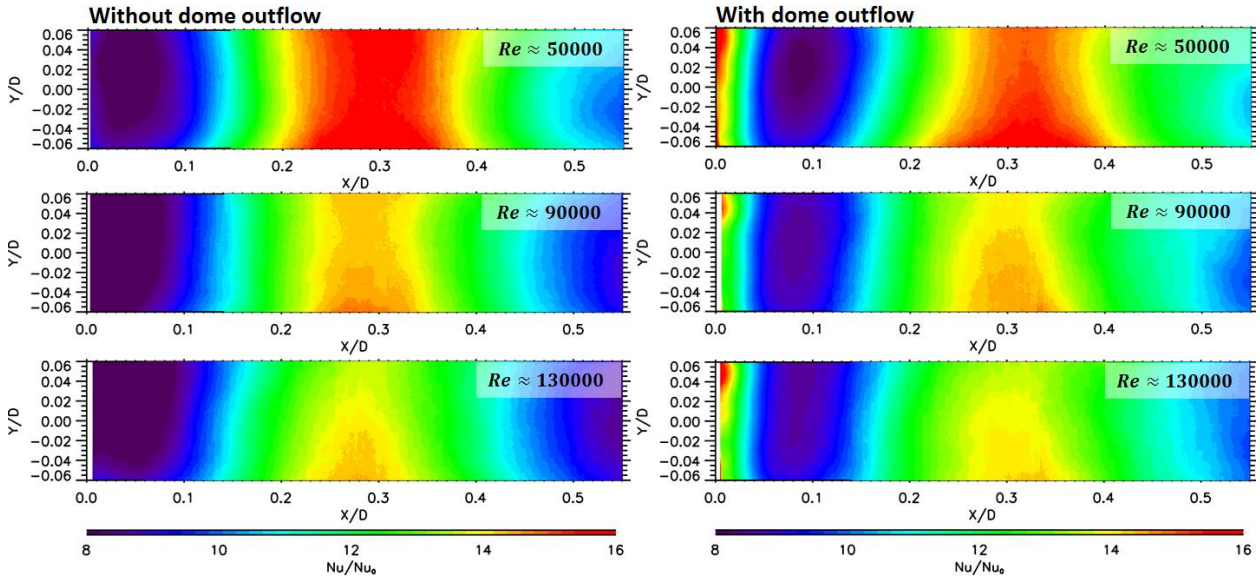


**Figure 24.** Nusselt number enhancement along the outer (concave) combustor liner wall with and without spent cooling from the backside of the heat shield. From [57].

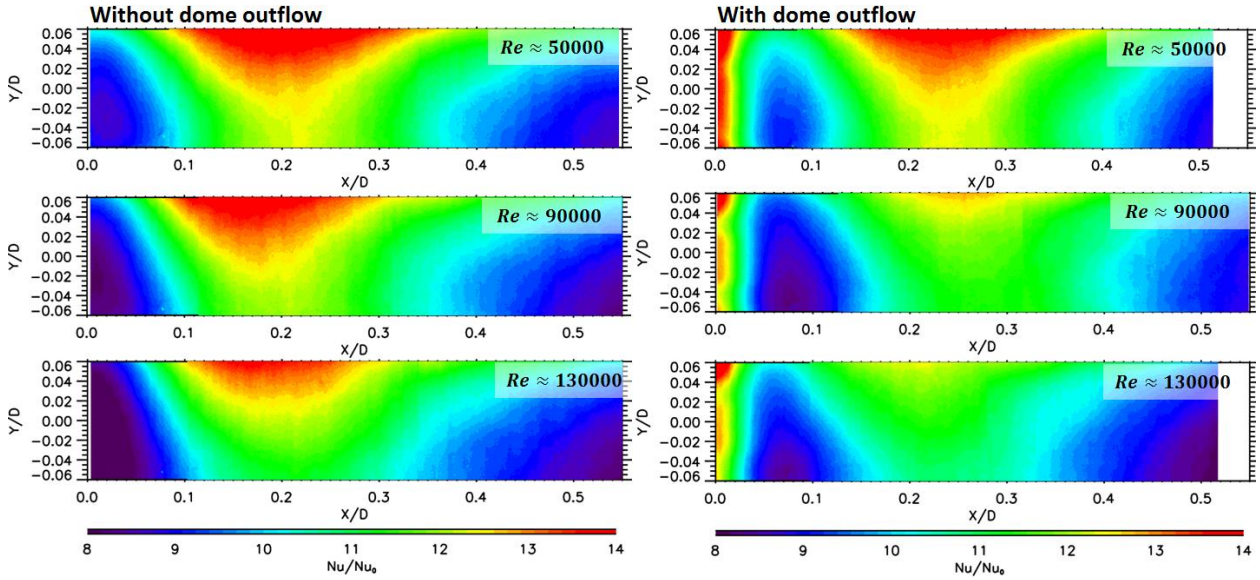


**Figure 25.** Nusselt number enhancement along the inner (convex) combustor liner wall with and without spent cooling from the backside of the heat shield. From [57].

As previously characterized and verified independently by others [54,56,58], the data suggests that the heat transfer enhancement with respect to the Dittus-Boelter correlation

decreases with increasing Reynolds number, however most of the differences are within the calculated uncertainties for the tested cases. Andreini and coworkers [58] presented normalized Nusselt number results while operating their combustor model at a $\Delta P/P_2 = 3.5\%$. The addition of slot cooling in their experiment led to a downstream shift in the peak heat transfer (up to $0.075D$) and a decrease in the maximum enhancement ($\sim 12.5\%$ decrease), consistent with the observations in this study.

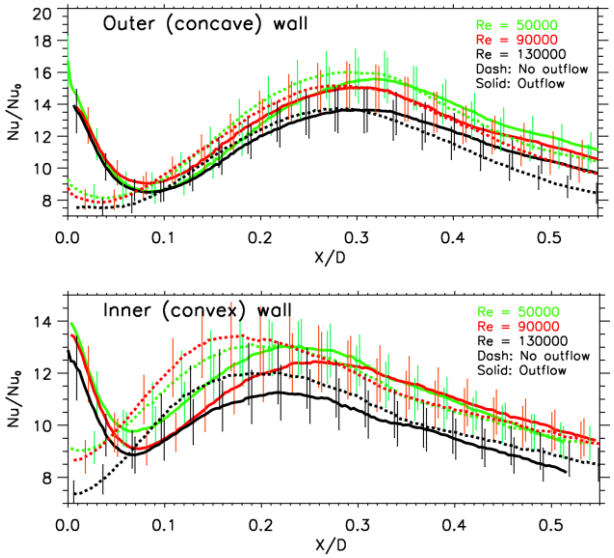


**Figure 26.** Vertically averaged enhancement along the concave and convex combustor walls. From [57].

Figure 14 shows a large enhancement in convective heat transfer ($> 50\%$) close to the dome wall ($X/D = 0$). Beyond $X/D = 0.07$ the outer and inner walls show negligible differences (within the errors) for the magnitude of the enhancement in the presence or absence of spent coolant. While still within the calculated uncertainties, the inner wall showed a more significant difference, the measured peak heat transfer decreased by $\sim 7\%$ in the presence of outflow for the 90 000 and 130 000 Reynolds number cases. This behavior is also consistent with the observations by Andreini and coauthors [58].

#### 2.3.4.1 Analysis of the uncertainty for the steady state heat transfer measurements

The sources of error for the liner heat transfer measurements included errors in the characterization of the optical properties for the surfaces/windows involved, uncertainty in the bulk flow temperature, and errors in the estimation of the heat loss. The IR camera was

calibrated at different temperatures yielding different surface emissivities and window transmissivities. The total error of $(T_W - T_\infty)$ was estimated as $\pm 1.5$ K accounting for calibration errors (<0.4 K), and TC errors of 0.5 K. Table 3 includes the average uncertainty introduced by each error component following the method of Kline and McClintock [115]. Note in Figure 26 that the uncertainties are larger at the impingement location (larger relative errors for $T_W - T_\infty$). The measured combustor Reynolds numbers ($Re_A$) were $51000 \pm 5000$, $88000 \pm 4000$, and $129000 \pm 3000$.

The convective heat transfer measurements on the liner wall were lower than what would be expected in a reacting combustor, particularly after the flame front, due to the increased turbulence levels associated with combustion. According to studies cited by Lilley et al. [20], in the presence of a flame the overall combustor flow field is maintained. The impingement locations and relative shifts due to the presence of the spent air along the liner are hence expected to be similar at reactive conditions, nevertheless this has to be experimentally verified. In a reacting combustor, the flame stabilizes in the inner shear layer of the swirling annular jet exiting the fuel nozzle. Downstream of the flame front, mass flow is conserved and axial velocities increase due to the reduced gas density. Moreover, the viscosity and thermal conductivity of the gas increase due to the high temperatures. Although the axial velocities increase downstream of the flame front, the Reynolds number decreases (viscosity) and hence Nusselt numbers would be impacted at reacting conditions compared to those measured isothermally. The reduction in Reynolds number is however counteracted with the increased turbulence in reacting swirling jets. Experiments in Chapter 5 will focus on characterizing combustor convective heat transfer under reacting conditions.

**Table 3.** Uncertainty estimate for the liner heat transfer measurements

| Uncertainty source | HTC Error Inner wall | HTC Error Outer wall |
|---|---|---|
| $(T_W - T_\infty) \pm 1.5$K | 10.4% | 12.3% |
| $Q_{loss}$ error | 1.7% | 3.2% |
| $Q_W \pm 1\%$ | 1.1% | 1.2% |
| Total uncertainty | 10.6% | 12.8% |

## 2.4 CONCLUSIONS ON ANNULAR STUDIES

The flow features induced by a radial swirler in a model annular combustor, as well as the corresponding heat transfer distribution along the liner walls with and without a heat shield, were experimentally investigated. The normalized flow was proven to be approximately constant independent of inlet Reynolds number ($\mathrm{Re} = 36000$ to $189000$), consistent with results from Patil et al. [56]. The measurements suggest that there is a slight decrease in the average normalized radial velocities with increasing Reynolds numbers, potentially impacting the expansion of the vortex and the impingement of the flow on the liner walls.

A recirculation zone was observed, consistent with the formation of a strong counter-rotating vortex within the primary zone of the combustor. The evolution of the vortex was captured, showing an asymmetrical development, most likely due to the annular shape of the combustor and the convex versus concave curvature of the opposite liner walls.

Heat transfer along the liner walls exceeded the calculated values from turbulent internal flow correlations, with maximum enhancements between 11 and 16 depending on the liner wall and Reynolds number. Moreover, the distribution of the convective heat load on the liner was not uniform, with a peak convective heat transfer at $X/D_H \sim 0.16$. The location of the maximum heat transfer appeared to shift slightly with varying Reynolds number. The magnitude of the enhancement also decreased with increasing Reynolds number.

The heat transfer coefficient on the backside of an industrial combustor heat shield design was also measured experimentally and simulated using the k-ω SST turbulence model. The CFD calculations overpredicted the measurements on average by 28% for a fully turbulent Reynolds number of 2500. Both the experiment and CFD calculation yielded lower spatially averaged Nusselt numbers compared to the correlation for multiple circular nozzles by Martin [112] (by at least 57% with respect to the experiments). It is shown that this discrepancy indicates that the correlation may not be applicable over the entire area of interest. Averaging at locations with conditions closer to those captured by the correlation yielded a maximum difference with the correlation of 22% (some locations in fact showed no difference with the correlation). These observations match the overprediction of 25% observed by Spring et al. [74] for a similar realistic heat shield study.

The effect that the spent air from the heat shield impingement cooling had on the liner convective heat transfer was also analyzed in the annular combustor model. Comparisons between the case with outflow and the case without outflow showed a >50% increase in the convective heat transfer close to the dome wall and a shift downstream in the maximum and minimum heat transfer of $0.03D - 0.07D$ along the combustor liner wall. The impingement location and the extent of the corner recirculation vortex were approximately constant with Reynolds number.

The present study contributes to the understanding on the performance of realistic industrial designs. The development of advanced combustor systems that satisfy future emission and efficiency requirements depends on understanding the convective loads within the burners and properly characterizing realistic cooling technologies.

## 2.5 NOMENCLATURE

| | |
|---|---|
| A | Area [$m^2$] |
| D | Diameter. No subscript refers to the hydraulic diameter of the combustor model annulus [m] |
| d | Target plate thickness [m] |
| F | Forcing function (Duhamel's integral) |
| f | Relative hole area |
| Fo | Fourier number $Fo=t\alpha/d^2$ |
| $G_x$ | Axial flux of axial momentum |
| $G_\phi$ | Axial flux of tangential momentum |
| H | Spacing between heat shield and dome wall [m] |
| h | Heat transfer coefficient [W $m^{-2}$ $K^{-1}$] |
| k | Thermal conductivity [W $m^{-1}$ $K^{-1}$] |
| L | Square root of the surface area covered by a single impingement jet [m] |
| Nu | Nusselt number |
| P | Power [W] |
| $P_s$ | Static pressure [Pa] |
| P2 | Static pressure at the inlet of the combustor [Pa] |

P3 Static pressure at the outlet of the combustor [Pa]

Pr Prandtl number

Q Heat rate [W]

R Heater resistance [Ω]

Re_j Reynolds number with respect to the impingement hole diameter (for impingement studies)

Re_A Reynolds number with respect to the hydraulic diameter of the annular combustor (for liner heat load studies)

$r_s$ Radial distance from the center of the swirler

$R_0$ Outer radius of the swirler hub

$S$ Swirl number

T Temperature [K]

t Time [s]

TC Thermocouple

$TKE$ Turbulent kinetic energy

U Velocity [m $s^{-1}$]

V Voltage [V]

$V_\infty$ Air velocity at the inlet of the combustor

$V_T$ Tangential velocity (from the center of the swirler)

$V_r$ Radial velocity (from the center of the swirler)

$V_x$ Air velocity component along X

$V_y$ Air velocity component along Y

$\boldsymbol{V_{xy}}$ Velocity vector in the X-Y plane

X Horizontal coordinate orthogonal to the mainstream [m]

Y Vertical coordinate orthogonal to the mainstream [m]

Z Coordinate in the mainstream direction [m]

α Thermal diffusivity [$m^2$ $s^{-1}$]

ΔP Static pressure drop across the combustor ($\Delta P = P_3 - P_2$) [Pa]

ν Kinematic viscosity [$m^2$ $s^{-1}$]

Ω Vorticity

| | |
|---|---|
| $\Psi$ | 1D-semi-infinite solid response function to a step change in the convective boundary condition. |

**Subscripts**

| | |
|---|---|
| Air | Air properties |
| H | Impingement hole |
| H | Hydraulic diameter |
| i,0,ref | Initial or reference, impingement point |
| J | Impingement jet |
| K | Time index |
| loss | Thermal losses |
| S | Swirler |
| sfc, w | Surface, wall |
| $\infty$ | Mainstream flow |

# CHAPTER 3.

# DESIGN OF FACILITY FOR REACTING MEASUREMENTS

The design of the facility at Virginia Tech included provisions for operation at higher pressures. Unfortunately, given budget and time constraints, high pressure design and operation are not completed at the moment of writing this dissertation. The design of the facility is described in this chapter, partially including the high pressure operation for future reference. This chapter only briefly comments on the design considerations; additional technical drawings are included as an appendix. It is important to point out that while these may help other groups or students while designing their systems, they should subject their designs to rigorous analysis of their own.

The strategy for the design of the test section is outlined in Figure 27. The first phase of the test rig involved building a low pressure combustor. Phase two consisted of building a pressure vessel to encase the low pressure design. In this way, the low pressure design does not see large pressure loads across its walls and the system can be built in relatively independent steps of incremental complexity.

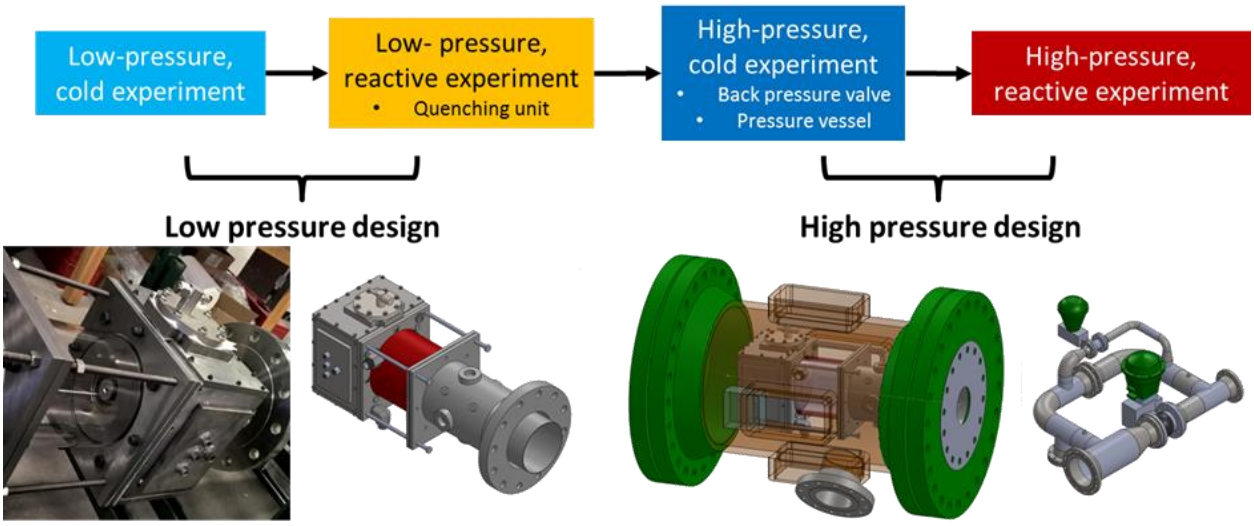


**Figure 27.** Design strategy for the optical combustor facility showing the different phases of the experimental campaign.

## 3.1 OTHER REACTING FACILITIES

The combustor system in a gas turbine operates under the most challenging environment, at some of the highest gas pressures and temperatures attained within the engine. The combustor is simultaneously a critical component, where the energy of the fuel is transferred into the main gas path. Combustor design, pollutant formation, thermal management, and flow have been major research areas during the past decades [12, 13, 26]. Measurements under realistic combustor operating conditions are however limited by the experimental methods and tools available. For this reason, combustor test beds have been developed by different institutions in an effort to characterize several aspects of gas turbine combustion systems.

Sidwell and coauthors [116] developed an optically accessible pressurized combustor rig at the National Energy Technology Laboratory (NETL), as part of a project named SimVal. The objective of their system was to support the validation of computational models for turbulent combustion. The test setup was able to handle operating pressures of up to 22 atm with a maximum inlet air flow of 1.23 kg/s and maximum inlet temperatures of 810K. The optically accessible quartz combustor was 30.5 cm (12 in) long and 17.8 cm (7 in) in diameter. Considerations were given to the acoustic, flow, and thermal boundary conditions. Studies for hydrogen/methane fuel mixtures were conducted on the SimVal rig including pollutant formation [116], flame shape [117], performance of low swirl injectors [118], among others. Isothermal flow characterization was also carried out for the SimVal swirl nozzles as detailed by Strakey and coauthors [36].

The combustion groups at the Deutsches Zentrum fur Luft-und Raumfahrt (DLR) have also done fantastic research on gas turbine combustors. Four high pressure combustor facilities were built at DLR, including an optically accessible sector model [119], as well as a setup to test cooling concepts at realistic gas turbine conditions [53, 120]. Work at the DLR combustors includes flame structure measurements [121], temperature, composition, and flow characterization [122], as well as different studies on flame stability [123]. Although extensive work has also been done to test cooling concepts [53], no efforts have been taken to characterize the heat loads generated by the flame within the combustor primary zone.

Academic institutions such as Georgia Tech and UC Irvine have developed realistic combustor test beds focusing on combustor instabilities and flame characterization studies. The Ben T. Zinn lab at Georgia Tech houses high pressure and atmospheric lean premixed, swirl

stabilized combustor simulators. Particle Image Velocimetry (PIV), OH chemiluminisence, and high speed visualization have been performed in their facilities to study the structure of the combustor flow field, flame speed, stability limits, and acoustic oscillations. The UC Irvine high pressure combustor test set up is described in [124]. Their pressure vessel is able to withstand internal pressures up to 18 atm and maximum inlet temperatures of 755K. Research on low swirl fuel injectors has been performed at this facility [124] focusing on emission, flash-back, and stability characterization.

The Virginia Tech combustor rig was intended to simulate realistic gas turbine combustor conditions, focusing on the measurement of heat loads along the liner walls; an area of combustor design and development that has not been heavily studied. These measurements will be used both to validate computational models and provide valuable information to industry. The system was based on the SimVal and UC Irvine rigs. Contrary to previous systems, the Virginia Tech burner uses no film cooling in the primary and secondary zones in order to simplify the validation efforts and the measurements of the flame side heat loads (the system is however flexible enough to allow for modifications that incorporate film cooling into the flame zone if needed). An industrial nozzle has also been installed to provide a realistic inlet boundary condition to the burner (realistic velocity and turbulent profiles at the inlet to the combustion zone). In spite of the number of research combustors that have been developed, there is limited information on the design methodology and engineering considerations followed by the different groups. This chapter outlines some of the main design challenges faced and details the first construction phase (low pressure operation), referring to the main documents, standards, and codes used for the design.

The Virginia Tech combustor was designed to test a low emission fuel nozzle from Solar Turbines Inc.®. The gas turbine model housing this nozzle produces 5.67MW of electric power and consumes $\sim 1300\ \mathrm{kg/hour\ of\ fuel}$ (heat rate of 11.43MJ/kW-Hr). Twelve nozzles are arranged circumferentially in its annular combustor, corresponding to a 108 kg/hour fuel consumption per nozzle. The nozzle operating conditions served as the design point for the system. The piping and instrumentation were specified to deliver a maximum test section pressure of 9.28 Bar (120 PSIG, at temperature), a maximum inlet temperature of 644 K (700 °F), and maximum continuous air and fuel massflows of 1.27 kg/s (2.8 lbm/s) and 163 kg/hour (360lbm/hour) respectively. Flexibility was paramount and hence the design allows

for the incorporation of other industrial injectors and a broad range of operating conditions. As part of the research initiative, the combustor was designed to be optically accessible and to include provisions for the characterization of flow, flame, and heat transfer.

The design of the research burner was divided into two construction phases as mentioned in the introduction. The first, which is detailed in the following sections, included the air and fuel delivery systems, as well as the design of an atmospheric combustor. The second phase introduces the pressure vessel that encloses the atmospheric burner to operate at higher pressures. The design of the low pressure burner was however heavily influenced by the requirement to enclose it within an optically accessible pressure vessel. The system is similar in this regard to the SimVal combustor [116] and the system at UC Irvine [124].

## 3.2 DESIGNED FLOW SYSTEMS FOR THE FACILITY

The facility was constructed within the Advanced Propulsion and Power Laboratory (APPL) at Virginia Tech. The laboratory houses two Boge compressors that provide a total of 1.27 kg/s (2.8 lbm/s) air massflow at an absolute pressure between 1.135-1.273 MPa (150-170 PSIG). The two compressors operate in a cyclic load-unload mode to control pressure, loading the system when the pressure drops below 1.135 MPa (150 PSIG) and unloading when the system reaches 1.273 MPa (170 PSIG). Downstream of the compressors, the air passes through an air dryer followed by a 18.93 $m^3$ receiver tank that attenuates large pressure excursions and provides capacity for blowdown tests. A schematic of the main air line is shown in Figure 28, where the components highlighted in blue represent the APPL equipment and the remainder corresponds to the systems designed for the test cell and research combustor. The air system in Figure 28 consists of a flow metering section, after which the flow is separated into a main air and a cooling line. The cooling air is metered and regulated in a similar way as the main air line before delivery to the critical burner components in direct contact with the flame. The pressure in the main air line is regulated using a 80 mm DN (3 inch NPS) Fisher EZR pressure reducing regulator, which can be bypassed for high pressure runs. The main air mass flow is throttled using a 100 mm DN (4 inch NPS) Fisher ES globe valve before passing through an electric pre-heater and going through the burner. The burner exhaust goes through a quenching system that injects water into the main gas path to generate steam and cool down the gases before reaching

the backpressure valves. The backpressure valves generate a controllable flow obstruction that allows for operation at different burner pressures.

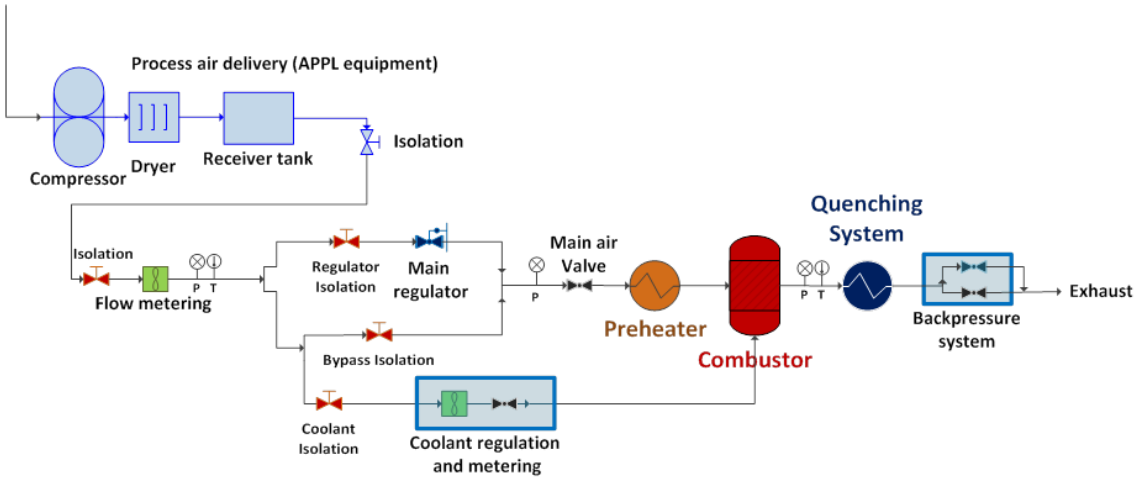


**Figure 28.** Simplified piping and instrumentation diagram for the research combustor test rig

The design of the system allows for simultaneous and independent control of the pressure and mass flow to the burner. For safety reasons, all the valves are remotely actuated using electronic positioners that are activated from a separate room. The valves in the system were sized following the calculations listed in the ISA-75.01.01 standard for control valve sizing [125]. The standard provides several formulations to calculate the valve flow coefficients depending on the units used and the available information on the working fluid. Per the standard, the valve flow coefficient, $C_v$, for compressible gases (assuming non-choked, turbulent flow, and no fittings attached to the valve) is proportional to the massflow through the valve, $W$, and approximately inversely proportional to $\sqrt{\mathrm{P}_1\,\Delta P}\,(1-\Delta P/P_1)$. $\Delta P/P_1$ is in general $\ll 1$ and hence the flow coefficient is roughly inversely proportional to $\sqrt{P_1\,\Delta P}$. The backpressure valves operate at a constant pressure differential defined by the test section and the exhaust pressures (atmospheric). This leads to a large range of required valve flow coefficients as the back pressure system must handle both low flowrates at high pressure differentials and high flowrates at low pressure differentials to maintain a broad range of possible operating conditions. In order to provide appropriate control of the backpressure at all cases, the backpressure system was designed to operate with two control valves in parallel (one with a low and the other with a high $C_v$ rating),

as shown in Figure 29. Fisher V150 Vee-Ball rotary control valves were selected for the back pressure system because of their lower cost and faster response. A 150 mm (6 inch) rupture disc prevents any dangerous pressure buildup upstream in case the valves are incapable of handing the steam generated in the quenching unit.

The main air inlet valve was specified under the assumption of a fixed pressure differential between its inlet and outlet; the size of the valve opening (percentage open) thus modifies the mass flow delivered. The pressure differential across the main air valve is determined by the upstream pressure reducing regulator and the test section pressure (controlled by the backpressure valves). Note that using a single valve to throttle the flow (i.e without the pressure reducing regulator upstream) would lead to a large range of required $C_v$ coefficients and hence an inadequate control of the mass flows.

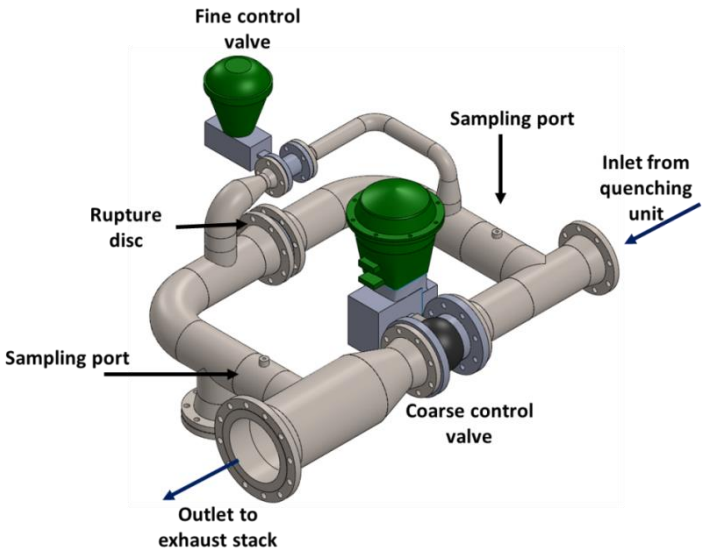


**Figure 29.** Design of the back-pressure system to control the burner operating pressure.

For the metering section, a turbine flowmeter was selected due to its accuracy, price, and turn down ratio. A 65 mm DN (2½ inch NPS) HO-series turbine flowmeter from Hoffer Flows Incorporated with a signal amplifier was used for metering the main air supply to an accuracy of 2% over the entire repeatable range extending from 0.024 kg/s (0.052 lbm/s) to 1.81 kg/s (4lbm/s) (turn down ratio of ~ 77). The meter was placed upstream of any changes in pressure in the line (immediately downstream of the process air delivery point to the test cell). This was done to prevent sizing over different operating pressures. Turbine flowmeters measure the volumetric flowrate and must be sized according to the actual volumetric flow through the meter,

operation at low and high pressures unnecessarily extend the required operating range. Temperature and line pressure measurements are sampled 10 diameters downstream of the meter to derive the mass flow. Similarly, the air used for cooling is metered using a 50 mm DN (2 inch NPS) HO series turbine flowmeter from the same company. The cooling air line includes a thermal mass flowmeter from Eldridge Products, Inc. (EPI) for redundancy. The different meters in the line allow for periodic consistency checks between devices.

Upstream of the test section an inline 192 kW electric pre-heater manufactured by OSRAM Sylvania was installed. The heater has a maximum temperature rating of 750 K (900 °F) with a maximum allowable working pressure of 1.48 MPa (200 PSIG). The heater is operated from a control box that includes a PID controller with multiple set-point and control strategies, as well as safety shutdowns in case of low air flow or a prohibitively high temperature condition.

Piping was selected and specified based on the applicable ASME B31 codes [126] for different portions of the pipe. Black carbon steel pipe schedule 40 (SA-53 Grade B type E) was used for all the components upstream of the burner. Stainless steel 316L was specified for the quenching and backpressure systems to withstand the higher temperature exhaust gases as well as the presence of water condensate (and the diluted carbonic acid forming from the combustion products). Material information was obtained from the ASME Boiler and Pressure Vessel Code (BPVC) [127] section II and pipe stresses were calculated from ASME B31 and BPVC formulations. Balancing material costs with corrosion and manufacturability was a major challenge during the design phase, primarily for the high temperature components. Limited information is available for the performance of engineering materials at typical gas turbine exhaust conditions. The work by Lai [128] provides an excellent summary on different tests that have been conducted for materials ranging from carbon steels to proprietary nickel alloys at high temperatures. Other ASME standards and codes were used for flange ratings (ASME B16.5), buttweld fittings (ASME B16.9), and forged fittings (ASME B16.11). The entire design of the facility is shown in Figure 30. A flexible metallic hose connects the backpressure system to the quenching unit to allow for the thermal expansion of both components. An expansion joint is also located downstream of the main air valve to allow for the expansion of the heater piping during operation. The spools are anchored at defined locations either before or after the expansion joints to direct the pipe movement in the appropriate direction.

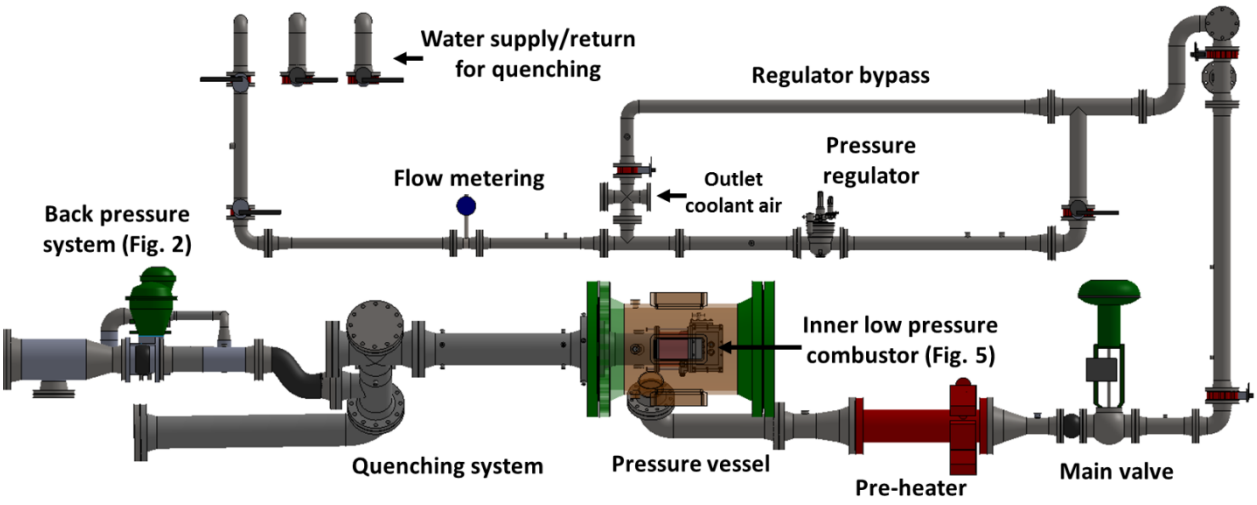


**Figure 30.** Test cell design for the combustor rig including high pressure components (preliminary designs).

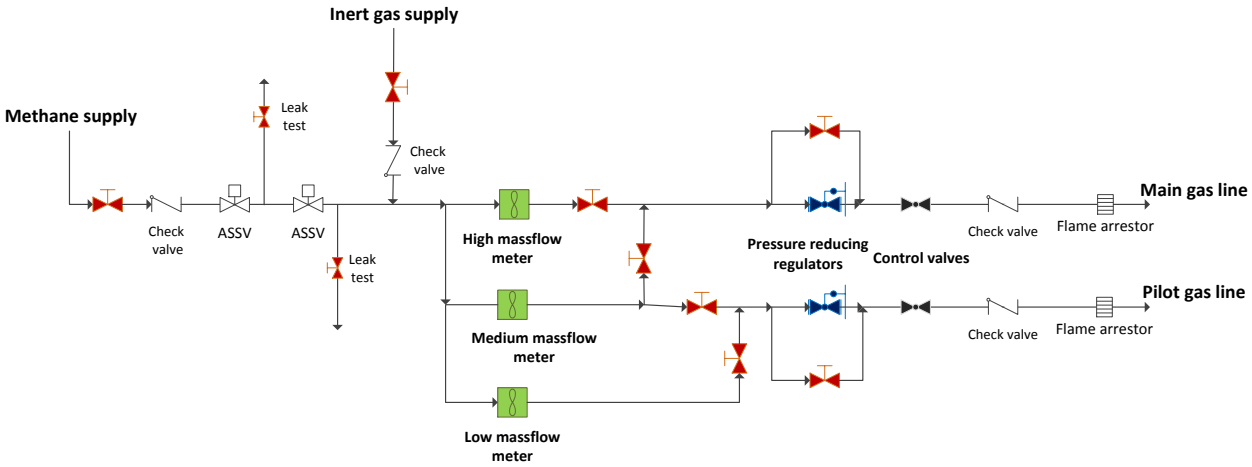


**Figure 31.** Simplified gas train diagram with the component arrangement for control of the main and pilot gas lines.

A schematic of the fuel system is shown in Figure 31, which was designed for operation with methane at an inlet pressure of 1.135 MPa (150 PSIG), either from stand-alone cylinders or from a natural gas compressor. The fuel line was based on the recommendations from NFPA code 37 (Standard for the Installation and Use of Stationary Combustion Engines and Gas Turbines [129]). The fuel line controls and delivers the appropriate main and pilot fuel mass flows. Three EPI thermal mass flowmeters are used for metering the gas flow, calibrated for different ranges providing metering between 0.33 and 163 kg/hour (0.0002 and 0.1 lbm/s) with at least 6% accuracy. The automatic safety shutoff valves (ASSV) consist of normally closed

solenoid valves that close in the event of power loss or signal interruption due to any fail condition in the system. The check valves and flame arrestors provide additional protection in case any pressure buildup in the combustor test section (due to the steam overheating in the quenching unit) forces air flow back into the fuel line. An inert gas line is also included to purge the system for maintenance.

## 3.3 BRIEF ACCOUNT OF THE EVOLUTION OF THE BURNER DESIGN

This section is included to justify the final burner design decisions and to add perspective to any future work on the facility by briefly commenting on the ideas that were considered during the design. One of the first design concepts is shown in Figure 32. It replicated a typical combustor consisting of a metal casing and liner, with the swirler nozzle directly mounted on the casing pipe. The main problem with this design was that it was impossible to properly isolate the swirler flow. Actual gas turbine engines are designed to achieve the appropriate combustor inlet air split, dividing it into the main gas path and coolant flows. For the experiment however, it was critical to meter the mass flow rate through the swirler nozzle to be able to run the burner at specific equivalence ratio and mass flow conditions. This could only be accomplished with independent coolant and main gas paths. Another problem with the design was the lack of flexibility. The casing pipe would only be suitable for a swirler with a particular length and mounting flange. The conceptual metal liner at this point included holders for square quartz windows. Sealing would have been difficult in this kind of arrangement, as well as properly cooling any metal exposed to the flame. One important idea that was taken from this concept was the casing setup. The casing was designed with openings that could hold either a window or a blank boss plate (alternatively with fittings for instrumentation). These metal plates would lower the cost (and risk) of multiple windows, without limiting the optical access to different parts of the burner.

The current design strategy described in the introduction to this chapter (Figure 27) was then formulated. One of the initial designs of the inner test section is shown in Figure 33. To maximize optical access to the primary zone, it was decided to make the liner out of two concentric quartz cylinders. The inner liner would be in contact with the flame and would handle the thermal stresses, whereas the outer liner would contain the coolant flows that would keep the inner liner at an acceptable temperature. Using quartz had the added benefit that this material can operate at high temperatures (softening point is 1683 °C) and can sustain thermal shocks, making

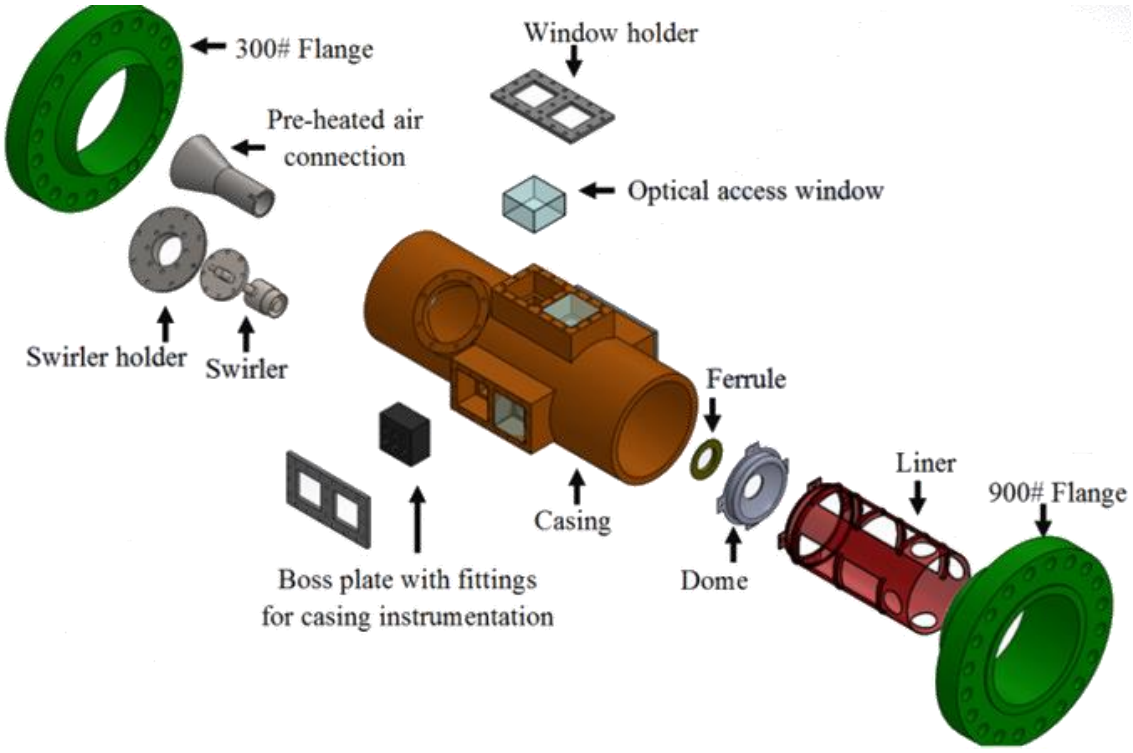


**Figure 32.** One of the initial conceptual designs for the burner test section.

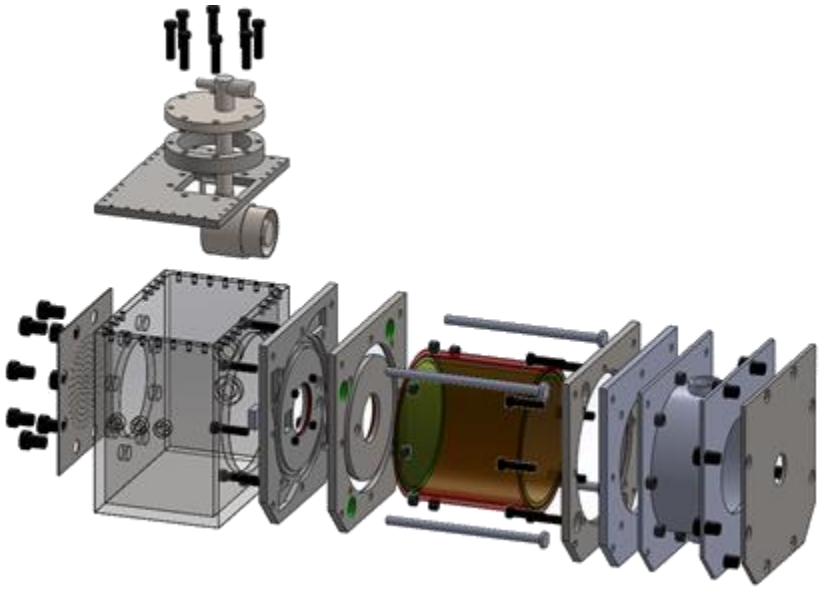

**Figure 33.** Initial design for the internal low pressure burner.

it ideal for the primary combustor zone. It has the disadvantage that it cannot sustain large tensile stresses (tensile strength is around 7000PSI, with a recommended maximum tensile load of 2000 PSI). Pressurizing the quartz liner was then impossible given the high safety risk involved if the liner were to brake. It was hence a priority to minimize the pressure drop across the thickness of either liner. In this preliminary design, the coolant passing through the liners was not directly connected to the main gas path, which would had made difficult to adequately match the coolant pressure to that within the burner. The final test section was designed to dump the liner coolant flow to the main gas path at the exit of the burner. In this way, any pressure excursions within the primary zone (at ignition for instance) would also be approximately seen on the coolant side, minimizing the pressure load on the quartz. Another idea for this burner was to use water for cooling the dome and transition piece (after the quartz liners). This was later discarded as described in the following section, due to the resulting large thermal stresses and potential accumulation of steam. If water were used for instance on the dome plate, the metal on the coolant side would almost be at the water temperature (even at low water flow rates), while the metal on the flame side would be (depending on material/thickness/assumed heat transfer coefficients on the flame side) at several hundreds of degrees Celsius. This large thermal gradient across the dome plate would require very thin metal pieces to keep the thermal stress within acceptable levels (minimize metal warping). The following section describes the final test section design and considerations.

## 3.4 COMBUSTOR TEST SECTION

The industrial nozzle provided by Solar Turbines® Incorporated was designed for operation within an annular combustor. Given the space and budget constraints, a can combustor was designed with a diameter of 203 mm (8 inches), approximately matching the expansion observed in the annular combustor. Numerical models can then be validated using the simplified can combustor and future numerical studies can explore the interaction between adjacent nozzles in an annular arrangement.

As mentioned in the introduction to this chapter, it was recognized that a combustor with small pressure differentials across its walls can be developed relatively independently from the optical pressure vessel that will eventually be used to increase the operating pressures (similar to

the liner/casing arrangement in actual gas turbine combustors). This motivated the split of the test section design into the two construction phases: Phase 1 consisting of the inner combustor (minimal pressure loads), and Phase 2, incorporating the enclosing pressure vessel. The design of the inner combustor however accounted for the thermal loads at final operating pressures which allow for higher mass flows (larger convective heat transfer coefficients), and which lead to increased flame radiation.

A cross-section of the designed test section for continuous operation at high temperatures is shown in Figure 34. The burner consists of a rectangular plenum chamber, where the dome assembly and fuel nozzle were mounted. The dome assembly consists of two dome plates attached directly to the plenum chamber, which compress a ceramic rope gasket around the fuel nozzle to minimize air leakage across the nozzle outer diameter. The primary combustion zone downstream of the nozzle is contained within two concentric cylindrical quartz liners in between which cooling air flows to maintain the internal quartz liner temperature below the annealing point of the material (1343K). The coolant flow from the quartz liner then flows through the transition piece, cooling a SS 310S jacket, finally impinging on the exit choke and mixing with the main gas path. The transition piece connects to the flange of either the pressure vessel (construction phase 2) or the quenching system (phase 1).

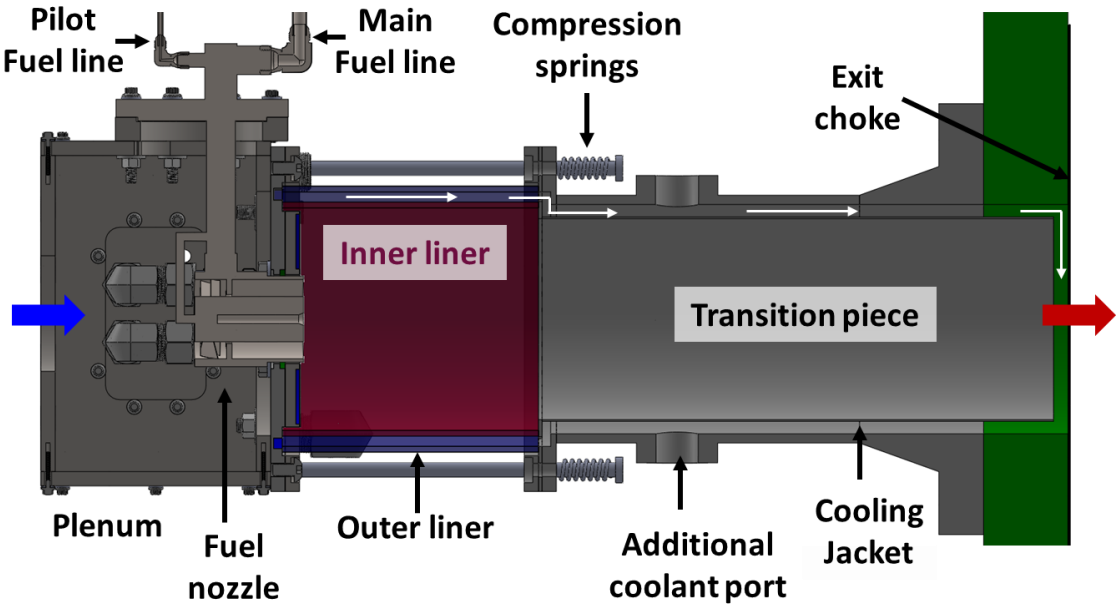


**Figure 34.** Test section cross-section. The blue and red arrows indicate the inlet and outlet respectively. The white arrows indicate the path taken by the liner coolant.

The plenum was made of carbon steel (ASTM A516, selected for its machinability while still being able to operate at the required combustor inlet temperatures). Ports on the side walls of the plenum allow for seed injection, and provide the capability to measure nozzle inlet temperature, pressure, and turbulence. The sharp edges of the plenum (where stress concentration occurs) were not a concern, since the test rig was designed to maintain small pressure differentials across the plenum walls (the inlet air pressure is approximately the same as the surrounding pressure).

The design of the dome pieces that attach to the plenum chamber is shown in Figure 35. The channels highlighted in blue are for coolant air flow and the channel highlighted in red is where the two concentric liners sit. Between the quartz liners and the dome pieces, a ceramic gasket was placed to achieve an airtight seal. The dome piece on the settling side includes channels that deliver coolant flow tangentially to the space between the quartz liners. The additional swirl velocity component due to the tangential coolant entry is expected to increase the backside heat transfer to the coolant and consequently lower the coolant requirement (calculation of the backside cooling heat transfer was performed assuming uniform, non-swirling flow through the channel). The thickness of the flame shield was decided based on the thermal stress it had to withstand. The calculated thickness (0.61 mm) was hard to achieve by machining a thicker metal piece, thus the flame shield was instead designed to be welded to the flame side dome piece, sealing the flame shield cooling channel. The cooling channel (blue region) highlighted for the central part of the flame side dome piece in Figure 6, is a recess of 3.2mm machined into the part to carry the coolant for the flame shield (the gap height was sized to keep the required heat transfer coefficients). This coolant enters and exits the central cooling chamber from the backside of the dome. Water cooling was initially considered for the flame shield, but the large heat transfer rates achieved with water led to prohibitively high thermal stresses. Moreover, water cooling was discarded due to the potential accumulation/formation of steam leading to hot spots and potential failure. Thermal stresses were also critical for the quartz liner, thus the cooling flowrates, as well as quartz thickness, were designed to maintain a maximum liner temperature of $\sim 1230K$ and temperature differentials of $\sim 170K$ at burner design conditions. The tensile strength of fused quartz can be as high as 48.3 MPa (7000 PSI), but design practice is to keep tensile stresses below 13.8 MPa ($\sim$ 2000 PSI), the calculations yielded thermal stresses $<$ 6.9 MPa.

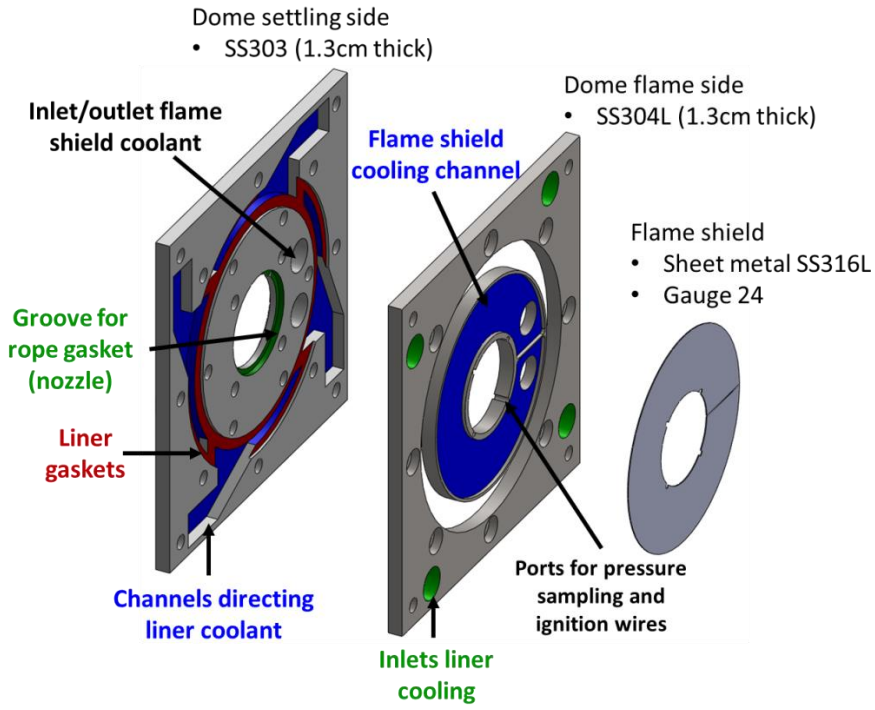


**Figure 35.** Dome pieces exploded view. Flow would travel from left to right. The nozzle would be placed on the central opening.

The quartz liners are compressed between the dome and the transition piece using a set of springs, similar to the UC Irvine design [124], to allow for the expansion of the quartz liner while minimizing leakage. Four guiding threaded rods extend from the dome to slightly past the start of the transition piece (the rods were fixed at the dome end). The transition piece was mounted on these guides and pressed against the liner and dome by compressing the springs at the end of the rods with a tightening nut. Similar to the dome side, alumina ceramic gaskets were placed between the liner and the transition piece to accomplish a proper seal. The springs were sized to provide a minimum sealing pressure of 0.238 MPa (20 PSIG). The compressive stress on the optical quartz was not a concern given its large compressive strength of ~ 1151 Mpa.

The length of the transition piece was defined based on the recommended allowances between welds for the pressure vessel (currently being designed), as well as the sizes of the required vessel flanges and optical windows. Both the dome and transition piece were also instrumented on the backside with K-Type thermocouples for health monitoring of the equipment. Supplementary cooling ports on the transition piece were also included. The coolant

flow to the dome piece, liner, and transition piece jacket can be independently metered and throttled, allowing for operation at different thermal states. It is speculated that different wall temperatures may modify the heat transfer characteristics along the liner by changing the local aerodynamics or by modifying the reaction rates close to the wall. Axial speeds along the liner are increased in reacting flow conditions due to the density gradients across the flame front (conservation of mass). Different wall temperatures could potentially impact the axial speed close to the liner and hence its heat transfer. This in addition is coupled with large gas property gradients close to the liner. The dynamic viscosity and thermal conductivity of air for instance increase by $> 20\%$ from the design liner temperature (1230 K) to typical adiabatic flame temperatures at the lean conditions tested ($\sim$ 1800 K). Liner temperatures could also affect the reaction rates close the wall and the quenching distance of the flame, impacting the thermochemical heat release to the liner.

The thermal loads were estimated following the calculations and analysis given by Lefebvre and Ballal [12] for the dome, liner, and transition piece. The analysis outlined by Lefebvre and Ballal includes estimates for the convective and radiative loads. Zirconia thermal barrier coatings from Aremco were procured to coat the dome flame shield and transition piece to improve the life of the pieces. The thermal barrier coatings were accounted for (assuming $0.05 - 0.1$mm thickness) in the calculation of the thermal loads and stresses. The allowable stresses of the different materials as obtained from the ASME BPVC Section II account for creep failure and are comfortably below the yield point at the operating temperatures as they already incorporate a safety factor. Material selection for the different pieces was based on cost, processing required (machining/welding), and properties (corrosion, high temperature resistance, strength). Stainless steel (SS) 303 for instance was specified for the upstream dome piece (settling side) due to its free-machining properties, while SS 304L and SS 316L were specified for welding the flame shield and dome on the flame side. The low carbon variety was used to prevent any sensitization problems during long term operation at high temperatures. Thermal expansion compatibility was also considered while selecting bolts and welds between materials. To prevent high stresses at the weld points of the flame shield, care was taken not to select a stainless steel with larger expansion coefficients compared to the base metal (SS 310 for instance). The different circumferential thermal expansion between the sitting metal and the quartz liner was also accounted for.

A picture of the first construction phase state showing the low pressure combustor directly connected to the pre-heater line is shown in Figure 36.

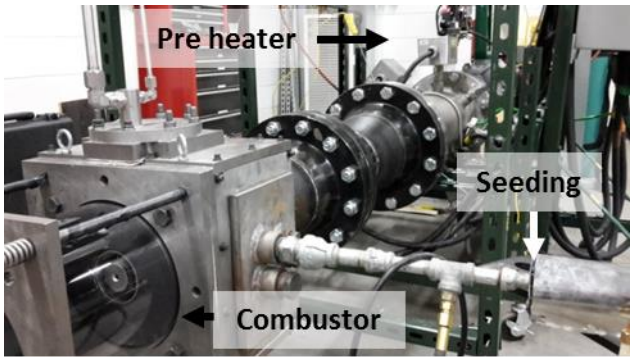


**Figure 36.** Phase 1 test section built and installed with the pre-heater in the background.

## 3.5 DISCUSSION ON THE OPERATION OF THE RIG

An initial concern during the design phase was the use of cylindrical liners instead of planar windows. Refraction of the laser sheet or acquired images are known to cause issues in some experiments, and corrective lenses are applied to cylindrical liners for beam steering. The measurements (particularly PIV) showed no significant image distortion. It is expected that during reacting conditions, the large density gradients could lead to larger errors in the PIV acquisitions. PIV acquisitions in some planes did show variations in the laser sheet intensity attributed to a combination of liner fouling and refraction across the glass. However, the effect was small and the error was removed by image pre-processing (background removal and normalization of the image intensity at all pixels). The drawbacks for the rectangular windows were the requirement for a holding structure on the liner, increased stresses (during ignition, rectangular windows could experience excessive stress particularly at the corners and edges), limited optical access, and the increased complexity of the numerical domain for simulations (different materials, no longer axisymmetric). Fouling of the windows is a recurrent issue for PIV measurements and accessibility to the window is paramount in these experiments. An entire cylindrical quartz liner can hence be more time consuming to clean or replace than a set of rectangular windows.

It is speculated, based on asymmetries observed on the flame shape, that the horizontal orientation of the test setup could lead to buoyant forces acting on the lower portion of the flame

leading to a distorted flow pattern. Other rigs have been oriented vertically [116,124], presumably avoiding asymmetries related to buoyant forces. Nevertheless, actual gas turbine combustors operate horizontally and hence any distortion in the flow pattern due to buoyancy should be characterized and studied.

# CHAPTER 4.

# CHARACTERIZATION OF THE ISOTHERMAL FLOW AND HEAT TRANSFER IN THE OPTICAL COMBUSTOR

This chapter presents the heat transfer and flow field measurements performed on the developed test rig at atmospheric and isothermal (single temperature, non-reacting) conditions, as a baseline for the subsequent reacting experiments. These experiments expand on the methodologies presented in Chapter 2. The velocity field measurements using PIV were taken one step further by performing a tripe decomposition to differentiate stochastic from the periodic fluctuations in the flow field. This is critical to understand the anisotropy generated by swirling flows and the instabilities that develop. The heat transfer measurements are similar to the steady state heat transfer measurements performed in Chapter 2 with the additional complication of imaging the infrared radiation through optical quartz, which is only partially transmissive in the IR (optically thin for wavelengths below $\sim 2.5\,\mu$m). A FLIR SC6700 IR camera was used for this measurement as its detector is sensitive for wavelengths between 1 μm and 5 μm. In this chapter, first the flow experiments are presented, followed by the heat transfer measurements.

## 4.1 FLOW FIELD WITHIN THE OPTICAL COMBUSTOR

Most of the available investigations in the open literature to date have been performed using idealized or representative fuel nozzles that allow for precise control of different geometrical or operating parameters [28, 36]. The work in this dissertation complements the information on idealized fuel nozzles with steady and unsteady flow field data from a modern industrial fuel injector (Solar Turbines Incorporated SoLoNOx nozzle). Particle image velocimetry (PIV) measurements were taken at three different normalized mass flows, one of which was equivalent to the nozzle design point, matching the corresponding inlet Mach numbers. This information is critical for designers using numerical tools and for the validation and development of computational codes.

To fully understand the unsteady features observed in the flow, the coherent and stochastic temporal components of the flow field were determined by means of a methodology based on Proper Orthogonal Decomposition (POD). In light of the vast amounts of data generated by modern measurements, it is essential to further develop and foment the use of exploratory data analysis techniques that can summarize the available information. Proper Orthogonal Decomposition (POD), also known in different fields as Principal Component Analysis (PCA) or Empirical Mode Decomposition (EMD), is known to be a suitable tool to study coherent structures in turbulent flows [130-134]. Recent work by Lengani et al. [130] have further improved current vortex identification methodologies [133,134] by incorporating a polynomial fit of the velocity fluctuations to better extract the coherent characteristics of the velocity field. These ideas have been recently applied by Berrino and coauthors [131] to study the effects of confinement in a double swirl nozzle, proving the potential of the technique to extract the embedded coherent structures in combustor flows and obtain their phase characteristics. Recent interest in alternative uses of POD within the combustion and gas turbine communities include its use for flow validation [135] and structure identification [34]. This chapter follows a methodology based on the work by Lengani and coauthors [130] to separate the PIV flow measurements into their mean, periodic, and stochastic components (triple decomposition), providing further information on the character of the turbulence generated by the industrial fuel injector.

### 4.1.1. Flow field experimental setup

As a reference, a schematic of the test section used to characterize the isothermal flow field is shown in Figure 37. Note that the transition piece described in Chapter 3 was not included to simplify cleaning and replacement of the optical liner. The mass flow rate was calculated from the readings of the turbine flow meter upstream of the setup, with coincident temperature and pressure measurements. The uncertainty in the mass flow measurement was $\sim 2.03\%$ for all cases. However, the compressor in the laboratory provided a cyclic loading that led to a low frequency oscillation ($< 0.005$ Hz) on the supplied mass flow to the combustor of $\pm 1.4\%$. Accounting for the compressor oscillation, the overall uncertainty in the mass flow delivered to the test section was $\pm 2.5\%$.

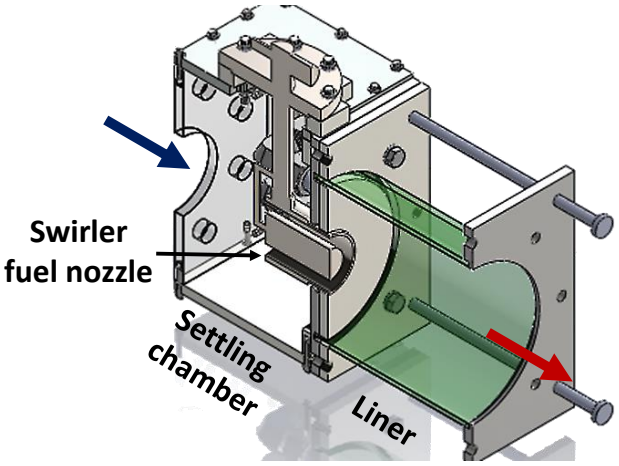


**Figure 37.** Schematic the test section.

As described in Chapter 3, the test section consisted of a settling chamber where the swirl nozzle was mounted flush with the dome plate, followed by a cylindrical quartz liner with an internal diameter of 203 mm and a length of 216mm. The primary zone of the combustor was purposely designed to be as simple as possible, with no film or effusion cooling, in order to simplify the validation of numerical models. Pressure and temperature were monitored upstream of the nozzle in the settling chamber.

The tests were performed at ambient pressures, which prevented any decoupling between Reynolds and Mach numbers for the setup. In the current work, both Mach and Reynolds numbers increased simultaneously for increasing mass flows. However, the Mach number is often a more relevant variable for the study of turbomachinery as it will determine the pressure loss characteristics and overall component performance. This is as long as the corresponding Reynolds number remains away from any critical transition points for the flow or boundary layer [21,25]. For this reason, the design non-dimensional mass flow ($\dot{m}_{ND}$) [12] for the fuel injector was matched in the experiments (Eq. 19).

$$\dot{m}_{ND} = \frac{\dot{m}\sqrt{RT_3}}{A\,P_3} \tag{19}$$

The design conditions of the fuel injector correspond to $\dot{m}_{ND} = 0.1359$. Additional measurements were taken for normalized mass flows (at ambient conditions) including 0.0377 and 0.0753. The three mass flows tested correspond to Reynolds numbers with respect to the fuel nozzle throat diameter of $\sim 50\,000$, $\sim 100\,000$, and $\sim 180\,000$. The measured static

pressure drops across the combustor were 0.52%, 1.37%, and 4.13% respectively with increasing mass flow.

### 4.1.2 Particle Image Velocimetry (PIV) methodology followed

Two dimensional planar particle image velocimetry (PIV) measurements were taken at the planes indicated in Figure 38. Planes A-C are referred to as axial planes (XZ planes) and planes D-G are referred to as cross-sectional, radial-tangential, or azimuthal planes (ZY planes). Planes C-G were located at $X/D_N =\sim$ 0.01, 0.16, 0.9, 1.54, and 2.4 respectively. Plane C captured the swirler exit profiles and plane D the initial jet expansion into the primary combustion zone. Planes E and F are before and after the impingement of the jet on the liner respectively, and Plane G was taken to capture the dynamics close to the outlet of the combustor. The coordinate system origin was defined at the center of the swirl nozzle (the figure shows it displaced for clarity). The measurements were performed using a Nano-L 135-15 dual Nd:YAG laser system, with a Flowsense 4M MkII camera ($2048 \times 2048$ pixel resolution), and Dantec Dynamics® acquisition software. Glycol droplets were seeded into the settling chamber upstream of the swirl nozzle to act as tracers for the PIV measurement. The seed particle sizes delivered to the test section were estimated to be $< 2.5\ \mu$ m [136] yielding an expected velocity delay of $\sim 20\ \mu$ s.

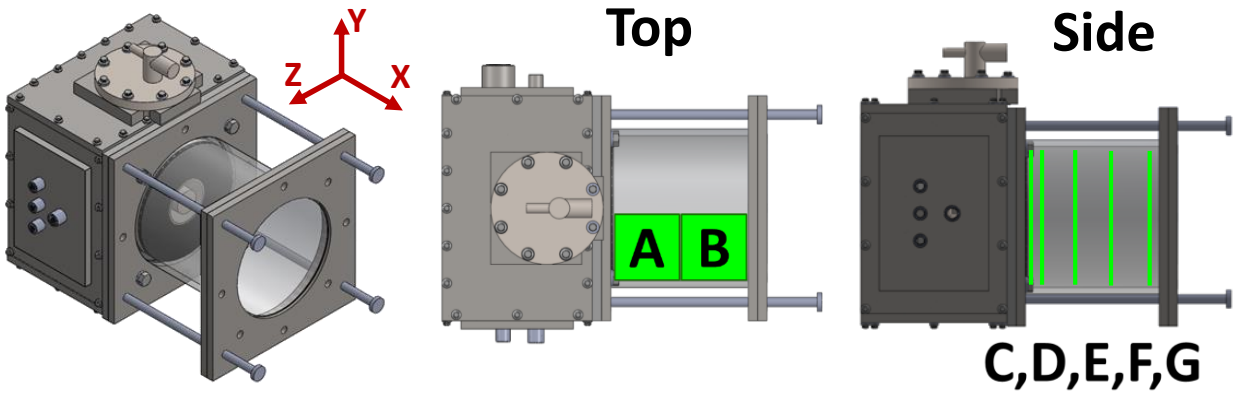


**Figure 38.** Measurement planes. The origin of the coordinate axis is located at the center of the nozzle (displaced in the figure for clarity).

The image pairs (frame A and B) were analyzed using an adaptive correlation procedure with a final interrogation area of $32 \times 32$ pixels and an initial interrogation area of $128 \times 128$

pixels. Neighborhood ($3 \times 3$ median) and peak (1.2 maximum to minimum peak correlation ratio) validations were used to identify unphysical vectors. The PIV software substituted the removed vectors based on neighboring velocities. This however can lead to a velocity bias close to walls or shear layers and hence no substituted vectors (replaced by the peak or neighborhood validation) were used in the analysis. 50% overlapping was used to increase the vector resolution and a total of 800 image pairs were acquired per plane. To acquire the data as accurately as possible, the acquisitions were split into 200 image pair runs, cleaning any fouling of the walls and optical liner between runs. Given the extent of the dataset, an automatic procedure to discriminate invalid velocity fields was implemented. This procedure consisted on removing any vector fields that had more than 80% substituted vectors, indicative of poor seeding, or incorrect background subtraction.

Challenges of PIV in confined spaces involve the presence of light reflections (glare) and background images in the acquisition which may bias or entirely prevent any reliable data retrieval. Variations in the laser intensity and seeding distribution prevent the satisfactory elimination of the background by the subtraction of the time averaged image. Moreover, because of uneven seeding in the flow, local normalization procedures, such as those suggested by Mejia-Alvarez and Christensen [137] for instance, are unsuccessful, as these amplify the noise in regions with few particles. The background removal procedure implemented consisted in 1) subtracting the local minimum for each image ($9 \times 9$ pixel sliding local minimum), 2) calculating the time averaged corrected image, and 3) normalizing all the corrected images with respect to the averaged image (times a constant factor to increase contrast). An example of the implemented background removal procedure applied to an acquisition of Plane D is shown in Figure 39. Another important challenge to note when measuring complex swirling flows is the large range of speeds that must be resolved. Too large a time delay between laser pulses led to particles exiting either the interrogation area or the laser sheet (due to the strong out of plane motion in swirling flows). Too short a delay on the other hand led to negligible movement of the particles. The higher mass flow measurement represented the more difficult acquisition because of the larger quantities of PIV seed required and the consequent quick fouling of the optical liner. The glycol accumulating on the walls changed the laser glare as the experiment progressed, causing errors in the background removal and limiting the observations close to the liner and dome.

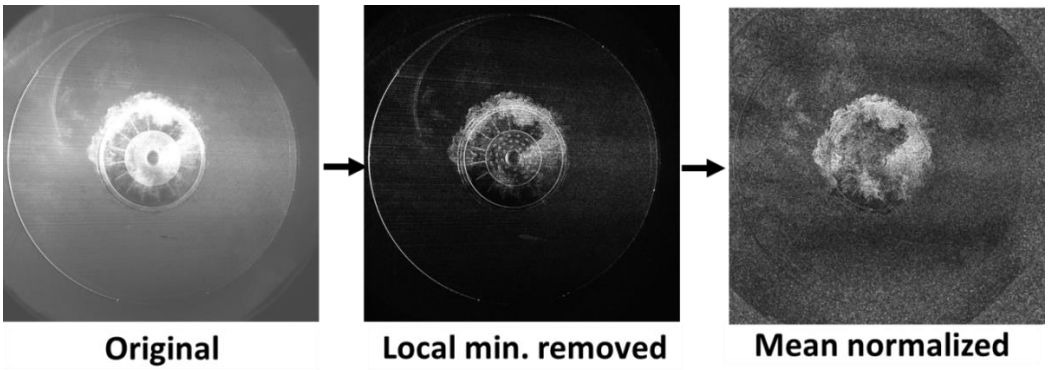


**Figure 39.** Background removal procedure example for PIV measurements.

The correlation algorithm yields an estimated subpixel accuracy of 0.1 pixels, which results in an error between $0.01V_{\text{ref}}$ and $0.06V_{\text{ref}}$ depending on the plane imaged. The data were also checked for consistency at the intersection between cross-sectional and axial planes, where the radial (Z) velocity was sampled twice independently. The average absolute difference in the radial velocities at the overlap between planes was $0.023V_{ref}$, consistent with the expected velocity accuracies. Additionally, the time-averaged axial velocity profile at $X/D_N = 0.05$ was used to estimate the airflow delivered to the test section (assuming axisymmetric flow) with an average discrepancy with the metered mass flows of 5.6%.

### 4.1.3 Analysis using Proper Orthogonal Decomposition (POD) to identify coherent structures

The PIV system was capable of acquiring image pairs at a rate of 7.4 Hz, which cannot resolve the high frequency oscillations in the data (such as the PVC) or the convective transport of vortices. Since the measurements taken were not time resolved, separation of the stochastic and coherent structures in the flow was accomplished using a POD methodology as outlined by Lengani and coworkers [130,131]. The instantaneous flow fields ($f$) were divided into three temporal components (triple decomposition) including a time average ($\bar{f}$), a periodic ($\tilde{f}$) and a stochastic ($\check{f}$) part as described by Eq. 20.

$$f = \bar{f} + \tilde{f} + \check{f} = \bar{f} + f' \tag{20}$$

Where $f'$ is equal to the total fluctuation with respect to the time averaged field.

Other authors have contributed with exhaustive explanations on the mathematics behind POD and its application to the analysis of turbulent flows [132-134]. For this reason the analysis procedure is only briefly described in the present work.

The velocity vector data for each time snapshot was originally arranged in a $ii \times jj$ matrix, with $i$ and $j$ corresponding to the horizontal and vertical locations where a velocity vector was obtained. To perform POD, the data for each time snapshot was first vectorized, that is arranged as a single data vector of length $p = ii * jj$, where each element corresponded to different locations within a single acquisition. The vectorization for snapshot $n$ of the $V$ velocity field is shown by Eq. 21 ($V$ is not restricted to a velocity component, as the analysis can also be applied to any other field such as vorticity or turbulent energy).

$$V_n = \left[v_{n,1}, v_{n,2} \ \dots \ v_{n,p}\right] \tag{21}$$

Which in matrix form, including all the PIV snapshots, becomes Eq. 22. The columns of matrix $\boldsymbol{V}$ contain a single snapshot at a given time, whereas the rows of the matrix contain all the observations at a single acquisition point.

$$\boldsymbol{V} = [V_1, V_2, \dots, V_n] = \begin{bmatrix} v_{1,1} & v_{2,1} & \cdots & v_{n,1} \\ v_{1,2} & v_{2,2} & \cdots & v_{n,2} \\ \vdots & \ddots & \ddots & \vdots \\ v_{1,p} & v_{2,p} & \cdots & v_{n,p} \end{bmatrix} \tag{22}$$

Subtracting the time-average of the dataset at all locations, $\bar{V} = \left[\overline{v_1}, \overline{v_2}, \dots, \overline{v_p}\right]^T$, yields the total fluctuation $\boldsymbol{V'}$.

$$\boldsymbol{V'} = \boldsymbol{V} - \bar{V}\mathbf{1} = \boldsymbol{V}\left(\boldsymbol{I} - \frac{\mathbf{1}^T\mathbf{1}}{n}\right) \tag{23}$$

Where $\mathbf{1}$ represents a row vector containing $n$ ones and $\boldsymbol{I}$ is the $n \times n$ identity matrix. The goal in POD is then to obtain the coefficient column vector $\chi_1$ of length $n$ that yields the maximum variance when the fluctuation dataset is projected onto it. In other words, the objective is to find

the linear combination $\chi_1$ of the $n$ flow field snapshots, such that $\boldsymbol{V'}\chi_1$ has maximum variance. The sample variance of $\boldsymbol{V'}\chi_1$ is calculated from Equation 24.

$$\mathrm{var}(\boldsymbol{V'}\chi_1) = \frac{1}{n-1}(\boldsymbol{V'}\chi_1)^T(\boldsymbol{V'}\chi_1) = \frac{1}{n-1}\left(\chi_1^T\,\boldsymbol{V'}^T\boldsymbol{V'}\chi_1\right) \tag{24}$$

Recognizing that the covariance matrix, $\boldsymbol{\Sigma}$, of the flow field fluctuations is given by Equation 25, Eq. 24 can be reduced to the form given by Eq. 26.

$$\boldsymbol{\Sigma} = \frac{1}{n-1}\left(\boldsymbol{V'}^T\boldsymbol{V'}\right) \tag{25}$$

$$\mathrm{var}(\boldsymbol{V'}\chi_1) = \chi_1^T\,\boldsymbol{\Sigma}\chi_1 \tag{26}$$

Equation 26 represents an eigenvalue problem. The eigenvectors of $\boldsymbol{\Sigma}$ provide a set of $p$ independent (i.e. uncorrelated) linear combinations $\chi_k$ of the PIV snapshots. The eigenvector with the highest eigenvalue $\lambda_1$ is equal to $\chi_1$, the eigenvector that yields the maximum projected variance $\mathrm{var}(\boldsymbol{V'}\chi_1)$.

The covariance is a measure of how observations of a variable change with respect to simultaneous or equivalent observations of a different variable. In this analysis, each velocity location is treated as an observation and each time snapshot as a different variable. Physically, the covariance matrix is a measure of how the fluctuations in the velocity field are related between acquisitions. It calculates how consistent are the features in the different snapshots (either overall positive or negative covariance). Periodic vortical structures convecting with the mean flow will show maximum positive covariance for two snapshots that capture the vortex in the same location (in phase), and decreasing covariance when the vortex signal is shifted (out of phase). The eigenvalues ($\lambda_k$) and eigenvectors ($\chi_k$) of the covariance matrix yield the significance of each PIV snapshot to the variance in the data. The eigenvalue represents the relative amount of variance captured by the corresponding eigenvector, while the eigenvectors weight each snapshot according to its significance. A geometric description of this process can be attained by visualizing each flow snapshot representing an axis in an $n$-dimensional space, where the entire velocity fluctuation data is plotted (e.g. the first point, corresponding to the

location $i = j = 1$ in all the snapshots would have coordinates $v'_{1,1}, v'_{2,1} \ldots v'_{n,1}$). The eigenvectors of the covariance matrix identify an orthogonal (independent) set of directions along which the plotted data is aligned.

The $k^{\text{th}}$ POD mode ($\phi_k$) represents the projection of the entire velocity fluctuation dataset ($V'$) into the $k^{\text{th}}$ eigenvector as calculated by Eq. 27.

$$\phi_k = \boldsymbol{V'}\chi_k \tag{27}$$

The elements of the eigenvector indicate how each PIV acquisition contributes to the corresponding mode. The first mode (formed with the eigenvector of the highest eigenvalue) represents the velocity field that captures the highest amount of time variability in the dataset. Subsequent modes (lower eigenvalues) capture decreasing amounts of time variability. The data can then be decomposed according to the matrix multiplication of the full eigenvector matrix ($\chi$) and the POD mode matrix ($\phi$) as shown by Eq. 28.

$$\boldsymbol{V'} = [\phi_1, \phi_2, \ldots \phi_n] \times [\chi_1, \chi_2, \ldots \chi_n]^{-1} = \boldsymbol{\phi\, \chi^{-1}} \tag{28}$$

This formulation can be used to filter a portion of the variation in the data according to selected POD modes, by setting the corresponding unwanted eigenvectors to zero. Other researchers have removed the low energy modes from the dataset to eliminate random errors during the measurement or the contributions of turbulence to the data [131,134]. Since identifying the turbulence is of importance for the current investigation, and POD is unable to differentiate between random errors in the acquisition and actual low energy flow perturbations, all the modes were retained.

Per the discussion in Legrand [133,134], periodic convective flows yield coupled POD modes, with the two most energetic modes and eigenvectors representing the sine and cosine components of a convecting flow oscillation. Figure 40 shows the first two POD modes for the axial velocity in plane A ($Re = 180\,000$). The patterns in these two modes are consistent with propagating vortices.

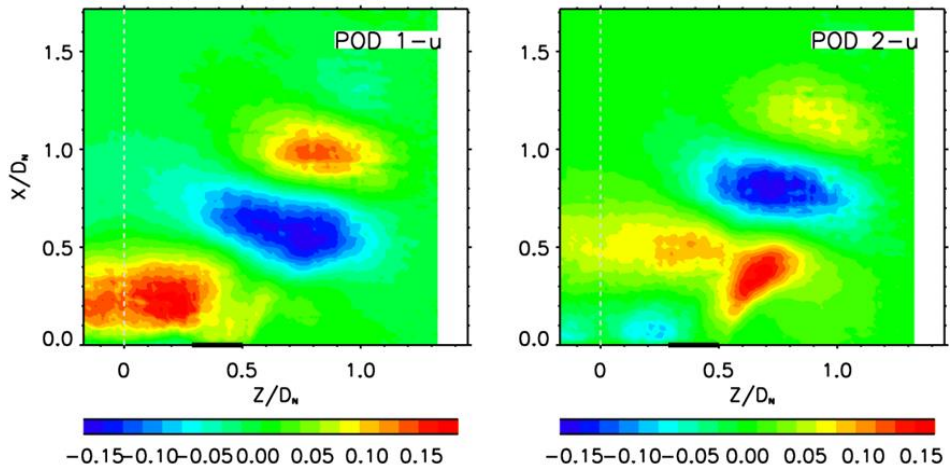


**Figure 40.** The two most energetic POD modes for the axial velocity component ($u$) observed for the measurements in plane A.

Regions of the velocity field where stochastic turbulence dominated, did not show a strong pattern. Hence, to extract the phase of the periodic oscillation in the flow, it was important to select locations in the flow field where the oscillation signal was highest. As done by Lengani et al. [130], a point in the region where each POD mode showed the highest signal was selected to extract the oscillation. Lengani and coauthors [130] showed that in order to obtain the appropriate propagation direction for the extracted vortical features, the location of lowest signal (most negative) in the first POD mode and the location of the highest signal (most positive) in the second POD mode must be selected.

The velocity components ($u$, $v$, $w$) are the actual variables that fluctuate, and hence the data was first projected to the two eigenvectors that carry the oscillation signal (Equations 29 and 30), and then the phase $\theta_n$ associated with each PIV snapshot within the oscillation was calculated (Eq. 31) from the assumption that the first eigenvector represented the sine component, and the second the cosine component of a convecting oscillation in the flow [130,133,134].

$$V'_{f,(1)} = [\phi_1, \phi_2, \dots \phi_n] \times [\chi_1, 0_2, \dots 0_n]^{-1} \qquad (29)$$

$$V'_{f,(2)} = [\phi_1, \phi_2, \dots \phi_n] \times [0_1, \chi_2, \dots 0_n]^{-1} \qquad (30)$$

$$\theta_n = \arctan\left(\frac{V'_{f,(1)}}{V'_{f,(2)}}\ \frac{\max\left(V'_{f,(2)}\right)}{\max\left(V'_{f,(1)}\right)}\right) \qquad (31)$$

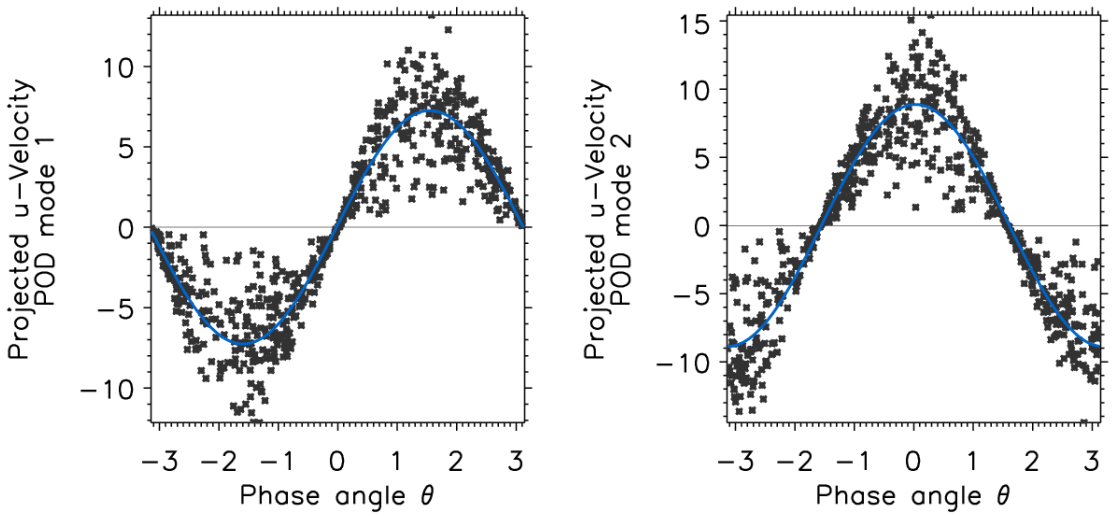


**Figure 41.** Filtered axial velocity measurements at the location of highest oscillation signal arranged according to the calculated phase.

The POD modes help in two ways, first to identify the location where the oscillation signal was most significant (highest variance in the data), and second to specify the corresponding eigenvector that defines how each PIV snapshot is contributing to the oscillation. After calculating the associated phase for each PIV snapshot, the data was rearranged according to the phase. Figure 41 shows the arranged filtered velocity at the location of highest oscillation signal ($V'_{f,(1)}$ and $V'_{f,(2)}$). Note that the signal reproduces the assumed sinusoidal pattern.

After identifying the phase of each PIV snapshot, the entire dataset was arranged according to its phase within the oscillation. To perform the phase averaged velocity measurements, Lengani et al. [130] suggest to fit a 5$^{th}$ order polynomial to the velocity history at each pixel location. A limitation of using a 5$^{th}$ order polynomial is that the fit may be heavily biased by outliers in the dataset, particularly at the end/start of the oscillation period. An alternative that was adopted in the current investigation was to instead use a Fourier polynomial at each pixel location as defined by Eq. 32.

$$V'(\theta) = a_0 + a_1\cos(\theta) + b_1\sin(\theta) + a_2\cos(2\theta) + b_2\sin(2\theta) + a_3\cos(3\theta) + b_3\sin(3\theta) \qquad (32)$$

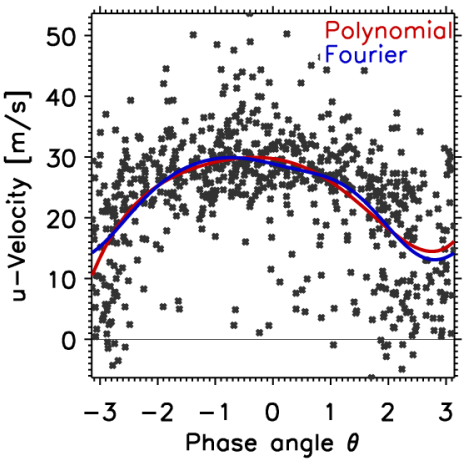


**Figure 42.** Comparison between 5th order and Fourier polynomial fits to the measured data arranged according to the calculated phase within the oscillation.

The advantages of the Fourier polynomial model is that the results are not heavily biased by the data points close to the end and start of the oscillation period ($\theta = -\pi$ and $\theta = \pi$), and that the fitted model is in better agreement with the underlying physical phenomenon of convecting periodic oscillations. Figure 42 compares the results obtained using a 5th order polynomial fit [130,131] and the Fourier model herein suggested for an arbitrary pixel in plane D that showed a significant oscillation signal. At a phase angle of $-\pi$, the polynomial and Fourier model differ by $\sim 30\%$. The noise introduced by the polynomial fit yielded a less uniform velocity field, compared to that obtained from the Fourier model. The disadvantages of the Fourier model were its complexity and the potential lack of convergence in regions where no oscillation was present.

The POD modes for the horizontal and vertical velocities for each plane were calculated, the decision between choosing either the horizontal or vertical velocity modes for phase identification was based on which captured the highest fluctuation energy percentage in the flow (based on the eigenvalues for the first and second eigenvectors).

### 4.1.4 Flow field results

The analysis of the time-averaged velocity fields is first presented, followed by the analysis of the total velocity fluctuations and unsteady fluid dynamics. Given the extent of the dataset, only measurements that were deemed relevant were discussed. For simplicity, the three operating conditions tested are referred to in terms of the equivalent Reynolds number. The velocity fields were normalized with respect to a reference velocity corresponding to the ideal average axial velocity exiting the swirler at the target mass flows. The reference velocities were equal to 11.01, 22.02, and 39.64 m $s^{-1}$ respectively for increasing operating mass flows.

The total fluctuating velocity components ($u', v', w'$) were readily available from the instantaneous measurements after the mean field ($\bar{u}, \bar{v}, \bar{w}$) had been computed. An overall turbulence (total fluctuation) kinetic energy (TKE), per the traditional Reynolds decomposition, was calculated according to Equation 33.

$$\mathrm{TKE_{XYZ}} = \frac{1}{2}\overline{u'^2} + \frac{1}{2}\overline{v'^2} + \frac{1}{2}\overline{w'^2} \tag{33}$$

The TKE was normalized with respect to the square of the reference velocity ($V_{ref}^2$) to maintain same order scales between the three operating mass flows tested. When only two components of the velocity field were available, a two-dimensional TKE was calculated (which underestimates the total three dimensional fluctuation energy at any given point). The total TKE as calculated by Eq. 33 is not representative of the actual turbulent field as it includes the contribution of coherent periodic structures in the flow. To obtain the underlying stochastic turbulent field, the overall TKE was separated into its coherent and stochastic components (triple decomposition).

The main non-dimensional parameter to characterize combustor rotating flows is the swirl number. The definition used in this study is given by Eq. 34.

$$S = \frac{G_\theta}{RG_x} \tag{34}$$

Where $G_\theta$ is the axial flux of angular momentum, $G_X$ is the axial flux of axial momentum and R is the throat radius of the fuel nozzle. The calculation of the momentum fluxes was simplified as

is typically done in the available literature. Fluctuating components were not accounted for, and the axial pressure distribution was not considered for the axial momentum.

#### 4.1.4.1 Time averaged results: Effect of increasing mass flow

Figure 43 and Figure 44 show the time averaged results for the maximum and minimum Reynolds numbers measured at planes A and D. The white outline in the velocity field of plane A indicates $\bar{u} = 0$, matching the mean location of the shear layers and the stagnation point at the combustor liner wall.

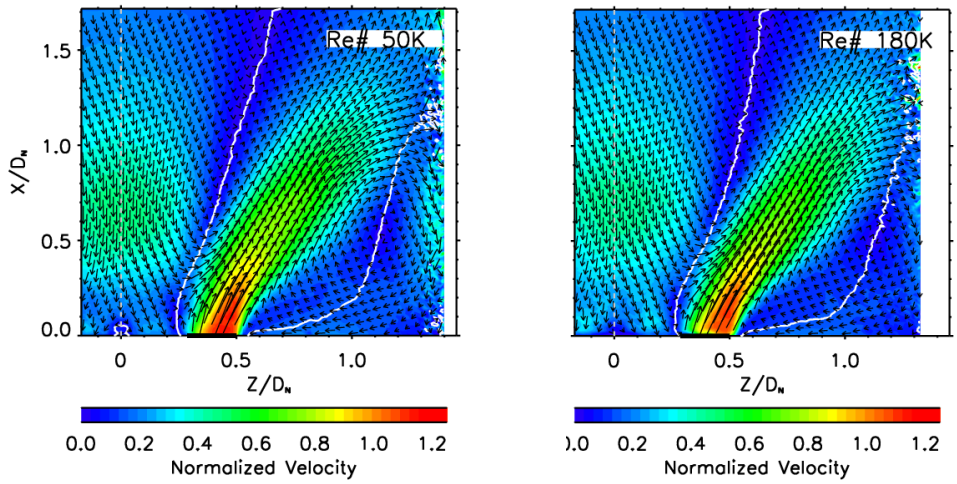


**Figure 43.** Time averaged results for Plane B at the minimum and maximum mass flows, flow direction is bottom to top.

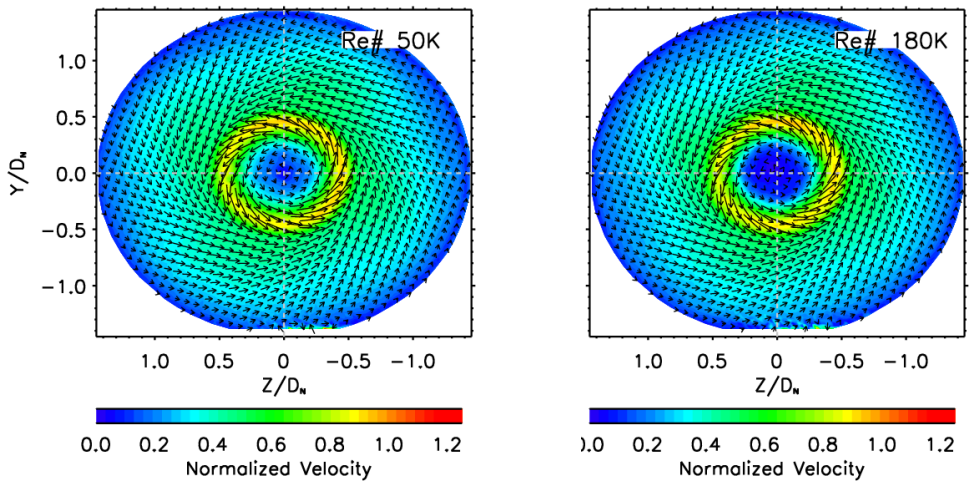


**Figure 44.** Time averaged results for Plane D at the minimum and maximum mass flows.

Other authors have reported that the normalized impingement location and overall flow field is approximately independent of mass flow after a self-similarity threshold [36, 54, 103]. The reason for the self-similarity is that the mechanisms that dominate the flow field within the combustor become inertia dominated (viscous effects are negligible). This self-similarity is of practical importance because it implies that the isothermal combustor flow field can be numerically simulated at lower Reynolds numbers, incurring in a lower computational cost, without significantly sacrificing the scalability of the results. For the range of mass flows tested, the time averaged results were approximately self-similar, with only small differences related to a slightly larger central recirculation zone with increasing mass flow as observed from the azimuthal cross-sections in Figure 44. The larger recirculation bubble further forced the swirling jets radially outward (barely observable in the time averaged flow of plane B). This larger recirculation for the $\mathrm{Re} = 180\,000$ case was not related to a significant upstream shift in the recirculation bubble. An analysis of the maximum and minimum time-averaged axial velocity along the combustor (planes A and B) showed that the maximum recirculation velocity occurred at $\mathrm{X/D_N} = 0.6 - 0.7$ with a magnitude of $-0.48\mathrm{V_{ref}}$ for the three mass flows tested. The maximum axial velocity decayed linearly from the nozzle outlet to $\mathrm{X/D_N} \approx 1.4$ and asymptoted to a constant value of $\sim 0.26\mathrm{V_{ref}}$. Past $\mathrm{X/D_N} \approx 1.4$, the maximum radial velocity also decayed to approximately $0.03\mathrm{V_{ref}}$, indicative of the swirling jet reaching an equilibrium in radial expansion as it was constrained by the liner wall.

At individual planes only two dimensional velocity components were available. However, at the intersection between axial and azimuthal planes, the three dimensional profiles were calculated. The time averaged velocity profiles and the total fluctuation kinetic energy (including both stochastic and coherent structures) are shown in Figure 45 and Figure 46 respectively for different axial stations along the combustor. The $X/D_N = 0.01$ location approximately captured the nozzle exit profiles (for the 180 000 Reynolds number case, the closest axial data available was at $X/D_N = 0.05$). The axial and tangential velocity profiles for $\mathrm{Re} = 180\,000$ had a shift in the radial direction ($\sim 0.02D_N$) for $X/D_N = 0.16$. The radial shift resulted from the slightly larger central recirculation zone at the highest mass flow as previously explained. The profiles in general are consistent with the self-similarity assumption. The swirl jet broadens from $X/D_N = 0.16$ to 0.91 due to shear and entrainment with the surrounding flow as

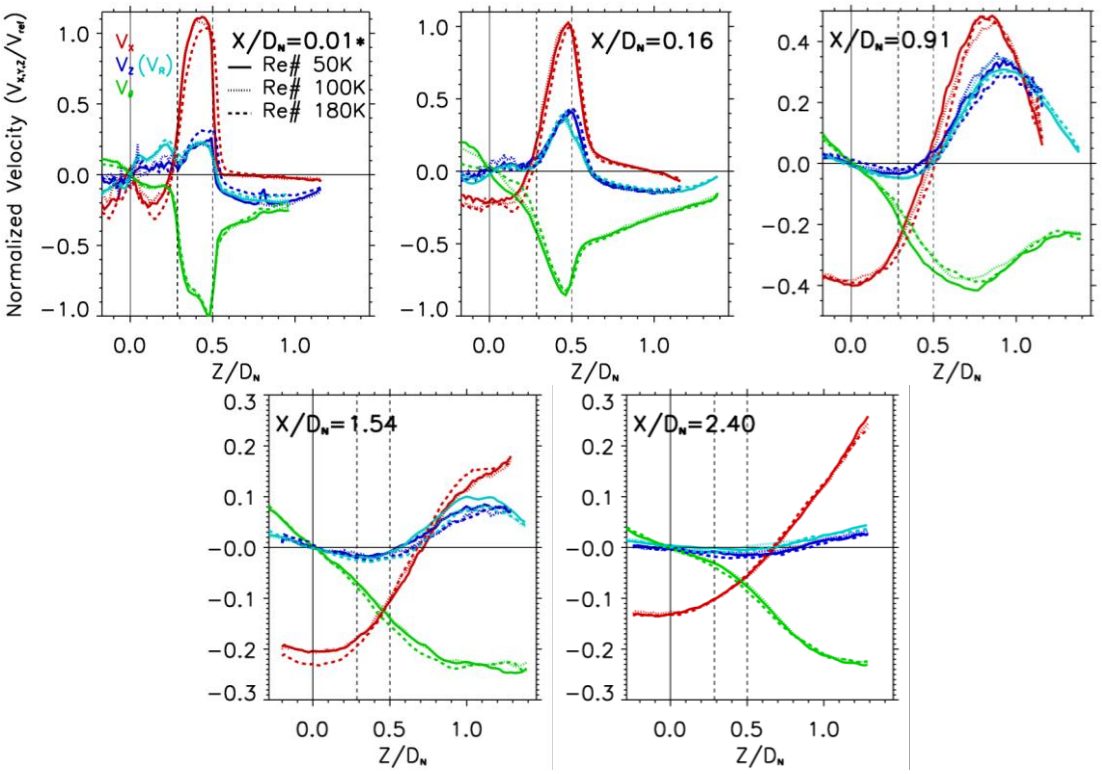


**Figure 45.** Velocity profiles at several axial locations along the combustor.

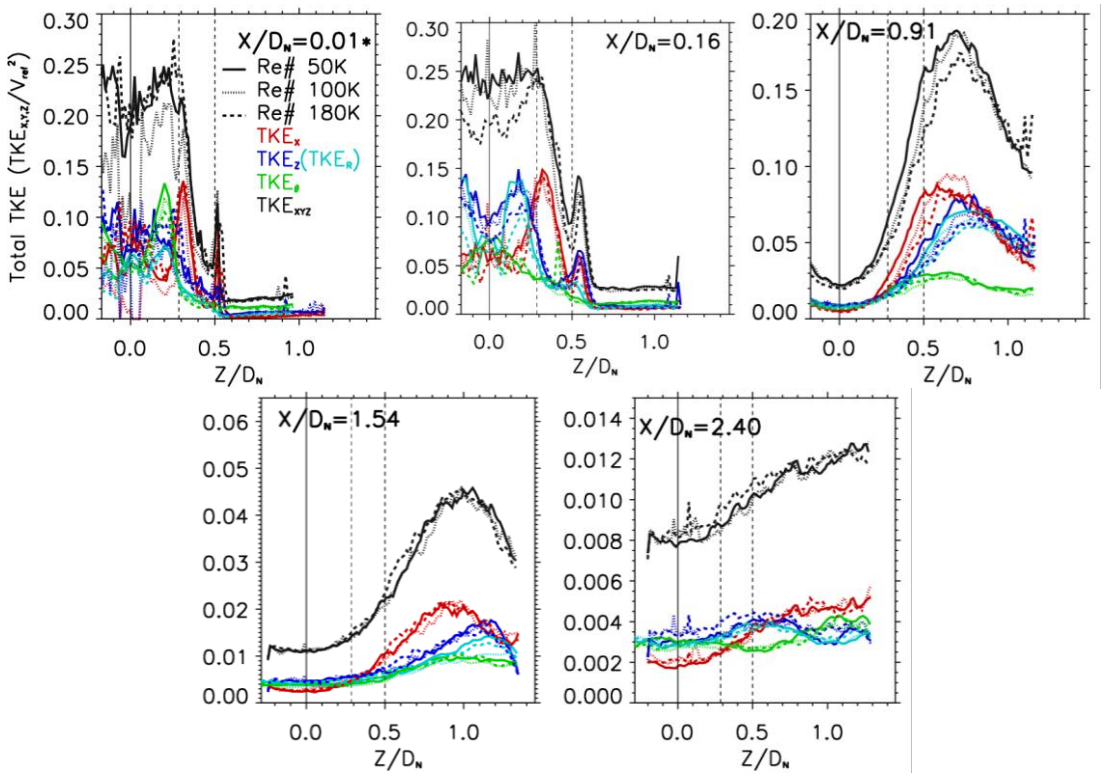


**Figure 46.** Total fluctuation kinetic energy including stochastic and coherent fluctuations at different $X/D_N$ locations along the combustor.

it exits the nozzle and expands into the primary combustion zone. Based on the $X/D_N = 0.01$ profiles, the swirl number at the exit of the nozzle (Eq. 16) was on average $0.74 \pm 0.04$ based on the three mass flows measured. Similarly, the mean flow turning angle $\alpha = \tan^{-1}(V_\theta/V_X)$ was $47.4° \pm 2°$ which compares well with the nozzle vane design angles.

The total fluctuation TKE shows strong anisotropy at all axial locations. It is now well understood that combustor flows feature strong asymmetry due to the presence of coherent structures close to the fuel nozzle, particularly the PVC [27,28]. For the cross-section at $X/D_N = 0.16$, the highest total fluctuation energy was located in the core of the vortex (dominated by the radial component), dropping abruptly across the jet. A second peak in the total TKE was observed at the outer shear layer of the swirl jet, associated with oscillations of the corner recirculation and separation at the edge of the nozzle. Within the jet (shifted slightly to the inner shear layer side), the main component of the fluctuations was in the axial direction. This will be shown in the following section to stem primarily from the coherent structures in the flow. The recirculated mass flow in the recirculation bubble appears to have fairly isotropic total turbulence beyond $X/D_N \geq 0.9$.

After impingement on the liner (estimated at around $X/D_N \approx 1.2$ per plane B measurements), the swirl jet attached to the wall until the flow exited the combustor. Measurements at representative axial locations past the impingement point of $X/D_N = 1.54$ and 2.40 show a distinct decay in the maximum TKE. Prior to the jet interacting with the liner wall, the total maximum TKE decayed due to viscous dissipation and expansion of the coherent vortices from $\sim 0.25V_{ref}^2$ to $\sim 0.16V_{ref}^2$ over a distance of $0.9D_N$. Interaction with the wall led to further attenuation of flow oscillations (dissipation of vortices), decreasing the maximum turbulent energy to 0.05 by $X/D_N = 1.54$.

#### 4.1.4.2 Coherent structures in the flow: The precessing vortex core

The total turbulence calculated from the time averaged velocity fields only provides a partial view of the system dynamics as it fails to distinguish between the flow variations introduced by coherent structures and the underlying stochastic turbulence. The distinction is relevant for the modeling of combustor flows. Coherent structures are periodic and arise due to instabilities in the flow that can be partially predicted by three dimensional unsteady RANS solvers [138]. Large Eddy Simulations (LES) predict both the stochastic and coherent structures, as well as

their interaction, at a higher computational cost. Computational models can hence be optimized with information on the scale of the stochastic and coherent structures and the location where either plays a primary role. This information is also relevant to understand how the coherent structures impact the mixing within the burner and the asymmetry of the flow.

As described in the methodology section, the periodic oscillations were extracted from the velocity field using a POD methodology [130,131,133,134]. Swirling flow studies [26-29] have shown that the center of the swirl generated vortex is not located at the geometric center of the swirl nozzle, as would be suggested by the time averaged fields, and actually precesses around the axis of the combustor. This is a well-known oscillation in swirling flows known as the Precessing Vortex Core (PVC). The PVC constitutes a periodic, non-random oscillation that is enhanced in burners operating with premixed fuel [28].

Figure 47 shows the result of the POD analysis for the measurements at Plane D for the highest mass flow. The progression of the vortex center along the inner shear layer was identified as it precessed around the geometric center of the swirl nozzle (with a precession radius of $R_p \approx 0.17 - 0.2D_N$). As it rotated, it convected a portion of the swirling jet mass towards the axis of the combustor. This led to a depleted swirl jet immediately downstream of the PVC, and to a degradation of the tangential velocity fields by $19 - 25\%$ with respect to the time averaged velocities. Similarly, upstream of the vortex core the PVC strengthened the swirling jets by the same amount by convecting flow from the axis of the combustor to the swirl jet. This enhanced entrainment generated by the PVC in and out of the central region of the combustor is critical to properly predict the mixing between the recirculated gases and the fresh air/fuel mixture carried by the nozzle exit swirl jet. A similar tangential velocity field around the swirling jet was reported by Syred [28] using LDA measurements, but the mixing between the vortex core and the swirling jet was not clear.

A convecting radial/axial vortex was also observed on plane A, as depicted by the phase-time progression shown in Figure 48 for the design mass flow case. The red outline shows the location of zero axial velocity for the instantaneous time-phase displayed, while the white outline shows that obtained from the time average (as given by Figure 43). The red outline traces the path of the shed axial/radial vortex along the shear layer. From Figure 47, the PVC location can be identified in an axial/radial plane (XZ) by the change in the radial velocities within the recirculation bubble that occur as the PVC crosses the plane. Negative radial velocities indicate

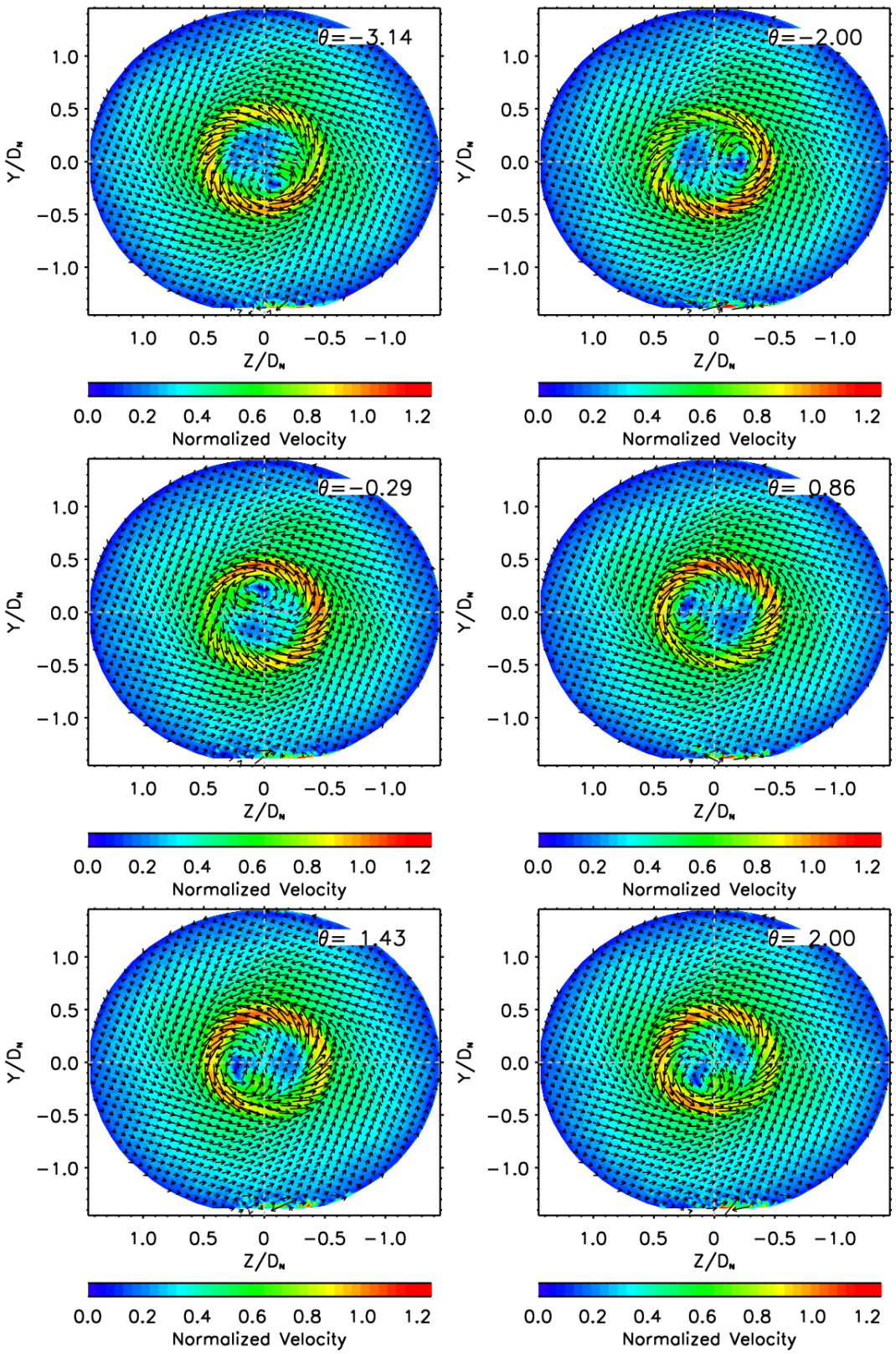


**Figure 47.** Phase progression showing the PVC at plane D for Reynolds number 180 000.

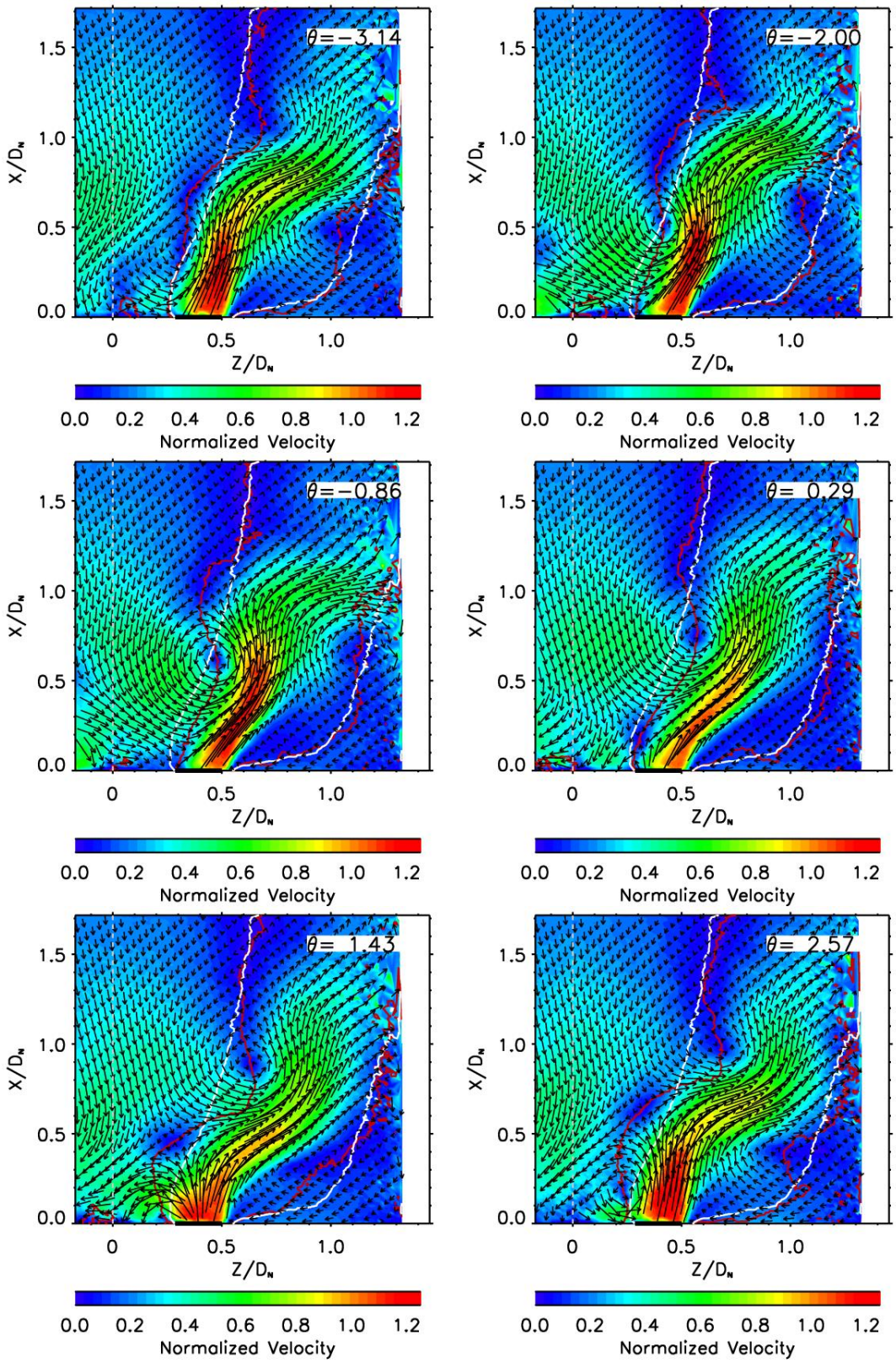


**Figure 48.** Phase progression at plane A showing the downstream convection of axial/radial vortices.

the start of the PVC, and positive radial velocities its end. Going back to the axial/radial eddies, it is then clear that these form as the PVC crosses the plane, with the center of the PVC matching the center of the axial eddies. These measurements however provide no evidence that the vortices are actually following an axial path (constrained only to the XZ plane) as suggested by Figure 48. The three dimensional nature of the flow cannot be neglected. The flow features observed in the instantaneous PIV measurements are more likely explained by an axial/radial vortex that rotates with the PVC along the inner shear layer while propagating downstream. The vortex would then follow a spiral pattern as has been previously reported in literature [26, 19].

The identified vortex propagates axially following a sinusoidal pattern around the time-averaged shear layer location. The shedding spatial wavelength, defined as the distance between two consecutive vortices along the inner shear layer (distance between two peaks in the red outline of Fig. 12), was $\sim 1.14D_N$. The axial vortex dissipated fully at approximately $X/D_N$ =1.2, as the vortex interacted with the liner wall. Between successive vortices there was a region of strong shear separating the swirl jet and the recirculation zone, similar to Kelvin-Helmholtz instability patterns [26].

The flow continues to be asymmetric until the jet collides and attaches to the wall. A strong coherent asymmetry was observed until $X/D_N = 0.91$, but no periodic flow oscillations could be identified for $X/D_N = 1.54$, as shown in Figure 49. This result suggests that the large coherent structures associated with the PVC are only relevant prior to interaction with the liner wall.

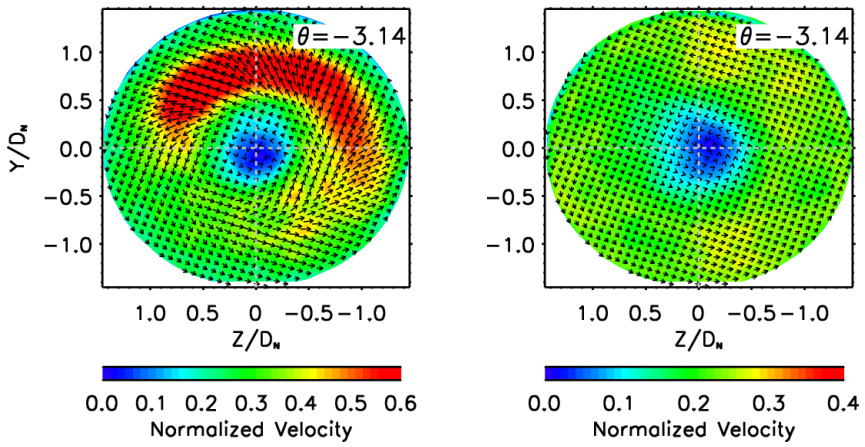


**Figure 49.** Extracted oscillations from plane E and F (left and right respectively) measurements. Plane E (left, $X/D_N = 0.9$) showed a significant propagating oscillation, Plane F (right, $X/D_N = 1.54$) showed no oscillation patterns. Note the different color scales.

An additional consequence of the PVC was an oscillation of the axial and radial velocities (and momentum) at the outlet of the fuel nozzle. For the phase-time $1< \theta < 2$ radians in Figure 48, the mean axial velocity exiting the swirl nozzle was maximum ($1.06 - 1.14\, V_{ref}$), decreasing on average by 44% for all mass flows tested at a phase-time of $-1 < \theta < -2$ radians. This decrease in axial flow speeds coincided with a simultaneous increase in radial speeds at the outlet of the nozzle as the trailing portion of the PVC pushed the jet radially outward.

#### 4.1.4.3 The stochastic turbulent field

The total fluctuation kinetic energy was separated according to its coherent and stochastic components. Figure 50 shows the areas dominated by coherent structures for planes A and D respectively. The coherent vortices play a significant role in the inner shear layer and recirculation zone close to the nozzle (> 40% of the total TKE in both the XZ and YZ planes). Close to the liner wall and beyond $X/D_N \approx 1.5$, the stochastic turbulence dominated (< 20% contribution to the total fluctuation kinetic energy was attributed to coherent structures). Profiles of the stochastic turbulent kinetic energy at the different cross-sections are shown in Figure 51.

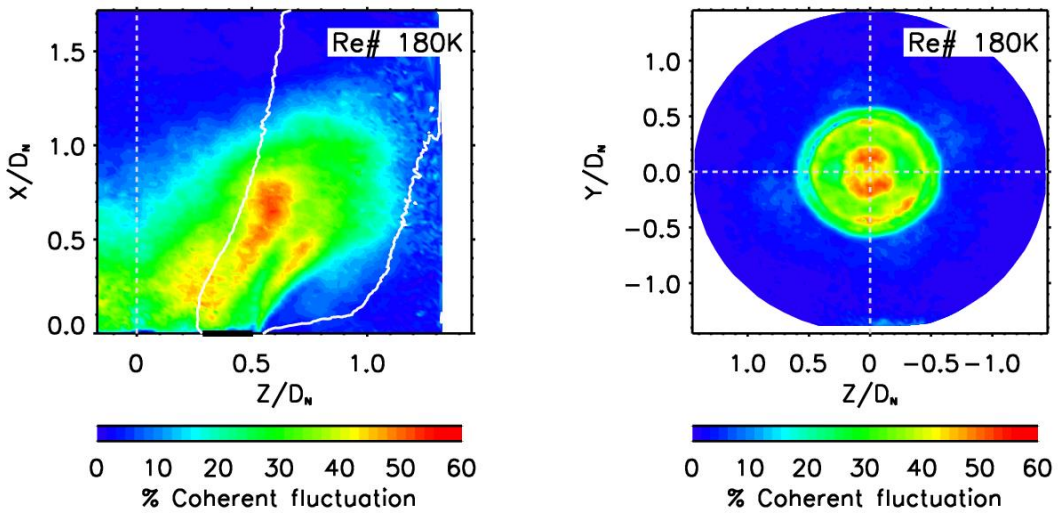


**Figure 50.** Coherence structure contribution to the total fluctuation kinetic energy (including coherent and stochastic components) for planes A (left) and D (right). Two dimensional.

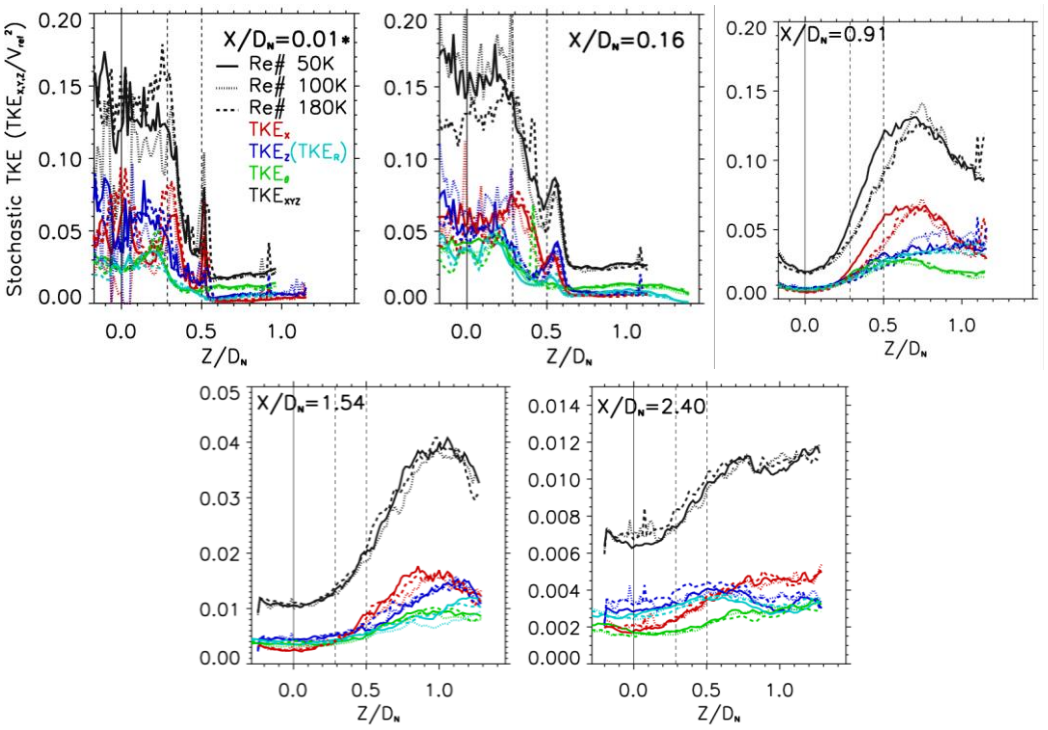


**Figure 51.** Stochastic turbulence properties at downstream locations along the combustor. The stochastic TKE was calculated according to triple decomposition.

Close to the combustor outlet, at $X/D_N = 2.4$, the stochastic turbulent kinetic energy is $\sim 7$ times smaller than the average observed at the nozzle outlet, but the turbulence intensity was on average 47% due to the low flow velocities (the recirculated intensity was 67%). The exiting flow along the combustor walls at $X/D_N = 2.4$ carries on average $\sim 1.3$ times higher stochastic turbulent energy ($0.011V_{ref}^2$) than does the flow recirculating back to the combustor ($0.0084V_{ref}^2$). The difference between the total and stochastic turbulence at $X/D_N = 2.4$ was $\sim 10\%$, indicating that the coherent structures only play a small role in the fluctuations at the combustor outlet.

## 4.2 HEAT TRANSFER ALONG THE LINER

Similar to the flow field experiment, the isothermal (non-reacting) heat transfer along the optical can combustor equipped with the SoLoNOx nozzle from Solar Turbines Incorporated was characterized at atmospheric pressure. Measurements were taken for Reynolds numbers between 11 500 to 140 000 with respect to the combustor inner diameter ($\mathrm{Re_C}$). In terms of the nozzle

diameter, as defined in the flow field section, these Reynolds numbers were equivalent to $\sim 50\,000$ and $\sim 600\,000$. The observed combustor static pressure drops $(1 - P_4/P_3)$ at these flowrates were between 0.61% and 30.42%. The lower mass flow cases reproduced typical combustor pressure drops (< 3%), while the higher mass flow cases reproduced typical combustor Reynolds numbers ($Re_C$> 100 000).

While the data presented at this point does not account for combustion effects, the results are still a necessary prerequisite to understand convective heat transfer within burners without the added complexities introduced by reaction, such as sharp property gradients and multiple heat transfer mechanisms. The optical combustor model developed is capable of operation at reacting conditions, which will be the focus of the next Chapter.

### 4.2.1 Experimental setup for the heat transfer measurement

The experimental setup used for the heat transfer measurements is shown in Figure 52, and matches the setup used for the isothermal flow field studies. As previously described (see Chapter 3 and Section 4.1), upstream of the main control valve there was a $\sim 2\%$ accurate flow metering section and a pressure regulator (not shown in the diagram). The pressure reducing regulator lowered the pressure to the required operating conditions and the main control valve throttled the flow to the desired mass flow rate. An inline 192kW heater was also installed but was not used for the current experimental results.

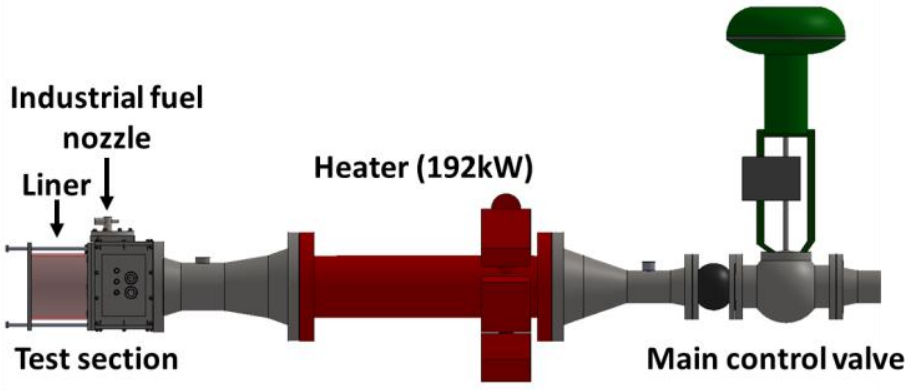


**Figure 52.** Experimental facility diagram.

The test section and coordinate system used for the heat transfer results is shown in Figure 53. The coordinate system was defined at the axis of the combustor but is again shown displaced in the figure for clarity. The heat transfer characteristics were observed to be

axisymmetric and hence only a small portion of the liner was used for the measurement of the convective heat transfer. The area used for the heat transfer measurement is plane A as highlighted in Figure 53. To support the heat transfer observations, the PIV measurements from Plane (B) in Figure 53 (plane A in Figure 38) were also analyzed.

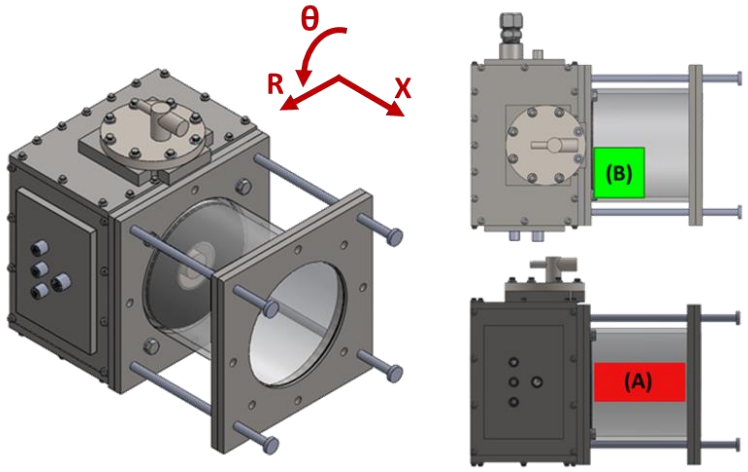


**Figure 53.** Test section. The coordinate system was defined at the axis of the combustor but is shown displaced for clarity. Measurement planes: (A) Heat transfer with IR thermography, (B) flow field with PIV.

### 4.2.2 Heat transfer methodology

To measure the heat transfer along the liner wall, a thin surface heater ($5\ \text{cm} \times 28\ \text{cm}$) was attached to the inner wall of the quartz liner providing a wall heat input ($Q_W$). The wall heat input was determined from the electrical resistance of the heater and the voltage supplied ($P = Q_w = V^2/R_\Omega$). The inner wall temperatures ($T_W$) were derived from infrared (IR) measurements using a FLIR SC6700 camera, with a detector spectral range of 1 to 5 μm. The acquisitions were taken after at least 60 minutes to ensure thermal equilibrium with the surroundings was attained.

A schematic of the heater placement on the liner is shown in Figure 54. The heater was covered with thin aluminum tape to evenly distribute the heat flux generated and coated with a high emissivity paint (emissivity of $\sim 0.88$) to increase the IR emission from the inner wall. The IR camera was positioned on the acquisition side, past the liner wall opposite to where the heater

was placed. The inner wall thermal radiation from the heater is partially transmitted through the quartz glass, reaching the IR detector along with the emission of the quartz liner itself.

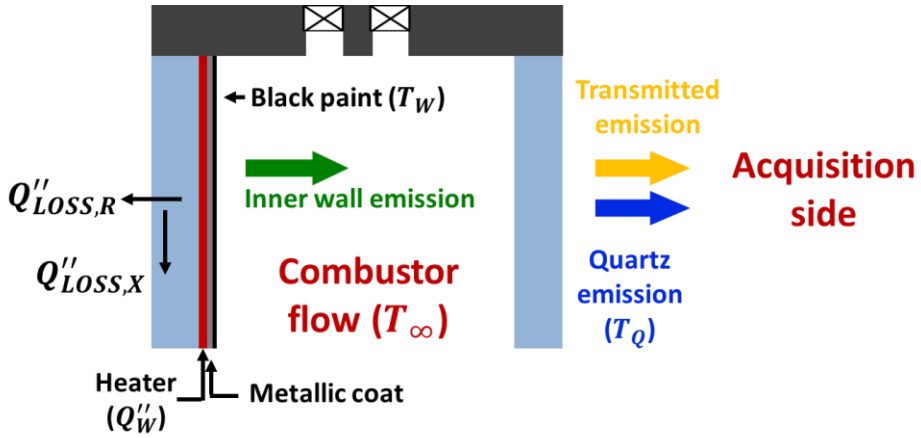


**Figure 54.** Top view schematic of the experimental setup for the heat transfer measurements.

During the experiment, air at ambient conditions was supplied to the test setup. The heater power was adjusted to achieve the maximum allowable temperature at the given air flow. The heat transfer coefficient, $h$, along the combustor liner wall was determined from Eq. 35.

$$h = \frac{Q''_W - Q''_{LOSS}}{(T_W - T_\infty)} \tag{35}$$

Where the wall temperature $T_W$ was determined from the IR acquisitions, $Q''_W$ is the heat flux applied to the surface, $T_\infty$ is the air flow temperature, and the heat flux lost to conduction $Q''_{loss}$ was calculated from experiments detailed in section 4.2.2.2 ($Q''_{LOSS} = Q''_{LOSS,R} + Q''_{LOSS,X} + Q''_{LOSS,\theta}$). $T_\infty$ was estimated from the average of two thermocouples, one immediately at the outlet of the fuel nozzle and another at the outlet of the combustor. The heat transfer coefficient acquisitions close to the combustor dome ($X/D_N = 0$), had large heat losses, making the data for $X/D_N < 0.2$ unreliable. The large heat losses were due to a combination of a lower heat flux distribution (that area corresponds to the edge of the surface heater) and higher lateral conduction losses (to the dome metal pieces).

#### 4.2.2.1 Calibration of the inner wall emission

It was important to demonstrate that the IR camera could measure the inner wall emission reliably, without being overwhelmed by the quartz liner IR emission. Selection of the appropriate heater setting was based on maximizing the inner wall signal received by the IR detector (transmitted emission) without exceeding the allowable temperature for the heater materials. Detailed absorption coefficient data for fused silica can be obtained from [139] and [140], which can be used to approximate the contribution from the inner wall to the overall acquired IR emission. The emissivity of the black coating ($\epsilon_W$) was estimated as 0.88 (at all wavelengths), while the spectral emissivity ($\epsilon_{\lambda,Q}$) and transmissivity ($t_{\lambda,Q}$) of the quartz liner were estimated from Lambert's and Kirckhoff's laws (Equations 36 and 37 respectively), neglecting the reflectivity of the quartz (typically less than 2%).

$$1 - a_{\lambda,Q} = t_{\lambda,Q} = \exp\left(-K_{\lambda,Q}L\right) \tag{36}$$

$$a_{\lambda,Q} = \epsilon_{\lambda,Q} \tag{37}$$

The spectral absorption coefficient $K_\lambda$ was taken from [139] for their KI glass at 1073 K (absorption increases with temperature, hence this represents a worst case scenario), and $L$ was equal to the quartz liner thickness (4 mm). The total emission from the inner wall was calculated by integrating Planck's Law ($B_\lambda$, Eq. 38) of spectral radiance over the IR detector spectral range as given by Eq. 39, accounting for the optical properties of the wall and liner.

$$B_\lambda(\lambda, T) = \frac{2h_P c^2}{\lambda^5} \frac{1}{\exp\left(\frac{h_P c}{\lambda K_B T}\right) - 1} \tag{38}$$

$$R_T = R_i + R_Q = \int_{1\mu m}^{5\mu m} t_{\lambda,Q}\epsilon_W B_\lambda(\lambda, T_W)d\lambda + \epsilon_{\lambda,Q} B_\lambda(\lambda, T_Q)d\lambda \tag{39}$$

The result of the ratio of transmitted emission ($R_i$) to total radiation received by the detector ($R_T$) for different quartz and inner wall temperatures are shown in Figure 55. During the experiment, the lowest wall temperature (at the point where the swirling jets impinge on the liner) was $\sim 360$ K, while the quartz temperature was approximately equal to the combustor

flow temperature $T_\infty$ and maintained below 293 K for all the cases tested. This implies that the transmitted inner wall emission contributed at least 50% to the total radiation received by the IR camera. The maximum temperatures observed along the liner were ~ 420 K, corresponding to >80% of the acquired signal due to the transmitted emission from the inner wall.

To characterize the effective emission from the heated inner wall surface, the IR readings were compared against in-situ thermocouple measurements. All the TCs used were T-Type (errors of $\pm$0.5 K) with diameters of 0.08 mm for faster response times. The results, shown in Figure 56, were fitted with a 6$^{th}$ order polynomial to obtain the calibration curve for the inner wall surface temperature in terms of the IR temperature reading. The polynomial curve obtained is given by Equation 40.

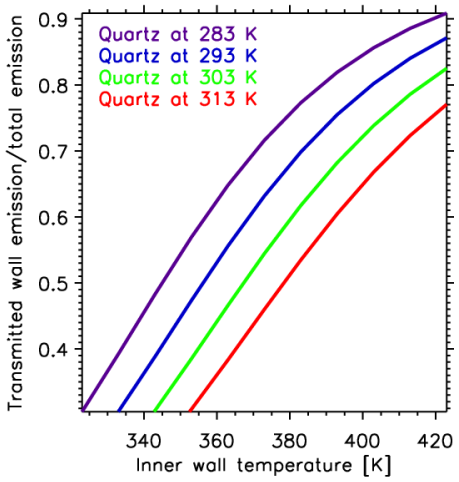


**Figure 55.** Estimated ratio of transmitted to total emission received by the IR detector, to validate that measurements of the inner wall are possible through quartz glass.

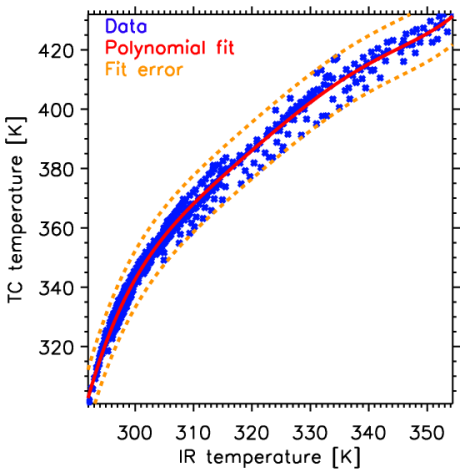


**Figure 56.** Calibration of the IR reading to the thermocouple reading of the inner wall temperature.

$$T_W = -1.06415 \times 10^{-11} T_{IR}^6 + 7.63843 \times 10^{-7} T_{IR}^5 - 1.23544 \times 10^{-3} T_{IR}^4 + 8.06158 \times 10^{-1} T_{IR}^3 - 2.63483 \times 10^{2} T_{IR}^2 + 4.30780 \times 10^{4} T_{IR} - 2.81716 \times 10^{6} \quad (40)$$

Where $T_w$ is the wall temperature measured by the thermocouples and $T_{IR}$is the reading from the IR camera, both in Kelvin. The total uncertainty band (three standard errors) in the fitted curve for calibration was $\pm$9.54 K as shown in the figure.

#### 4.2.2.2 Three dimensional heat loss characterization

The heat lost to the quartz liner and surroundings ($Q_{\mathrm{LOSS}}$) was measured by applying a heat flux to the wall while there was no flow through the combustor. Since there is no flow, the heat flux applied is primarily dissipated by the wall on the backside of the heater. Several heat loss experiments at different heat inputs were carried out to obtain a loss curve that relates the heat lost, to the temperature difference between the surface of the heater and the ambient air (the heat sink temperature). Investigators [54,56,57] typically place the heater on an insulating surface (foams/cork with thermal conductivities around 0.04 W $m^{-1}K^{-1}$) to minimize the heat loss and neglect any three dimensional conduction effects. This latter assumption is unfortunately not valid for the quartz liner, as its thermal conductivity is ~1.4 W $m^{-1}K^{-1}$ [141] at ambient conditions. The energy balance for a heat loss (no flow) experiment is given by Equation 41, where the supplied heat is lost to natural convection within the combustor and to conduction losses in the radial, azimuthal, and the axial directions.

$$Q_{W,\text{no flow}} = Q_{\mathrm{LOSS,R}} + Q_{\mathrm{LOSS,X}} + Q_{\mathrm{LOSS},\theta} + h_{\mathrm{nat}} A (T_W - T_\infty) \tag{41}$$

For the heat loss calculations, the azimuthal component was approximated as a vertical component to simplify the analysis, i.e. $Q_{LOSS,\theta} \approx Q_{LOSS,Y}$. The natural convection component within the combustor was estimated according to standard correlations for free convection from a vertical surface as given by Equation 42.

$$\overline{\mathrm{Nu}_L} = 0.68 + \frac{0.67\ \mathrm{Ra}_L^{1/4}}{(1 + (0.492/\mathrm{Pr})^{9/16}\ )^{4/9}} \tag{42}$$

Where $\mathrm{Ra_L}$ is the Rayleigh number ($L = 51$ mm), with properties evaluated at the corresponding film temperature. According to the calculations, $h_{\mathrm{nat}} \approx 8.4$ $\mathrm{Wm^{-2}K^{-1}}$, which on average accounted for the dissipation of 14.5% of the total heat load applied to the wall. A conservative uncertainty of 20% was assumed for the natural convection dissipation while calculating the errors associated with the heat loss characterization.

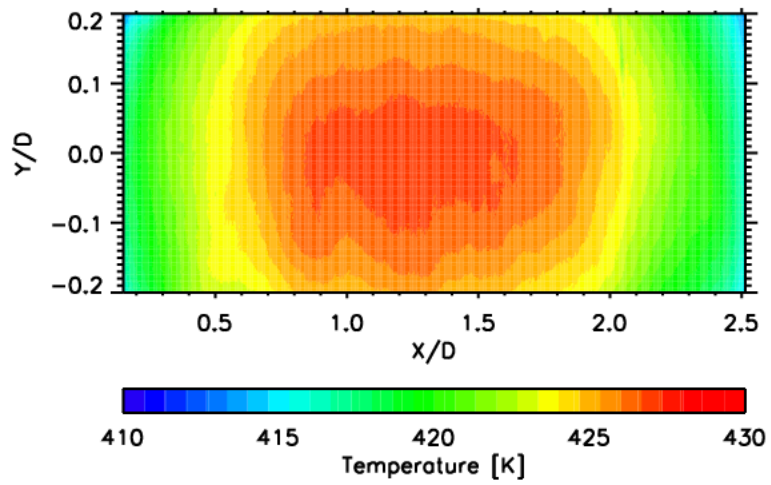


**Figure 57.** Temperature distribution of the heater surface during a no-flow experiment to calculate the conduction heat losses.

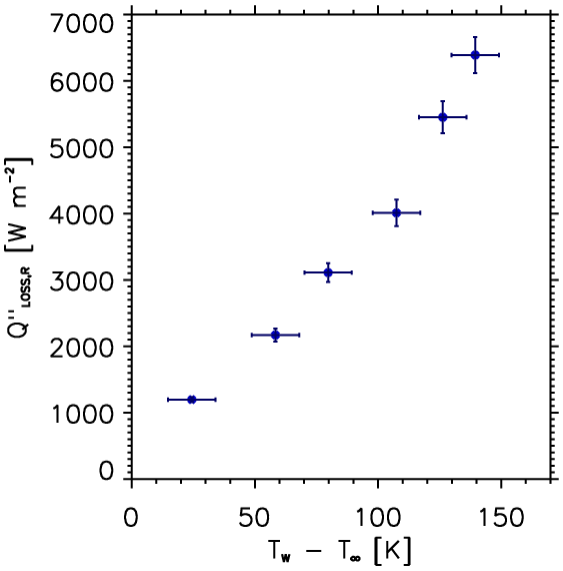


**Figure 58.** Radial heat flux lost due to conduction.

An example of the heater temperature distribution after a steady state heat loss measurement is shown in Figure 57. Close to the center of the heater a temperature maximum was observed, indicative of significant conduction in the X and Y directions, assuming $Q_{W,no\ flow}$ provided by the heater was uniform. The point of maximum temperature during any heat loss experiment corresponds to zero conduction heat losses along the azimuthal and axial direction ($Q_{LOSS,Y} = Q_{LOSS,X} = 0$), there is only conduction into the quartz liner ($Q_{LOSS,R}$) and natural convection occurring. This is because the temperature gradients along $Y$ and $X$ at that

location are zero. Figure 58 shows the measured $Q_{LOSS,R}$ curve obtained from the maximum temperature area for the six heat loss measurements taken for this study. It is important to note that while the radiative heat loss is not explicitly accounted for, it is part of $Q_{LOSS,R}$. The radiative heat transfer from the surface contributes at most 30% to the total radial heat loss.

At any other point on the heater surface, the remainder of the heat supplied after removing the convective loss and $Q_{LOSS,R}$ was due to the azimuthal and axial heat losses. To estimate these components, the locations along the heater where the axial and azimuthal temperature gradients were zero were identified, which equal to zero heat loss in the respective direction. The zero azimuthal temperature gradient corresponded to the point of maximum temperature at each axial location. At these locations there was no azimuthal heat loss and the axial conduction loss could be estimated. This was similarly done for the azimuthal component of the heat loss. For the case of the radial heat loss, the temperature potential driving the heat flux could be clearly identified (ambient temperature constitutes the sink temperature), this however is not the case for the axial and azimuthal heat loss components as these components depend on the instantaneous temperature gradient in those directions. The noise in the raw experimental data complicated the extraction of the local temperature gradient. For this reason, the maximum temperature profiles along $X$ and $Y$ (where the alternate heat loss component was zero) were fitted with a $6^{th}$ order polynomial from which the temperature gradient was determined. Figure 59 shows the resulting heat loss in the axial and azimuthal directions as a function of $T_W dT_W/dL$ (where L is either $Y$ or $X$ for the azimuthal and axial heat loss components respectively) from the different heat loss experiments. The discrepancies between cases and directions are due to non-linear effects (conductivity changes with temperature), errors in the temperature gradient, and non-uniformities in the heat flux applied. The heat losses calculated are representative of an effective conductivity in each of the directions. For a constant conductivity case, it would be expected that the heat loss curves shown in Figure 58 and Figure 59 would be linear, which is approximately satisfied by all the heat loss components.

Using the calculated heat loss characterization for the pixels that were subjected to the three heat loss components resulted in less than 2% unaccounted heat flux. While the errors in the axial component of the heat loss are large, its contribution to the total heat loss is one order of magnitude smaller compared to that of the radial heat loss.

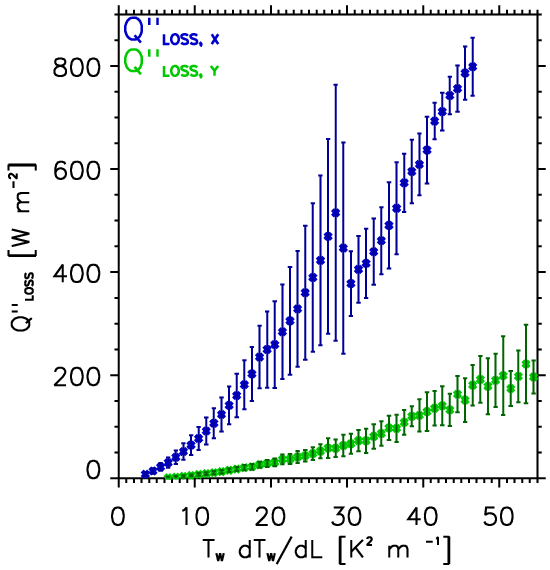


**Figure 59.** Axial and azimuthal heat flux lost due to conduction.

#### 4.2.2.3 Total uncertainty for the heat transfer measurement

The overall uncertainty in the heat transfer experiment was attributed to errors in $T_W$, $T_\infty$, $Q''_W$, and $Q''_{loss}$. Errors in the inner wall temperature ($T_W$) were 9.62 K, accounting for the calibration error (three standard deviations, 99% of the observations) and the thermocouple accuracy of $\pm 0.5$ K. The total uncertainty for the combustor flow temperature ($T_\infty$) was 1.92 K, including the difference between the combustor inlet and outlet temperature and the accuracy of the thermocouples. The wall heat flux error was calculated from errors in the heater electrical resistance of $\pm 0.3$ Ω and errors in the voltage supplied of $\pm 0.5$ V, this error was also considered during the heat loss calculation. The heat loss errors were estimated according to the errors shown in Figure 58 and Figure 59. The total relative error for the heat transfer coefficient was on average between 5.1% and 10.8% depending on the mass flow case. The majority of the error was due to the inner wall calibration uncertainty. Errors in $Q''_{loss}$ and $Q''_W$ combined accounted for at most 3.2% uncertainty in the HTC.

Experiments were tested for repeatability at different heater settings (lower temperature) with statistically insignificant differences smaller than 2%. It was also verified that the steady state condition was reached after 60 minutes by comparing results for data acquisitions after 60, 120, 180, and 240 minutes; the results were on average within $\pm 1.3$% of the 60 minutes result.

### 4.2.3 Experimental results

Results are presented in terms of the Nusselt numbers (non-dimensional HTC) as given by Equation 43.

$$\mathrm{Nu} = \frac{h\, D_C}{k_\infty} \tag{43}$$

The Nusselt number introduces an ambiguity to the result when defining the reference temperature for the calculation of gas properties. In the case of the experiment, the bulk flow properties were used for the Reynolds number and Nusselt number following the convention adopted by modern turbulent pipe flow correlations [45-47]. The Nusselt numbers were normalized with respect to the Dittus-Boelter correlation for fully developed turbulent pipe flow and the result is reported as an enhancement along the combustor wall as done by Patil et al. [56] and Andreini et al. [58]. Other correlations for turbulent pipe flow are shown to yield only small differences, with increasing significance at higher Reynolds numbers.

#### 4.2.3.1 Heat transfer and comparison to the flow field

The heat transfer distribution on the liner was observed to be invariant along the azimuthal dimension, as expected from the symmetry of the swirling flow and test setup. For this reason, the HTC obtained from the IR imaging was vertically (azimuthally) averaged and only the variation along the axial dimension is reported (vertical variability was <1.5%). The Nusselt numbers obtained for Reynolds numbers extending from 12 000 to 138 000 are shown in Figure 60. The normalized Nusselt numbers with respect to the fully developed flow correlation is shown in Figure 61 (fluid properties were evaluated at the estimated bulk flow temperature).

The overlap between the different mass flows indicates that the correlation approximately captures the scaling of the heat transfer measurement with Reynolds number ($\mathrm{Re}^{0.8}$), similarly observed by Andreini et al. [58]. While there is some suggestion in the figure of decreasing enhancement with increasing Reynolds number, as observed in [56] and [49], the decrease in enhancement is barely outside of the uncertainty bands for the measurement. Andreini and coauthors [58] also showed coincident enhancements away from the impingement location, with only a small decrease in peak enhancement with increasing Reynolds. This is an important

observation, because it implies that measurements at lower Reynolds numbers can capture the location of maximum heat transfer along the combustor and the approximate distribution of isothermal convective heat loads. The data suggest that the area of high heat transfer broadened at higher Reynolds numbers, extending from $X/D_N \approx 1$ to 1.3, however this could also be due to experimental uncertainties. The highest mass flows required high heat inputs (electrical currents) leading to significant heater non-uniformities that caused the apparent axial oscillations observed in the data.

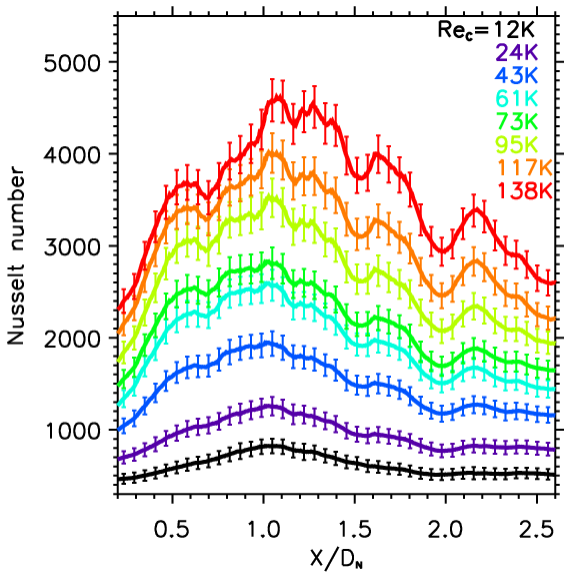


**Figure 60.** Experimental Nusselt numbers for several Reynolds numbers

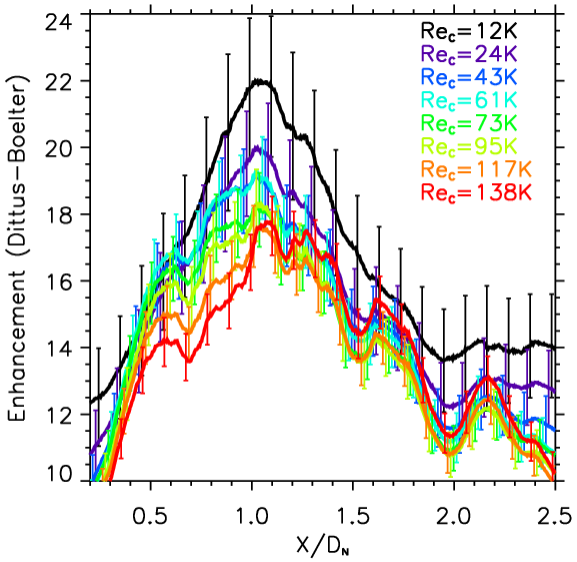


**Figure 61.** Normalized Nusselt numbers (enhancement or augmentation) with respect to the Dittus-Boelter correlation for fully developed pipe flow.

While Figure 61 suggests that there is a slight decrease in maximum enhancement with increasing Reynolds, this is possibly related to the limitations of the Dittus-Boelter equation. Modern correlations for fully developed turbulent pipe flow heat transfer such as those proposed by Gnielinski [46,47] (based on the work of Pethukhov[45]) and Sleicher and Rouse [48] apply to a broader range of conditions and have been validated against more extensive sets of experiments. While the difference in the heat transfer result is small between correlations (<10% for the conditions in the current investigation), there is a noticeable difference at higher Reynolds numbers. Figure 62 shows the spatially averaged and maximum enhancement with respect to different formulations for fully developed pipe flow heat transfer. The lower enhancement at

higher Reynolds numbers as suggested when using the Dittus-Boelter equation, weakens when normalizing with respect to other correlations. This seems to imply that the decrease in enhancement may be partly due to errors in the scaling with Reynolds number as given by the Dittus-Boelter equation ($Re^{0.8}$), compared to that of for instance Sleicher and Rouse [48] ($\mathrm{Re}^{0.83}$). Evaluating the Nusselt number with properties at the film temperature further reduced this apparent decrease in enhancement.

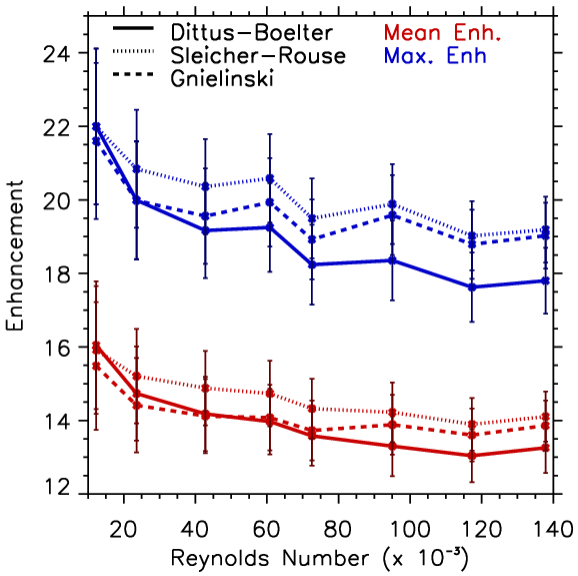


**Figure 62.** Maximum and axially averaged enhancement with respect to different correlations for fully developed turbulent pipe flow.

Based on the normalized flow field as shown in Figure 43, the point of flow reattachment on the liner was observed at $X/D_N \approx 1.15$, downstream of the location of peak heat transfer, which was observed at $X/D_N = 1.03 \pm 0.02$ for all mass flow cases. A consistent observation was also made by Dellenback et al [49], with their peak heat transfer on average $\sim 0.33$ step heights ($0.16D_N$ for their setup) upstream of their re-attachment point. For the current experiments the peak heat transfer appeared to match the location where corner recirculation flow starts at around $X/D_N \approx 1$ in Figure 43. The mismatch between the reattachment point and the peak heat transfer was not reported in other investigations [56, 58]. This mismatch could be due to the increased shear (and mixing) as the flow at the impingement location turns into the corner recirculation. The normalized flow field studied in Section 4.1 suggested that the flow is self-similar for the range of Reynolds numbers measured. This is further supported by the

constant heat transfer distribution and peak location at all mass flows, implying that there were no significant transitions in the fluid dynamics at higher Reynolds numbers as has also been reported by others [36, 58].

#### 4.2.3.2 Comparison to other datasets

The main challenge when comparing measurements from past investigations is that each has adopted different reference quantities, working fluids, swirl generators, and downstream geometries. The work of Dellenback et al. [49] used water as the working fluid, calculated the Nusselt number in terms of the pipe diameter downstream of the expansion ($D_C$), and evaluated the Reynolds number in terms of the pipe diameter upstream of the same ($D_N$). The research by Andreini et al. [58], Patil et al. [56], and Gomez-Ramirez et al. [57] was done for annular combustors. [58] chose the hydraulic diameter of their test section for their calculations, while [56,57] used the hydraulic diameter of the full annulus.

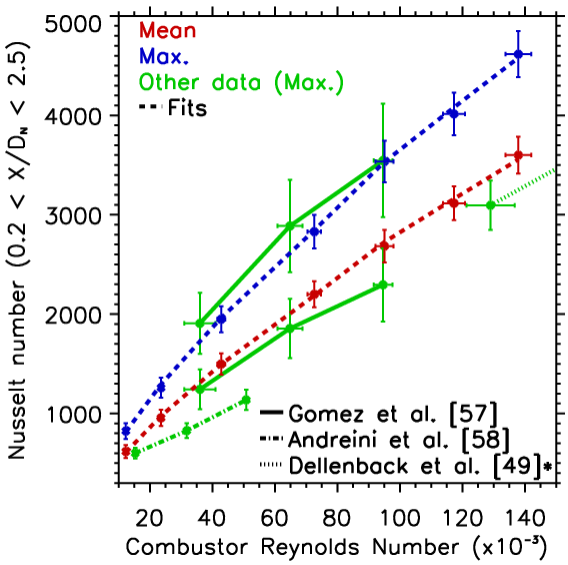


**Figure 63.** Comparison between the results from the can optical combustor and the maximum Nusselt numbers observed in other investigations.

Figure 63 shows the maximum Nusselt number obtained in different investigations, evaluated with property values at the bulk flow temperature. Only investigations for which sufficient information was available to define the Reynolds number as given by Eq. 44 were considered.

$$Re_C = \frac{\dot{m}\, D_C}{\mu_\infty\, A_C} \tag{44}$$

Where $\mu_B$, $\dot{m}$, $D_C$, and $A_C$ are the dynamic viscosity of the working fluid at the bulk temperature, mass flow, reference combustor diameter (hydraulic diameter of the test setup), and cross-sectional area of the combustor respectively. Figure 63 also includes the axial average of the results from $0.2 < X/D_N < 2.5$. Reiterating, this definition is different from that used for the flow field characterization which was in terms of the nozzle diameter ($D_N$).

The annular combustor studies [56-58] showed a two-dimensional heat transfer distribution on the liner, with the peak occurring downstream of the nozzle and decreasing both in the axial and annular circumference directions. Lateral (circumferential) averages of the data were calculated to visualize the heat transfer enhancement as a function of axial location, yielding a lower peak enhancement than actually observed [56-58]. The annular combustor results with no dome outflow from Gomez-Ramirez and coauthors [57] reported a different heat transfer distribution for the inner and outer annulus walls, which were averaged for the comparison in the present study. From the work of [57], both the maximum Nusselt number from the lateral average (axial enhancement) and the maximum observed in the two dimensional distribution were plotted in Figure 63. The former matched approximately with the axial average of the present results (lower by 10.5%), whereas the latter is $\sim 6.1\%$ higher than the maximum observed in the can combustor. If a similar Nusselt number decay rate is observed circumferentially in the annular combustors, the peak enhancement of the spatial average would approximately match the axial average in the current investigation as observed in the figure. Similarly, the spatial average peak enhancement from the work of Andreini et al. [58] is shown in the figure to be 8.5% lower than the axial average in the current investigation.

An important factor to consider between investigations is the different swirl numbers and expansion ratios used. There are two phenomena by which convective heat transfer is enhanced in isothermal combustor flows compared to fully developed pipe flow: 1) due to swirl, and 2) due to the reattaching flow after the expansion into the primary zone. The addition of swirl to the flow adds a tangential velocity component, introduces a centrifugal acceleration to the flow, modifies the impingement location on the liner, and triggers a central recirculation for swirl

numbers greater than 0.6 [28]. Dellenback [49] experimentally characterized the effect of swirling flow on the local magnitudes of heat transfer downstream of a sudden pipe expansion for a fixed $D_N$ / $D_C$ ratio of 0.51. Their geometry is similar to that of can combustors, except for their swirl generator. Their results showed that an increase in swirl number, $S$, led to an upstream shift in the impingement location and to higher heat transfer enhancement. Based on their data for $Re_N$ of 60 000 and 100 000 ($Re_C$ of ~30 000 and ~50 000), the heat transfer increased with swirl number according to $S^{0.235}$. Similarly for their higher swirl numbers ($S > 0.6$), the peak Nusselt number increased with respect to $\mathrm{Re}_C^{0.437}$. The enhancement due to reattaching flow after an expansion has been characterized by Baughn et al [51], who showed that a decrease in the expansion ratio $D_N/D_C$ corresponds to an increase in peak heat transfer. The work by Dellenback et al. [49] ($D_N/D_C = 0.51$) would hence result in lower heat transfer compared to the present investigation ($D_N/D_C = 0.34$). This may also partially explain the lower maximum Nusselt numbers observed by Andreini. If the expansion ratio for the annular combustor studies is defined as the ratio of the nozzle diameter to the annular height, the work of Andreni and coworkers [58] would correspond to an expansion ratio of 0.42, and that of Gomez et al. [57] to 0.36. According to the results by Baughn et al. [51], peak heat transfer increases according to $\sim (D_N/D_C)^{-1.053}$, however this relationship is likely different in the presence of swirl. The results from Dellenback and coworkers [49] in Figure 63 were corrected to account for the different Prandtl numbers of water and air, and the enhancement due to the difference in expansion ratio. Despite the corrections, the modified result from Dellenback was still 22.5% lower than the axially averaged Nusselt number for this investigation.

Discrepancies in the data could also be attributed to the reference temperature. Modern turbulent pipe flow correlations have shown that evaluating the Nusselt number at the bulk flow temperature requires a correction to correlations of the form $(T_\infty/T_W)^{n_T}$ to account for property changes near the wall [45-47]. The experimental data in the present investigation were correlated with Equations 45 and 46, following Gnielinski's formulation [46, 47] for fully turbulent pipe flow and adding a factor $K_S\mathrm{Re}^{\mathrm{ns}}$ to account for the enhancement due to swirl and flow reattachment. Gnielinski's correlation was chosen because it was derived from the Chilton-Colburn analogy, and hence relies on a strong theoretical basis. In-built into the equation are provisions to account for different wall roughness (through the Darcy-Weisbach friction factor $f$) and the effects due to property changes with temperature.

$$\mathrm{Nu_B} = K_S \mathrm{Re}_{C,\infty}^{\mathrm{ns}} \frac{(f/8)\left(\mathrm{Re_{C,\infty}} - 1000\right)\mathrm{Pr}_\infty}{1 + 12.7\sqrt{f/8}\left(\mathrm{Pr}_\infty^{2/3} - 1\right)} \left(\frac{T_\infty}{T_W}\right)^{n_T} \tag{45}$$

$$f = (1.8 \log_{10} \mathrm{Re}_B - 1.5)^{-2} \tag{46}$$

Where Eq. 46 applies for a smooth pipe, and the temperature dependence exponent $n_T$ proposed by Gnielinski [46] was 0.45, applicable for $0.5 < T_W/T_\infty < 1.5$ (Pethukhov's formulation [45] includes expressions for the coefficients and $n_T$ exponent in Eq. 45 that depend on Prandtl and Reynolds numbers). The factor $K_S$ was equal to 39.15 and 61.06 for the mean and maximum Nusselt number trends respectively. Similarly, the exponential dependence on the Reynolds number, $n_S$, was $-0.0684$ and $-0.0846$ for the mean and maximum heat transfer cases respectively, which reflects the weak decrease in enhancement with increasing Reynolds. The exponent $n_S$ has a strong influence on the coefficient $K_S$; assuming $n_S \approx 0$, $K_S$ was 17.85 and 23.13 for the mean and maximum heat transfer. It is speculated that the $K_S \mathrm{Re}_{\mathrm{C},\infty}^{\mathrm{ns}}$ factor is related to the swirler and combustor geometry, as has been shown by the work of Baughn et al. [51] and Dellenback et al. [49]. The amount of data available is not sufficient to establish a robust correlation and Equation 45-46 is only an empirical fit of the experimental data. Additional data at different swirl numbers and expansion ratios for different Reynolds numbers would allow for a correlation for combustor heat transfer.

## 4.3 CONCLUDING POINTS ON THE ISOTHERMAL AERODYNAMICS AND HEAT TRANSFER

In this chapter, the isothermal steady and unsteady fluid dynamics generated by an industrial low emission fuel nozzle at atmospheric pressures were characterized. A triple decomposition of the velocity field was performed based on a POD methodology, resulting in the separation of the instantaneous velocity into its time-averaged, coherent (periodic), and stochastic components. The methodology allowed for the study of the PVC and its downstream propagation.

It was observed that the coherent structures account for over 30% of the total fluctuation kinetic energy along the inner shear layer and within the recirculation zone close to the nozzle exit plane. No dominant coherent fluctuations were identified beyond the point at which the swirl jet impinged on the combustor wall. These results imply that to properly capture mixing between the swirling jet and the recirculated gases, coherent structures must be accounted for in numerical models.

The anisotropy in the stochastic turbulent properties was observed to be most significant within the jet (particularly the axial component of the fluctuations) while the inner recirculation had relatively isotropic stochastic turbulence. The coherent structures further magnified the anisotropy in the total fluctuation. Strong asymmetry was also observed in the flow velocities, with the PVC causing oscillations compared to the time-averaged results in the axial and tangential velocities close to the nozzle exit of 44% and over 19% respectively. The data presented is critical to understand turbulent mixing and the dynamics within combustors, and to develop accurate models of combustor flows.

Furthermore, the non-reacting heat transfer for the optical gas turbine combustor model was characterized experimentally. The experiments were carried out for Reynolds numbers with respect to the combustor diameter between 12 000 and 138 000. The obtained Nusselt numbers were normalized with respect to several correlations for fully developed turbulent pipe flow to study the heat transfer augmentation with Reynolds number. The augmentation results in general were approximately constant, indicating that the correlations captured the increase in heat transfer with operating Reynolds number properly. A slight decrease in enhancement was suggested by the augmentation results, however this decrease is barely outside the uncertainties in the measurements. The decrease in augmentation is further diminished when using modern correlations, instead of the traditional Dittus-Boelter equation. This result implies that the characterization of the isothermal heat transfer at lower Reynolds numbers can be adequately scaled to other operating mass flows according to the Reynolds scaling given by the correlations. The experimental heat transfer results were compared with the annular combustor measurements from chapter 2 yielding a difference of ~ 6.1% for the maximum observed heat transfer along the liner. The laterally averaged Nusselt numbers from annular combustors at the location of maximum enhancement were within 10.5% of the average Nusselt numbers observed axially along the can combustor in this investigation. The agreement between the lateral average from

annular combustors and the axial average for the can combustor model can be explained if the decay in the augmentation laterally and axially are similar.

The maximum and average heat transfer were also correlated according to a modified Gnielinski correlation to account for the augmentation within the combustor primary zone. The study presented in this chapter highlights the need for additional data to characterize combustor heat transfer for different burner geometries. In particular, there is no comprehensive data set on the simultaneous impact of nozzle to combustor expansion ratio and nozzle swirl number on the liner heat transfer.

## 4.4 NOMENCLATURE

| | |
|---|---|
| $A$ | Cross-sectional area of the fuel nozzle or area of the surface heater [$m^2$] |
| a,b | Fourier polynomial coefficients |
| a | Absorptance |
| $B_\lambda$ | Spectral radiance from Planck's Law [W $m^{-3}$ $sr^{-1}$] |
| c | Speed of light [299 792 458 m $s^{-1}$] |
| CRZ | Central Recirculation Zone |
| $D$ | Diameter |
| $D_N$ | Nozzle diameter |
| $f$ | Generic field (velocity/turbulence) |
| $\bar{f}$ | Time averaged field |
| $\tilde{f}$ | Coherent/periodic field |
| $f'$ | Stochastic field |
| G | Axial flux of momentum [N] |
| $h$ | Heat transfer coefficient [W $m^{-2}$ $K^{-1}$] |
| $h_P$ | Planck's constant [$6.62607004 \times 10^{-34}$ $m^2$ kg / s] |
| $ii$ | Total number of vectors in the $i$ direction |
| $jj$ | Total number of vectors in the $j$ direction |
| K | Absorption coefficient |
| $k$ | Conductivity |
| $K_B$ | Boltzmann constant [$1.38064852 \times 10^{-23}$ $m^2$ kg $s^{-2}$ $K^{-1}$] |

| | |
|---|---|
| L | Thickness of the quartz liner [4 mm]/reference length or direction [m] |
| $\dot{m}$ | Mass flow [kg/s] |
| $\dot{m}_{ND}$ | Non-dimensionalized mass flow |
| Nu | Nusselt number |
| PIV | Particle Image Velocimetry |
| POD | Proper Orthogonal Decomposition |
| PVC | Precessing Vortex Core |
| P | Power [W] |
| $P_4$ | Pressure at the combustor outlet |
| $P_3$ | Pressure at the combustor inlet |
| Pr | Prandtl number |
| $P_s$ | Static inlet pressure to the combustor |
| $Q$ | Heat rate [W] |
| $Q''$ | Heat flux [W $m^{-2}$] |
| R | Radiance [W $m^{-2}$ $sr^{-1}$] |
| $R$ | Nozzle throat radius |
| $R_\Omega$ | Resistance [Ω] |
| Re | Reynolds number |
| $S$ | Swirl number |
| TKE | Turbulent Kinetic Energy |
| $T_s$ | Static inlet temperature to the combustor |
| $T$ | Temperature |
| t | Transmittance |
| $u$ | X-velocity component |
| $V$ | Velocity [m $s^{-1}$], bold indicates matrix of all points |
| V | Voltage [Volts] |
| $V_{ref}$ | Reference velocity for different mass flows [m $s^{-1}$] |
| $v$ | Y-velocity component |
| $w$ | Z-velocity component |
| $X$ | Axial coordinate along the combustor axis (direction of the bulk flow) [m] |
| $Y$ | Vertical coordinate perpendicular to the combustor axis [m] |

| | |
|---|---|
| $Z$ | Horizontal coordinate perpendicular to the combustor axis [m] |
| $\chi$ | Eigenvector , bold indicates matrix of eigenvectors |
| $\epsilon$ | Emissivity |
| $\lambda$ | Wavelength [m] |
| $\phi$ | POD mode, bold indicates matrix of POD modes |
| $\theta$ | Phase within the period of the coherent fluctuation |
| $\mu$ | Dynamic viscosity [kg $m^{-1}$ $s^{-1}$] |
| $\mathbf{\Sigma}$ | Covariance matrix |

## Subscripts

| | |
|---|---|
| C | Combustor primary zone |
| F | Evaluated at the film temperature |
| IR | Refers to the infrared camera |
| k | Eigenvector index |
| $LOSS$ | Refers to thermal conduction heat losses |
| n | Snapshot index (PIV) |
| N | Nozzle |
| nat | Refers to natural convection |
| Q | Refers to the quartz liner |
| R | Radial component |
| $W$ | Evaluated at the wall or at the wall temperature |
| $X$ | Axial component |
| Y | Vertical component (perpendicular to axial) |
| Z | Horizontal component (perpendicular to axial) |
| $\theta$ or $\phi$ | Tangential component |
| $\lambda$ | Spectral |
| $\infty$ | Evaluated at the flow bulk temperature |

# CHAPTER 5

# REACTING STUDIES OF HEAT TRANSFER AND FLOW

This chapter details the experiments and methodologies developed to study the optical combustor at reacting conditions. Both heat transfer and flow visualization experiments were carried out. Due to time constraints, the extent of the dataset is limited and emphasis was placed on the development of the methodologies. These methodologies can be applied by other researchers to study combustor heat transfer for different operating conditions beyond what was included in this chapter.

The chapter first describes the development of the heat transfer measurement technique, which relied on IR temperature acquisitions from the liner inner (flame side) and outer (coolant/ambient side) walls to determine the instantaneous (time-dependent) heat flux from the gas. The methodology is based on numerically estimating the temperature profile across the material to calculate the heat flux at the boundaries. This is simpler than traditional inverse methods, since only the forward model is being evaluated based on the boundary conditions provided by the IR camera (no inverting was done). Traditional inverse method techniques have been validated numerically in many instances [142-146], and have been used experimentally to develop 3D heat transfer methods as detailed by [147,148]. Time-dependent heat transfer on the other hand has not been experimentally explored to a large degree, particularly in the gas turbine community. Only recently, while writing this dissertation, a new patent was assigned for a similar time-dependent methodology [149]. The reason for the lack of information on time dependent heat transfer is likely because for most of the rotating engine components (turbine blades and compressor), the mechanical stresses dominate (aerodynamic and centrifugal loading [10]), with thermal stresses playing only a secondary role. Moreover, thermal transients are of such a high frequency that effectively act as a constant load on the material. The temperature of these components is of course critical as it impacts the strength of the material and creep characteristics. In the combustor however, transients associated with ignition or shut-down lead to low cycle fatigue (LCF) and have a significant impact on the burner durability. Shut-down is particularly dangerous, as the material is at high temperature (low strength) and is subjected to large thermal loads as the flame is extinguished. The methodology here presented, due to its

applicability to time-dependent problems, can be extended to study the transients that occur during ignition or shutdown. The method was experimentally validated by running an experiment without reaction and comparing the results to those obtained in Chapter 4. The method was then applied to several representative reacting cases.

The combustor flow field was studied using two methods; the first was by taking flame images and the second using particle image velocimetry (PIV). Only a representative case of the reacting PIV and flame imaging is included in this dissertation as this will be the research topic of future students. Reacting PIV represents an important milestone for the project and for this reason was included in the dissertation.

## 5.1 HEAT TRANSFER EXPERIMENTS FOR SURFACES AT LOW TEMPERATURES

A schematic of the main components used for these experiments is shown in Figure 64 (same setup as used in Chapter 4). Further details of the facility capabilities and accuracy of the instruments are detailed in Chapter 3. No transition piece or exhaust systems were installed for these measurements (to reproduce the results obtained in Chapter 4). The reason for the simplification was to facilitate instrumentation of the primary combustion zone (using thermocouples) and cleaning of the liner (soot fouling, or coating failures).

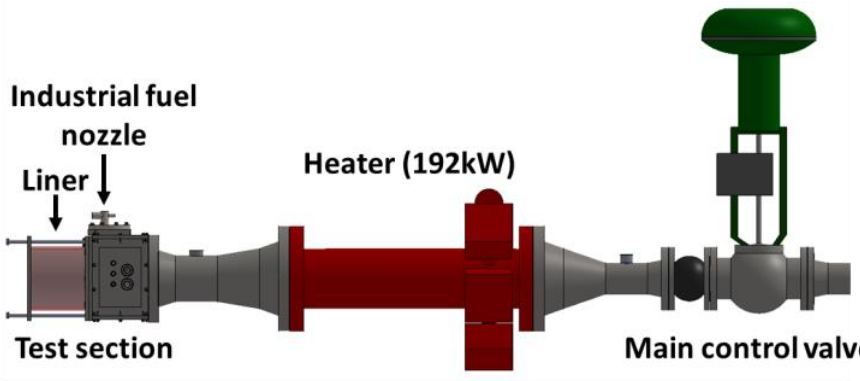


**Figure 64.** Experimental facility diagram.

The simplified test section consisted of a single quartz liner optical can combustor, equipped with the industrial low emission, fuel pre-mixed swirl nozzle provided by Solar Turbines Incorporated (SoLoNOx ® nozzle). A cross-section of the test section is shown in

Figure 65, where the blue and red arrows indicate the test section inlet and outlet. Details of the liner and fuel nozzle can be found in Chapters 3 and 4. As a brief summary, the liner was made out of a fused silica (quartz) cylinder with an inner diameter of 203 mm, a thickness of 4 mm, and a length (including the end metal piece) of 216 mm. The fuel nozzle consisted of an axial swirler with fuel injectors immediately downstream of the swirler vanes for fuel pre-mixing. Fuel was delivered to the nozzle through a pilot and a main fuel line, both of which were independently controlled and metered.

Initial measurements of the liner wall temperature displayed an axisymmetric pattern (no variation along the circumferential direction, as described in Chapter 4). This allowed for the simultaneous acquisition of the inner and outer liner wall temperature profiles by measuring both at different azimuthal locations on the liner wall. The inner (flame side) and outer (coolant/ambient side) liner walls were coated with a high temperature opaque black paint (Rust-Oleum®). The outer black coat was only applied to the top half of the imaged liner surface, allowing for acquisition of the inner wall temperature on the bottom half. Because of the axisymmetric heat load, both measurements were assumed to be concurrent and collocated along the liner. All the surface temperatures were derived from infrared (IR) measurements using a FLIR SC6700 camera, with a detector spectral range of 1 to 5 μm.

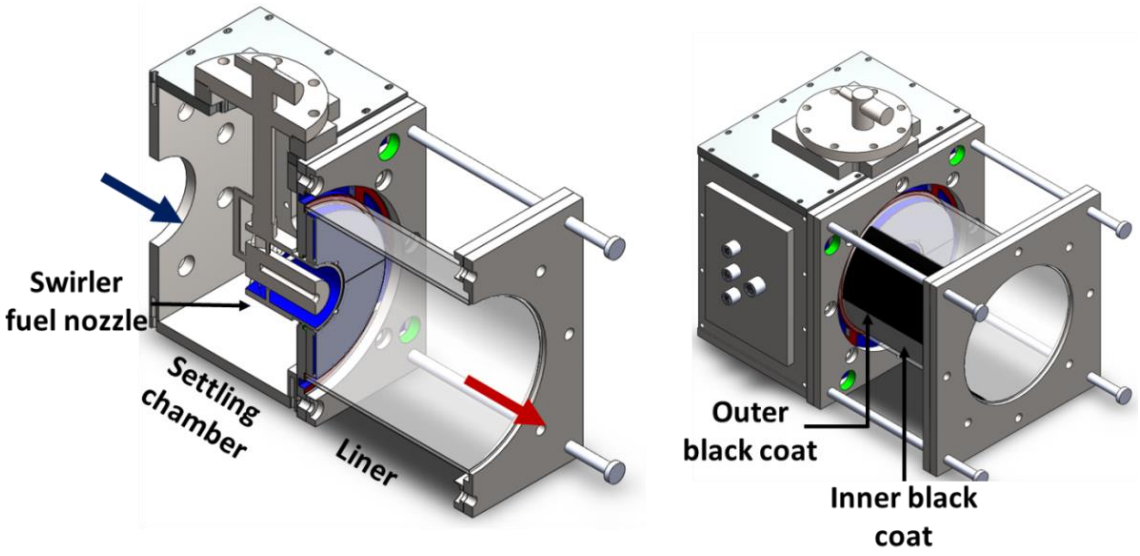


**Figure 65.** Schematic the setup for the heat transfer measurements.

The Reynolds number in terms of the combustor diameter was defined according to Equation 44 (Chapter 4), with the gas properties evaluated at the combustor inlet temperature. As described in the following section, the temperature at the inlet of the combustor changed throughout the time-dependent experiments, modifying the gas viscosity and by consequence the Reynolds number. The Nusselt number (Nu) was defined similarly, in terms of the combustor diameter and using properties at the combustor inlet temperature.

A non-reacting experiment was carried out to validate the methodology by comparing the results to the steady state measurements using a thin wall heater presented in Chapter 4. The validated methodology was then applied to representative reacting cases.

### 5.1.1 Unsteady non-reacting experiments

Non-reacting unsteady measurements were performed for burner Reynolds numbers with respect to the combustor diameter of approximately $11\,500$, $24\,000$, $43\,000$, and $72\,600$. These experiments consisted of setting the appropriate mass flow, followed by increasing the working fluid temperature steadily until a set point of $\sim 475$ K was reached. The ramp up period lasted between 120 and 200 seconds depending on the controller settings of the inline 192 kW heater (to maintain stability the response had to be slower for the higher mass flow cases). The unsteady non-reacting experiments lasted 240 seconds.

The temperatures within the combustor model for the non-reacting cases were monitored using 40 AWG gage T-type thermocouples (TCs), with an accuracy of 0.5 K and response time constants of $\sim 0.05$ seconds (for air at a speed of 20 m $s^{-1}$) per the manufacturer specifications. Two TCs were placed at the fuel nozzle outlet (one at the top and the other at the bottom of the nozzle), with a third TC located approximately 1 cm normal to the liner wall at the location of peak heat transfer based on preliminary measurements (this TC was to estimate the impinging jet temperature close to the liner wall). The temperature at the top of the nozzle was taken as the reference to calculate the heat transfer coefficient. Particularly for the lower Reynolds cases, what appeared to be temperature stratification was observed (differences between the top and bottom temperatures were 12K). The temperature at the exit of the nozzle for the highest and lowest mass flow cases are shown in Figure 66.

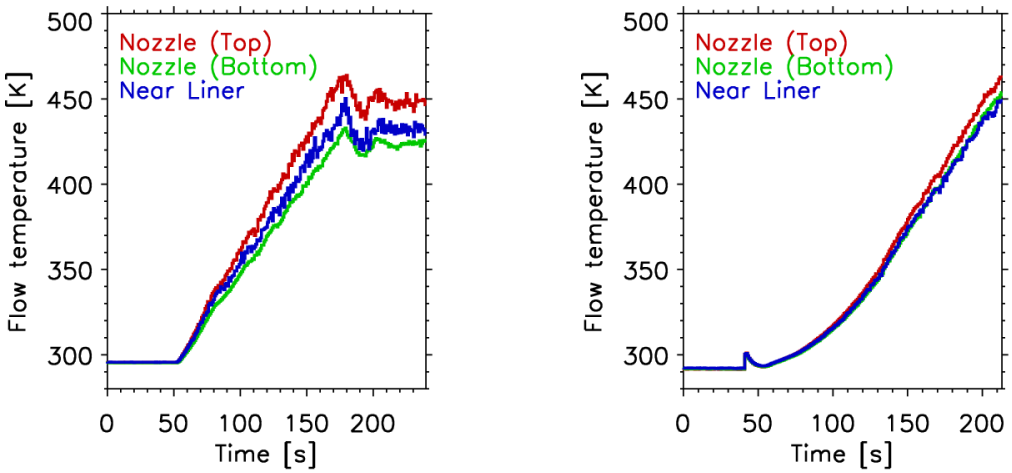


**Figure 66.** Temperature during an unsteady experiment at different locations within the combustor model for a Reynolds number of ~ 12 000 and 73 000 (left and right respectively).

At the highest Reynolds numbers, turbulent mixing minimized the temperature difference compared to the lower Reynolds number. The discrepancy can be further attributed to the uncertainty in the location of the thermocouple with respect to the exit temperature profile from the nozzle. While the thermocouples were placed at the centerline of the nozzle annular channel, the combustor flow was sufficient to shift the thermocouples out of position. While for the top thermocouple the shift would keep the TC within the jet area, the bottom TC could have potentially moved into the inner shear layer (because of the jet expansion angle and where the thermocouples were pivoted). Assuming the pre-heater exit profile is approximately uniform, the difference was attributed to experimental error and the maximum temperature observed was used for the analysis.

### 5.1.2 Steady state non-reacting validation experiments

The steady-state measurements taken in Chapter 4 served as validation for the unsteady results. Readers can refer to that chapter for a complete description of the experiment. As a summary, the validation experiments consisted of applying a surface heat flux to the inner wall of the combustor using a thin heater (Figure 67). The heat transfer coefficient was evaluated according to Equation 35 (Chapter 4). The heat flux lost to conduction $Q''_{LOSS}$ was calculated from a separate set of experiments ($Q''_{LOSS}$ was on average $0.32Q''_W$). $T_\infty$ was estimated from the average of two thermocouples, one immediately at the outlet of the fuel nozzle and another at the outlet

of the combustor. The heat transfer coefficient acquisitions close to the combustor dome ($X/D_N = 0$), had large heat losses, making the data for $X/D_N < 0.2$ unreliable.

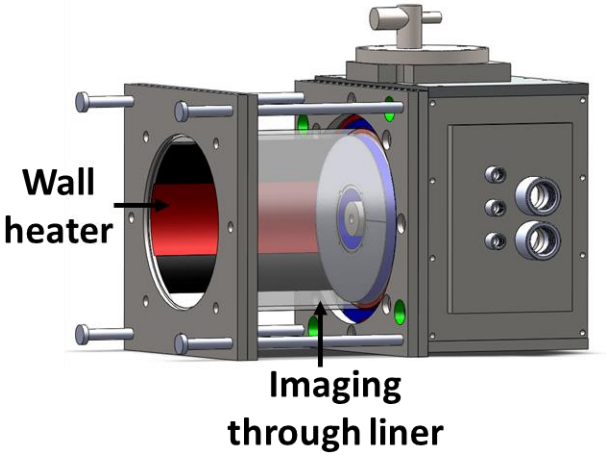


**Figure 67.** Side view schematic of the setup indicating the location of the wall heater for the steady state validation experiments.

### 5.1.3 Unsteady reacting experiment

A single reacting experiment to test the methodology was taken. The IR camera sensor saturated at 575 K, which limited the measurements to low wall temperatures. Adding a neutral density (ND) filter to the IR sensor could have increased the maximum measurable range but would have prevented accurate acquisitions near ambient temperatures. The methodology developed relied on the complete temperature history of the liner and thus these initial measurements were taken without the ND filter. Section 5.2 details experiments with a guessed initial condition when using a filter to measure higher temperatures.

The reacting experiment was taken at the lowest Reynolds number with respect to the combustor diameter (11 500) for an equivalence ratio of $\sim 0.5$. This was done to maintain low wall temperatures for a longer period of time, increasing the amount of data available to characterize the heat transfer. The air and fuel mass flows, as well as the equivalence ratio throughout the experiment are shown in Figure 68 and Figure 69. Figure 70 shows different time snapshots of the flame at important transition times in the flame structure. The peak in fuel at around $t = 40$ s (Figure 68) corresponded to the activation of the fuel valves prior to ignition.

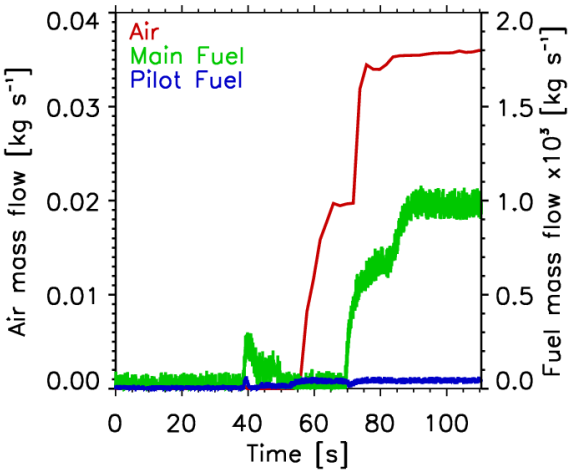


**Figure 68.** Air and fuel mass flows during the reacting experiment. The scales for the air and fuel are shown on the left and right axis respectively.

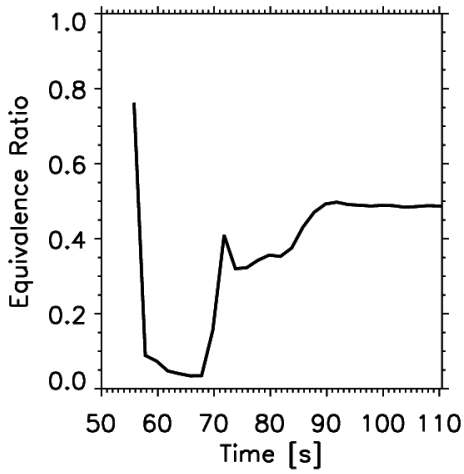


**Figure 69.** Equivalence ratio calculation based on the mass flows during the experiment.

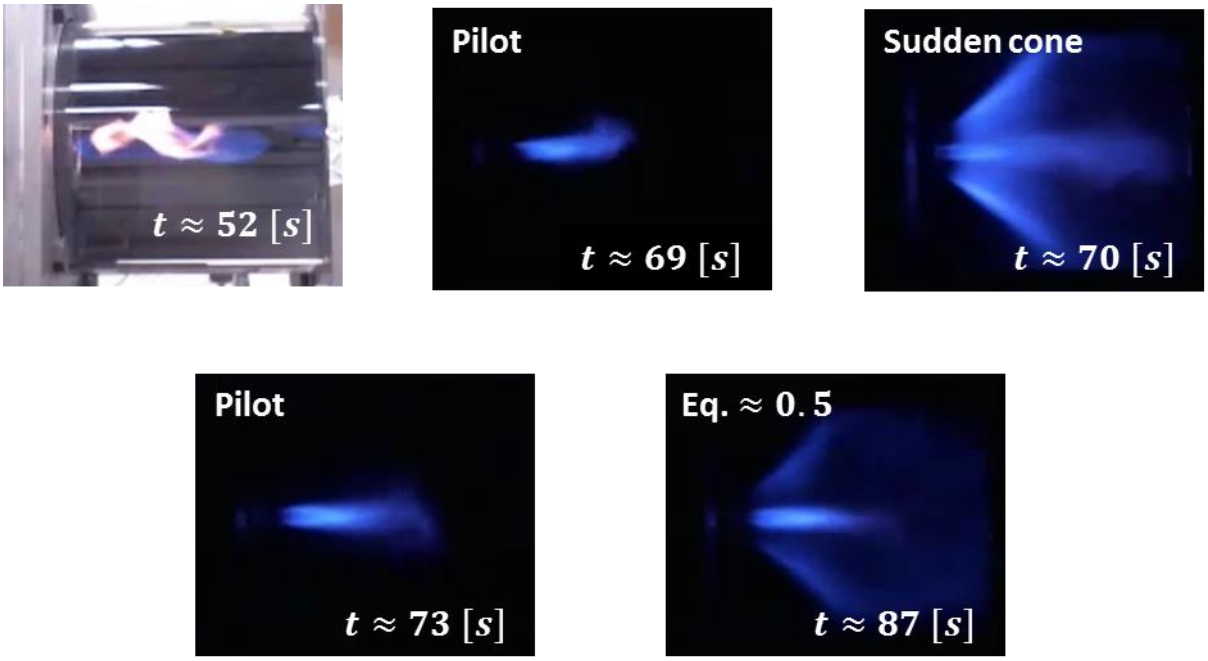


**Figure 70.** Flame pictures at times when the flame structure changed. The conical structure at $t \approx 70$ s was maintained for less than 4 seconds.

First the pilot flame was ignited with no air flow, at around $t = 52$ s. Once the pilot flame was ignited, the air flow was slowly increased to make the pilot flame lean, followed immediately by the gradual introduction of fuel to the main air path for pre-mixing. At around

$t = 70$ s, the conical flame structure formed by the pre-mixed swirl jets exiting the nozzle first appeared, lasting for only a few seconds as the main air was further increased to reach the air mass flow set point. The equivalence ratio time series plotted in Figure 69, also shows a peak at around $t = 70$ s. The magnitude of the peak was likely higher but was not properly captured due to the time resolution of the air flow meter. At around $t = 87$ s, the final flame was obtained which lasted for approximately 30 seconds before the wall temperatures reached the calibration limit of the IR camera.

### 5.1.4 Analysis methodology for unsteady heat transfer

The analysis consisted of acquiring the time evolution of the inner (flame side) and outer (ambient/coolant side) wall temperatures on the combustor liner. These temperatures were then used as boundary conditions in a finite difference model to calculate the temperature distribution across the liner thickness. From the inner wall temperature gradient in the solved temperature distribution, the heat flux from the working fluid into the material was estimated. This heat flux was finally used to calculate the heat transfer coefficient based on a reference temperature of the working fluid.

As mentioned previously, it was observed experimentally that the heat transfer characteristics were invariant along the azimuthal direction. That is, there were no variations in the temperature around the liner circumference at any given axial location. This was an important observation, because it allowed the modeling of the combustor liner as a two dimensional solid with only temperature variations along the axial and radial coordinates. The azimuthal boundaries in the numerical model were considered adiabatic surfaces ($\partial T/\partial \theta = 0$). The solution of a two-dimensional cylindrical solid temperature distribution is a standard problem in conduction heat transfer, where the heat equation for the temperature of an inner point within the liner thickness at a given time is expressed by Eq. 47.

$$\rho C_p \frac{\partial T}{\partial t} = \frac{\partial}{\partial x}\left(\gamma \frac{\partial T}{\partial x}\right) + \frac{1}{r}\frac{\partial}{\partial r}\left(\gamma r \frac{\partial T}{\partial r}\right) \tag{47}$$

The conductivity of the quartz $\gamma$, and the product $\rho C_p$ are a function of temperature, and hence implicitly a function of location and time. Equation 47 was discretized using the implicit

Euler method, with first order finite differences in time and second order in space. The discretized equation is given by Eq. 48 in terms of the space node indices $i$ and $k$ ($x$ and $r$ coordinates respectively), and time index $n$. To simplify the numerical solution, the thermal properties of the quartz where assumed to be constant for the evaluated time step, with their values updated based on the temperature from the previous time step. The model radial dimension extends from $r_0 = 101.5$ mm (at the inner liner boundary) to $r_{kk} = 105.5$ mm (at the outer boundary). The axial dimensions extend from the dome plate at $x_0 = 0$ mm to $x_{ii} \approx 160$ mm (limited by the field of view of the IR camera).

$$\begin{aligned}
&\left(\rho C_p\right)_{i,k}^{n-1} \frac{T_{i,k}^{n} - T_{i,k}^{n-1}}{\Delta t} \\
&= \gamma_{i,k}^{n-1} \left(\frac{T_{i+1,k}^{n} - 2T_{i,k}^{n} + T_{i-1,k}^{n}}{\Delta x^2}\right) \\
&+ \frac{1}{r}\left[\gamma_{i,k}^{n-1}\left(\frac{T_{i,k+1}^{n} - T_{i,k-1}^{n}}{2\Delta r}\right)\right. \\
&\left. + \gamma_{i,k}^{n-1} r \left(\frac{T_{i,k+1}^{n} - 2T_{i,k}^{n} + T_{i,k-1}^{n}}{\Delta r^2}\right)\right]
\end{aligned} \tag{48}$$

After rearranging unknown terms to the left of the equation and known terms to the right, the formulation at each node in the solid becomes Equation 49.

$$\left.\begin{aligned}
&T_{i,k}^{n}\left(\frac{\left(\rho C_p\right)_{i,k}^{n-1}}{\Delta t} + \frac{2\gamma_{i,k}^{n-1}}{\Delta r^2} + \frac{2\gamma_{i,k}^{n-1}}{\Delta x^2}\right) \\
&+ T_{i,k+1}^{n}\left(-\frac{\gamma_{i,k}^{n-1}}{2\mathrm{r}\Delta r} - \frac{\gamma_{i,k}^{n-1}}{\Delta r^2}\right) \\
&+ T_{i,k-1}^{n}\left(\frac{\gamma_{i,k}^{n-1}}{2\mathrm{r}\Delta r} - \frac{\gamma_{i,k}^{n-1}}{\Delta r^2}\right) \\
&+ T_{i+1,k}^{n}\left(-\frac{\gamma_{i,k}^{n-1}}{\Delta x^2}\right) \\
&+ T_{i-1,k}^{n}\left(-\frac{\gamma_{i,k}^{n-1}}{\Delta x^2}\right)
\end{aligned}\right\} = \frac{\left(\rho C_p\right)_{i,k}^{n-1}}{\Delta t} T_{i,k}^{n-1} \tag{49}$$

The coefficients for the unknown temperatures were input into a square matrix of size $ii * kk \times ii * kk$ with a solution vector given by the right hand side of Eq. 49. The system of equations was solved using the Armadillo C++ library (based on the LAPACK library). The constant temperature boundary conditions at $k = 0$ and $k = kk$ were given by the IR readings and the axial boundaries were modeled as adiabatic ($T^n_{0,k} = T^n_{1,k}$ and $T^n_{ii,k} = T^n_{ii-1,k}$). The heat flux normal to the inner liner wall (from Fourier's law) was equated to the heat transfer from the working fluid according to an energy balance at the boundary as shown by Eq. 50.

$$-\gamma \frac{\partial T}{\partial r}_{r=r_0} = h\left(T_{r=r_0} - T_\infty\right) \tag{50}$$

In terms of the discretized variables and node indices, the heat transfer coefficient was evaluated according to Eq. 51.

$$h^n_i = -\gamma^{n-1}_{i,k} \frac{T^n_{i,k0} - T^n_{i,k1}}{\Delta r} \frac{1}{\left(T^n_{i,0} - T_\infty\right)} \tag{51}$$

Where $k0$ and $k1$ are the reference elements taken to estimate the temperature gradient. For the results presented $k0 = 0$ and $k1 = 2$ were used in the grid with a total of $kk = 15$ elements along $r$. Using $k0 = 1$ and $k1 = 3$ significantly lowered the variability of the results but also lowered the heat transfer coefficients and heat fluxes by $\sim 5\%$ and $\sim 8$ respectively.

The implicit Euler method was selected due to its stability and simplicity. However, because the material properties were evaluated based on the previous time-step, a conservative grid resolution of $nn = 1000$, $kk = 15$, and $ii = 50$ was selected for experimental runs 240 seconds long. This grid yielded acceptable spatial resolution at reasonable computational times (solving for the entire time evolution would take approximately 2 hours with a personal computer using an Intel® Core™ i7-2620M 2.70MHz processor).

#### 5.1.4.1 Infrared acquisition through quartz glass

The SC6700 FLIR infrared (IR) camera spectral sensitivity range between 1 and 5 μm overlapped with the fused silica absorption spectrum. A similar spectral radiance analysis as that

presented in Chapter 4 was used to evaluate if the wall temperatures could be reliably acquired across the quartz glass. A schematic of the setup in the experiment is shown in Figure 71. The schematic shows the black opaque coating for both the inner and outer liner walls, however it is important to reiterate that the outer black coating was only applied to half of the liner (the inner coat was for the entire liner, see Figure 65). In other words, from the perspective of the IR camera, the top and bottom halves of the liner are representative of the outer and inner wall temperatures respectively. As previously discussed, given the symmetry of the system, this allows for the simultaneous acquisition of the inner and outer wall temperatures.

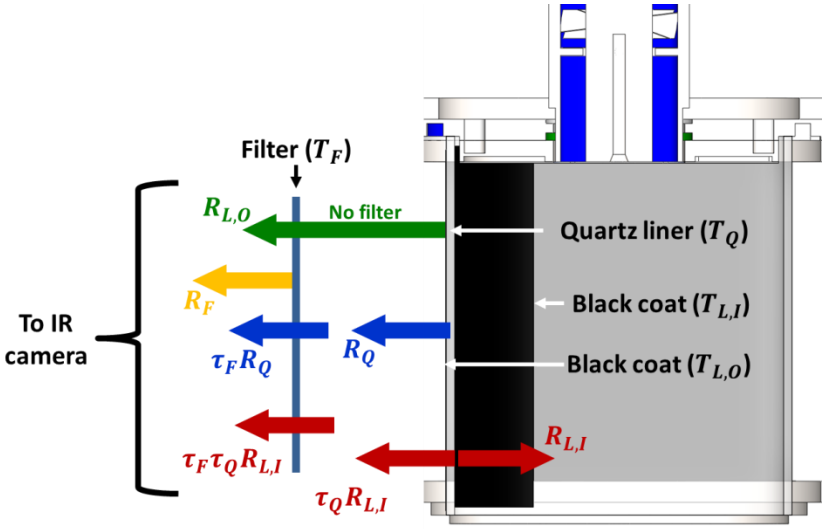


**Figure 71.** Top view schematic of the combustor setup for the unsteady heat transfer measurements showing the relevant components of the radiance received by the IR detector.

Calibration of the inner and outer walls was accomplished by comparing the IR measurement to coincident surface thermocouple data (T-Type, 0.5 K accuracy). Quartz glass has low transmittance and high emittance for wavelengths above $\sim 2.6\,\mu m$. Without any provisions to limit the quartz emission in the IR recording, the calibration of the inner wall would be heavily dependent on the instantaneous quartz temperature. For this reason, a filter, with spectral transmittance $\tau_{\lambda,F}$ and emittance $\epsilon_{\lambda,F}$, was added for the inner wall temperature measurement (as shown in Figure 71). The filter would then reduce the radiance from the quartz liner and improve the calibration consistency throughout the experiment. This was only necessary for the inner wall emission, since the outer wall emission was not contaminated by the

thermal radiance from the quartz liner. Kirckhoff's law of thermal radiation (Eq. 52) states that the spectral emittance ($\epsilon_\lambda$) and absorptance ($a_\lambda$) of a material are equal to each other when in thermodynamic equilibrium.

$$a_\lambda = \epsilon_\lambda \tag{52}$$

Hence, a suitable filter material to absorb the radiation from quartz at high temperatures (emitting according to $\epsilon_{\lambda,Q}$) could be another piece of quartz at low temperature ($a_{\lambda,F} = a_{\lambda,Q} = \epsilon_{\lambda,Q}$), which would preferentially absorb at the wavelengths were the quartz liner emittance is highest. In turn, given the filter is at approximately a constant temperature, it would emit a relatively constant (and lower) radiation throughout the experiment, therefore improving the calibration for the inner wall. Using a cold piece of fused silica as a filter assumed that the spectral characteristics of the quartz do not vary significantly for the range of temperatures in the experiment [139,140]. Prior to the experiment, it was important to determine the viability of measuring the inner wall temperature by filtering the quartz liner radiation. Detailed absorption coefficient data for fused silica (quartz) at 293 K were taken from [140] to estimate the spectral emittance ($\epsilon_{\lambda,Q}$) and transmittance ($\tau_{\lambda,Q}$) of quartz according to Lambert's (Eq. 53) and Kirckhoff's laws (Eq. 52). Reflectance was neglected and the material thickness $L$ was 4 mm for the liner and 6.4 mm for the filter.

$$1 - a_{\lambda,Q} = \tau_{\lambda,Q} = \exp\left(-K_{\lambda,Q}L\right) \tag{53}$$

The total radiance ($R_T$) received by the IR camera from the filter ($R_F$), quartz liner ($R_Q$), and coatings at the surface walls ($R_{L,I}$ and $R_{L,O}$) was determined by integrating Planck's Law ($B_\lambda$, Eq. 54) over the IR detector spectral range, accounting for the spectral emittance and transmittance of the different materials. Equations 55 and 56 are the total radiance formulations for the inner and outer liner respectively (for this theoretical analysis atmospheric transmission was neglected).

$$B_\lambda(\lambda, T) = \frac{2h_P c^2}{\lambda^5} \frac{1}{\exp\left(\frac{h_P c}{\lambda K_B T}\right) - 1} \tag{54}$$

$$R_{T,I} = R_{L,I} + R_Q + R_F =$$

$$\int_{1\mu m}^{5\mu m} \tau_{\lambda,F}\tau_{\lambda,Q}\epsilon_W B_\lambda(\lambda, T_{L,I})d\lambda + \tau_{\lambda,F}\epsilon_{\lambda,Q}B_\lambda(\lambda, T_Q)d\lambda + \epsilon_{\lambda,F}B_\lambda(\lambda, T_F)d\lambda \quad (55)$$

$$R_{T,O} = R_{L,O} = \int_{1\mu m}^{5\mu m} \epsilon_W B_\lambda(\lambda, T_{L,O})d\lambda \quad (56)$$

The emissivity of the black coating ($\epsilon_W$) was estimated as 0.80 (at all wavelengths). Since the filter material analyzed was also quartz glass, $\epsilon_{\lambda.F} = \epsilon_{\lambda,Q}$ and $\tau_{\lambda,F} = \tau_{\lambda,Q}$. The relative spectral radiance over the IR detector range for the inner wall measurement with and without filter is shown in Figure 72 for $T_Q = T_{L,I} = 450$ K with $T_F = 293$ K. Table 4 summarizes the results for two other temperature cases as well. Figure 72 indicates that without the filter, the quartz radiation would dominate (72-84%) the total signal received by the IR camera. The addition of a filter lowered the contribution of the quartz liner to the total detected radiance to below 38% per this theoretical analysis.

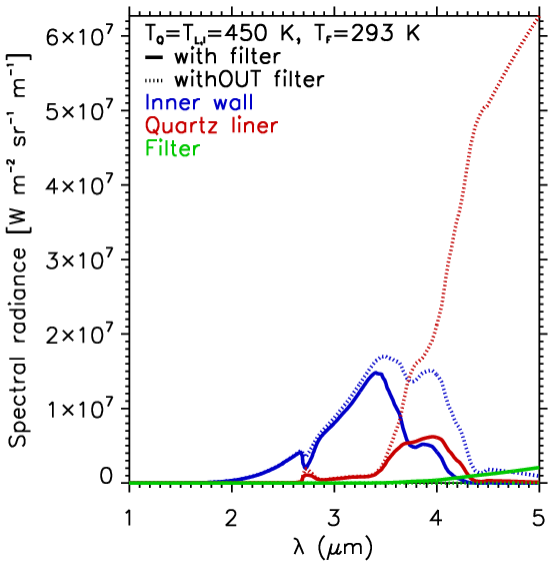


**Figure 72.** Theoretical calculation of the radiance from the fused silica (quartz) liner and the inner wall with and without the filter. The liner radiance was significantly reduced.

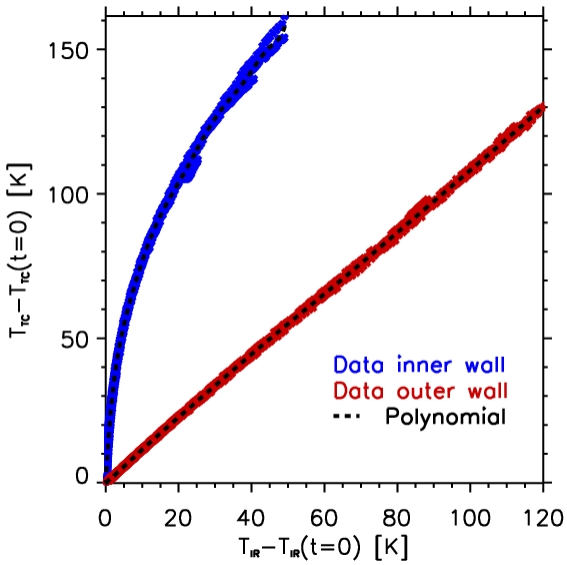


**Figure 73.** Calibration of the inner and outer wall IR temperature readings as measured from five experimental runs.

**Table 4.** Estimated radiance detected by the IR camera for the inner combustor wall measurement with and without filter at different temperatures.

| Temperature case | With filter [W m$^{-2}$ sr$^{-1}$ m$^{-1}$] | | | | Without filter [W m$^{-2}$ sr$^{-1}$ m$^{-1}$] | |
|---|---|---|---|---|---|---|
| | $R_{L,I}$ | $R_Q$ | $R_F$ | $R_{L,I}/R_Q$ | $R_{L,I}$ | $R_Q$ |
| $T_Q = T_{L,I} = 320$ K, $T_F = 293$ K | 0.26 | 0.16 | 1.3 | 1.63 | 0.58 | 3.02 |
| $T_Q = T_{L,I} = 385$ K, $T_F = 293$ K | 2.49 | 1.12 | 1.3 | 2.22 | 4.62 | 16.31 |
| $T_Q = T_{L,I} = 450$ K, $T_F = 293$ K | 12.9 | 4.67 | 1.3 | 2.77 | 21.43 | 55.0 |

The radiation from the outer liner wall had no contamination (other than absorption from the atmosphere) and the calibration was straightforward with surface thermocouples. The calibration curves for the inner and outer walls are shown in Figure 73 from five experiments at different heating rates and temperature ranges. The standard error in the inner and outer wall calibration polynomials was respectively 1.5 K and 0.56 K.

#### 5.1.4.2 Uncertainties in the measurement

The calculation of the heat transfer coefficient at the wall was obtained from Eq. 51. The total uncertainty in the heat transfer coefficient was calculated by propagating the error from the different variables in the formulation. The total uncertainty was hence given by uncertainties in the temperature gradient ($\sigma_{\mathrm{d}T/\mathrm{d}r}$), the thermal properties of the material ($\sigma_\gamma = 5\%$), and the surface ($\sigma_{L,I} = 3.0$ K, as a worst case scenario) and flow temperatures ($\sigma_\infty = 0.5$ K). The uncertainty in the temperature gradient was estimated from the maximum uncertainty in the difference between the inner and outer liner wall temperatures and the liner thickness; resulting in an estimated uncertainty of 900 K m$^{-1}$. The resulting total uncertainty for the heat transfer coefficient varied depending on the time step. Close to the start of the experiment, the heat flux to the liner wall was negligible and no accurate heat transfer coefficients could be acquired. For a wall heat flux of 5 kW m$^{-2}$, the uncertainties were $\sim 25\%$, decreasing to below 14% for heat fluxes greater than 10 kW m$^{-2}$.

### 5.1.5 Unsteady non-reacting combustor heat transfer

The 42 800 Reynolds number case corresponded to the design Mach numbers through the Solar Turbines Incorporated fuel nozzle used and was taken as the baseline for the analysis of the

results (equal to $Re_N = 180\,000$ in Chapter 3, with respect to the nozzle diameter). The calculated temperature profile across the liner thickness for different time steps is shown in Figure 74. Each black line corresponds to a different axial location along the liner. The approximation of the temperature gradient near the inner wall (radial distance equal to zero) for the heat flux calculation is shown in red. The experiment started at $t \approx 60$ s. As the experiment progressed, the temperature in the inner and outer wall increased, maintaining a logarithmic profile across the liner (as expected from the cylindrical geometry).

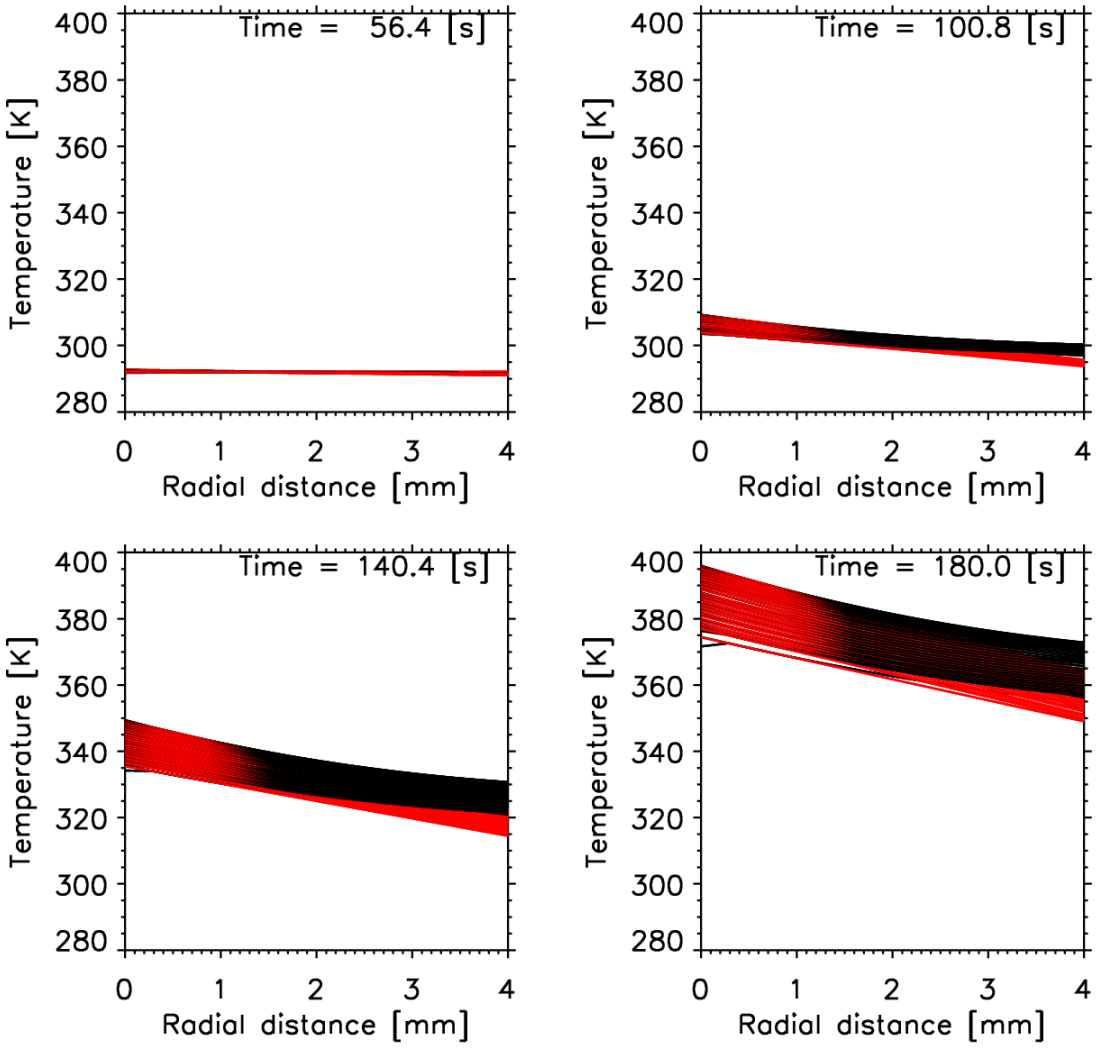


**Figure 74.** Temperature profile (black) across the fused silica liner at different time steps as calculated from the Re = 42 800 case. The linear fit near the wall is also shown and extrapolated through the entire liner thickness (red).

The heat flux result for the $\mathrm{Re} \approx 42\,800$ experiment, including temporal (vertical axis) and spatial (horizontal axis) variability, is given by Figure 75 according to the heat flux formulation included as part of Eq. 51. For this Reynolds number, the wall reached the calibration temperature by $t \approx 205$ s (the processing stopped when the temperatures were greater than the calibration limit) and it did not show the decrease in the heat flux as the mainstream temperature stabilized. For this reason, the result for the $Re \approx 11\,500$ case is also shown (right). The convective heat load reached a maximum around $t = 177$ s for the low Reynolds number case, when the mainstream temperature reached the set point and the temperature of the wall kept increasing (decreasing the temperature potential between the wall and the mainstream). This was an important verification of the method capturing the temporal evolution of the heat load after the flow temperature became constant.

The heat transfer coefficient depends not only on the heat flux distribution but also on the temperature potential ($T_{r=r_0} - T_\infty$). The obtained heat transfer coefficient (HTC) distribution according to Eq. 51 is shown in Figure 76 for the $\mathrm{Re} \approx 42\,800$ experiment. The HTC was relatively constant after the heat flux reached a minimum value of $\sim 5$ kW m$^{-2}$. Below this heat flux, the temperature signal was small and no accurate measurement was possible.

During the non-reacting experiments the Reynolds number decreased significantly for a given mass flow, primarily due to changes in the gas viscosity. The kinematic viscosity ($\nu$) of air at 450 K (heater set point) is 2.08 times higher than at ambient conditions (293 K). Moreover, as the temperature of the mainstream was increased, conservation of mass led to higher air flow velocities in the test section, and consequently higher pressure losses in the system. Since the main control valve opening was kept constant throughout, this led to a reduction of $\sim 4\%$ in the air mass flow delivered to the test section with increasing temperature (this reduction was also partially due to 1.5% oscillations in the compressor loading used in the air supply line). A constant HTC with decreasing Re as shown in Figure 76 may at first appear inconsistent with typical correlations for turbulent flow heat transfer. However, correlations relate the Reynolds number to the Nusselt number. The latter also decreased during the experiment as the temperature increased, due to the rise in the thermal conductivity of the working fluid (by a factor of 1.45 from 293 K to 450 K). The maximum and average Nusselt number variation with Reynolds number for all the non-reacting experiments are shown in Figure 77.

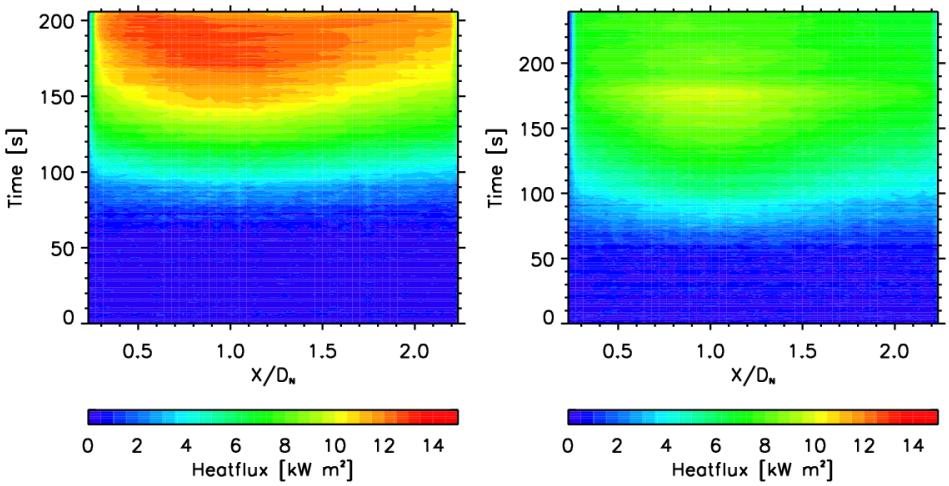


**Figure 75.** Heat flux contour for the Re = 42 800 (left) and Re = 11 500 (right) cases. The lower Reynolds number case is shown because it captured the decrease in the heat flux as the working fluid temperature reached its maximum temperature.

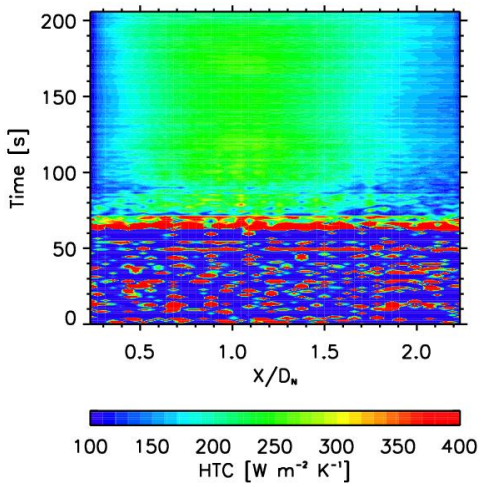


**Figure 76.** Heat transfer coefficient (HTC) obtained for the Re = 42 800 case.

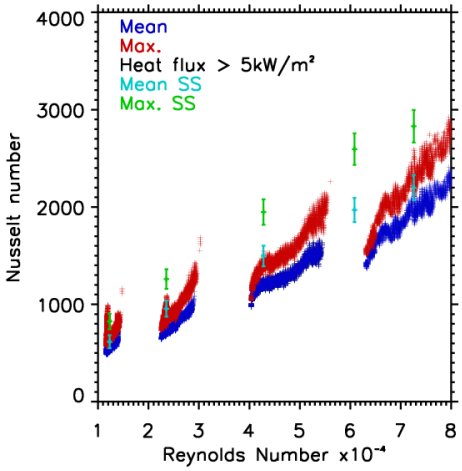


**Figure 77**. Nusselt numbers obtained from the different non-reacting experiments, compared with the results obtained at steady state (SS).

A comparison between the results obtained from the four unsteady experiments and the validation steady state experiments (Chapter 4) using the surface heater is shown in Figure 78. The blue, black and red lines correspond respectively to the steady state data, the instantaneous HTC result, and the instantaneous heat flux. The time steps plotted correspond to that at which the unsteady and steady state experimental Reynolds numbers were approximately equal. The

differences between the two independent experiments were between 3.0% and 17.3%, in general within the uncertainties of both measurements.

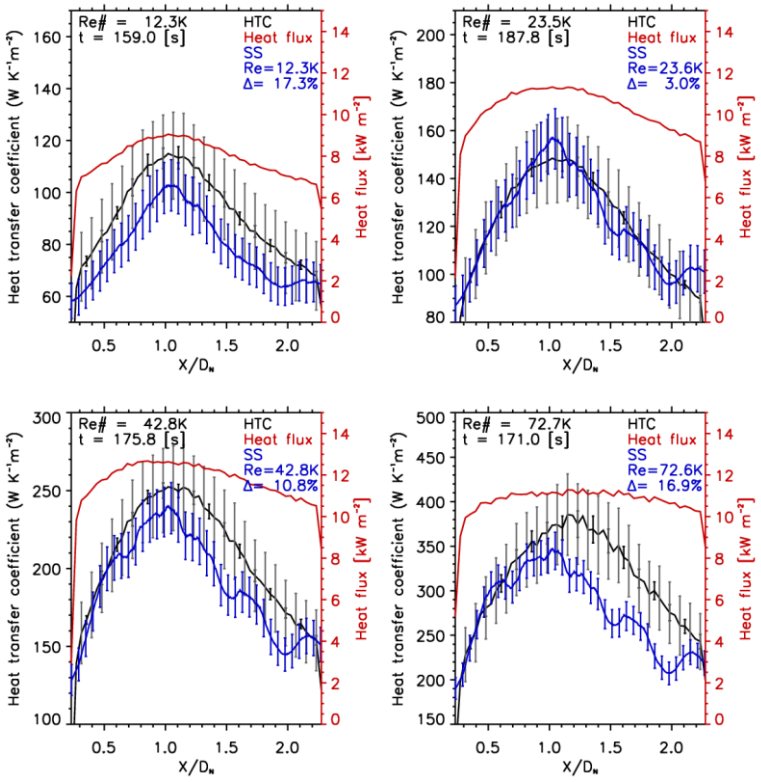


**Figure 78.** Comparison between the unsteady results and the steady state validation experiments for four different mass flow cases. The time snapshot from the unsteady results that most closely approached the steady state Reynolds number (based on combustor inlet temperatures) was selected.

### 5.1.6 Effects of time and space grid size on the isothermal results

The sensitivity of the finite difference solution to different grid sizes, both in space and time, were investigated, with no significant difference observed between the results. The output of the finite difference methodology is the wall heat flux, and is only dependent on the IR temperature acquisitions (no dependence on thermocouple flow temperature measurements). The heat flux distribution was hence compared for different grid resolutions for the Reynolds number $\sim$ 43 000 baseline case. Figure 79 shows the results using twice the space grid resolution ($kk = 30$ and $ii = 100$), with no change to the time resolution. The difference, compared to the results in Figure 75 was negligible.

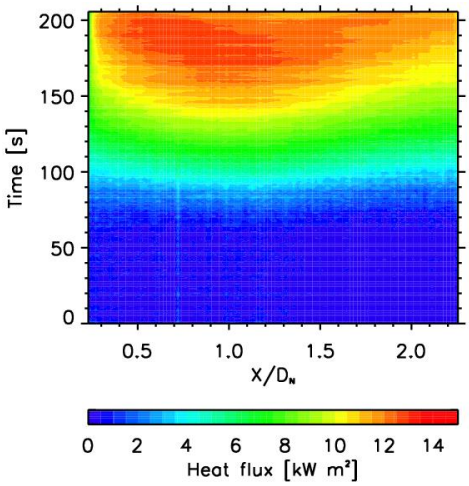


**Figure 79.** Heat flux time and space distribution for a spatial grid with twice the resolution ($kk = 30$ and $ii = 100$) compared to that used for the presented results. Negligible differences were observed.

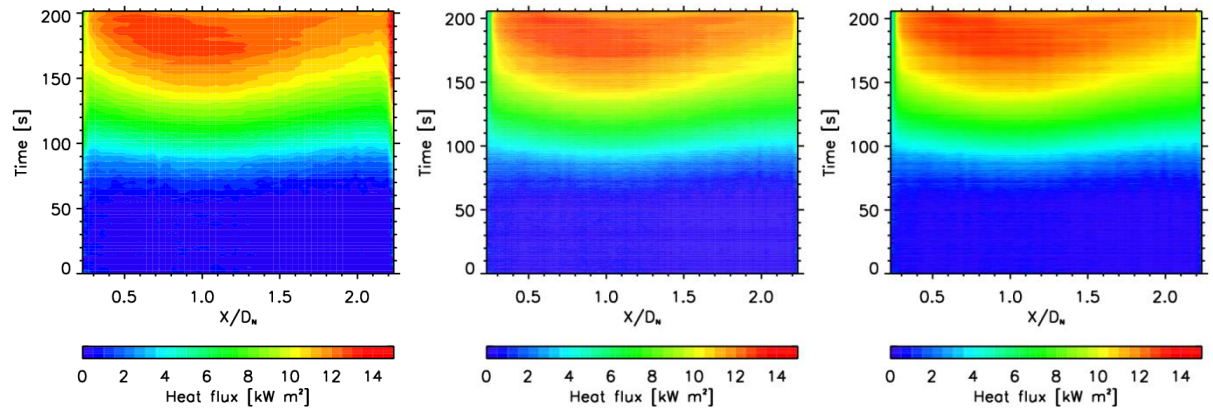


**Figure 80.** Heat flux time and space distribution for different time resolutions. The left, center and right plots correspond respectively to the results using $nn = 100$, 1000 and 5000.

Similarly, the effects of the time resolution were investigated with a spatial resolution of $kk = 15$ and $ii = 50$. The results using a total $nn$ time steps of 100, 1000, and 5000 are shown in Figure 80. No appreciable difference was observed beyond $nn = 1000$. Even the results using $nn = 100$ correctly capture the heat flux and do not show signs of instability. The main concern for the lowest resolution result was the larger errors at the axial boundaries (these are also present using the other time resolution, but are not as prominent). The main advantage of using higher time resolution is the ability to study phenomena that occur within shorter time-scales. However, given the IR camera acquisition rate of 15Hz, for a 4 minute run, more than 3600 time steps provides no additional information. The fact that the time resolution has no impact on the

stability of the result was one of the main reasons for selecting the implicit Euler method for the solution of the conduction problem.

### 5.1.7 Applying the validated measurement to an unsteady reacting combustor case

The heat flux distribution throughout the reacting experiment at low wall temperatures is shown in Figure 81. The increased heat load at $t \approx 70$ s and again at $t \approx 90$ s is consistent with the appearance of the main flame (cone) as shown in Figure 70 in section 5.1.3. As expected, due to the higher temperatures in the reacting case, the heat flux was in general $\sim$ 1.6 times higher compared to the non-reacting case at the same air mass flow. To put the heat flux in perspective, Figure 82 shows the heat flux normalized with respect to the equivalent maximum flame heat flux that could be delivered to the wall. The maximum flame heat flux was calculated using the total fuel heat release (lower heating value of methane assuming 100% combustion efficiency) divided by the inner wall surface area of the liner.

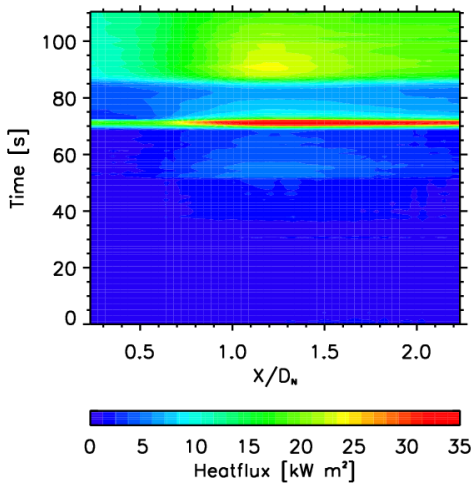


**Figure 81.** Heat flux results for the reacting case at a mass flow equivalent to a combustor inlet Reynolds number of $\sim$ 12 000.

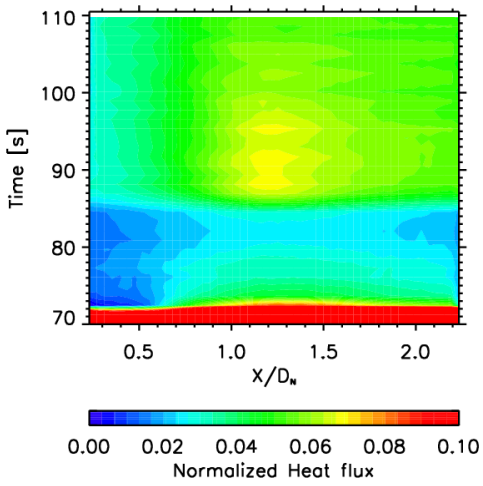


**Figure 82**. Liner heat flux normalized with respect to the fuel heat release according to its lower heating value (LHV), divided by the total liner inner wall surface area.

The portion of the liner wall imaged (74% of the liner length) accounted on average for 46.4% of the total heat release after $t > 90$ s. Assuming the same amount of heat rate is applicable for the remainder of the liner, the liner heat rate accounted for approximately 63% of the fuel heat release. The theoretical flame temperature (using GRI-MECH 3.0 [150]) after

removing the liner heat loss was 775.5 K (for reference, the adiabatic flame temperature for the average equivalence ratio after $t > 90$ s was 1450 K). The measured temperature at the outlet of the combustor reached a maximum value of $\sim 650$ K, still below the calculated flame temperature accounting for the thermal loss through the liner. However, this is possible since dome wall heat transfer was neglected, 100% combustion efficiency was assumed, and the thermocouples were not corrected for time delay. These heat loads are only applicable during the combustor startup, when the liner wall temperatures are cold. Once the liner wall temperatures reach a steady state value, the heat losses to the liner would be smaller. This is also suggested by the available data in Figure 82 for $t > 90$ s, showing a decreasing maximum heat flux with time. Nevertheless, calculation of the instantaneous heat loads during ignition is critical to predict the durability of the liner, as these will determine the maximum thermal gradients during startup and hence a large thermal stress the liner must withstand.

One challenge for reacting experiments is choosing a reference gas temperature for the calculation of the heat transfer coefficient, given the sharp temperature and composition gradients across the flame front. Different empirical and theoretical definitions are often used in internal flow experiments, including the bulk flow or the log-mean temperatures. Calculating the temperature potential for the wall according to an empirically defined temperature is acceptable as long as the heat transfer coefficient is not changing with time and the heat loads are evaluated with respect to the same reference temperature. Strictly speaking however, the adiabatic wall temperature observed for a given flow provides an unambiguous definition for the reference gas temperature. The adiabatic wall temperature accounts for compressibility effects in high speed flows, and in reacting flows it can account for near wall thermochemical heat release. For non-catalytic combustor walls (as is the case in this study), the adiabatic wall temperature would approximately equal the adiabatic flame temperature for the instantaneous equivalence ratio. However, using this as a reference may be inappropriate as the actual flow temperatures during the reacting experiment were lower than the adiabatic flame temperature. Calculating bulk flow temperatures at every axial location and time step was also impractical, and would not aid gas turbine designers as they do not have access to detailed air temperature measurements in the combustor. For the results presented in this section, two reference gas temperatures were considered. The first was the instantaneous average of the temperature observed in the recirculation zone and the combustor outlet (near the liner wall), shown in Figure 83 (left). While

this definition was arbitrary, it was partially representative of the entire burner and reflected approximated temperatures throughout the experiment. However, the main disadvantage of this reference was the response times for the thermocouples, which severely affected the results near flame transition points. The bead diameter of the TCs used was 0.762 mm, which per the manufacturer's data has an approximate time response of 1.5 seconds. Thinner thermocouples could not be used during the flame experiments due to breakage at the high temperatures. Also important to note is that the thermocouple leads were covered by ceramic tubes (to protect them from the hot combustion gases) which could further lead to flow stagnation at the bead and hence higher response times.

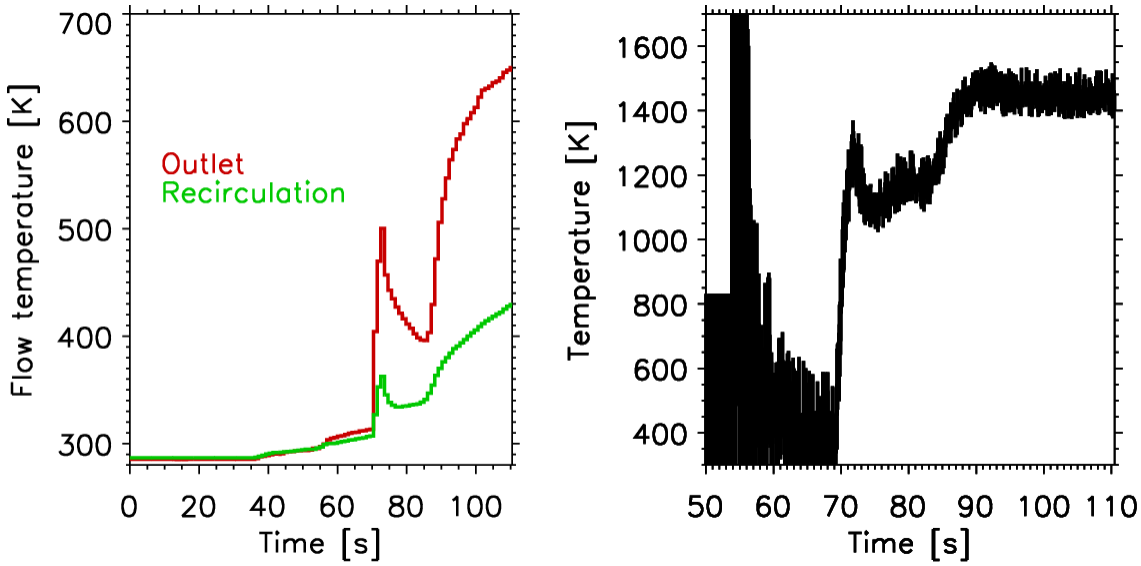


**Figure 83.** Reference temperatures considered for the calculation of the reacting heat transfer coefficient. Thermocouple measurements at the outlet of the combustor and in the recirculation region (left), compared to the adiabatic flame temperature based on GRI-MECH 3.0 [150] (right). Plots have different time scales.

As an alternative, the second reference temperature considered for the heat transfer coefficient calculation was the instantaneous average of the adiabatic flame temperature (Figure 83 –right-) and the inlet temperature to the combustor, the latter assumed to be ambient as measured at the beginning of the experiment. This definition can be easily evaluated by designers, based on their inlet conditions and operating equivalence ratio. Further investigation is required to identify a reference temperature that best correlates the data, including non-reacting and reacting results. For reacting cases, effects such as flame quenching near a cold wall,

thermochemical heat release, and incomplete combustion may make the adiabatic wall temperature reference inappropriate. In an adiabatic wall, no flame quenching would occur, and incomplete combustion would be less likely (no heat losses). Moreover the distribution of near wall thermochemical heat release would change, as reaction of incomplete combustion products may occur further downstream on the liner in a non-adiabatic burner. These issues highlight the importance of detailed flow temperature (either experimentally or computationally) to better understand the instantaneous temperature difference driving the heat transfer to the wall.

The obtained heat transfer coefficient profile for $t \approx 96$ and 110 s is shown in Figure 84 using the reference flow temperature from the average of the measured combustor recirculation and outlet temperatures. Figure 85 shows the heat transfer coefficient at approximately the same instantaneous times, using the average of the adiabatic flame temperature and the inlet temperature as the reference. Both figures include as well the non-reacting steady state measurement used for validation at the same air mass flow (in blue). The peak heat transfer location shifted by $\sim 0.2D_N$ for the reacting case, consistent with the expected increase in the pre-mixed swirl jet axial velocities as the gas temperature increases across the flame front and matching the approximate location where the flame attached to the wall according to flame imaging (see section 5.3).

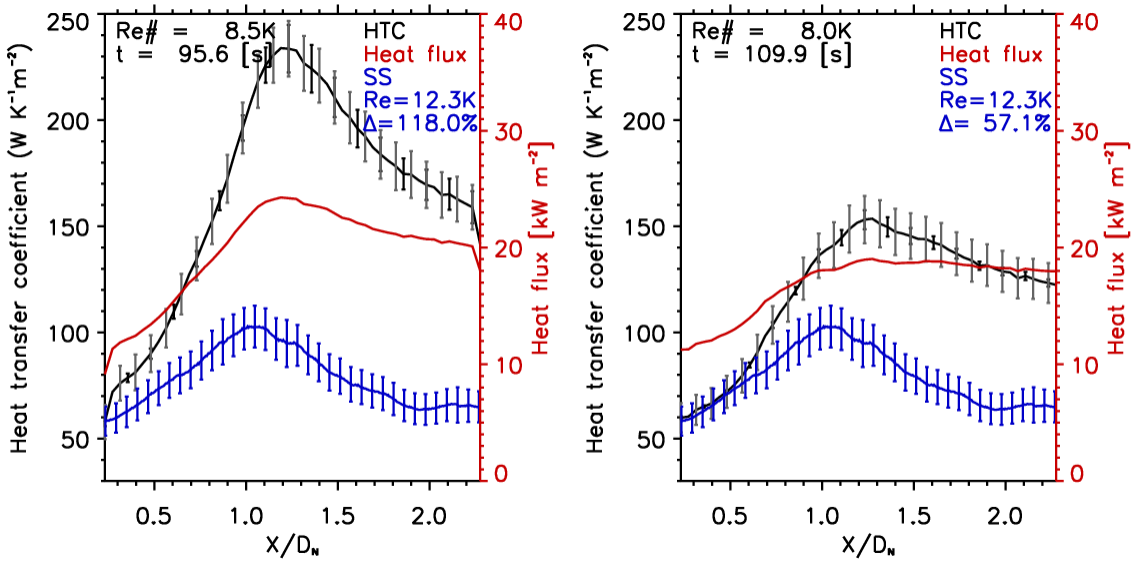


**Figure 84.** HTC distribution at a single time step as calculated with respect to the average of the outlet and recirculation temperatures, measured with a K-Type thermocouple.

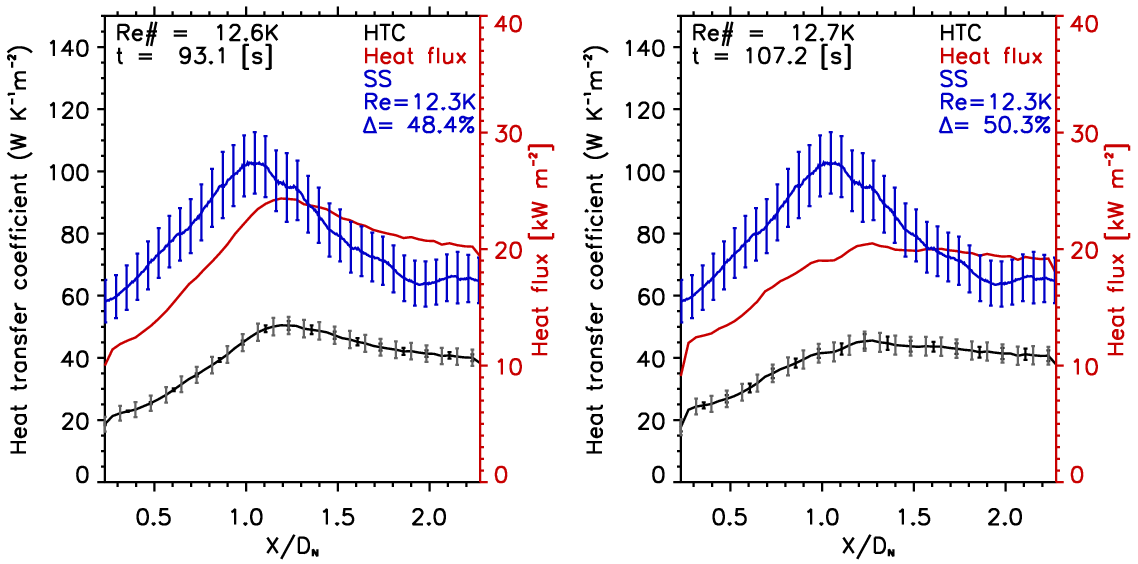


**Figure 85.** HTC distribution at a single time step as calculated with respect to the average of the adiabatic flame temperature and combustor inlet temperature.

The difference between the two reference flow temperatures used was observed both in the structure and magnitude of the heat transfer coefficient distribution. Figure 84 shows that using the first reference led to a decreasing heat transfer coefficient with time, which occurred because of the time response of the thermocouple. Near fast temperature transients, the thermocouples registered a lower temperature than what was actually driving heat transfer in the burner, leading to an overestimation of the HTC. Once the thermocouple temperature stabilized, so did the HTC. This problem was not present when using the second reference, as shown in Figure 85. While the HTC decreased with time, the effect was much smaller. The problem with using the second reference, is that the magnitudes were on average 2 times lower than those observed at isothermal conditions. Moreover, because the second reference temperature was much larger than the wall temperature during the experiment, small wall temperature changes along the liner did not impact the heat transfer distribution. This again highlights the importance of acquiring detailed flow temperature distributions, to correctly account for the temperature potential driving the heat transfer to the wall.

The time series of maximum and average HTC and heat flux using the two different reference flow temperatures are shown in Figure 86. The heat flux was continuous, except at around 70 s, when the conical flame structure first appeared for a few seconds. The peak heat transfer coefficient based on the first flow reference temperature changed abruptly during flame

structure transitions at $t \approx 70$ s and $t \approx 85$ s due to the unaccounted time delay in the thermocouple response. The magnitudes however were in better agreement with the isothermal measurements. Using the second flow reference (based on the adiabatic flame temperature) yields results that were independent of thermocouple errors, but that unfortunately may not capture the actual temperature driving the heat transfer to the wall. Given the time delay in the thermocouple temperature measurements, the reference gas temperature calculated from thermocouple data was not considered for the remainder of the reacting experiments.

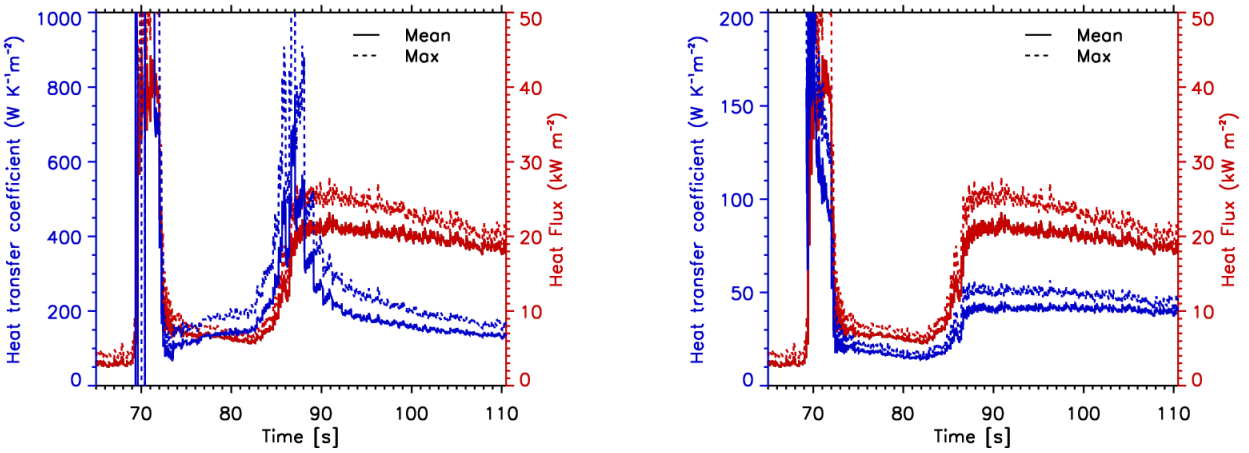


**Figure 86.** Time series of the maximum and average HTC and heat flux using the outlet-recirculation, and the adiabatic flame temperature-inlet reference temperatures (left and right respectively). The high heat transfer coefficients during flame transitions when using the outlet-recirculation reference are due to the time response lag of the thermocouple.

## 5.2 EXTENDING THE HEAT TRANSFER MEASUREMENTS TO SURFACES AT HIGH TEMPERATURES

As described in the previous section, one of the limitations of the heat transfer measurement in reaction was the maximum temperature that could be recorded with the IR camera (~573 K). Another potential opportunity to improve the method was in the amount of quartz radiation received by the IR detector, which was reduced but not completely eliminated by the cold quartz filter. Research on different optical filters led to the identification of the Schott KG family of glasses as a potential filter to remove the quartz radiation almost entirely, and increase the maximum temperature measurable by the IR camera.

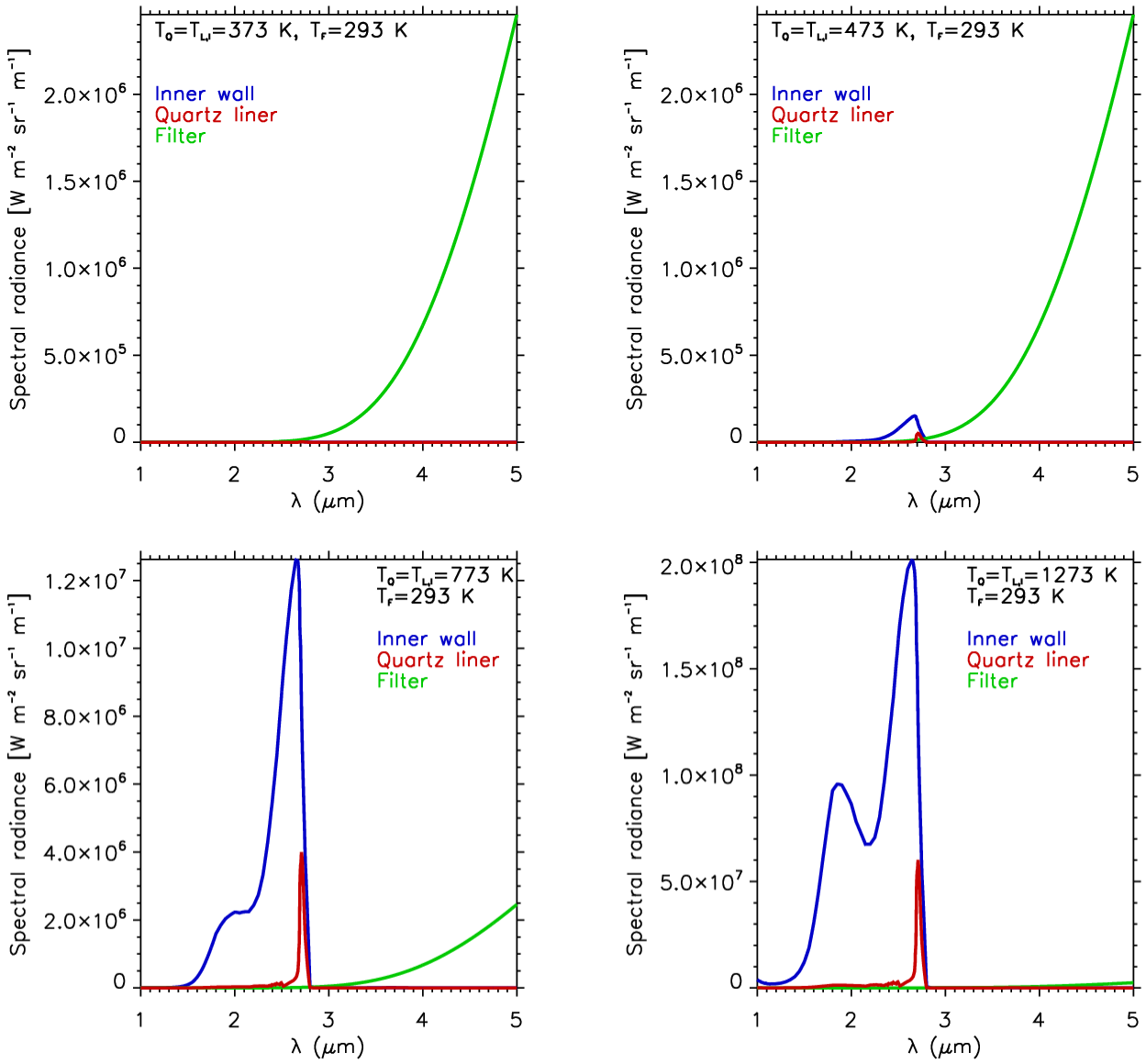


**Figure 87.** Theoretical calculation of the contribution from inner wall, quartz liner, and KG1 filter to the total radiance received by the IR camera for different temperature scenarios.

A theoretical analysis of the radiance received by the IR camera (described in section 5.1.4.1) was performed using a KG1 glass, 3 mm thick, as a filter; with spectral absorption given by [151]. The results are plotted in Figure 87. The filter practically eliminated the contribution to the total radiance from the quartz liner, but limited the lowest detectable temperature by the IR sensor to $\sim 425$ K. As observed in Figure 87, for an inner wall and quartz temperature of 373 K, the filter radiance dominated the spectral range of the detector and the wall signal was within the noise. Above $T_Q = T_{L,I} = 473$ K the inner liner wall signal was detectable. The error in $T_{L,I}$

incurred when neglecting the radiance from the quartz (assuming it is part of the inner liner radiance) is $< 2$ K for temperatures $(T_Q = T_{L,I}) < 1273$ K. The inner liner radiance, per the theoretical calculations, is between 11.6 and 23.8 times larger than the quartz radiance (at 473 K and 1273 K respectively), a significant improvement compared to the results using a cold quartz as the filter.

The calibration of the emissivity of the paint was done in a separate experimental setup where a K-Type surface thermocouple (flat bead) was clamped between two pieces of quartz glass (same manufacturer as that used for the quartz liners). The black coating was applied to the backside of the top quartz piece. Four calibrations of the paint were performed, two behind the glass and the other two with the paint exposed directly to the IR detector. All calibrations were consistent as shown in Figure 88. The lowest temperature captured by the IR camera corresponded to thermocouple temperatures of $\sim 450$ K.

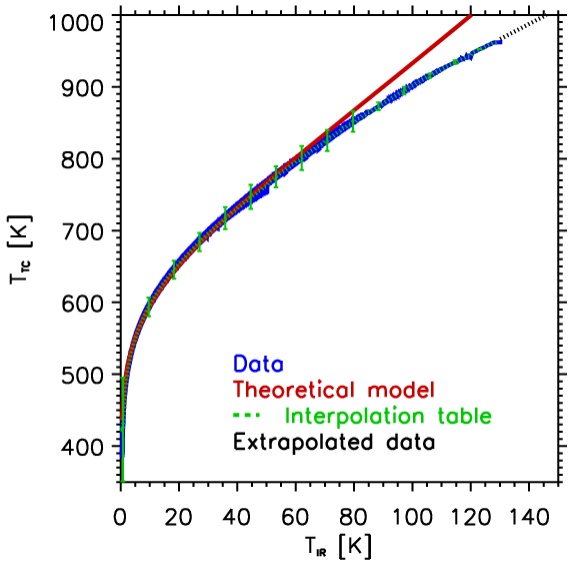


**Figure 88.** Calibration curve of the IR temperature readings with respect to actual wall temperatures according to a K-Type thermocouple. The results were also compared against the theoretical calculation for a 3 mm thick Schott KG1 glass filter.

Figure 88 shows, in addition to the thermocouple calibration, the calculated theoretical curve for a black coating emissivity of 1, taking the transmission of the KG1 Schott glass[1]

[1] Full disclosure, there was a discrepancy with the procured KG glasses. A purchase was done for a KG2 Schott glass, which would theoretically allow for measurements at lower temperatures. However, the response obtained matched well with the KG1

according to the data provided in [151]. The theoretical results matched with the thermocouple data up to $T_{TC} \approx 830$ K, further evidence supporting that the calibration was accurate. The calibration curve was extrapolated up to 1000 K ($T_{TC}$) based on the linear trend observed in the data. Any results that rely on wall temperatures beyond 950 K are based on the extrapolated calibration. Fitting the curve with a polynomial was not successful (the polynomials failed to accurately capture the sharp step in the calibration temperature at $T_{IR} - T_{IR}(t = 0) < 10$ K) and an interpolation table was created to correct the IR acquisitions.

### 5.2.1 Experimental results using Schott KG1 glass filter

Two Reynolds numbers were measured including $\sim 12\,000$ and $\sim 24\,000$ based on the combustor diameter and inlet temperature. The objective of these measurements was to study the behavior of the burner at equivalence ratios of 0.6-0.8 and the heat flux produced during shutdown. Shutdown represents the most dangerous condition for the combustor in terms of stresses, as the liner wall strength is lowest (highest temperature), and shutdown introduces high thermal loads (thermal stresses). Due to the lower detectable temperature limit, results during the fuel/air ramp-up and results for lower equivalence ratios were not available.

Similar to the low wall temperature experiments described in section 5.1.3, these experiments started first with ignition of the pilot flame with < 0.01 kg $s^{-1}$ air mass flow, followed by a ramp up of the air and main fuel. To avoid stability problems during ignition of the main flame, sufficient main fuel mass flow was introduced to raise the equivalence ratio between 0.6-0.7 leading to a sudden high temperature state, that was approximately maintained until the air mass flow target was achieved. The equivalence ratio hence started high when the main flame was ignited and was lowered to about an equivalence ratio below 0.6 when the experiment began.

---

transmission data (Figure 88), which raised the question of whether the purchased glass was in fact KG2. The provider of the KG2 glass had transmission data for wavelengths less than 1.1μm, and could not guarantee that the transmission beyond this wavelength would correspond to that of the Schott KG2 glass (as was expected when procuring the glass). The experiments were therefore ran with a filter labelled 'KG2', but theory appears to indicate that the filter received was in reality a KG1 in the spectral range of interest. This would further explain the discrepancy between the theoretical model and the data at higher temperatures, when the spectral radiance becomes biased to lower wavelengths. Regardless, the calibration with the thermocouple is independent of the theoretical analysis and hence the glass type assumed had not impact on the accuracy of the results.

These experiments lasted more than 6 minutes and had sharp condition changes. For this reason, a total of 3000 time steps were used, which resulted in a time step resolution of at least 0.15 seconds. Moreover, these experiments imaged a longer portion of the liner (up to $X/D_N = 2.7$) and hence the number of grid elements in the axial direction was increased from 50 to 63 in order to maintain the same spatial resolution as in the measurements at low wall temperatures.

#### 5.2.1.1 Results for 12 000 Reynolds number

Photographs of important transitions in the flame structure throughout the run are shown in Figure 89. The wall temperature signal throughout the experiment is given in Figure 90, indicating that only data beyond $t \approx 250$ s was above the minimum temperature threshold for the entire imaged liner. Even at $t \approx 210$ s, most of the imaged liner had a significant temperature signal, and partially provides data for the 0.6 equivalence ratio ($\phi$). The equivalence ratio and massflows during the run are plotted in Figure 91 and Figure 92.

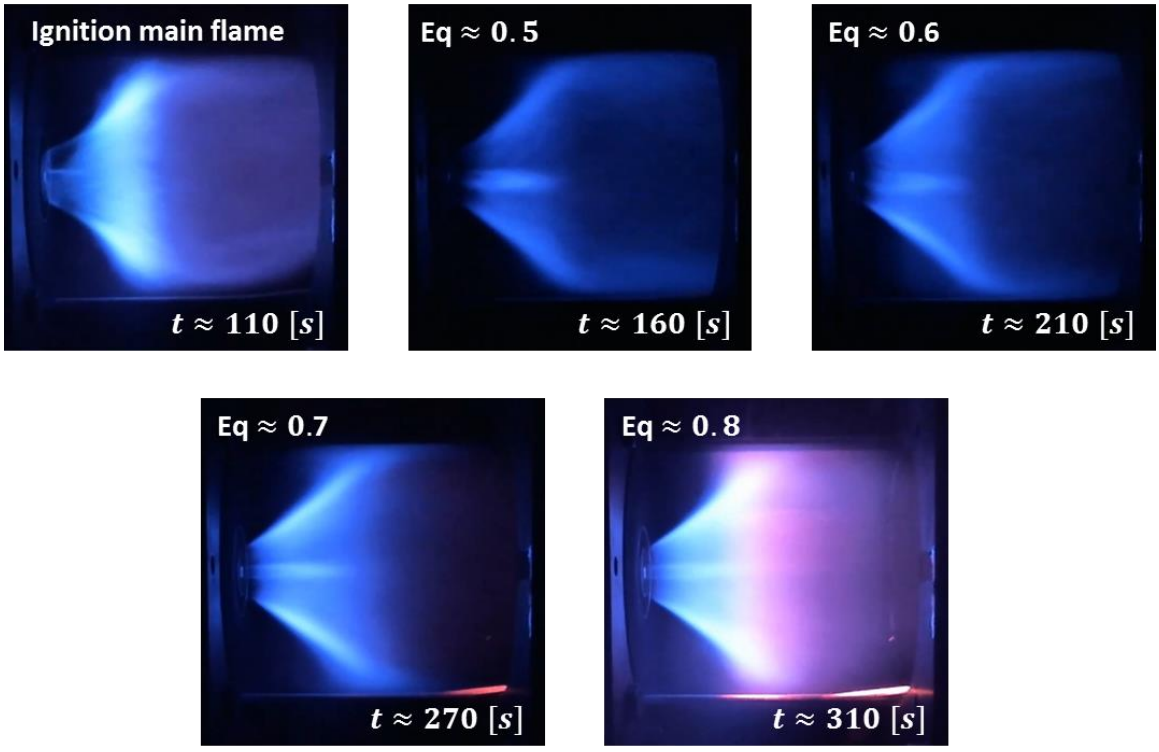


**Figure 89.** Flame photographs at different times throughout the experiment for Reynolds number ~ 12 000 based on combustor inlet conditions.

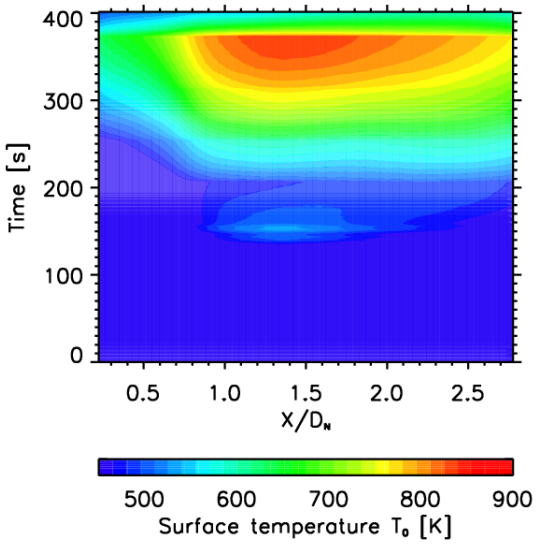


**Figure 90.** Surface temperature throughout the high temperature run for Reynolds number of ~ 12 000. The calibration is only valid for temperatures greater than 450 K and hence the color scale starts at that value.

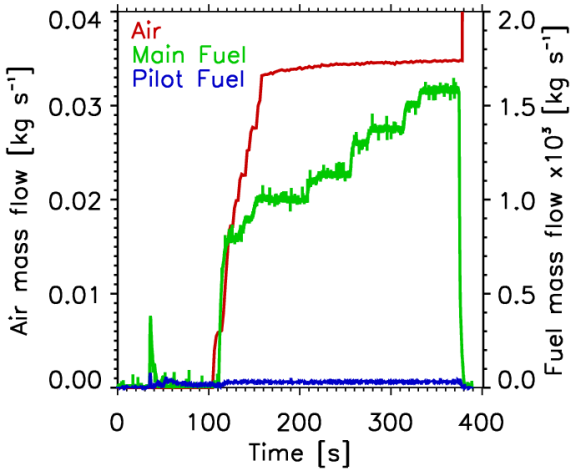


**Figure 91.** Air and fuel mass flows for the high temperature case at $Re_C \approx 12\,000$.

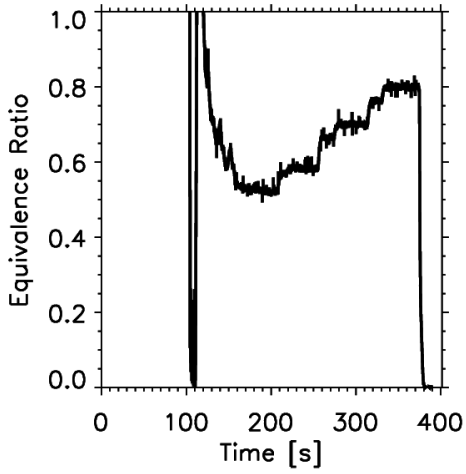


**Figure 92.** Equivalence ratio for the high temperature case at $Re_C \approx 12\,000$.

The normalized heat flux (with respect to the total fuel heat release divided by the liner inner surface area) is plotted in Figure 93. High relative heat fluxes were observed starting at $X/D_N \approx 0.8$, extending throughout the length of the liner, between $t = 255$ s to 290 s, matching with times at which the equivalence ratio was raised in the burner. In other words, when the equivalence ratio was raised, the heat flux increased for a short period of time as the liner wall heated up.

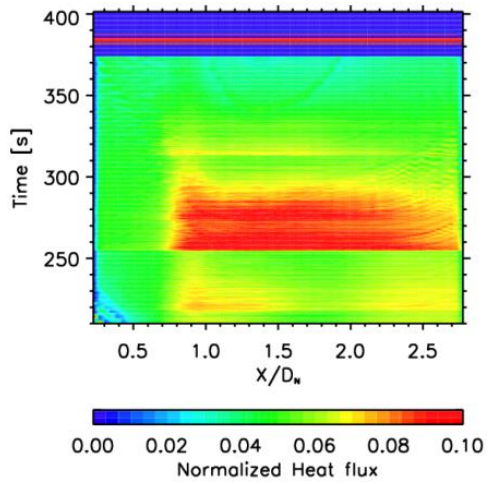


**Figure 93.** Normalized heat flux along the liner with respect to the lower heat of combustion of the fuel introduced divided by the inner surface area of the liner. $Re_C \approx 12\,000$.

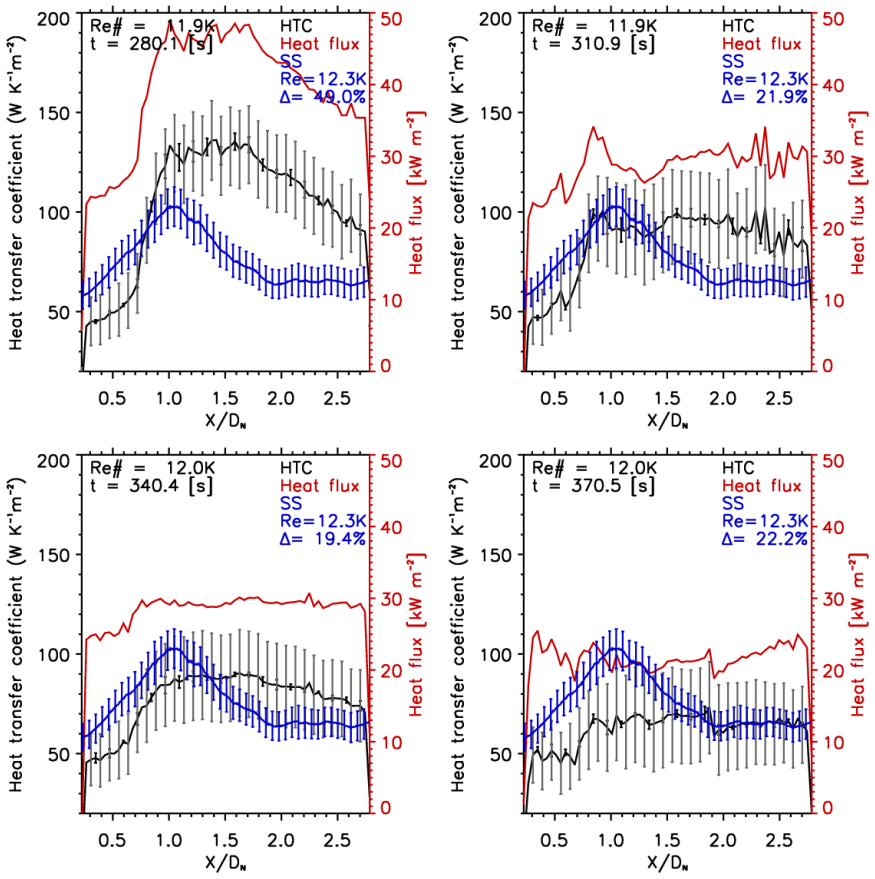


**Figure 94.** Heat transfer and heat flux spatial distribution at different instants in time for the experiment at a Reynolds number of ~ 12 000. The top and bottom row correspond respectively to equivalence ratios of ~ 0.7 and 0.8. The left and right column represent the time when the equivalence ratio was first obtained and the moment before the next state in the flame, showing a decrease in the reference heat transfer and heat flux as time progressed.

Without an appropriate flow reference temperature, the heat transfer coefficient calculated is not representative of steady state conditions. In fact, for the results at low wall temperatures (shown in Section 5.1.7), where the heat flux was closer to steady state, the heat transfer coefficients had less than half the magnitude observed in this experiment. The shape of the distribution however is similar as shown in Figure 94, except that the heat transfer coefficient appeared to peak upstream of where the isothermal peak was observed. As will be shown in Section 5.4, when the reacting flow field is briefly described, this may be due to combustion products carried into the corner recirculation.

At the moment of shutdown, the heat flux was on average over 43 kW $m^2$. The observed heat transfer coefficient rapidly converged to the measured shape at isothermal conditions (Figure 95). The air mass flow was increased during shutdown to cool down the liner walls, which resulted in a higher Reynolds number than the baseline during the reacting case. The fact that the shape was consistent with that at isothermal conditions was further evidence of accurate time-dependent heat transfer retrievals by this methodology (it will be even clearer for the higher Reynolds number run, when the air mass flow was not significantly increased during shut down).

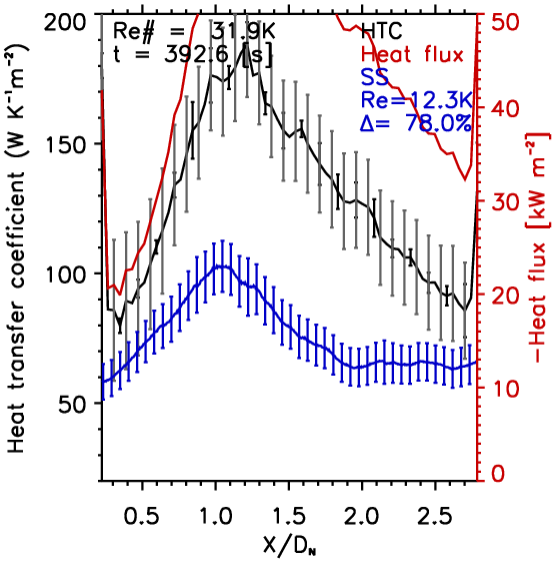


**Figure 95.** Heat transfer coefficient distribution during shutdown, reproducing the isothermal shape obtained. The mismatch in magnitude is due to the Reynolds number during shutdown being 1.8 times higher than the isothermal measurement shown.

### 5.2.1.2 Results for 24 000 Reynolds number

The procedure for this case was the same as that explained in section 5.2.1.1. The progression of flame transitions is shown in Figure 96. An interesting feature in the photographs is the presence of two peaks in high temperature along the liner wall, as seen at $t \approx 420$ s and 450 s. This was also observed with the IR detector and is reflected in the heat transfer coefficient at this Reynolds number.

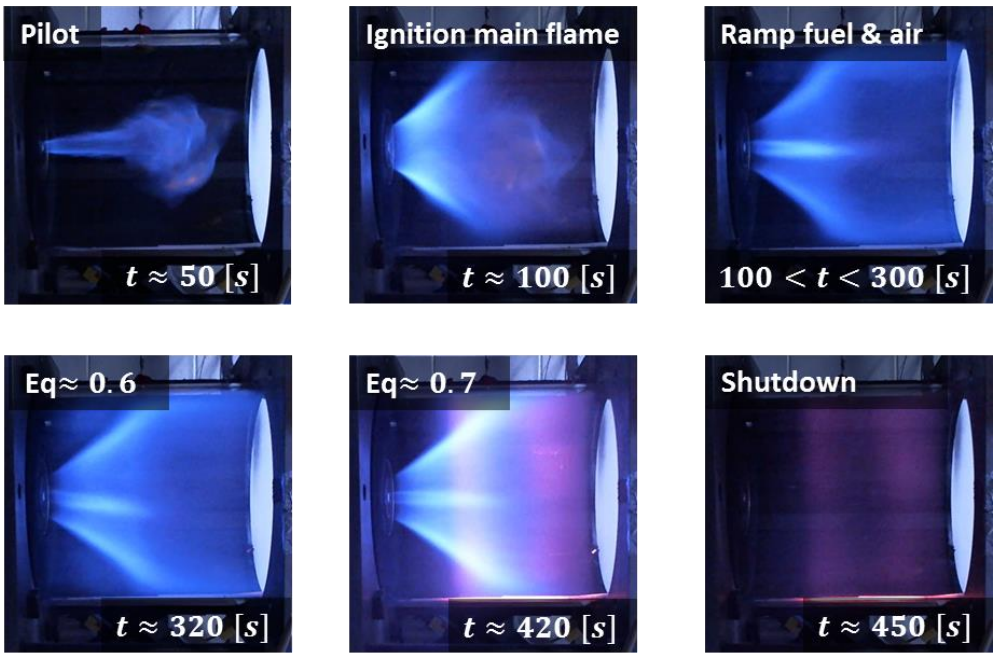


**Figure 96.** Flame photographs at different times throughout the experiment for Reynolds number ~ 24 000 based on combustor inlet conditions.

The liner wall surface temperature is shown in Figure 97, for $t > 300$ s the temperature was above the minimum calibration and only those results were valid. The equivalence ratio and mass flows during the experimental run are plotted in Figure 98 and Figure 99.

Contrary to what was observed for the $\mathrm{Re_C} \approx 12000$ experiment, at this Reynolds number a two peak heat transfer structure was observed. The normalized heat flux contour in Figure 100 shows a peak in heat flux at $X/D_N \approx 0.8$ and another beyond $X = 2.4D_N$, with a minimum heat flux observed at around $X/D_N = 1.75$. This structure suggests that the flame is being quenched at the impingement location and combustion is completed upstream and

downstream of the impingement point. This structure persists beyond $t = 400$ s, as evidenced by the distribution of the heat transfer coefficient at different snapshots shown in Figure 101.

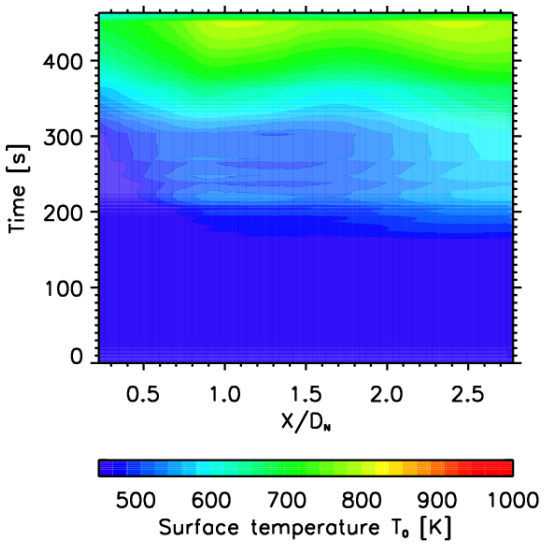


**Figure 97.** Inner wall surface temperature for the reacting experiment at a Reynolds number of ~24 000. Temperature range truncated at 450K, the lower limit measurable when using the KG1 filter.

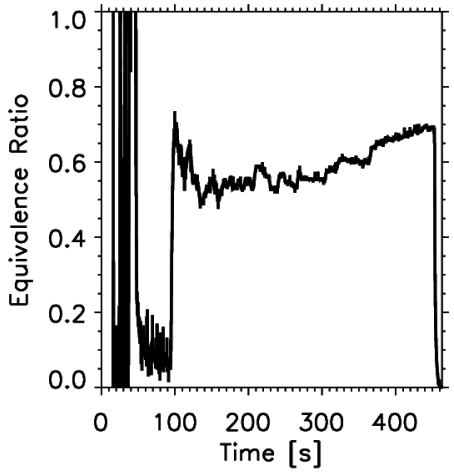


**Figure 98.** Equivalence ratio for the reacting experiment at a Reynolds number of ~ 24 000.

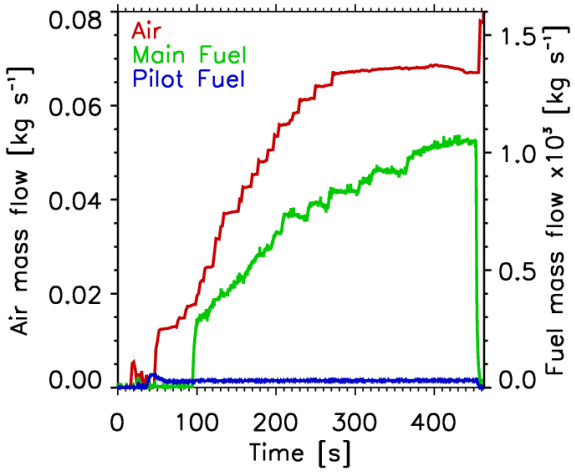


**Figure 99.** Air and fuel mas flows for the reacting experiment at a Reynolds number of ~ 24 000.

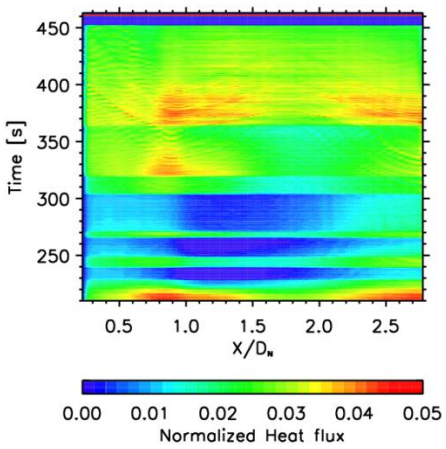


**Figure 100.** Same as Figure 93 for a Reynolds number of ~ 24 000.

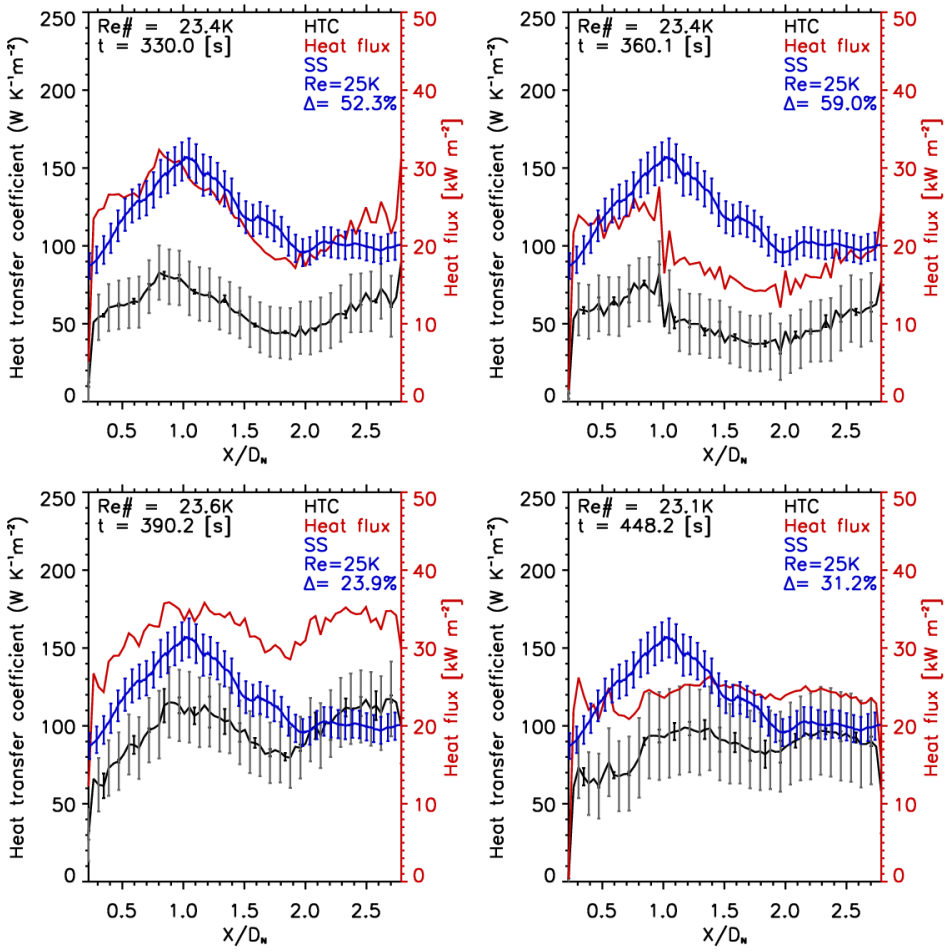


**Figure 101.** Same as Figure 94 for the experiment at a Reynolds number of ~ 24 000.

At shutdown, the heat flux along the liner was on average greater than 43 kW $m^{-2}$. The heat transfer coefficient distribution, rapidly converged to the results at isothermal conditions as shown in Figure 102. This further corroborated that the methodology was robust, reproducing the isothermal result when the wall temperatures were over 700 K and while using the Schott KG1 glass filter.

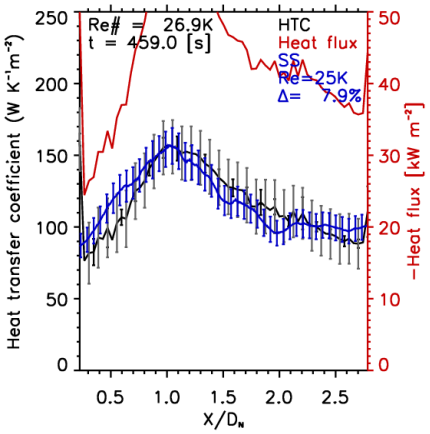


**Figure 102.** Heat transfer coefficient distribution during shutdown, reproducing the isothermal results obtained at approximately the same Reynolds number with respect to the combustor inlet temperature.

### 5.2.2 Effect of the initial conditions

The main disadvantage of using the KG1 Schott glass as a filter was that it did not allow for the measurement of temperatures below 450 K. To capture the time dependence of the heat loads, the methodology developed relied on the complete temperature history of the material (which is not available using the KG1 filter). In order to investigate the effect of the initial condition on the results, the data was processed assuming two initial conditions. Results at these different initial conditions match after an inner wall temperature of 450 K is reached as demonstrated by Figure 103. The reason for this is that regardless of initial condition, after a finite amount of time, the material would reach a pseudo steady-state where the temperature across the material would not be changing significantly. Past this point, the measurements would be accurate. This was verified experimentally in Figure 103 by analyzing the data using two different initial conditions. In one case the temperature of the quartz liner was assumed to be ~ 295 K at all times until the filter minimum temperature threshold was crossed. In the second case, the initial temperature of the quartz liner was maintained at ~ 450 K until the detected signal was equivalent to a higher

temperature. The results are indistinguishable once the wall temperature was above 450 K (Figure 97).

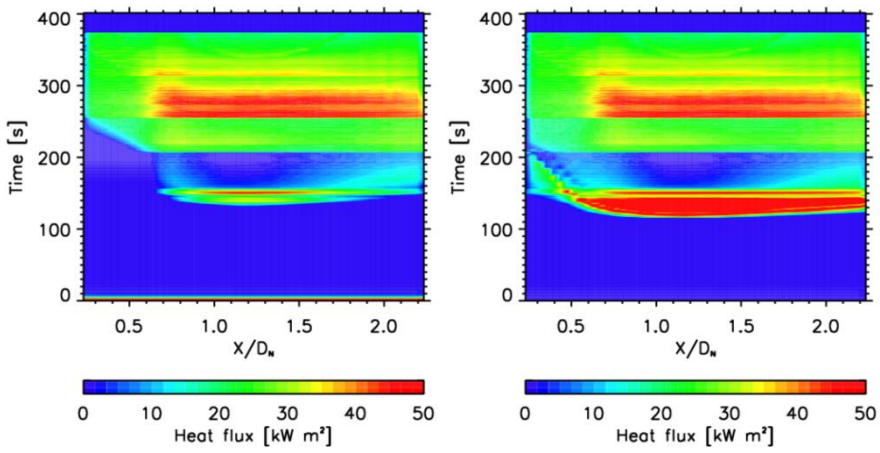


**Figure 103.** Comparison of the heat flux results from the finite difference methodology using two different initial conditions. No sensitivity to initial conditions once the minimum calibration temperature is reached.

## 5.3 FLAME IMAGING TO STUDY FLAME SHAPE

The initial attempt to study the flame structure and dynamics was done by looking at images of the flame. A picture of the combustor during operation for an inlet air mass flow of 0.034 kg/s (0.075lbm/s) and equivalence ratio of 0.7 (2% of the total fuel mass flow going through the pilot for flame stability) is shown in Figure 104. The pilot flame was barely visible, with a clear image of the high intensity flame formed by the exiting premixed swirling jets. A shape of the flame structure was conical. To qualitatively characterize the flame envelope and relate it to the isothermal velocity field (measured in Chapter 4), images of the flame with the Flowsense 4M MKII camera were taken.

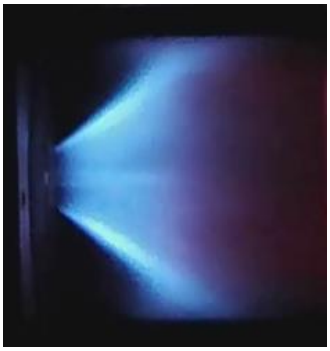

**Figure 104.** Operational research combustor. The pilot flame is barely visible along the axis of the combustor, the main flame is conical and impinges on the combustor wall.

A total of 200 images of the flame were acquired and the average normalized intensity (normalized against the detector maximum pixel intensity) is shown in Figure 105. The images represent a line of sight average as the depth of view was large (aperture was small to prevent saturating the camera sensor). The radiation intensity is an arbitrary quantity but gives a qualitative idea of the flame location. A strong asymmetry of the flame was observed, with the intensity at $Y/D_N < 0$ broadening around $X/D_N = 1.5$, this could point to uneven fuel distribution or an asymmetric flow field. The standard deviation for the pixel intensity, normalized in the same way as the mean averages, shows that there is high absolute variation along the flame outer edge and at the pilot location (Figure 106). The flame also appeared to liftoff from the dome plate, with the flame emission intensity being significant only after $X/D_N$ between 0.15 and 0.25.

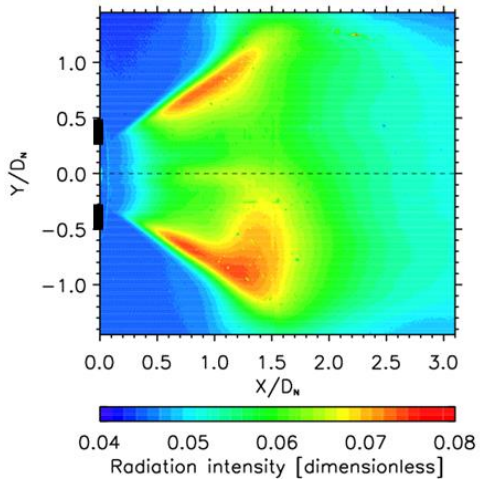


**Figure 105.** Time averaged intensity for the recorded flame images (normalized with respect to the maximum possible pixel intensity).

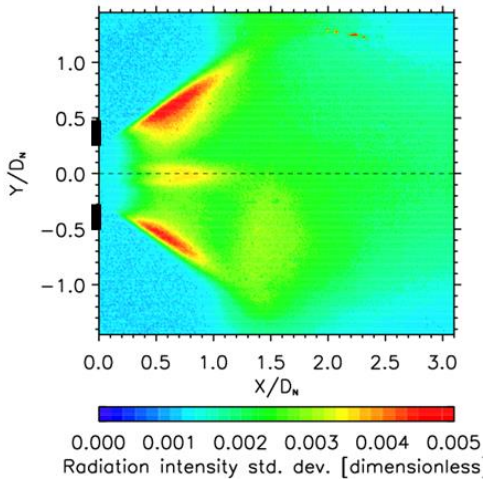


**Figure 106.** Absolute standard deviation for the flame image acquisition normalized as in Figure 105.

Figure 107 shows the normalized $TKE_{2D}$ at isothermal conditions with the location where large vortical structures were observed (along the inner shear layer) and labels for the jet and recirculation. To relate the flame location with this isothermal field, Figure 108 shows the emission intensity from the flame with the shear layer location overlaid (white contour line), and

three contour lines for the normalized $TKE_{2D}$, corresponding to 0.05, 0.1, and 0.15 from dark to light grey respectively.

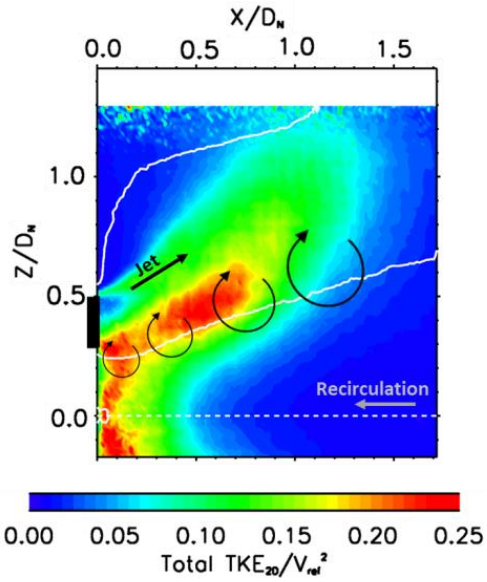


**Figure 107.** Normalized isothermal turbulent kinetic energy as the jet exits the swirl nozzle (from results in Chapter 4). Overlaid are schematics of the vortices forming at the exit of the nozzle as the recirculating flow interacts with the swirling jet.

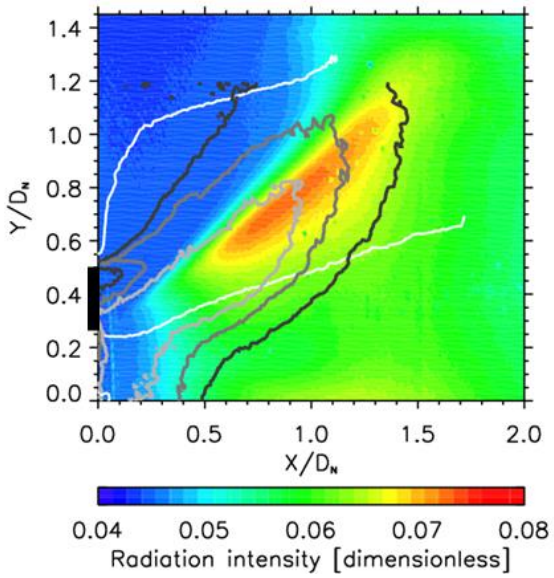


**Figure 108.** Time-averaged intensity with overlaid shear layer and representative contours of turbulent kinetic energy. Shear layer is indicated in white and was defined as the zero axial velocity contour line.

The flame does not follow the location of the shear layers as is often suggested, however it seems to follow the turbulent kinetic energy contour. The data also suggest that the flame variability was aligned with the turbulent kinetic energy contours for the isothermal measurements (Figure 109). High turbulent kinetic energy is indicative of strong mixing. As suggested by these observations, the location where the hot recirculated gases mixed with the fresh incoming mixture was where ignition occurred and where the flame front was established. This is also corroborated with the data from Figure 109, which indicates that the maximum variability in the flame matches the location of maximum time-averaged variability in the isothermal flow field. The agreement observed between the isothermal and reactive cases is only qualitative however.

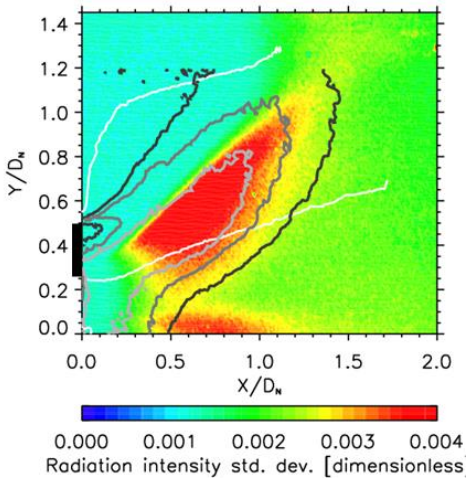


**Figure 109.** Same as Figure 14 for the absolute deviation.

An important distinction between the isothermal and reactive cases is that the isothermal measurements did not include any pilot flow. For the reactive case however, the pilot mass flow corresponds to ~ 0.08% of the total massflow delivered to the burner. Terhaar and coauthors [34] have recently studied the effects of axial air injection on the structure of the central recirculation zone generated by a swirler. Their measurements indicated only small flow field differences in the swirling jets when injecting up to 10% of the flow axially (most of the changes in the flow field were constrained to the central recirculation), for this reason the pilot injection was considered not to have significantly impacted the conical structure. This however may not be the case at higher pilot flowrates, which may distort the central recirculation and impact the expansion of the swirling jets into the primary combustion zone. An expected result of reaction however is that the combustion products and associated gas temperatures will increase the axial flux of axial momentum (conservation of mass), and cause a concurrent decrease in the effective swirl number, S, as defined by Eq. 34. The decrease in the effective swirl number is expected to lead to a weaker central recirculation zone and again a potential shift downstream of the jet impingement location (as the central recirculation becomes smaller).

This measurement is being taken forward by other researchers and is in essence a form of simple chemiluminescence that does not target any particular molecular species. In other words the line of sight emission detected corresponds to several emission lines from the flame and cannot be used to quantitatively identify the flame front or any species concentration. However, the data was successfully related to the isothermal flow field measured in Chapter 4,

demonstrating that the flow characteristics at isothermal conditions may provide information of the flame location and shape.

## 5.4 REACTING PARTICLE IMAGE VELOCIMETRY

Particle image velocimetry was setup in the laboratory and has been used to study the reacting flow field. This however will be fully characterized in future research and only the initial measurements are shown here, highlighting some of the challenges faced. For these measurements, the test section transition piece and exhaust systems were connected, to limit researcher exposure to the fine particles. The test section including the transition piece and quenching systems is described in Chapter 3, no back-pressure systems or pressure vessel were installed. This differs from the heat transfer measurements taken, and future heat transfer measurements will be taken with the closed test section.

A photograph during laser alignment on the test section is shown in Figure 110. A set of photographs during the acquisition, including before and after seed injection, as well as while firing the laser, are shown in Figure 111 (different perspective, from the top). The seed consisted of titanium oxide ($TiO_2$) particles, with a diameter of 1-2μm; introduced into the settling chamber upstream of the nozzle using a cyclone seeder designed in house [152]. The flame is more luminous during injection of seed particles. This is expected due to the emission from the particles at high temperatures. Note that the emission is constrained primarily to the inner shear layer of the exiting jets and the central recirculation zone, consistent with the expected location of the highest temperatures. Since no soot deposits were observed on the optical glass, it is unlikely that the increased emission is due to soot formation when introducing the $TiO_2$ (the seed particles could act as nucleation sites for soot particles).

The increased emission however led to glare issues in the acquired PIV snapshots. A narrowband filter centered around 532 nm (MIDOPT BN532) was used to attempt to isolate the scattered laser light from the flame emission, with acceptable results. There was however still some contamination due to the flame, attributed to either near infrared emission from the flame (the filter does not block wavelengths beyond 1 μm that can still be detected by the CCD camera) or $C_2$ emission (Swan bands) in the 500-550nm wavelength range. Current work in the

test setup includes design and procurement of a filter with a shorter bandpass to obtain more reliable flow data within the flame.

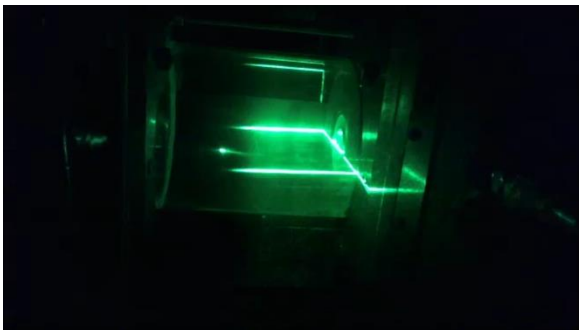

**Figure 110.** Photograph during laser alignment along the combustor center line.

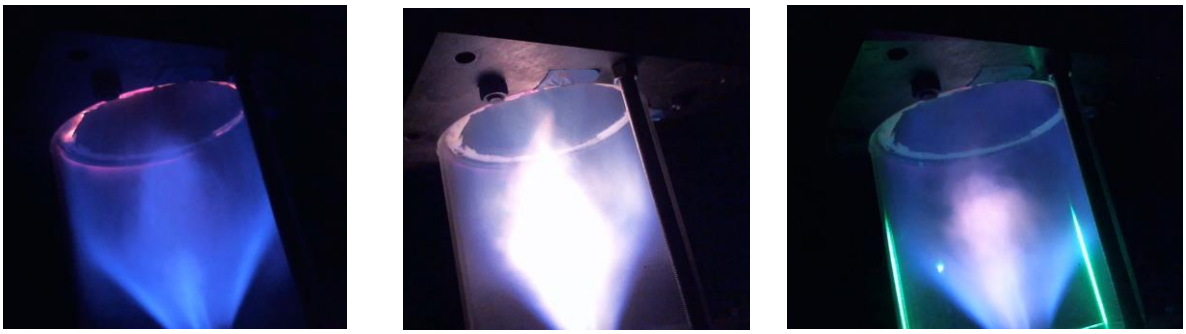

**Figure 111.** Photographs at different stages during the PIV measurement including before injection of seed particles (left), during seed injection (center), and while firing the laser (right).

### 5.4.1 Comparison of closed versus open combustor flow fields

The response time constant for the $TiO_2$ particles following changes in the flow direction and speed due to drag is given by Equation 60 (assuming Stokes flow).

$$\tau_s = d_p^2 \frac{\rho_p}{18\mu} \tag{60}$$

The time delay ($\tau_s$) was of 51 µs, assuming a worst case scenario particle size of 2 µm ($d_p$), a particle density ($\rho_p$) of 4230 kg m$^{-3}$, and an air viscosity ($\mu$) of $1.845 \times 10^{-5}$ kg m$^{-1}$s$^{-1}$. The seeding used in Chapter 4 had a time delay of $\sim 20$ µs and hence was better able to capture the dynamics of the flow. In reaction however, the viscosity of the fluid increases (by a factor of 2 at 800 K), decreasing the time delay.

To investigate any potential changes to the flow introduced by fully closing the test section, isothermal (non-reacting) measurements were taken at the lowest Reynolds number and

compared against the measurements presented in Chapter 4. The results of the non-reacting flow field with a fully closed test section are shown in Figure 112. For comparison, the results from Chapter 4 are shown again in Figure 113. It appears that the impingement location was pushed downstream to $X/D_N \approx 1.4$, compared to $X/D_N \approx 1.2$ observed for the setup with no transition piece. This appears to indicate that the central recirculation became weaker. This is supported by the shift in the inner shear layer closer to the combustor centerline. The velocity magnitudes and overall features however were retained.

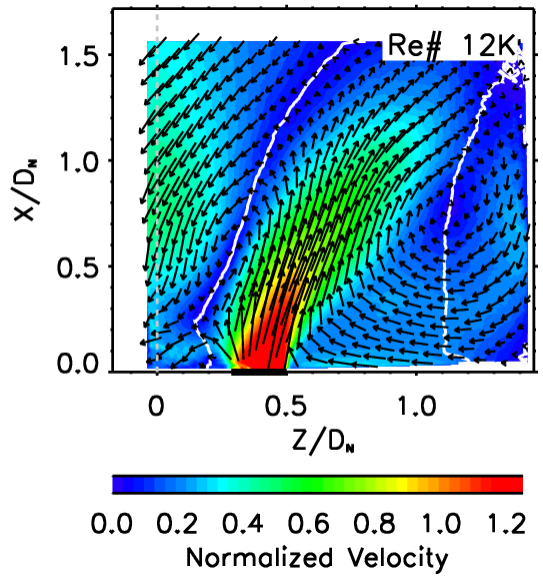


**Figure 112.** Isothermal flow exiting the swirl nozzle for the closed test section using the $TiO_2$ seed particles.

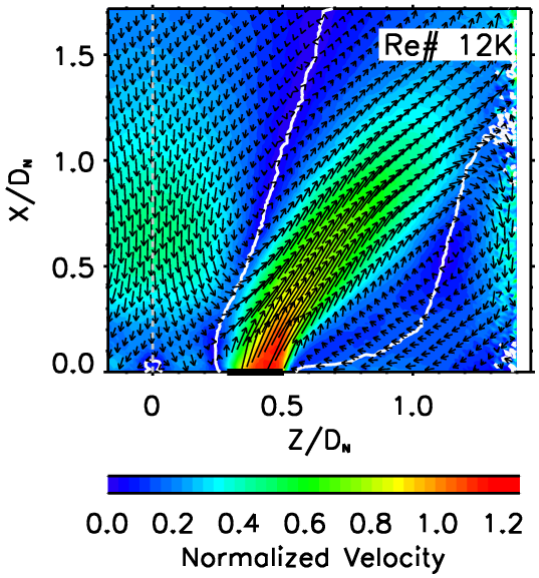


**Figure 113.** Isothermal flow exiting the swirl nozzle for the open test section using the glycol seed particles.

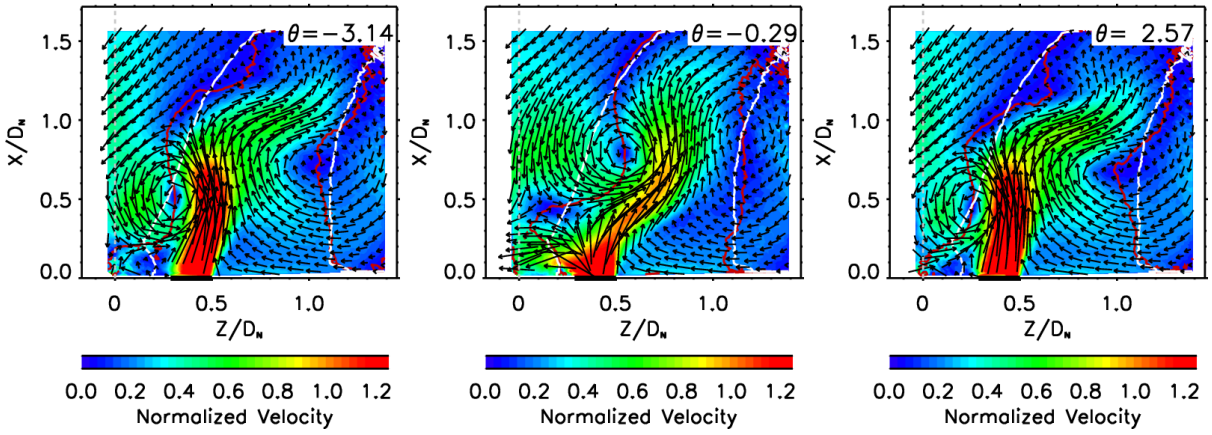


**Figure 114.** Phase results for the axial-radial vortices along the inner shear layer for the closed combustor configuration.

The isothermal dynamics obtained in the closed burner were also investigated, yielding very similar results as those obtained in Chapter 4. Figure 114 shows the results at three different phase angles of the propagating vertical structure along the inner shear layer.

The distribution of the total turbulent kinetic energy was also similar (Figure 115), with the maximum fluctuation energy shifted to the inner shear layer due to the developed axial-radial eddies.

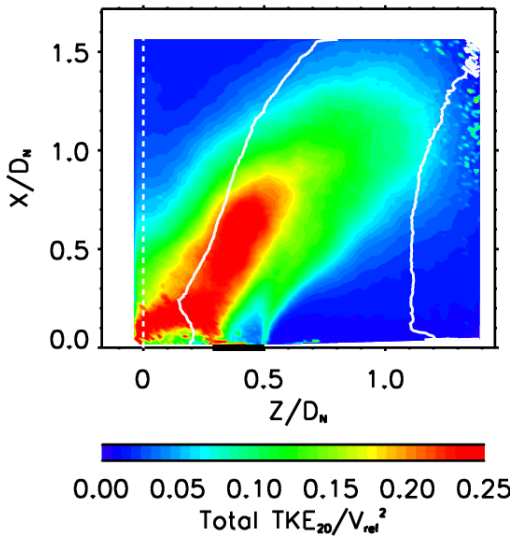


**Figure 115.** Distribution of the total turbulent kinetic energy (total fluctuation including stochastic and coherent flow features) for the closed combustor.

### 5.4.2 Reacting flow field

The time-averaged flow field measured for a combustor Reynolds number of ~ 12 000 (based on air properties at the inlet combustor temperature) is shown in Figure 116. The most salient feature is the pilot flame observed along the centerline of the burner. The data in this region is not accurate because of the difficulty in getting enough seed into the area (only the premixed jets were seeded). The pilot flame generated a second shear layer and the central recirculation occurred between the exiting swirl jet and the pilot flame. The velocity magnitudes along the jet were ~30% higher than observed for isothermal conditions. The angle of the jet however remained almost identical to the isothermal case, with the jet appearing to impact the wall slightly upstream compared to the isothermal condition. Near wall flow measurements were

obscured by the glare from the wall (flame+laser), hence identifying the location of flow reattachement on the wall at reacting conditions was not possible.

Another important feature of the time-average flow field was the large velocity magnitudes of the corner recirculation speeds near $X/D_N = 0.7$, implying potential transport of combustion products along the wall. This could partially explain the double peak heat transfer distribution observed at high Reynolds numbers, however further measurements are still required.

The total fluctuation energy normalized with respect to the mean bulk velocity within the nozzle (based on the mass flow supplied) is shown in Figure 117. The distribution is drastically different to that observed isothermally. Given the glare, and lack of available data, the results near the liner wall and in the pilot flame region were unreliable and are not shown. The maximum fluctuation energy was observed along the inner and outer shear layer (equal distribution), suggesting that no significant axial-radial eddies were formed. Given the relationship between the axial-radial eddies and the precessing vortex core (PVC), this results can an indication of the suppression of the PVC. This is possibly associated with the high axial velocities near the centerline of the burner introduced by the pilot flame.

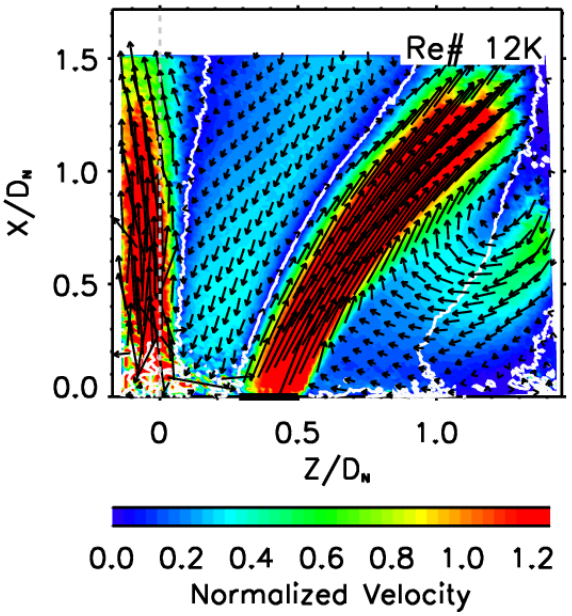


**Figure 116.** Reacting flow field for a combustor inlet Reynolds number of ~ 12 000 and an equivalence ratio of 0.7.

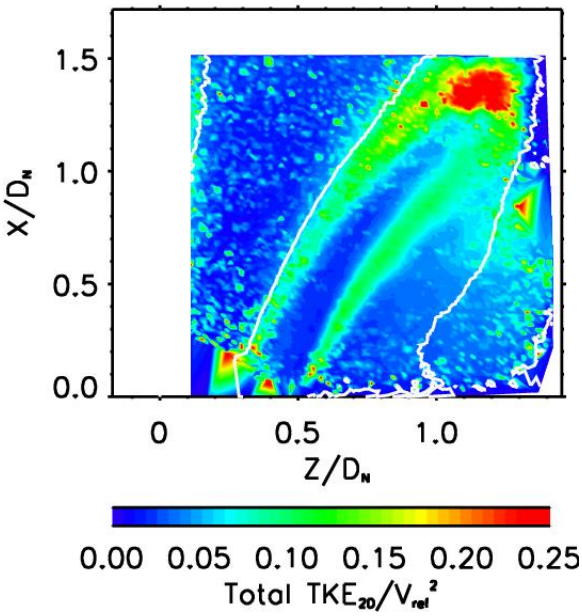


**Figure 117.** Total fluctuation kinetic energy observed for the reacting combustor with an inlet Reynolds number of ~ 12 000 and an equivalence ratio of 0.7.

This is however only a small sample of data and further work will be performed to improve and expand the dataset. Flow field data is critical as part of the continued research efforts to understand the reacting flow field and relate it to the heat transfer characteristics observed

## 5.5 CONCLUSIONS

The main objective of this chapter was to describe the development of the measurement technique for combustor heat loads at reacting conditions. Given the prohibitively high fuel costs of running steady state experiments, a transient measurement method was designed. The measurement relied on the acquisition of the inner and outer surface temperatures of the liner wall, and using these data to estimate the heat flux from the gas to the liner. The heat flux was calculated using a time-accurate finite difference code, using the surface temperature acquisitions as the boundary conditions.

The methodology was first validated at isothermal conditions, by comparing an experiment with variable heat transfer to the steady state results obtained in Chapter 4. The results in the time dependent heat transfer experiment differed from the steady state measurements by 3.0 to 17.3% depending on the mass flow case. Once the methodology was validated it was applied to a reacting combustor case. The peak heat load was shifted downstream by $0.2D_N$ in reaction compared to isothermal conditions. Moreover, contrary to the isothermal heat transfer coefficient, which quickly decreased downstream of the impingement location, the reacting peak heat load decreased slowly downstream. These initial results were performed at low wall temperatures, limited by the maximum temperature that the IR detector could measure.

To overcome the temperature limit imposed by the saturation of the IR camera, an optical filter (Schott KG1 glass) was used. An additional benefit of this filter was that it almost entirely blocked the emission from the quartz material making the temperature measurement of the inner and outer surfaces of the liner more robust (not dependent on the liner temperature). Two measurements at two different Reynolds numbers ($\sim 12\,000$ and $\sim 24\,000$) were taken to verify the performance of the technique using the Schott KG1 filter glass. The results yielded a

two peak heat transfer structure for the higher Reynolds number, which was associated with the quenching of the combustion reaction at the location where the jet impinged on the wall.

To further support the heat transfer measurements, initial reacting flow measurements were presented. The reacting flow field was still a work in progress at the time of writing and will be the topic of investigation of future students. Representative results for a Reynolds number of $\sim 12\,000$ were included to show that the milestone of reacting flow field measurements had been achieved (part of the objectives for this portion of the project). The flow field showed that the pilot flame had a significant impact on the central recirculation zone dynamics. The annular swirl jet velocity magnitudes were higher by $\sim 30\%$ compared to the isothermal flow field, attributed to the gas expansion across the flame front.

It is important to note that the reacting heat load presented includes the contribution due to both radiation and convection. In the same way, the heat transfer coefficient reported is in fact an effective heat transfer coefficient which also includes the radiative load. For the current conditions (atmospheric pressure and lean equivalence ratios), the radiative heat load is estimated to be small. Flame impingement studies at similar conditions have reported a radiative contribution to the total heat load $< 10\%$ [97,98]. Per the correlations given by Lefebvre and Ballal [12], the estimated radiative heat load to the liner (at atmospheric conditions and design mass flows) was 14% of the total.

The heat transfer measurements presented in this chapter highlighted the importance of selecting an appropriate reference temperature for the gas, which is not trivially defined for reacting flows. This motivates the pursuit of a full understanding of the temperature field within the burner, to properly define the gas temperature driving the heat loads to the wall.

## 5.6 NOMENCLATURE

| | |
|---|---|
| A | Area[$m^2$] |
| $B_\lambda$ | Spectral radiance from Planck's Law [W $m^{-3}$ $sr^{-1}$] |
| c | Speed of light [299 792 458 m $s^{-1}$] |
| $C_P$ | Specific heat at constant pressure |
| $D$ | Diameter [m] |
| $G_X$ | Axial flux of axial momentum [N] |

$G_\phi$ Axial flux of tangential momentum [N]

$h$ Heat transfer coefficient [W $m^{-2}$ $K^{-1}$]

$h_P$ Planck's constant [$6.62607004 \times 10^{-34}$ $m^2$ kg / s]

IR Infrared

$ii$ Total number of axial nodes

$kk$ Total number of radial nodes

$K_B$ Boltzmann constant [$1.38064852 \times 10^{-23}$ $m^2$ kg $s^{-2}$ $K^{-1}$]

$\dot{m}$ Mass flow (air) [kg $s^{-1}$]

Nu Nusselt number

$nn$ Total number of time steps

$r$ Radial dimension along with origin at the combustor axis.

R Combustor primary zone radius [m] or radiance [W $m^{-2}$ $sr^{-1}$]

S Swirl number

Re Reynolds number

$T$ Temperature [K]

$t$ Time [s]

$Q''$ Heat flux [W $m^{-2}$]

X, x Axial dimension along the axis of the combustor.

$\Delta$ Step size (can refer to axial, radial or time steps)

$a$ Absorptance

$\epsilon$ Emittance

$\gamma$ Thermal conductivity

$\rho$ Density

$\sigma$ Error

$\tau$ Transmittance

$\tau_S$ Time delay for seed particles

$\mu$ Dynamic viscosity [kg $m^{-1}$ $s^{-1}$]

$\nu$ Kinematic viscosity [$m^2$ $s^{-1}$]

**Subscripts**

C Refers to the combustor primary zone

| | |
|---|---|
| F | Refers to the any filter. |
| IR | Refers to temperatures acquired through the Infrared camera. |
| $i$ | Axial node index |
| $k$ | Radial node index |
| LOSS | Refers to losses |
| L,I | Liner, inner surface |
| L,O | Liner, outer surface |
| N | Refers to the nozzle (diameter) |
| $n$ | Time step index |
| p | Refers to the seed particles |
| TC | Refers to temperatures obtained from thermocouples |
| Q | Refers to the quartz liner itself (not the surfaces) |
| W | Refers to the liner wall |
| $\infty$ | Refers to the working fluid/gas |
| $\lambda$ | Spectral (varies with wavelength) |

# CHAPTER 6.

# CONCLUSIONS

These are exciting times for the research combustor facility constructed, as it is finally operational. What was included in this dissertation only represents a small portion of the fascinating research that can be carried out with a fully operation optical burner. The main contributions of this work were the construction of a fully operational research combustor facility and the development of methodologies to study heat transfer in reacting environments, specifically within gas turbine combustors. The problem was not solved in its entirety; particularly, the distribution of the working gas temperature is still an important aspect that was not tackled. To understand heat transfer, the temperature potential driving the energy flux to a wall must be known. The methods and ideas in this work can be used to calculate the heat flux to a surface and measure only one of the components of the temperature potential, namely the surface temperature. This work highlighted the critical need to understand the other component, the reference gas temperature, in order to characterize reacting heat transfer coefficients. An innovation of the presented work was the use of Schott KG glasses to filter out the thermal emission from fused silica (quartz) windows, allowing for high temperature measurements through optical quartz with an infrared (IR) camera (spectral range above 1μm). This is important to study combustors and other high temperature reactors given the benefits of quartz for optical access including its inexpensive cost (relative to other traditional IR window materials such as Zinc Selenide), ease of manufacture into different shapes, and excellent handling of thermal shock and high temperatures (up to ~1300 K).

Isothermal (non-reacting) heat transfer coefficients in an annular combustor at ambient conditions were first investigated, continuing the work by [54, 56, 111, 153-156]. The two dimensional distribution of heat transfer along the inner and outer liner walls were characterized and Particle Image Velocimetry (PIV) was used to study the flow field within the combustor model. This work allowed for the investigation of secondary flow effects on the distribution of the heat transfer along the liner, both due to the annular walls and the spent coolant exiting the dome cooling systems. The secondary flow along the annular walls led to an asymmetry in the heat transfer characteristics between the inner and outer combustor walls. The spent coolant from

the dome cooling on the other hand shifted the location of peak heat transfer downstream. An additional study on the performance of a dome cooling system was also carried out, showing that typical correlations for impingement cooling may not accurately reproduce the overall heat transfer of industrial impingement arrays.

These measurements were an important starting point for the implementation and development of experimental methods that could be applicable to an optical combustor. While these initial measurements provided insight into how the fluid dynamics within combustors relate to the liner heat transfer, these combustor models could not account for the effects introduced by combustion. To take the characterization of combustor heat transfer forward, a realistic gas turbine combustor facility was designed and constructed. The facility was designed to operate at 120 PSIG, but due to time and budget constraints, current operation was limited to near atmospheric pressure. The burner was equipped with an industrial fuel nozzle provided by Solar Turbines Incorporated, the SoLoNOx nozzle, a lean premixed low emission fuel injector system. A preheater upstream of the combustor test section was capable of increasing the temperature up to 700 K, and the air flow systems could throttle the air mass flow to $\sim$ 1.3 kg $s^{-1}$ at all operating pressures. The system was designed to accurately control and meter the air and fuel introduced into the system.

The non-reacting characteristics of the optical burner were first investigated. The fluid dynamics showed the presence of periodic coherent oscillations in the flow associated with the precessing vortex core (PVC – a well known oscillation in lean premixed burners). The coherent turbulence accounted for over 30% of the total fluctuation kinetic energy along the inner shear layer. No dominant coherent structures were identified after the point where the swirling jet impinged on the liner wall. The flow was shown to be anisotropic, primarily due to the development of the coherent vortices. The isothermal steady state heat transfer results on the other hand were symmetric, with less than 1.5% circumferential variability, despite the asymmetries in the flow. The heat transfer results showed that correlations for fully developed turbulent pipe flow approximately capture the scaling of the results with Reynolds number (relatively constant augmentation). The optical combustor isothermal steady state heat transfer measurements were compared against the results from Chapter 2, yielding an average difference of 6.1% for the maximum observed heat transfer along the can and annular liners. The

measurements however, highlighted the need for systematic studies at different swirl numbers and combustor expansion ratios to properly correlate the results from different experiments.

After characterizing the isothermal steady state heat transfer, a methodology was developed to calculate the time-dependent heat flux to the liner wall, in order to characterize the changing heat loads on the combustor walls during reaction. The methodology developed relied on the simultaneous acquisition of the inner and outer surface temperatures of the liner, which were input into a numerical conduction code to estimate the heat flux to the wall. The steady state isothermal heat transfer measurements were then used to validate the methodology developed, by running non-reacting cases with a time-dependent flow temperature (ramp). The results from the time-dependent non-reacting experiments differed from the steady state experiments by 3%-17.3%, within the experimental uncertainties of both measurements. The two measurements were entirely independent and relied on different methodologies.

The validated heat transfer methodology was applied to a reacting experiment at an equivalence ratio close to 0.5, and a Reynolds number (with respect to the combustor diameter) of $\sim 12\,000$. The results showed that the peak heat load shifted downstream by $0.2D_N$. Contrary to the isothermal heat transfer coefficient, which quickly decayed downstream of the peak, the heat load on the reacting combustor decreased slowly.

One of the limitations of the first experiments was that high wall temperatures could not be measured due to saturation of the IR camera used. The Schott KG family of glasses was identified to be able to reduce the radiance received by the IR camera (so that higher temperatures could be measured) and simultaneously block the majority of the fused silica (quartz) radiance. The limitation of these glasses was that while allowing a higher temperature to be measured, lowered temperatures remained inaccessible because the filter radiance dominated. Regardless, reacting measurements were performed with a KG1 glass filter for two combustor Reynolds numbers of $12\,000$ and $24\,000$ at equivalence ratios greater than 0.6. The results showed a two peak heat load structure, particularly for the higher Reynolds number, centered around the location of flame impingement on the wall. It was speculated that this was caused by the cold wall quenching the flame near impingement, with combustion completing both upstream and downstream of the impingement point. PIV in reaction further corroborated the presence of a strong corner recirculation, which could be carrying combustion products downstream from the impingement point.

## 6.1 WHAT LIES AHEAD?

The research presented, while answering some questions regarding combustor heat transfer, has also brought to attention areas where knowledge was limited. There is still a need to continue acquiring data with the methods developed, particularly in reaction. The heat transfer measurements were taken for only short periods of time and for a limited set of conditions. Allowing the burner to stabilize will yield non-changing reacting heat transfer coefficients that can then be better compared, analyzed, and correlated.

The heat transfer methodologies and the use of the Schott KG glasses as filters can be used to study other high temperature environments. For instance, using the filter proposed, the temperatures within a turbine cascade with optical access can be studied. The heat transfer methodology can be applied in other systems where the symmetric assumption is valid, for instance to study other combustor geometries, or flame heat transfer. Even when the symmetry assumption is not satisfied, the inner and outer surface temperatures can be recorded by looking at discrete locations, alternating between the inner and outer surface, evenly distributed throughout the wall.

An advantage of the method that was not explored in the current study is that it also provides information on the back (coolant) side of the liner. Just as the temperature gradients are used to estimate the heat flux at the inner surface, the temperature gradients on the coolant side wall can be used to simultaneously study the heat transfer rate to the coolant (that is if the coolant side heat transfer distribution is also axisymmetric). This will be particularly important once cooling for the liner is operational (as described in Chapter 3).

Another important aspect brought up by these results is the need to develop methods to measure the gas temperature within the burner to characterize the temperature potential driving the heat transfer. One promising technology that can be used to accomplish this is thermographic phosphors (TPs) [80]. TPs have already been used to obtain planar temperature profiles for low temperature gases by seeding the TP particles into the flow and using a laser sheet to excite the particles [157]. The PIV setup in the laboratory already includes the laser and seeding mechanisms, and TP technology could potentially be quickly implemented to acquire temperature maps. Alternatively, the IR camera with the Schott KG1 glass filter can be used to directly image the emission from the flame through the quartz liner. The radiance detected can

then be used with an effective emissivity to calculate the temperature. An issue with the latter idea is that it would correspond to a line of sight measurement. As has been observed for the mean flow field, one may presume that the time-averaged temperature field will be axisymmetric. If this is the case, the line of sight data can be transformed to yield the equivalent planar time-averaged temperature field within the burner (inverse Abel transformation). If the flame emissivity is too low at the IR wavelengths of interest, the flow can be seeded with high emissivity particles (to emulate black body radiation, as occurs during soot formation). While these measurements are doable, one of the main challenges for these techniques will be the accurate calibration of the measurement at high temperatures.

Simple cooling features can also be studied with the quartz glass liner by machining holes into the fused silica cylinder. The heat transfer methodology however, can be combined with the ideas presented by Rippe and Lattimer [92] to obtain heat transfer in metal liners, which then would allow for more flexibility in terms of cooling features. Finally, studying stability of the flame and pollutant formation may also be important areas of research that are possible within the optical research combustor.

There are several opportunities for interesting research in the optical research combustor developed. Not to mention the flexibility in the design to incorporate other nozzles, other combustor geometries, or attachments downstream. While the problem has not been fully solved, the work presented here has hopefully provided some insight into the challenges and possible methods to characterize heat transfer within gas turbine combustors and other high temperature environments.

# REFERENCES


[1] Saravanamuttoo, H.I.H., Rogers, G.F.C., and Cohen H., 2001, *Gas Turbine Theory*, 5th ed., Pearson Education Limited. ISBN-10: 0-13-015847-X.

[2] Han, J.C., Dutta, S. and Ekkad, S., 2012. *Gas turbine heat transfer and cooling technology*. CRC Press.

[3] Price, J.R., 2009, "Advanced Materials For Mercury 50 Gas Turbine Combustion System". Final Report submitted to U.S. Department of Energy, under Federal Contract DE-FC26-00CH11049.

[4] Nelson, W.A. and Orenstein, R.M., 1997. TBC experience in land-based gas turbines. *Journal of Thermal Spray Technology*, *6*(2), pp.176-180.

[5] Miriyala, N., Fahme, A. and van Roode, M., 2001, June. Ceramic Stationary Gas Turbine Program: Combustor Liner Development Summary. In *ASME Turbo Expo 2001: Power for Land, Sea, and Air* (pp. V004T02A009-V004T02A009). American Society of Mechanical Engineers.

[6] Corman, G.S., Dean, A.J., Brabetz, S., Brun, M.K., Luthra, K.L., Tognarelli, L. and Pecchioli, M., 2000, May. Rig and engine testing of melt infiltrated ceramic composites for combustor and shroud applications. In *ASME Turbo Expo 2000: Power for Land, Sea, and Air* (pp. V004T02A019-V004T02A019). American Society of Mechanical Engineers.

[7] Bradshaw, S. and Waitz, I., 2009. Impact of manufacturing variability on combustor liner durability. *Journal of Engineering for gas turbines and Power*, *131*(3), p.032503.

[8] Kim, K.M., Yun, N., Jeon, Y.H., Lee, D.H. and Cho, H.H., 2010. Failure analysis in after shell section of gas turbine combustion liner under base-load operation. *Engineering Failure Analysis*, *17*(4), pp.848-856.

[9] Tinga, T., Van Kampen, J.F., De Jager, B. and Kok, J.B., 2007. Gas turbine combustor liner life assessment using a combined fluid/structural approach. *Journal of Engineering for Gas Turbines and Power*, *129*(1), pp.69-79.

[10] Carter, T.J., 2005. Common failures in gas turbine blades. *Engineering Failure Analysis*, *12*(2), pp.237-247.

[11] Correa, S.M., 1993. A review of NOx formation under gas-turbine combustion conditions. *Combustion science and technology*, *87*(1-6), pp.329-362.

[12] Lefebvre A. H., and Ballal D. R., 2010, Gas Turbine Combustion, Alternative Fuels and Emissions, 3rd ed., CRC press, FL, USA.

[13] Mellor, A.M., 1990. *Design of modern turbine combustors*. Academic Pr.

[14] Image by Jeff Dahl. https://en.wikipedia.org/wiki/Turbojet#/media/File:Jet_engine.svg

[15] Photo by Oliver Cleynen, https://en.wikipedia.org/wiki/Combustor#/media/File:Combustor_on_Rolls-Royce_Nene_turbojet_%281%29.jpg

[16] Cowell, L., 2001, "Proven Solution Solar", Solar presentation in CORE Symposium.

[17] Environmental Protection Agency (EPA), 2006, "40 CFD Part 60, Standards of Performance for Stationary Combustion Turbines; Final Rule," *Federal Register,* 71:38482-38506.

[18] Kurz, R., Brun, K., Meher-Homji, C. and Moore, J., 2012. Gas turbine performance and maintenance. In *41st Turbomachinery Symposium, Houston, TX, Sept* (pp. 24-27).

[19] Huang, Y., and Yang, V., 2009, "Dynamics and stability of lean-premixed swirl-stabilitzed combustion," Progress in Energy and Combustion Science, 35, pp. 293-364.

[20] Lilley, D., 1977, "Swirl Flows in Combustion: A Review,"AIAA Journal, 15, No.8, pp. 1063–1078.

[21] Beer, J.M., and Chigier, N.A., 1983, "Combustion Aerodynamics," Robert E. Krieger Publishing Company, Fl, USA.

[22] Syred, N., and Beer, J.M., 1974, "Combustion in Swirling Flows: A Review,"Combustion and Flame, No.23, pp. 143-201.

[23] Gupta, A.K., Lilley, D.G., and Syred, N., 1984, "Swirl Flows," Abacus Press, MA, USA.

[24] Sloan, D., Smith, P.J., and Smoot, D., "Modeling of swirl in turbulent flow systems,", Progress in Energy and Combustion Science, Vol. 12, No.3, pp. 163-250. DOI:10.1016/0360-1285(86)90016-X

[25] Hill, P.G., and Peterson, C.R., 1992, Mechanics and Thermodynamics of Propulsion, 2nd ed., Prentice Hall.

[26] Lieuwen, T.C., 2012, Unsteady Combustor Physics, 1st ed., Cambridge University press, NY, USA.

[27] Lucca-Negro, O., and O'Doherty, T., 2001, "Vortex Breakdown: a review,"Progress in Energy and Combustion Science, No.27, pp. 431-481.

[28] Syred, N., 2006, “A review of oscillation mechanisms and the role of the precessing vortex core (PVC) in swirl combustion systems,” Progress in Energy and Combustion Science, No.32, pp. 93-161.

[29] Leibovich, S., 1984, “Vortex Stability and Breakdown: Survey and Extension,” AIAA Journal, Vol. 22, No.9, pp. 1192-1206.

[30] Faler, J.H., and Leibovich, S., 1977, “Disrupted states of vortex flow and vortex breakdown,” Physics of Fluids, Vol. 20, No.9, pp. 1385-1400. DOI: 10.1063/1.862033

[31] Kilik, E., 1976, "The influence of swirler design parameters on the aerodynamics of downstream recirculation region" (Doctoral Dissertation), Cranfield University.

[32] Farokhi S., Taghavi R., and Rice E.J., 1989, "The effect of initial swirl distribution on the evolution of a turbulent jet," AIAA Journal, Vol. 27, No. 6. DOI: 10.2514/3.10168

[33] Hallet, W.L.H., and Toews, D.J., 1987, "The effects of inlet conditions and expansion ratio on the onset of flow reversal in swirling flow in a sudden expansion", Experiments in Fluids, Vol. 5, No.2, pp. 129-133.

[34] Terhaar, S., Reichel, T.G., Schrodinger, C., Rukes, L., Paschereit, C.O., and Oberleithner, K., 2015, “Vortex Breakdown Types and Global Modes in Swirling Combustor Flows with Axial Injection,”Journal of Propulsion and Power, 31, No.1, pp.219-229.

[35] Carmack, A., Ekkad, S., Kim, Y., Moon, H.-K., Srinivasan, R., 2013, “Comparison of Flow and Heat Transfer Distributions in a Can Combustor for Radial and Axial Swirlers Under Cold Flow Conditions,” Journal of Thermal Science and Engineering Applications, Vol.5, 031012.

[36] Strakey, P.A., and Yip, M.J., 2007, “Experimental and Numerical Investigation of a Swirl Stabilized Premixed Combustor Under Cold-Flow Conditions,” Transactions of the ASME, Vol. 129, pp. 942-953.

[37] Ji, J., and Gore, J.P., 2002, "Flow structure in lean premixed swirling combustion," Proceedings of the Combustion Institute, Vol. 29, pp. 861-867.

[38] Grinstein, F.F., Young, T.R., Gutmark, E.J., Li, G., Hsiao, G., and Mongia, H.C., 2002 "Flow dynamics in a swirl combustor, " Journal of Turbulence," Vol.3, No. 30.

[39] Lefebvre A. H., and Herbert, M.V., 1960, "Heat-Transfer Processes in Gas-Turbine Combustion Chambers," Proceedings of the Institution of Mechanical Engineers, Vol. 174, No. 1, pp. 463-478. DOI: 10.1243/PIME_PROC_1960_174_039_0

[40] Viskanta, R., and Menguc, M.P., 1987, "Radiation heat transfer in combustion systems", Progress in Energy and Combustion Science, Vol. 13, No. 2, pp. 97-160. DOI: 10.1016/0360-1285(87)90008-6

[41] Viskanta, R., 1993, "Heat Transfer to impinging isothermal gas and flame jets," Experimental Thermal and Fluid Science, Vol. 16, no. 2, pp. 111-134.DOI: 10.1016/0894-1777(93)90022-B

[42] Lefebvre, A.H., 1984. Flame radiation in gas turbine combustion chambers. *International journal of heat and mass transfer*, *27*(9), pp.1493-1510.

[43] Burmeister, L.C., 1993, Convective Heat Transfer, 2nd ed., Wiley, ISBN: 047157709X

[44] Lienhard, J.H., and Lienhard, J.H., 2015, A Heat Transfer Textbook, 4th ed., Phlogiston Press, Cambridge, Massachusetts, USA.

[45] Petukhov, B.S., 1970. "Heat transfer and friction in turbulent pipe flow with variable physical properties," Advances in heat transfer, Vol. 6, No. 503, pp 503-564.

[46] Gnielinski, V., 1975. "Neue Gleichungen für den Wärme-und den Stoffübergang in turbulent durchströmten Rohren und Kanälen," Forschung im Ingenieurwesen A, Vol. 41, No. 1, pp.8-16.

[47] Gnielinski, V., 2013. "On heat transfer in tubes. International Journal of Heat and Mass Transfer," 63, pp.134-140.

[48] Sleicher, C.A. and Rouse, M.W., 1975. "A convenient correlation for heat transfer to constant and variable property fluids in turbulent pipe flow," International Journal of Heat and Mass Transfer, Vol. 18 No. 5, pp.677-683.

[49] Dellenback, P.A., Metzger, D.E. and Neitzel, G.P., 1987. "Heat transfer to turbulent swirling flow through a sudden axisymmetric expansion," Journal of heat transfer, Vol. 109, No. 3, pp.613-620.

[50] Yilmaz, M., Comakli, O., Yapici, S. and Sara, O.N., 2003. "Heat transfer and friction characteristics in decaying swirl flow generated by different radial guide vane swirl generators," Energy Conversion and Management, Vol. 44, No. 2, pp.283-300.

[51] Baughn, J.W., Hoffman, M.A., Takahashi, R.K. and Launder, B.E., 1984. "Local heat transfer downstream of an abrupt expansion in a circular channel with constant wall heat flux," Journal of heat transfer, Vol. 106, No. 4, pp.789-796.

[52] Schulz, A., 2001. “Combustor liner cooling technology in scope of reduced pollutant formation and rising thermal efficiencies,” Annals of the New York Academy of Sciences, Vol. 934, No. 1, pp.135-146.

[53] Behrendt, T., Lengyel, T., Hassa, C. and Gerendás, M., 2008. “Characterization of advanced combustor cooling concepts under realistic operating conditions,” In ASME Turbo Expo 2008: Power for Land, Sea, and Air (pp. 1801-1814). American Society of Mechanical Engineers.

[54] Patil, S., Abraham, S., Tafti, D., Ekkad, S., Kim, Y., Dutta, P., Moon, H.K. and Srinivasan, R., 2011. “Experimental and numerical investigation of convective heat transfer in a gas turbine can combustor,” Journal of Turbomachinery, Vol. 133, No. 1, p.011028.

[55] Kedukodi, S., Ekkad, S., Moon, H.K., Kim, Y. and Srinivasan, R., 2015, June. “Numerical Investigation of Effect of Geometry Changes in a Model Combustor on Swirl Dominated Flow and Heat Transfer,” In ASME Turbo Expo 2015: Turbine Technical Conference and Exposition (pp. V05CT17A011-V05CT17A011). American Society of Mechanical Engineers.

[56] Patil, S., Sedalor, T., Tafti, D., Ekkad, S., Kim, Y., Dutta, P., Moon, H.K. and Srinivasan, R., 2011. “Study of flow and convective heat transfer in a simulated scaled up low emission annular combustor,” Journal of Thermal Science and Engineering Applications, Vol. 3, No. 3, p.031010.

[57] Gomez-Ramirez, D., Dilip, D., Ravi, B.V., Deshpande, S., Pandit, J., Ekkad, S.V., Moon, H.K., Kim, Y. and Srinivasan, R., 2015. “Combustor Heat Shield Impingement Cooling and its Effect on Liner Convective Heat Transfer for a Model Annular Combustor With Radial Swirlers,” In ASME Turbo Expo 2015: Turbine Technical Conference and Exposition (pp. V05CT17A010-V05CT17A010). American Society of Mechanical Engineers.

[58] Andreini, A., Caciolli, G., Facchini, B., Picchi, A. and Turrini, F., 2015. “Experimental investigation of the flow field and the heat transfer on a scaled cooled combustor liner with realistic swirling flow generated by a lean-burn injection system,” Journal of Turbomachinery, Vol. 137, No. 3, p.031012.

[59] Mazzei, L., Andreini, A., Facchini, B. and Turrini, F., 2016. “Impact of Swirl Flow on Combustor Liner Heat Transfer and Cooling: A Numerical Investigation With Hybrid

Reynolds-Averaged Navier Stokes–Large Eddy Simulation Models," Journal of Engineering for Gas Turbines and Power, Vol. 138, No. 5, p.051504.

[60] Faulder, L., Abreu M.E., Srinivasan, R. and Lane, M.A., 2010, Splash plate dome assembly for a turbine engine. US Patent 7,730,725 B2, filed June 8, 2010.

[61] Borns, F.G., and Riahi A., Gas Turbine Combustor Heat Shield Impingement Cooling Baffle. US Patent 6,792,757 B2, filed September 21, 2004.

[62] North, G.L., and Dodds, W.J., Methods and Systems for Cooling Gas Turbine Engine Combustors. US Patent 6,546.733 B2, filed April 15, 2003.

[63] Riahi A., and Borns, F.G., 2004, "Gas Turbine Combustor Heat Shield Impingement Cooling Baffle," ASME Paper No. GT2004-53160. DOI: 10.1115/GT2004-53160

[64] Han, B., and Goldstein, R., 2001, "Jet-Impingement Heat Transfer in Gas Turbine Systems," Ann. N. Y. Acad. Sci., 934, pp. 147–161. DOI: 10.1111/j.1749-6632.2001.tb05849.x

[65] Jambunathan, K., E. Lai, M. A. Moss, and B. L. Button, 1992, "A review of heat transfer data for single circular jet impingement," International Journal of Heat and Fluid Flow 13(2), pp. 106-115. DOI: 10.1016/0142-727X(92)90017-4

[66] Zuckerman, N. and N. Lior, 2005, "Impingement heat transfer: correlations and numerical modeling". Journal of heat transfer, 127(5): pp. 544-552. DOI: 10.1115/1.1861921

[67] Metzger, D. E., L. W. Florschuetz, D. I. Takeuchi, R. D. Behee, and R. A. Berry, 1979, "Heat transfer characteristics for inline and staggered arrays of circular jets with crossflow of spent air." Journal of Heat Transfer 101(3): pp. 526-531. DOI: 10.1115/1.3451022

[68] Ekkad, Srinath V., and David Kontrovitz, 2002, "Jet impingement heat transfer on dimpled target surfaces," International journal of heat and Fluid Flow 23(1):pp. 22-28. DOI: 10.1016/S0142-727X(01)00139-4

[69] Xing, Yunfei, and Bernhard Weigand, 2010 "Experimental investigation of impingement heat transfer on a flat and dimpled plate with different crossflow schemes," International Journal of Heat and Mass Transfer, 53 (19): pp. 3874-3886. DOI: 10.1016/j.ijheatmasstransfer.2010.05.006

[70] Wang, Ting, Mingjie Lin, and Ronald S. Bunker, 2005, "Flow and heat transfer of confined impingement jets cooling using a 3-D transient liquid crystal scheme," International Journal of Heat and Mass Transfer 48 (23): pp. 4887-49

[71] Esposito, E. I., S. V. Ekkad, Yong Kim, and Partha Dutta, 2009, "Novel jet impingement cooling geometry for combustor liner backside cooling," Journal of thermal science and engineering applications, 1(2): pp. 021001. DOI: 10.1115/1.3202799

[72] Liu, Yao-Hsien, Siao-Jhe Song, and Yuan-Hsiang Lo, 2013, "Jet impingement heat transfer on target surfaces with longitudinal and transverse grooves," International Journal of Heat and Mass Transfer 58 (1): pp. 292-299. DOI: 10.1016/j.ijheatmasstransfer.2012.11.042

[73] Hansen, L. G., and B. W. Webb, 1993, "Air jet impingement heat transfer from modified surfaces," International journal of heat and mass transfer, 36(4): pp. 989-997. DOI: 10.1016/S0017-9310(05)80283-2

[74] Spring, S., Lauffer,D., Weigand, B., and Hase, M., 2010, "Experimental and numerical investigation of impingement cooling in a combustor liner heat shield," Journal of Turbomachinery 132(1):pp. 011003. DOI: 10.1115/1.3103924

[75] Luff, J.K., and McGuirk J.J., 2001 “Conjugate Heat Transfer Predictions on a Combustor Heatshield Containing Pedestals,” Proceedings of the RTO AVT Symposium. RTO-MP-069(I).

[76] Ruedel, U., Trbojevic, B., Benz, U., Zajadatz, M. and Doebbeling, K., 2013, June. Development of an Annular Combustor Chamber. In *ASME Turbo Expo 2013: Turbine Technical Conference and Exposition* (pp. V03CT17A009-V03CT17A009). American Society of Mechanical Engineers.

[77] Lörstad, D., Lindholm, A., Pettersson, J., Björkman, M. and Hultmark, I., 2013, June. Siemens SGT-800 industrial gas turbine enhanced to 50MW: Combustor design modifications, validation and operation experience. In *ASME Turbo Expo 2013: Turbine Technical Conference and Exposition* (pp. V01BT04A038-V01BT04A038). American Society of Mechanical Engineers.

[78[ Sen, B.A., Guo, Y., McKinney, R.G., Montanari, F. and Bedford, F.C., 2012, June. Pratt and Whitney gas turbine combustor design using ANSYS fluent and user defined functions. In *ASME Turbo Expo 2012: Turbine Technical Conference and Exposition* (pp. 1547-1556). American Society of Mechanical Engineers.

[79] Lai, M.K., 1997, June. CFD analysis of liquid spray combustion in a gas turbine combustor. In *ASME 1997 International Gas Turbine and Aeroengine Congress and Exhibition* (pp. V002T06A044-V002T06A044). American Society of Mechanical Engineers.

[80] Aldén, M., Omrane, A., Richter, M. and Särner, G., 2011. Thermographic phosphors for thermometry: a survey of combustion applications. *Progress in energy and combustion science*, *37*(4), pp.422-461.

[81] Brübach, J., Hage, M., Janicka, J. and Dreizler, A., 2009. Simultaneous phosphor and CARS thermometry at the wall–gas interface within a combustor. *Proceedings of the combustion institute*, *32*(1), pp.855-861.

[82] Brübach, J., Pflitsch, C., Dreizler, A. and Atakan, B., 2013. On surface temperature measurements with thermographic phosphors: a review. *Progress in Energy and Combustion Science*, *39*(1), pp.37-60.

[83] Feist, J.P., Heyes, A.L., Choy, K.L. and Su, B., 1999. Phosphor thermometry for high temperature gas turbine applications. In *Instrumentation in Aerospace Simulation Facilities, 1999. ICIASF 99. 18th International Congress on* (pp. 6-1). IEEE.

[84] Feist, J.P., Heyes, A.L. and Seefelt, S., 2003. Thermographic phosphor thermometry for film cooling studies in gas turbine combustors. *Proceedings of the Institution of Mechanical Engineers, Part A: Journal of Power and Energy*, *217*(2), pp.193-200.

[85] Borman, G. and Nishiwaki, K., 1987. Internal-combustion engine heat transfer. *Progress in energy and combustion science*, *13*(1), pp.1-46.

[86] Alkidas, A.C. and Myers, J.P., 1982. Transient heat-flux measurements in the combustion chamber of a spark-ignition engine. *Journal of Heat Transfer*, *104*(1), pp.62-67.

[87] Vosen, S.R., Greif, R. and Westbrook, C.K., 1985, December. Unsteady heat transfer during laminar flame quenching. In *Symposium (International) on Combustion* (Vol. 20, No. 1, pp. 75-83). Elsevier.

[88] Vega, T., Wasson, A.R., Lattimer, B.Y., and Diller, T.E., 2015, "Partitioning measurements of convective and radiative heat flux" *International Journal of Heat and Mass Transfer 84, pp.* 827-838.

[89] T.E. Diller, *Heat flux measurement, Ch8, in:* M. Kutz (Ed.), Handbook of Measurement in Science and Engineering, Jon Wiley & Sons, NY, 2013.

[90] Lattimer, B.Y., Vandsburger, U., and Langley, L.W. "Detecting fires using a thin-film heat flux microsensor, in"*ASME Winter Annual Meeting,*Chicago, Illinois, HTD,vol.296 (1994): 137-142.

[91] Frankman, D., Webb, B.W., Butler, B.W., "Time-resolved radiation and convection heat transfer in combusting discontinous fuel beds," *Combust. Sci. Technol. 182,* no10 (2010): 1391-1412.

[92] Rippe, C.M. and Lattimer, B.Y., 2015. Full-field surface heat flux measurement using non-intrusive infrared thermography. *Fire Safety Journal*, *78*, pp.238-250.

[93] Baukal, C.E. and Gebhart, B. "A Review of Flame Impingement Heat Transfer Studies Part 1: Experimental Conditions" *Combustion Science and Technology* 104, no. 4-6 (1995): 339-357. DOI: 10.1080/00102209508907727

[94] Baukal, C.E. and Gebhart, B. "A Review of Flame Impingement Heat Transfer Studies Part 2: Measurements" *Combustion Science and Technology* 104, no. 4-6 (1995): 359-385. DOI: 10.1080/00102209508907728

[95] Baukal, C.E. and Gebhart, B. "A review of empirical flame impingement heat transfer correlations" *International Journal of Heat and Fluid Flow* 17, no. 4 (1996): 386-396.

[96] Viskanta, R. "Heat Transfer to impinging isothermal gas and flame jets" *Experimental Thermal and Fluid Science* 16, no. 2 (1993): 111-134.

[97] Baukal, C.E. and Gebhart, B. "Surface condition effects on flame impingement heat transfer" *Experimental Thermal and Fluid Science* 15, no. 4 (1997): 323-335.

[98] Chander, S. and Ray, A. "Flame Impingement heat transfer: A review" *Energy Conversion and Management 46* (2005): 2803-2837.

[99] Fletcher, T.H., Ma, J., Rigby, J.R., et. al, "Soot in coal combustion systems" *Progress in Energy and Combustion Science 23,* no. 3 (1997): 283-301.

[100]Siegel, R., and Howell, J., *Thermal Radiation Heat Transfer*, 4th ed., Taylor & Francis, New York, NY, 2002, Chap. 11.

[101] Keramida, E.P., Liakos, H.H., Founti, M.A., et. al, "Radiative heat transfer in natural gas-fired furnaces" *International Journal of Heat and Mass Transfer 43,* no. 10 (2000): 1801-1809.

[102] Hindasageri, V., Vedula, R.P., and Prabhu, S.V., "Heat Transfer distribution for impinging methane-air premixed flame jets," *Applied Thermal Engineering.73,* (2014): 461-473.

[103] Gomez, D., Kumar, V., Ekkad, S., Danesh, T., Kim Y.W., Moon H.X., Srinivasan R., "Flow Field and Liner Heat Transfer for a Model Annlar Combustor Equipped with Radial Swirlers," 50th AIAA/ASME/SAE/ASEE Joint Propulsion Conference, July 2014.

[104] Ekkad, S.V., and Han, J.-C., 2000, “A Transient Liquid Crystal Thermography Technique for Gas Turbine Heat Transfer Measurements”. Meas. Sci. Technol. 11: pp. 957-68. DOI: 10.1088/0957-0233/11/7/312

[105] Ireland, P.T. and Jones, T.V. 2000, “Liquid Crystal Measurements of Heat Transfer and Surface Shear Stress”. Meas. Sci. Technol. 11: pp. 969-86. DOI: 10.1088/0957-0233/11/7/313

[106] Kwak, J.S., 2008, "Comparison of Analytical and Superposition Solutions of the Transient Liquid Crystal Technique," Journal of Thermophysics and Heat Transfer, 22 (2): pp. 290-295. DOI: 10.2514/1.34274

[107] Yan, Y., and Owen, M., 2002, “Uncertainties in transient heat transfer measurements with liquid crystal”. Int. Journal of Heat and Fluid Flow, 23: pp. 29-35. DOI: 10.1016/S0142-727X(01)00125-4

[108] Zu, Y., Yan, Y., and Maltson, J., 2009, “CFD prediction for multi- jet impingement heat transfer”. ASME Paper No. GT2009-59488. DOI: 10.1115/GT2009-59488

[109] Sagot, B., et al., 2008, “Jet impingement heat transfer on a flat plate at a constant wall temperature,” International Journal of Thermal Sciences, 47(12): pp. 1610-1619. DOI: 10.1016/j.ijthermalsci.2007.10.020

[110] El-Behery, S.M. and M.H. Hamed, 2009, “A comparative study of turbulence models performance for turbulent flow in a planar asymmetric diffuser,” Proc. World Academy of Science, Eng. Technol, 53: pp. 769-780.

[111] Kumar, V.M., “3D Numerical Simulation to Determine Liner Wall Heat Transfer and Flow through a Radial Swirler of an Annular Combustor,” Master of Science Thesis, Dept. of Mechanical Engineering, Virginia Polytechnic Institute and State University, Blacksburg, VA, 2013.

[112] Martin, H., 1977, “Heat and Mass Transfer Between Impinging Gas Jets and Solid Surfaces,” Adv. Heat Transfer, 13, pp. 1–60.

[113] Obot, N.T., and Trabold, T.A., 1987, “Impingement Heat Transfer Within Arrays of Circular Jets: Part 1 – Effect of Minimum, Intermediate, and Complete Crossflow for Small and Large Spacings”, Journal of Heat Transfer, 109: pp. 872-879. DOI: 10.1115/1.3248197

[114] Kercher, D.M., Tabakoff, W., 1970, “Heat Transfer by a Square Array of Round Air Jets Impinging Perpendicular to a Flat Surface Including the Effect of Spent Air, ” Journal of Engineering for Power, 92 (1): pp. 73-82. DOI: 10.1115/1.3445306

[115] Kline, S.J. and McClintock, F.A., 1953, “Describing Uncertainties in Single Sample Experiments,”Mech. Eng. Am. Soc. Mech. Eng., 75, pp. 3-8.

[116] Sidwell, T., Richards, G., Casleton, K., Straub, D., Maloney, D., Strakey, P., Ferguson, D., Beer, S., and Woodruff, S., 2006, "Optically Accessible Pressurized Research Combustor For Computational Fluid Dynamics Model Validation." AIAA Journal 44 (3).

[117] Strakey, P.A., Woodruff, S., Williams, T.C., and Schefer, R.W., 2008, “OH-Planar Fluorescence Measurements of Pressurized, Hydrogen Premixed Flames in the SimVal Combustor.” AIAA Journal 46 (7).

[118] Cheng, R.K., Littlejohn, D., Strakey, P.A., and Sidwell, T., 2009, “Laboratory Investigations of a Low-Swirl Injector with $H_2$ and $CH_4$ at Gas Turbine Conditions.” Proceedings of the Combustion Institute 32.

[119] Meier, U., Lange, L., Heinze, J., Hassa, C., Sadig, S., and Luff, D., 2015, “Optical Methods for Studies of Self-Excited Oscillations and the Effect of Dampers in a High Pressure Single Sector Combustor”. Journal of Engineering for Gas Turbines and Power 137 (No. 072505).

[120] Behrendt, T., and Hassa, Ch., 2008, “A test rig for investigations of gas turbine combustor cooling concepts under realistic operating conditions”. Proceedings of the Institution of Mechanical Engineers, Part G: Jorunal of Aerospace Engineering 222 (2), pp. 169-177.

[121] Stopper, U., Meier, W., Sadanandan, R., Stohr, M., Aigner, M., and Bulat, G., 2013, “Experimental study of industrial gas turbine flames including quantification of pressure influence on flow field, fuel/air premixing and flame shape,” Combustion and Flame, 160, pp. 2103-2118.

[122] Weigand, P., Meier, W., Duan, X.R., Stricker, W., and Aigner, M., 2006, “Investigations of swirl flames in a gas turbine model combustor I. Flow field, structures, temperature and species distributions,” Combustion and Flame 144, pp. 205-224.

[123] Meier, W., Weigand, P., Duan, X.R., and Giezendanner-Thoben R., 2007, “Detailed characterization of the dynamics of thermoacoustic pulsations in a lean premixed swirl flame,” Combustion and Flame 150 (1-2), pp. 2-26.

[124] Beerer, D., 2013, “Combustion Characteristics and Performance of Low-Swirl injectors with Natural Gas and Alternative Fuels at Elevated Pressures and Temperatures,” Dissertation, Dept. of Mechanical and Aerospace Engineering, Univervisity of California Irvine, Irvine, CA.

[125] International Society of Automation (ISA), 2007, “ISA-75.01.01: Flow Equations for Sizing Control Valves,” 60534-2-1 Mod.

[126] American Society of Mechanical Engineers (ASME), 2012, “ASME B31-Standards for Pressure Piping”.

[127] American Society of Mechanical Engineers (ASME), 2004, “ASME Boiler and Pressure Vessel Code (BPVC)”.

[128] Lai, G.Y., 2007, High-Temperature Corrosion and Materials Applications, ASM International, Ohio, US.

[129] National Fire Protection Association (NFPA), 2015, “NFPA 37: Standard for the installation and use of stationary combustion engines and gas turbines,”.

[130] Lengani, D., Simoni, D., Ubaldi, M., and Zunino, P., 2014, "POD analysis of the unsteady behavior of a laminar separation bubble," Experimental Thermal and Fluid Science, Vol. 58, pp. 70-79.

[131] Berrino, M., Lengani, D., Satta, F., Ubaldi, M., Zunino, P., Colantuoni, S., and Di Martino, P., 2015, “Investigation of the Dynamics of an Ultra-Low NOx Injection System by POD data Post-Processing,”Proceedings of ASME Turbo Expo 2015, 4A, Paper Number: GT2015-42638, pp. V04AT04A049, doi:10.1115/GT2015-42638.

[132] Berkooz, G., Holmes, P., and Lumley, J.L., 1993, “The Proper Orthogonal Decomposition in the Analysis of Turbulent Flows,”Annu. Rev. Fluid Mech., No. 25, pp. 539-575.

[133] Legrand, M., Nogueira, J., and Lecuona, A., 2011, “Flow temporal reconstruction from non-time-resolved data part I: mathematical fundamentals,”Experimental Fluids, 51, pp. 1047-1055. DOI: 10.1007/s00348-011-1111-5.

[134] Legrand, M., Nogueira, J., Tachibana, S., Lecuona, A., and Nauri, S., 2011, “Flow temporal reconstruction from non-time-resolved data part II: practical implementation, methodology validation, and applications,” Experimental Fluids, 51, pp.861-870. DOI: 10.1007/s00348-011-1113-3

[135] Blanchard, R., Wickersham, A.J., Ma, L., Ng, W., and Vandsburger, U., 2014, "Simulating Bluff-Body Flameholders: On the use of proper orthogonal decomposition for combustion dynamics validation," Journal of Engineering for Gas Turbines and Power, Vol. 136, 121504.

[136] Liu, S., and Novoselac, A., 2014, "Transport of Airborne Particles from an Unobstructed Cough Jet," Aerosol Science and Technology, Vol. 48, pp. 1183-1194.

[137] Mejia-Alvarez, R., Christensen, K.T., 2013, "Robust Suppression of Background Reflections in PIV images," Measurement Science and Technology, 24, No. 2, pp. 027003.

[138] Benim, A.C., Pasqualotto, E., and Suh, S.H., 2008, "Modelling turbulent flow past a circular cylinder by RANS, URANS, LES and DES, " Progress in Computational Fluid Dynamics, An Int. J., Vol. 8 No. 5, pp: 299-307.

[139] Dvurechenskii, A.V., Petrov, V.A., Reznik, V.Y., Kornev, V.V. and Levenfel'd, G.Y., 1979. "Investigation of spectral absorption coefficient of KI and KV quartz glasses in IR region to upper temperature limit," Journal of Applied Spectroscopy, Vol. 31, No. 3, pp.1157-1160.

[140] Loenen, E. and Van der Tempel, L., 1996. "Determination of absorption coefficients of glasses at high tempera-tures, by measuring the thermal emission," Philips Research.

[141] Sergeev, O.A., Shashkov, A.G. and Umanskii, A.S., 1982. "Thermophysical properties of quartz glass," Journal of engineering physics, Vol. 43, No. 6, pp.1375-1383.

[142] Chantasiriwan, S., 1999. Inverse heat conduction problem of determining time-dependent heat transfer coefficient. International Journal of Heat and Mass Transfer, 42(23), pp.4275-4285.

[143] Haghighi, M.G., Eghtesad, M., Malekzadeh, P. and Necsulescu, D.S., 2008. Two-dimensional inverse heat transfer analysis of functionally graded materials in estimating time-dependent surface heat flux. Numerical Heat Transfer, Part A: Applications, 54(7), pp.744-762.

[144] Huang, C.H. and Wang, S.P., 1999. A three-dimensional inverse heat conduction problem in estimating surface heat flux by conjugate gradient method. International Journal of Heat and Mass Transfer, 42(18), pp.3387-3403.

[145] Huang, C.H. and Tsai, Y.L., 2005. A transient 3-D inverse problem in imaging the time-dependent local heat transfer coefficients for plate fin. Applied Thermal Engineering, 25(14), pp.2478-2495.

[146] Lee, H.L., Chang, W.J., Chen, W.L. and Yang, Y.C., 2012. Inverse heat transfer analysis of a functionally graded fin to estimate time-dependent base heat flux and temperature distributions. Energy Conversion and Management, 57, pp.1-7.

[147] Wang, T., Lin, M. and Bunker, R.S., 2005. Flow and heat transfer of confined impingement jets cooling using a 3-D transient liquid crystal scheme. International Journal of Heat and Mass Transfer, 48(23), pp.4887-4903.

[148] Lin, M. and Wang, T., 2002. A transient liquid crystal method using a 3-D inverse transient conduction scheme. International journal of heat and mass transfer, 45(17), pp.3491-3501.

[149] Rutledge, J.L. and Mccall, J.F., The United States of America, as represented by the Secretary of the Air Force, 2016. Method for determining time-resolved heat transfer coefficient and adiabatic effectiveness waveforms with unsteady film cooling. U.S. Patent 9,316,547.

[150] Gregory P. Smith, David M. Golden, Michael Frenklach, Nigel W. Moriarty, Boris Eiteneer, Mikhail Goldenberg, C. Thomas Bowman, Ronald K. Hanson, Soonho Song, William C. Gardiner, Jr., Vitali V. Lissianski, and Zhiwei Qin, GRI-Mech 3.0, http://www.me.berkeley.edu/gri_mech/

[151] Schott KG1datasheet. http://www.howardglass.com/pdf/kg_1_datasheet.pdf

[152] Melling, A., 1997. Tracer particles and seeding for particle image velocimetry. Measurement Science and Technology, 8(12), p.1406.

[153] Abraham, S., "Heat Transfer and Flow Measurements on a One-Scale Gas Turbine Can Combustor Model," Master of Science Thesis, Dept. of Mechanical Engineering, Virginia Polytechnic Institute and State University, Blacksburg, VA, 2008.

[154] Carmack, A.C., "Heat Transfer and Flow Measurements in a Gas Turbine Engine Can and Annular Combustors," Master of Science Thesis, Dept. of Mechanical Engineering, Virginia Polytechnic Institute and State University, Blacksburg, VA, 2012.

[155] Sedalor, T., “Heat Transfer and Flow Characteristics Study in a Low Emission Annular Combustor,” Master of Science Thesis, Dept. of Mechanical Engineering, Virginia Polytechnic Institute and State University, Blacksburg, VA, 2009.

[156] Goh, Y-S., “Heat Transfer and Flow Characteristics inside a Gas Turbine Combustor,” Master of Science Thesis, Dept. of Mechanical Engineering, Louisiana State University, Baton Rouge, LA, 2003.

[157] Omrane, A., Petersson, P., Aldén, M. and Linne, M.A., 2008. Simultaneous 2D flow velocity and gas temperature measurements using thermographic phosphors. Applied Physics B, 92(1), pp.99-102.

# APPENDIX

## A. TECHNICAL DRAWINGS AND PHOTOGRAPHS OF THE COMBUSTOR FACILITY

These technical drawings are presented in the order in which they were designed, matching the order in which the facility was constructed. Each piece/spool had its own technical drawing with the appropriate dimensions for fabrication, but these are not shown to reduce the number of technical drawings (over 60 total). Only the design of the main components are included for future reference.

First the test cell dimensions were measured. This was important while tracing the piping to avoid blocking the cell window, and allowing sufficient space for walking and other components in the room. The valve and heater line were then designed, followed by the actual burner test section. The beginning of the provisions for high pressure operation are also included here. The pressure vessel design, although conceptually complete has not been through engineering analysis/detailed design and is hence not included.

### A.1 Test cell and air line design drawings

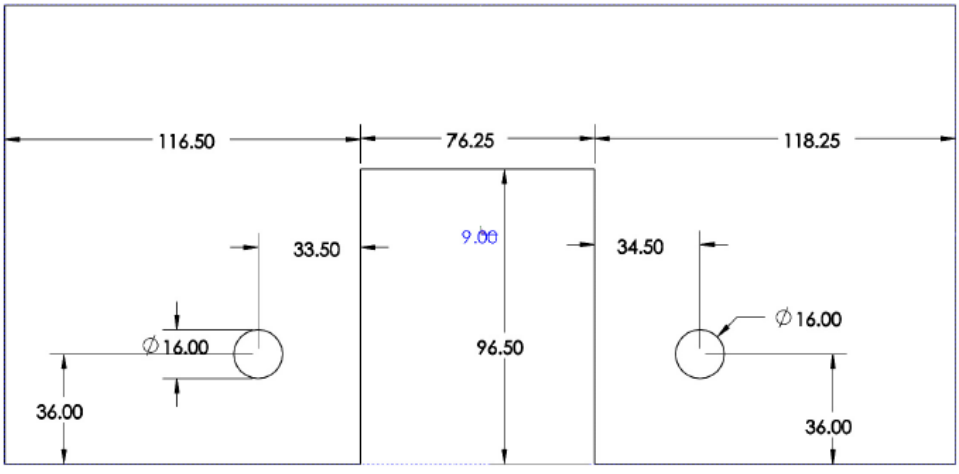


**Figure 118.** Dimensions of the backdoor wall. Double door in the center and exhaust ports to the sides.

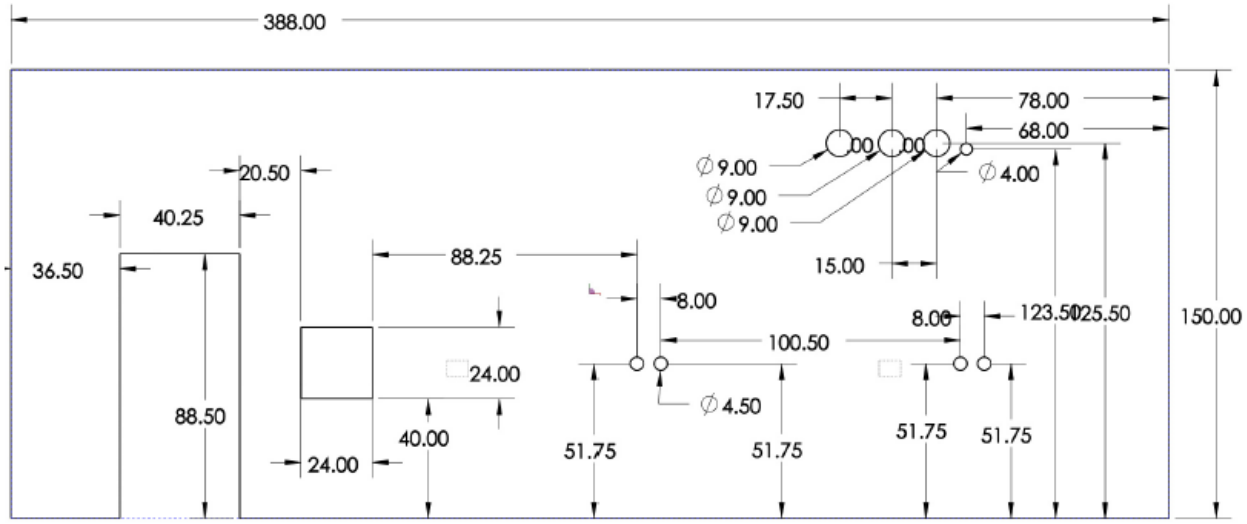


**Figure 119.** Side wall technical drawing (inverted horizontally). Door and window are shown as well as ports for instrumentation along the wall. The top right openings indicate the location where the process air pipeline and water lines came into the room.

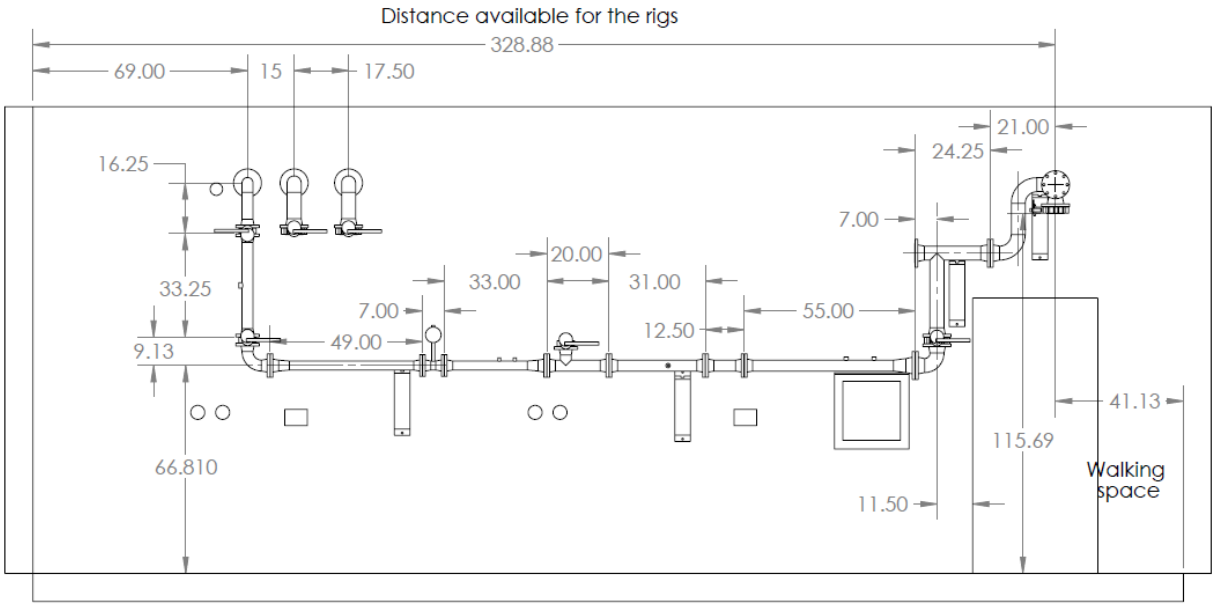


**Figure 120.** Design of the process air pipe line.

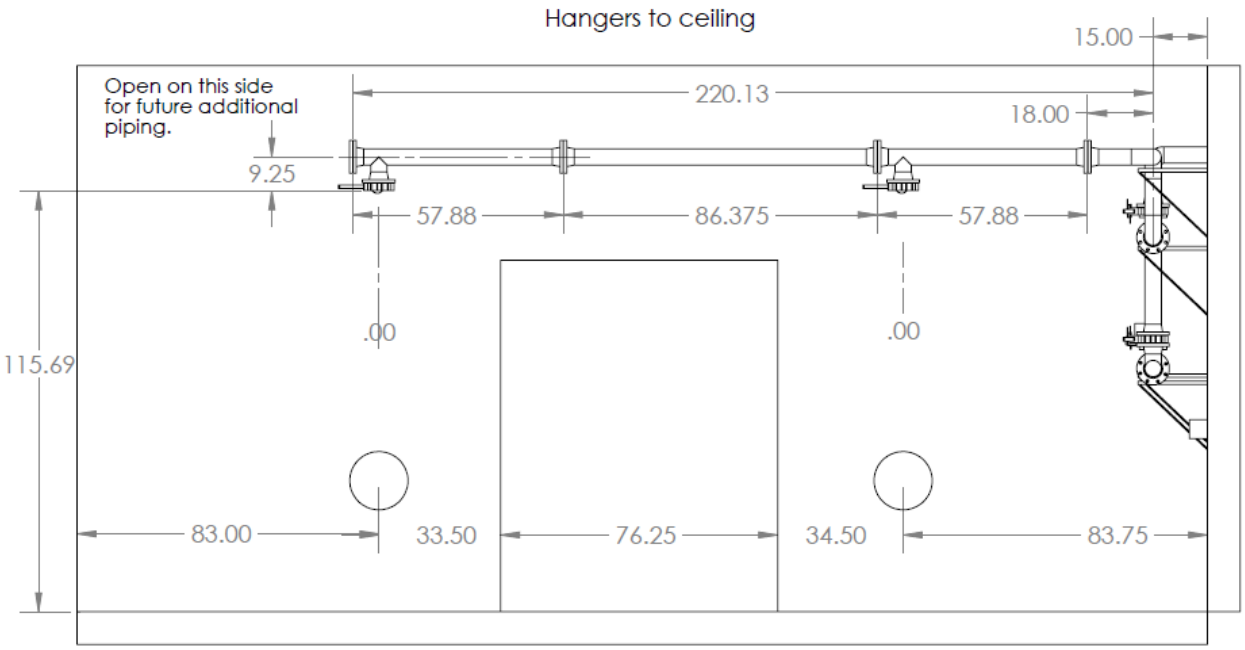


**Figure 121.** Design of the process pipe line showing the location of the drops for the experimental setups.

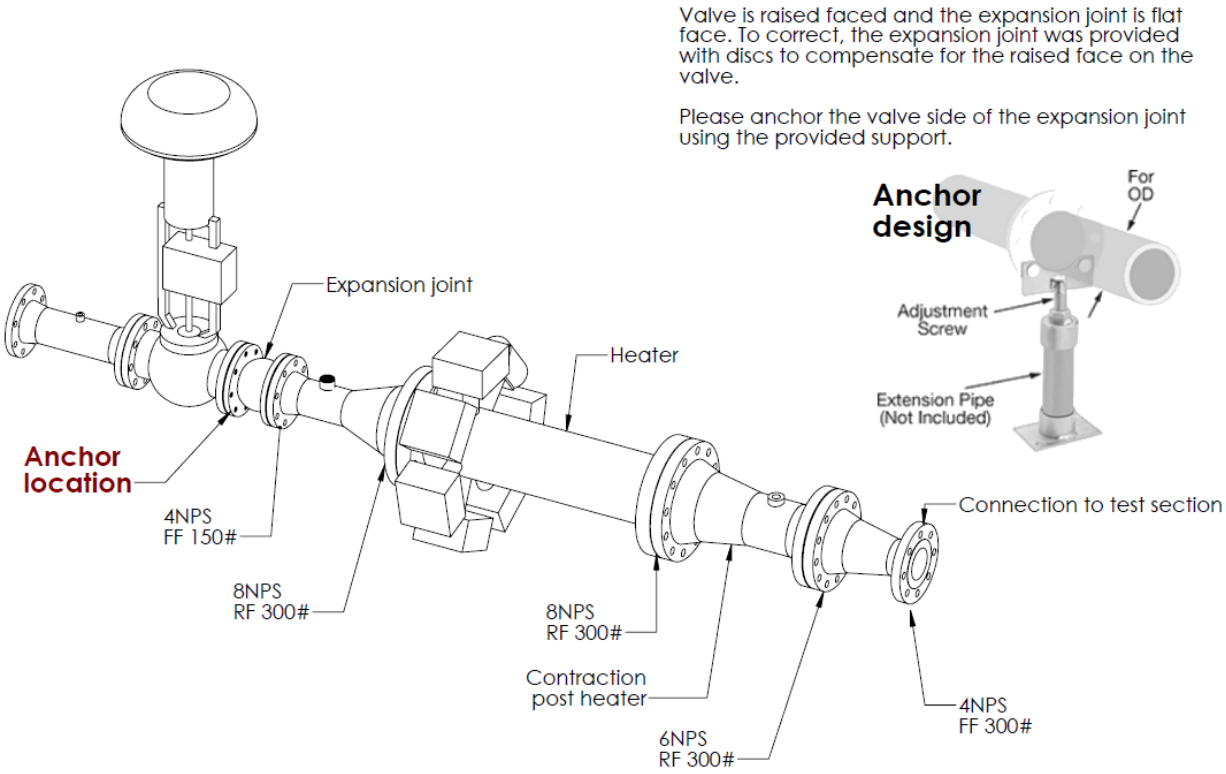


**Figure 122.** Design of the main valve and preheater line. The anchor was placed downstream of the main air valve to control the thermal expansion of the downstream pipeline.

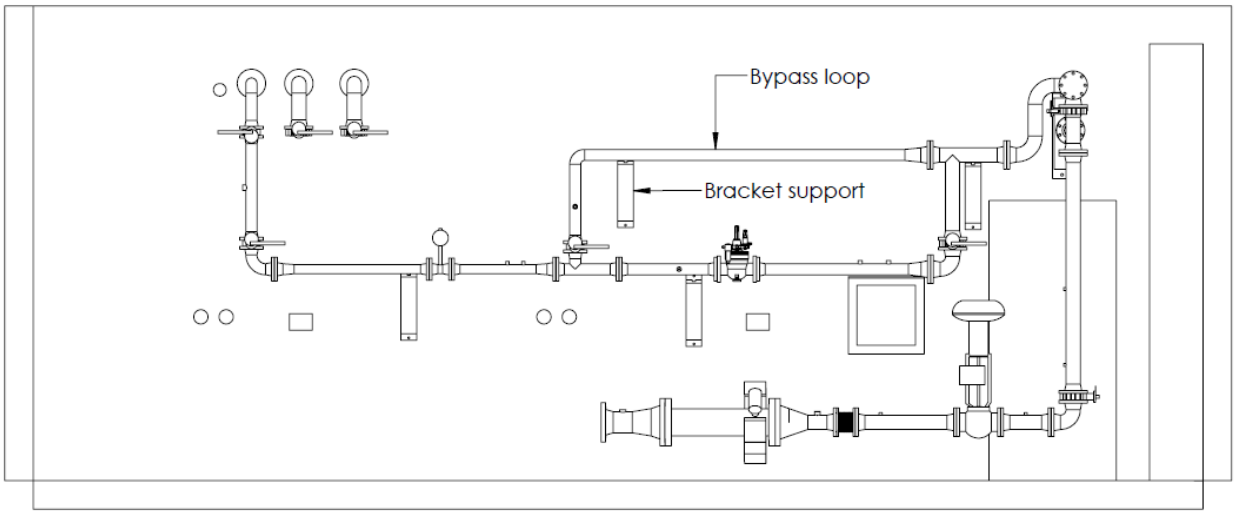


**Figure 123.** Design drawing of the components upstream of the test section, showing the pressure regulator bypass loop for operation at high pressure.

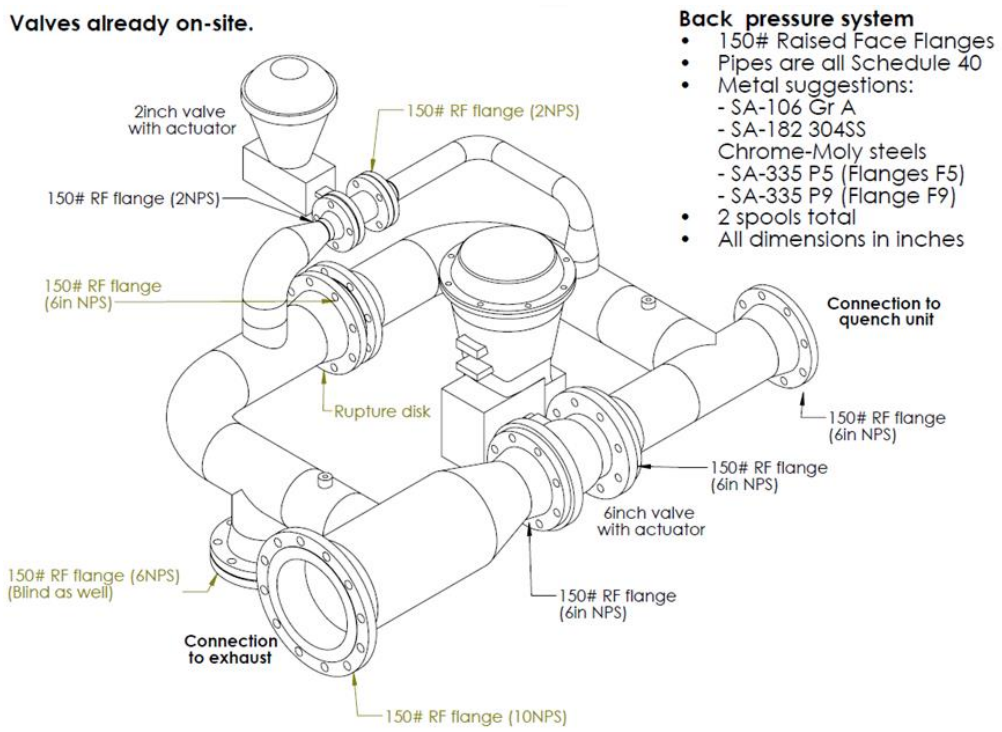


**Figure 124.** Back pressure system design (not yet manufactured due to budget constraints).

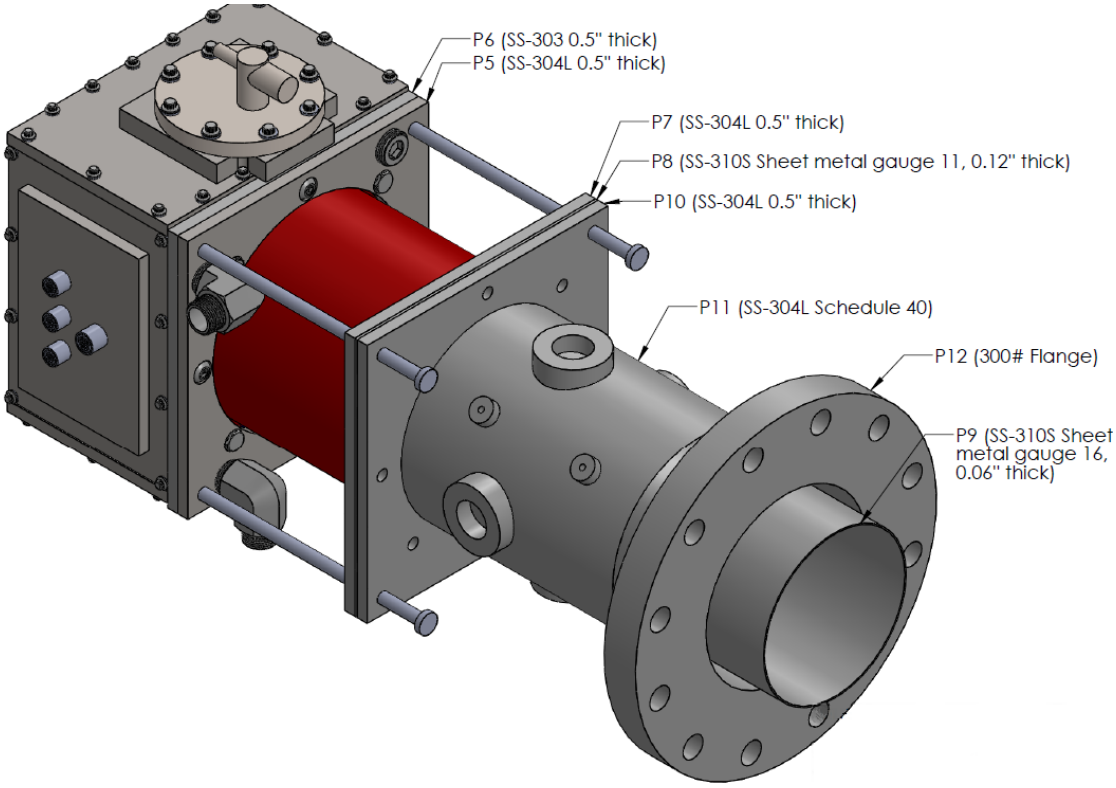


**Figure 125.** Test section components, indicating the material used for each portion. ASTM A516 ½ inch thick carbon steel plates (12 × 12 inches) were used for the upstream settling chamber. See chapter 3 for further details on the test section design.

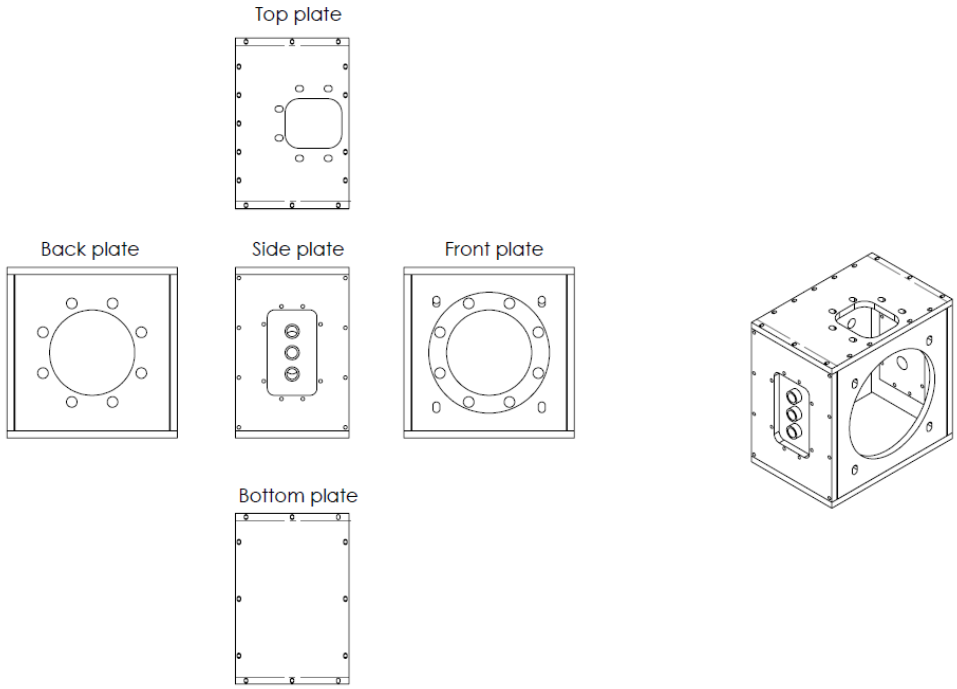


**Figure 126.** Settling chamber design. The back plate connects to the upstream piping. The front plate connects to the dome plates that hold the liner (see Chapter 3). The top plate holds the fuel nozzle and the side plates were designed for instrumentation.

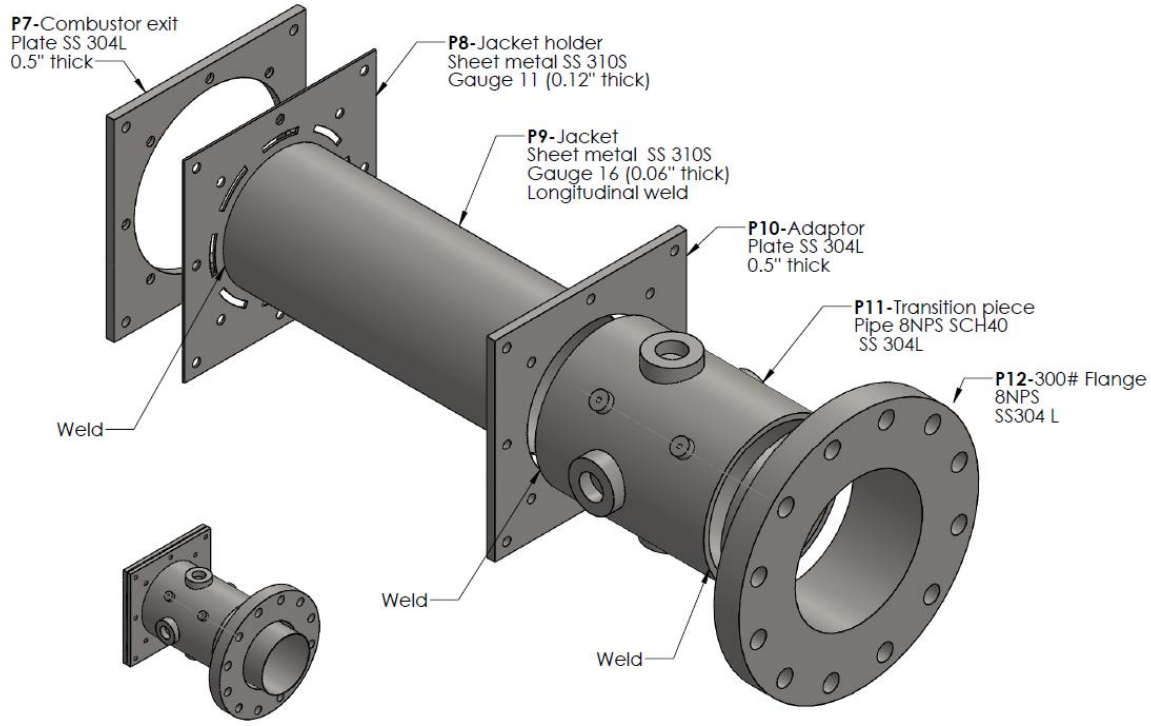


**Figure 127.** Transition piece design. This piece connects the quartz liners to the exhaust piping. The slots in part P8 allow coolant to pass from between the two liners into the transition piece jacket (P9). Additional cooling can be introduced through the ports in P11. At the time of writing only the ports on P11 were used, successfully cooling the transition piece during the experiments.

## A.2 Test cell photographs

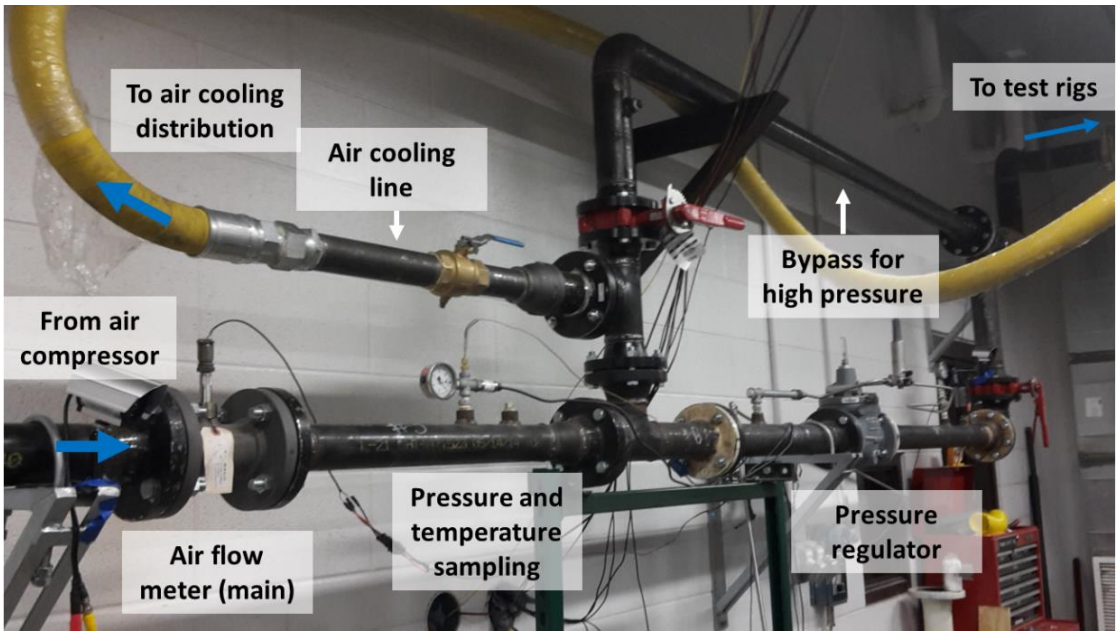


**Figure 128.** Main air pipeline showing the flow meter, pressure regulator and connection to the air cooling distribution system.

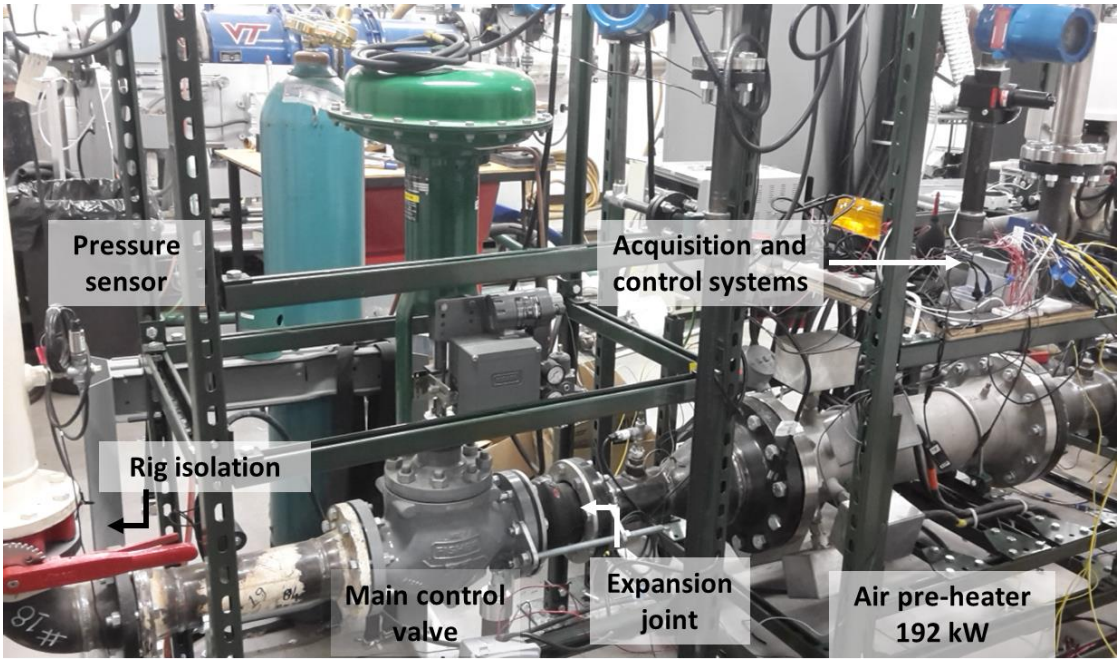


**Figure 129.** Main air control valve and pre heater. See Figure 122.

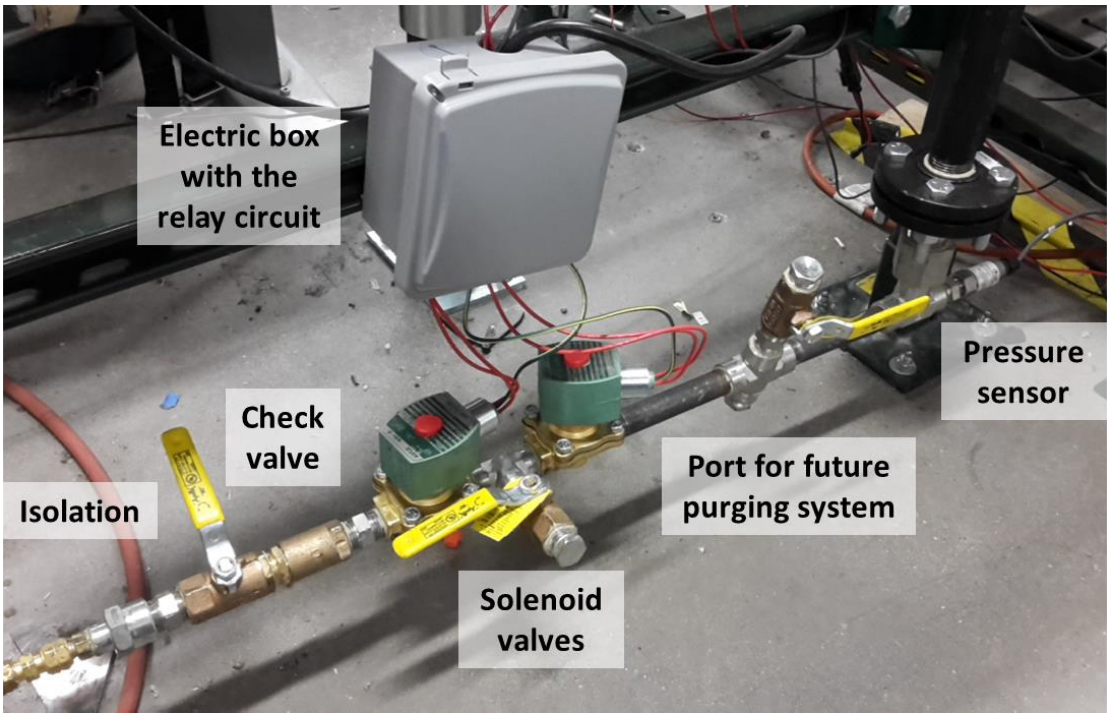


**Figure 130.** Fuel line connection and control using solenoid valves.

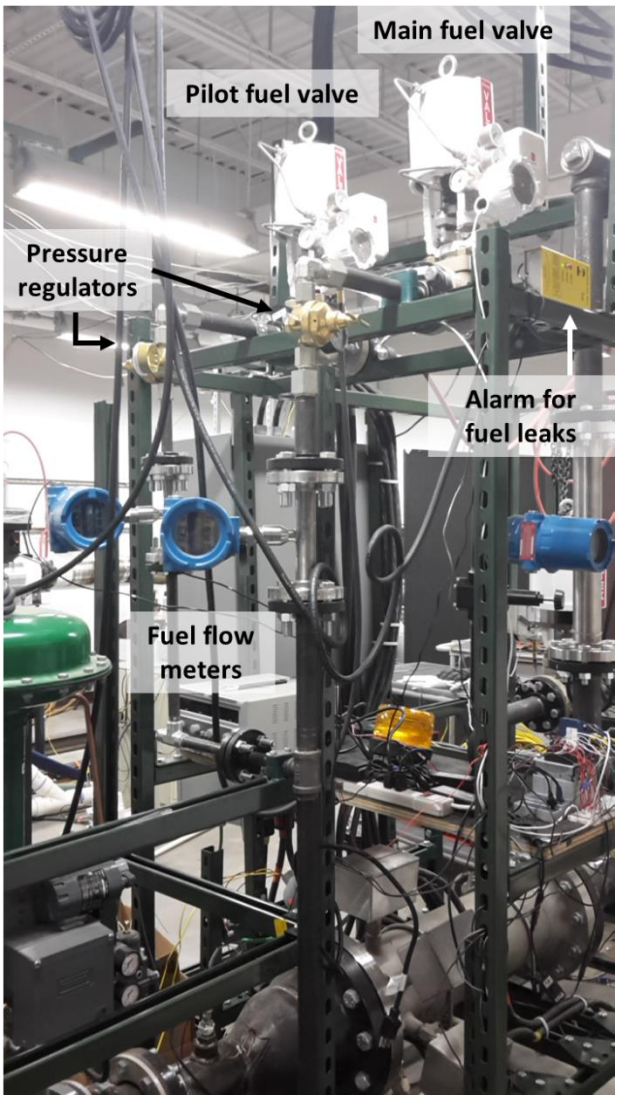


**Figure 131.** Fuel line mass flow metering and control valves.

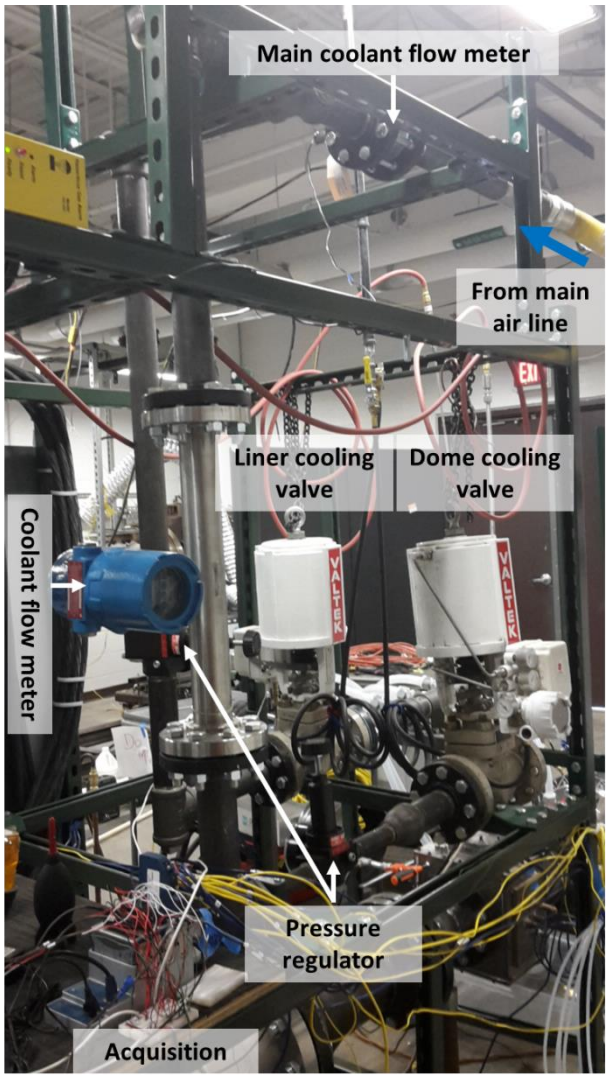


**Figure 132.** Air cooling distribution.

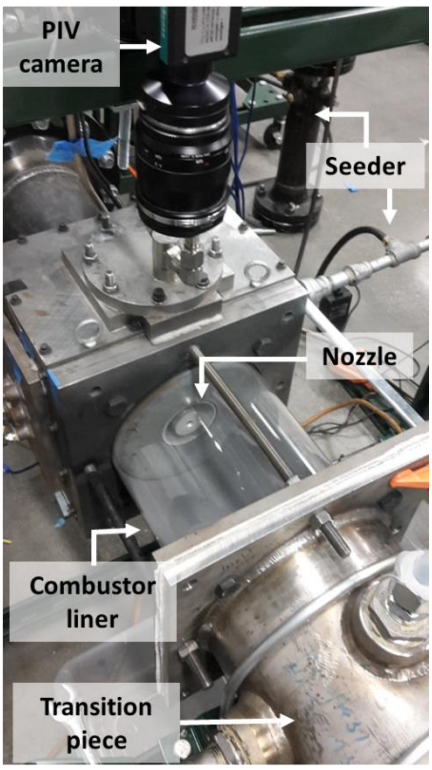


**Figure 133.** Top view of the test section designed. Instrumentation for the PIV was installed when taking this photograph.

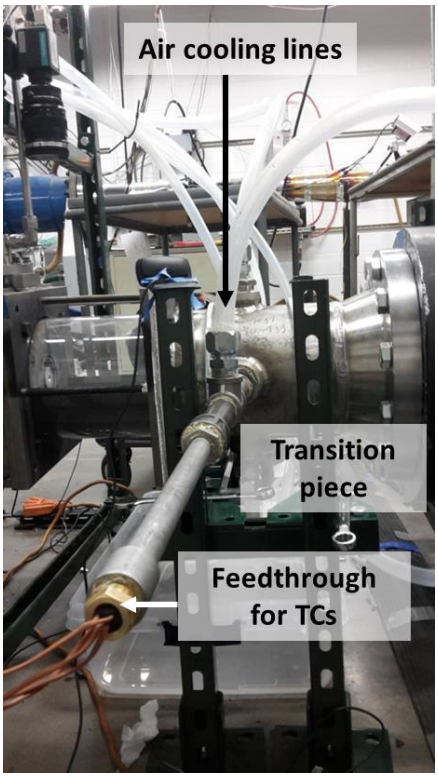


**Figure 134.** Transition piece with feedthrough for the TC (feedthrough can withstand up to 120 PSIG). The coolant hoses for low pressure operation are shown (at high pressure these will be replaced by stainless steel tubing).

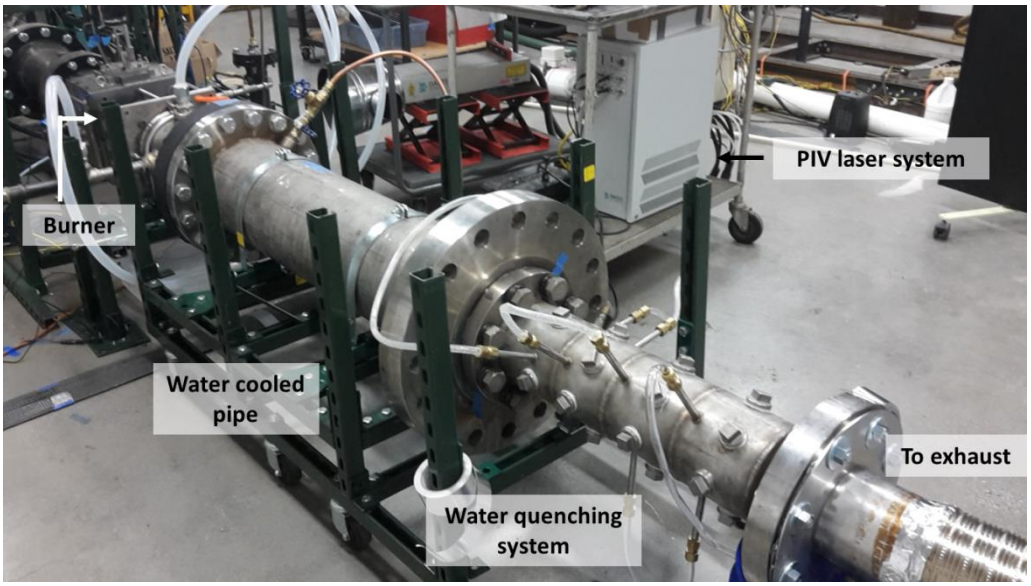


**Figure 135.** Water cooling systems and connection the exhaust. The quenching unit supports, as well as the testing of the quench and water cooling systems were performed by Siddhartha Gadiraju.